Institut für Physik und Astronomie

Arbeitsgruppe Prof. Dr. Anders Levermann

The Marine Ice Cliff Instability of the Antarctic Ice Sheet

A theory of mélange-buttressed cliff calving and its application in the Parallel Ice Sheet Model

Kumulative Dissertation

zur Erlangung des akademischen Grades
"doctor rerum naturalium" (Dr. rer. nat.)
in der Wissenschaftsdisziplin "Klimaphysik"

eingereicht an der
Mathematisch-Naturwissenschaftlichen Fakultät
der Universität Potsdam

angefertigt am
Potsdam-Institut für Klimafolgenforschung

von

Tanja Schlemm

Berlin, im Juni 2022

Betreuer und Erstgutachter:	Prof. Anders Levermann
Zweitbetreuerin und Zweitgutachterin:	Prof. Ricarda Winkelmann
Drittgutachter:	Dr. Martin Stendel
Prüfungskommission:	Prof. Ralf Metzler (Vorsitz) Prof. Ulrike Herzschuh Prof. Markus Rex

Published online on the
Publication Server of the University of Potsdam:
https://doi.org/10.25932/publishup-58633
https://nbn-resolving.org/urn:nbn:de:kobv:517-opus4-586333

Declaration of authorship

Name: Schlemm
First name: Tanja

I declare to the Institut für Physik und Astronomie that I have completed the submitted dissertation independently and without the use of sources and aids other than those indicated. The present thesis is free of plagiarism. I have marked as such all statements that are taken literally or in content from other writings. This dissertation has not been submitted in the same or similar form in any previous doctoral procedure.

I agree to have my thesis examined by a plagiarism examination software.

Date: _____ Signature: _____

Abstract

The Antarctic ice sheet is the largest freshwater reservoir worldwide. If it were to melt completely, global sea levels would rise by about 58 m (Fretwell et al., 2013). Calculation of projections of the Antarctic contribution to sea level rise under global warming conditions is an ongoing effort (Church et al., 2013a, Slangen et al., 2017, Levermann et al., 2020) which yields large ranges in predictions. Among the reasons for this are uncertainties related to the physics of ice sheet modeling (Noble et al., 2020, Pattyn and Morlighem, 2020). These uncertainties include two processes that could lead to runaway ice retreat: the Marine Ice Sheet Instability (MISI), which causes rapid grounding line retreat on retrograde bedrock (Weertman, 1974, Schoof, 2007), and the Marine Ice Cliff Instability (MICI), in which tall ice cliffs become unstable and calve off, exposing even taller ice cliffs (DeConto and Pollard, 2016).

In my thesis, I investigated both marine instabilities (MISI and MICI) using the Parallel Ice Sheet Model (PISM, Bueler and Brown (2009), Winkelmann et al. (2011)), with a focus on MICI.

To investigate MISI, I participated in the Antarctic BUttressing Model Intercomparison Project (ABUMIP, Sun et al. (2020)), which considered an extreme mass-loss scenario in which all Antarctic ice shelves were removed instantaneously. This resulted in an ice mass loss equivalent to a sea level rise of 1–12 m in 500 a. This result demonstrates the enormous potential of MISI to contribute to global sea level rise, but also highlights the large model uncertainties.

For the main part of the thesis, I focused on MICI and developed two simple models that parameterize the processes most relevant to MICI. First, I investigated the instability of large ice cliffs. Bassis and Walker (2011) had shown that tall ice cliffs are unstable, but did not provide a calving rate which could be implemented in a large-scale ice sheet model. I used a simple numerical model and assumed shear failure as the main failure process for cliff calving. From this, I derived a calving rate that grows exponentially with ice thickness (Schlemm and Levermann, 2019). These calving rates can become unrealistically large. Therefore, I next analyzed ice mélange, a mixture of sea ice and icebergs, which has been observed to buttress calving glaciers (Walter et al., 2012). I proposed a negative feedback loop, in which calving produces mélange and mélange buttressing limits calving

rates. This provides an upper limit to the cliff calving rate I derived previously (Schlemm and Levermann, 2021).

Finally, I implemented both parameterizations in PISM. Since glaciers in the Amundsen region of the West Antarctic Ice Sheet are vulnerable to MISI (Joughin et al., 2014) and possibly to MICI (Wise et al., 2017, Lhermitte et al., 2020), I performed and analyzed simulations for this region. Ice shelf removal similar to the ABUMIP study, but only locally in the Amundsen region, triggers MISI and results in a sea level rise of 0.7 m in a century. If cliff calving is added, the additional contribution of MICI depends on the strength of mélange buttressing and ranges from less than 0.1 m in the case of strong buttressing to more than 2 m in the case without buttressing. I have also found that regardless of initial mélange strength, as MICI progresses, mélange buttressing increases, thereby slowing further progress of MICI. This study shows that the MICI contribution to sea level is still subject to great uncertainty, but it also shows that the MICI can be slowed after its onset (Schlemm et al., 2022).

Zusammenfassung

Der antarktische Eisschild ist das größte Süßwasserreservoir der Welt. Würde er vollständig schmelzen, würde der globale Meeresspiegel um etwa 58 m ansteigen (Fretwell et al., 2013). Die Ermittlung von Prognosen über den Beitrag der Antarktis zum Anstieg des Meeresspiegels infolge der globalen Erwärmung ist ein fortlaufender Prozess (Church et al., 2013a, Slangen et al., 2017, Levermann et al., 2020), der große Unterschiede in den Vorhersagen zur Folge hat. Einer der Gründe dafür sind Ungewissheiten im Zusammenhang mit der Physik der Eisschildmodellierung (Noble et al., 2020, Pattyn and Morlighem, 2020). Zu diesen Unsicherheiten gehören zwei Prozesse, die zu einem unkontrollierten Eisrückzug führen könnten: die Marine Ice Sheet Instability (MISI), die zu einem schnellen Rückzug der Grundlinie auf rückläufigem Grundgestein führt (Weertman, 1974, Schoof, 2007), und die Marine Ice Cliff Instability (MICI), bei der hohe Eisklippen instabil werden und abkalben, wodurch noch höhere Eisklippen freigelegt werden (DeConto and Pollard, 2016).

In meiner Dissertation untersuchte ich beide marinen Instabilitäten (MISI und MICI) mit Hilfe des Parallel Ice Sheet Model (PISM, Bueler and Brown (2009), Winkelmann et al. (2011)), wobei der Schwerpunkt auf MICI lag.

Zur Untersuchung von MISI habe ich am Antarctic BUttressing Model Intercomparison Project (ABUMIP, Sun et al. (2020)) teilgenommen, bei dem ein extremes Massenverlustszenario betrachtet wurde, bei dem alle antarktischen Schelfeisflächen unmittelbar entfernt wurden. Dies führte zu einem Eismassenverlust, der einem Anstieg des Meeresspiegels im Bereich von 1–12 m in 500 Jahren entspricht. Dieses Ergebnis zeigt das enorme Potenzial von MISI, zum globalen Meeresspiegelanstieg beizutragen, verdeutlicht aber auch die großen Modellunsicherheiten.

Im Hauptteil der Arbeit habe ich mich auf MICI konzentriert und zwei einfache Modelle entwickelt, mit denen die für MICI wichtigsten Prozesse parametrisiert werden. Zunächst untersuchte ich die Instabilität von großen Eisklippen. Bassis and Walker (2011) hatte bereits gezeigt, dass hohe Eisklippen instabil sind, aber keine Kalbungsrate geliefert, die in ein großräumiges Eisschildmodell implementiert werden könnte. Ich verwendete ein einfaches numerisches Modell und nahm Scherbruch als Hauptversagensprozess für das Kalben von Klippen an. Daraus leitete ich eine Kalbungsrate ab, die exponentiell mit der Eisdicke zunimmt (Schlemm and Levermann, 2019). Diese Kalbungsraten können unrealistisch groß

werden. Daher analysierte ich als Nächstes die Eismelange, eine Mischung aus Meereis und Eisbergen, von der beobachtet wurde, dass sie kalbende Gletscher abstützt (Walter et al., 2012). Ich schlug eine negative Rückkopplungsschleife vor, in der das Kalben Mélange erzeugt und die Abstützung durch Mélange die Kalbungsrate begrenzt. Dies ergibt eine Obergrenze für die von mir zuvor abgeleitete Kalbungsrate von Eisklippen (Schlemm and Levermann, 2021).

Schließlich habe ich beide Parametrisierungen in PISM implementiert. Da die Gletscher in der Amundsen-Region des Westantarktischen Eisschilds für MISI (Joughin et al., 2014) und möglicherweise für MICI (Wise et al., 2017, Lhermitte et al., 2020) anfällig sind, habe ich Simulationen für diese Region durchgeführt und analysiert. Die Entfernung von Schelfeis ähnlich wie in der ABUMIP-Studie, allerdings nur lokal in der Amundsen-Region, löst MISI aus und führt zu einem Meeresspiegelanstieg von 0.7 m in einem Jahrhundert. Wenn das Kalben von Klippen hinzukommt, hängt der zusätzliche Beitrag von MICI von der Stärke der Mélange-Abstützung ab und reicht von weniger als 0.1 m im Fall einer starken Abstützung bis zu mehr als 2 m im Fall ohne Abstützung. Ich habe auch festgestellt, dass unabhängig von der anfänglichen Mélange-Stärke mit fortschreitender MICI die Mélange-Abstützung zunimmt und damit das weitere Fortschreiten der MICI verlangsamt wird. Diese Studie zeigt, dass der MICI-Beitrag zum Meeresspiegel immer noch mit großer Unsicherheit behaftet ist, aber sie zeigt auch, dass MICI nach seinem Einsetzen verlangsamt werden kann (Schlemm et al., 2022).

Contents

Introduction

1.1 The Antarctic Ice Sheet in a warming climate

About 10% of the world's population live in coastal areas that are less than 10 m above the present sea level (McGranahan et al., 2007). Due to global warming (Church et al., 2013b), these coastal areas worldwide are threatened by global mean sea level rise (Brooks et al., 2006, McGranahan et al., 2007, Hauer et al., 2020).

Since 1900 global mean sea level has risen by (18 ± 4) cm (Frederikse et al., 2020). Mountain glaciers have contributed about 8 cm, the Greenland ice sheet about 5 cm, ocean thermal expansion about 4 cm and the Antarctic Ice Sheet about 1 cm to this sea level rise (Frederikse et al., 2020). The relative contributions change with time: The current speedup in sea level rise is driven by the accelerating thermal expansion of the ocean and increasing mass loss from the Greenland ice sheet (Frederikse et al., 2020). Over 1993–2018, the ocean thermal expansion contributed 1.19 mm/a, mountain glaciers 0.67 mm/a, the Greenland ice sheet 0.65 mm/a and the Antarctic Ice Sheet 0.32 mm/a to the global mean sea level rise rate (Frederikse et al., 2020).

Global mean sea level projections until 2100 have large uncertainty and depend on the greenhouse gases emission scenario: the expected global mean sea level rise lies between 0.5–1.2 m under the high emissions scenario RCP 8.5 (RCP - representative concentration pathway), between 0.4–0.9 m under the moderate emissions scenario RCP 4.5 and between 0.3–0.8 m under the low emissions scenario RCP 2.6 (Kopp et al., 2014). Calculating projections of the contributions from the Greenland and Antarctic Ice Sheet to sea level rise is ongoing work (Church et al., 2013a, Kopp et al., 2014, Ritz et al., 2015, DeConto and Pollard, 2016, Mengel et al., 2016, Kopp et al., 2017, Slangen et al., 2017, Golledge et al., 2019, Levermann et al., 2020, Edwards et al., 2021, DeConto et al., 2021). For example, the Antarctic Ice Sheet may contribute between 9–36 cm under RCP 8.5 or 7–24 cm under RCP 2.6 to global sea level rise until 2100 (Levermann et al., 2020). The large range in predictions of the Antarctic contribution is due to uncertainties regarding the physics of ice sheet modelling (Noble et al., 2020, Pattyn and Morlighem, 2020).

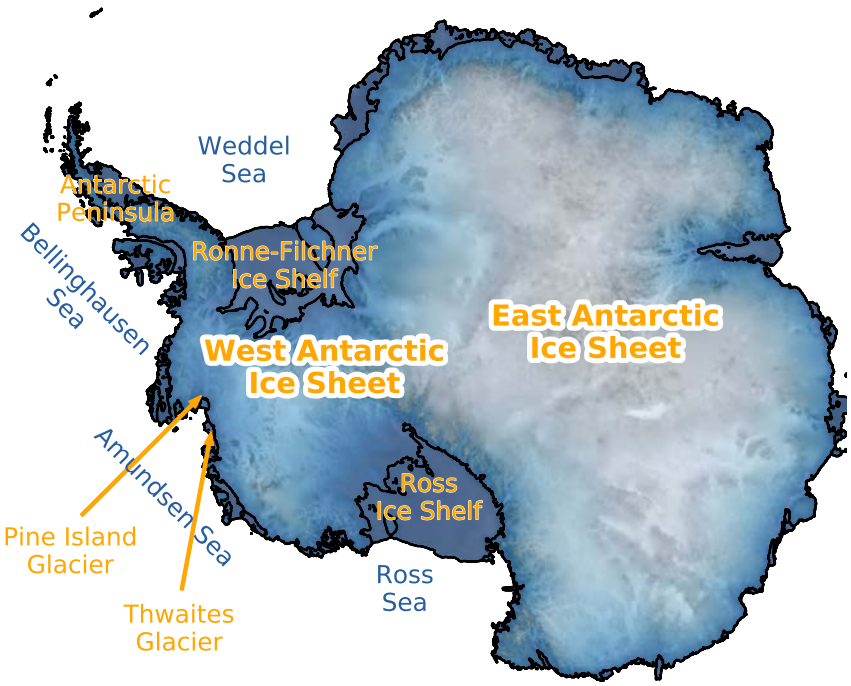

Fig. 1.1. A map of the Antarctic Ice Sheet. The West Antarctic Ice Sheet is especially vulnerable to ice sheet instabilities because it is grounded on bedrock below sea level.

The response time of ice sheets to climatic changes is slow compared to other elements of the climate system. Therefore the evolution of ice sheets is especially important in the long-term on centennial to millennial time scales. Even low emissions scenario have a larger overall sea level commitment over several centuries (Mengel et al., 2018). If all ice was to melt, the ice sheets in Greenland and Antarctica would account for potential sea-level contributions of 7.4 m (Morlighem et al., 2017) and 58.3 m (Fretwell et al., 2013), respectively. Smaller ice caps and glaciers would account for an additional 0.42 m (Vaughan et al., 2014). Burning all fossil fuels from currently accessible resources would be sufficient to melt the Antarctic Ice Sheet completely within 10.000 years (Winkelmann et al., 2015).

1.2 Processes determining the mass balance of the Antarctic Ice Sheet

The sea level contribution of the Antarctic Ice Sheet is determined by its mass balance: Ice sheets gain mass by accumulation of snow and lose mass by surface or basal melting and calving of icebergs. An overall mass loss corresponds to a positive sea level contribution.

For the Antarctic Ice Sheet, basal melting and calving discharge are the main contributors to mass loss, while surface melting contributes less due to the cold regional climate (Rignot et al., 2019).

Whereas the Greenland ice sheet experiences widespread surface melting (Mernild et al., 2011, Ryan et al., 2019) and extreme melt years (Nghiem et al., 2012), there are only few regions of the Antarctic Ice Sheet where surface melting is important, e.g., on the Antarctic peninsula with a surface melt rate of 30 cm/a (Trusel et al., 2015). Some of Antarctica's mass losses are offset by snowfall: Currently, Antarctica has a mean snowfall accumulation rate of 17 cm/a (Palerme et al., 2014). As the atmosphere warms, the warmer air can hold more moisture and snowfall in Antarctica may increase (Frieler et al., 2015).

Basal melting of ice shelves is the main contribution to Antarctica's mass loss (Depoorter et al., 2013). Ocean warming around Antarctica (Schmidtko et al., 2014) increases the basal melt rates under Antarctic ice shelves (Naughten et al., 2018). As a consequence, ice shelves become thinner (Paolo et al., 2015), particularly in the Amundsen and Bellinghausen regions (Shepherd et al., 2018). While ice shelves do not contribute to sea level rise directly, they buttress the glaciers flowing into the shelf (Schoof, 2006). If the shelves are weakened due to thinning, the ice flow accelerates (Reese et al., 2018), increasing Antarctic ice loss (Smith et al., 2020). For a glacier on a retrograde bed, such as Thwaites Glacier, this acceleration may lead to runaway ice retreat in a process called the Marine Ice Sheet Instability (MISI) (Weertman, 1974, Scambos et al., 2017).

Icebergs calve from ice shelves or grounded glaciers. Grounded glaciers, such as tidewater glaciers in Greenland, produce icebergs with a horizontal extent smaller than the ice thickness (van Der Veen, 1996, Chapuis and Tetzlaff, 2014, Benn et al., 2017b). Ice shelves surrounding the Antarctic Ice Sheet produce tabular icebergs (Lazzara et al., 1999), preceded by the formation of rifts (Joughin and MacAyeal, 2005). In rare events, when large amounts of surface melt water forms melt ponds and deepens crevasses, an ice shelf can completely disintegrate into many small icebergs (Scambos et al., 2000, MacAyeal et al., 2003). As a result, inflowing glaciers speed up (Scambos et al., 2004, Rignot et al., 2004) and grounded ice cliffs may be exposed. Depending on the bed topography and ice geometry, this could lead to a self-reinforcing ice retreat, called the Marine Ice Cliff Instability (MICI).

1.3 Iceberg Calving

Modelling calving by describing the nucleation and spreading of crevasses (Pralong and Funk, 2005) is computationally intense and difficult to apply. In order to parametrize calving processes, several approaches have been used:

Based on observations of calving glaciers, semi-empirical height-above-floatation calving laws relate the calving rate to the water depth or the ice thickness (Meier and Post, 1987, van Der Veen, 1996, Vieli et al., 2002). Calving can also be described based on a crevasse criterion: The formation of crevasses was first described by Nye (1957). The applications of the crevasse formulation to calving differ in what crevasse depth is required to separate an iceberg from the glacier terminus (Benn et al., 2007, Nick et al., 2010, Todd et al., 2018). Materials science methods such as linear elastic beam theory (Hughes, 1992) and linear elastic fracture mechanics (Krug et al., 2014) have also been adopted for describing ice failure. However, these approaches are only valid for floating glacier termini (Jiménez and Duddu, 2018). Finally, analytical (Bassis and Walker, 2011) and numerical approaches (Morlighem et al., 2016, Ma et al., 2017, Mercenier et al., 2018) have been used to solve the stress balance in the vicinity of a grounded glacier terminus and to determine the onset and size of calving events, depending on a yield stress criterion.

All these approaches agree on the basic physics of glacier calving: Thicker ice at the terminus leads to larger calving rates. Glaciers terminating in water are stabilized by the water's back-pressure and have smaller calving rates.

1.4 Marine Ice Cliff Instability (MICI)

Uncertainties in the physical modeling of ice sheets mean that projections of the Antarctic Ice Sheet's contribution to global mean sea level rise have a large range. (Noble et al., 2020, Pattyn and Morlighem, 2020). One such uncertainety is iceberg calving, in particular calving from large ice cliffs.

1.4.1 Theory

In an analytical analysis of depth-averaged stresses in the vicinity of the calving front, Bassis and Walker (2011) found that ice cliffs towering more than 100 m above sea level are inherently unstable. If such an ice cliff is situated on retrograde bed topography with ice thickening further inland, ice cliff collapse exposes higher cliffs which are also unstable. This process is called the marine ice cliff instability (MICI) and could lead to runaway ice retreat (Pollard et al., 2015). The interior of the West Antarctic Ice Sheet and overdeepended basins in the East Antarctic Ice Sheet are potentially vulnerable to this instability. Taking MICI into account, the Antarctic Ice Sheet may lose ice faster than previously thought, contributing up to 1 m of sea level rise until 2100 (DeConto and Pollard, 2016).

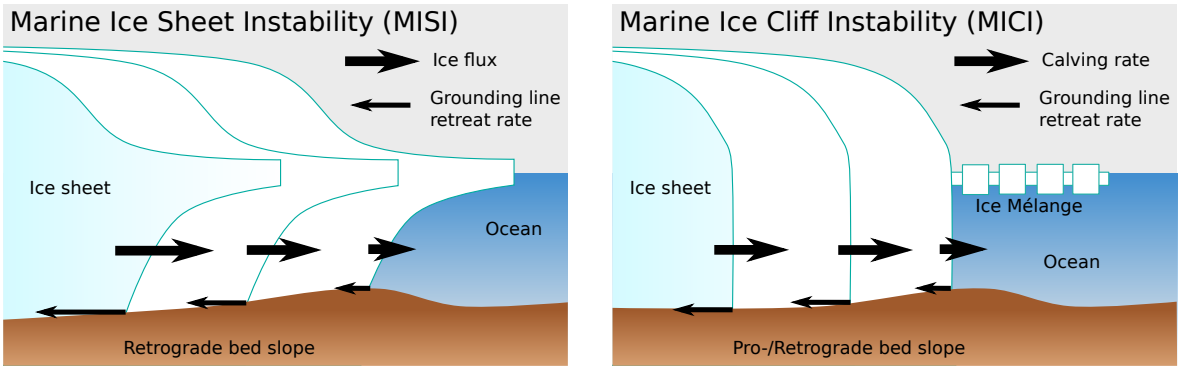

Fig. 1.2. Schematic overview of the marine ice instabilities relevant for the Antarctic Ice Sheet.

1.4.2 Observational evidence

While modeling studies show that Antarctic ice loss during the middle Pliocene and last interglacial can be explained without MICI (Edwards et al., 2019), there is evidence that MICI played a role during the last deglaciation: Iceberg plow marks on the seafloor suggest that MICI was active during the last deglaciation in the Amundsen region of the Antarctic Ice Sheet (Wise et al., 2017) as well as during the retreat of Petermann Glacier in Greenland (Jakobsson et al., 2018).

Only few observations of glaciers currently high enough for cliff calving have been made so far. The terminus of the Jakobshavn Glacier in Greenland towers about 100 m above sea level and its retreat since 1998 (Joughin et al., 2008) suggests that it may be at the beginning of cliff calving (Bassis and Walker, 2011, DeConto and Pollard, 2016). However, due to regional ocean cooling, Jakobshavn Glacier has made a renewed advance since 2016: Decreased frontal melting and increased mélange buttressing at the terminus has stopped the glacier's retreat (Khazendar et al., 2019). This suggests that changes in regional climate conditions may slow or prevent grounding line retreat caused by cliff calving.

Thus, the evidence is not conclusive, neither for the existence of MICI nor for its relevance. However, because it could be tremendously important for future sea level rise, further studies are needed before reliable projections can be made. In particular, the processes relevant to MICI need to be better understood.

1.5 Scope and contents of the thesis

The aim of this thesis is to better understand the processes driving MICI and to estimate its contribution to the sea level potential of the Antarctic Ice Sheet. I studied both marine instabilites (MISI and MICI) using the Parallel Ice Sheet Model (PISM). In the context of a model intercomparison study, I investigated MISI: the buttressing ice shelves of the Antarctic

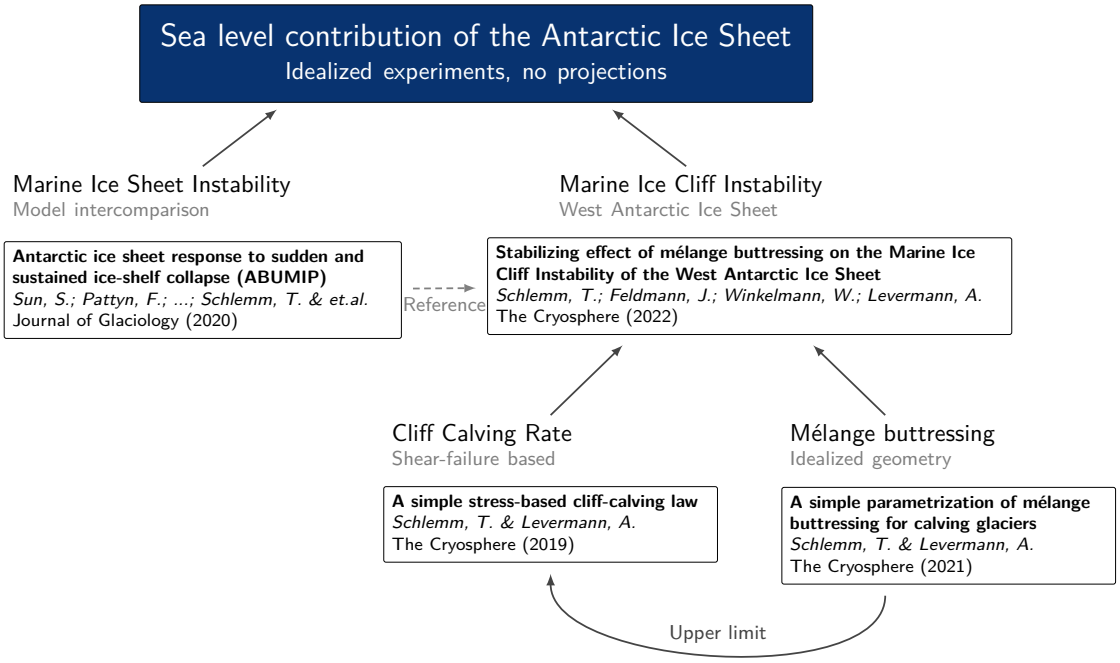

Fig. 1.3. Overview over the papers comprising the thesis

Ice Sheet were removed, which resulted in a runaway ice retreat. In order to estimate the potential sea level contribution of MICI, I developed parametrizations for calving processes and ice mélange. I first derived a cliff calving parametrization based on shear failure, using a numerical model of stresses in the vicinity of an ice cliff. Because cliff calving produces large amounts of icebergs, I parametrized the buttressing effect of ice mélange (a mix of icebergs and sea ice) on the calving front. Finally, I applied mélange-buttressed cliff calving to study the onset and progress of MICI in the West Antarctic Ice Sheet.

Sec. 1.6 gives an overview over the papers comprising the thesis, which are summarized in more detail in chapter 2. This is followed by a discussion in chapter 3 and a conclusion in chapter 4. The original maunscripts can be found in the appendix A.

1.6 Overview of the manuscripts

This thesis comprises four scientific articles, of which three are first-author papers (see fig. 1.3).

1.6.1 Antarctic Ice Sheet response to sudden and sustained ice-shelf collapse (ABUMIP)

Sun, S.; Pattyn, F.; Simon, E. G.; Albrecht, T.; Cornford, S.; Calov, R.; Dumas, C.; Gillet-Chaulet, F.; Goelzer, H.; Golledge, N. R.; Greve, R.; Hoffman, M. J.; Humbert, A.; Kazmierczak, E.; Kleiner, T.; Leguy, G. R.; Lipscomb, W. H.; Martin, D.; Morlighem, M.; Nowicki, S.; Pollard, D.; Price, S.; Quiquet, A.; Seroussi, H.; **Schlemm, T.**; Sutter, J.; van de Wal, R. S. W.; Winkelmann, R. & Zhang, T.

In this model-intercomparison study, the buttressing effect of ice shelves in Antarctica is investigated by removing the ice shelves in numerical ice sheet simulations. This leads to a strong acceleration of the glaciers flowing into the ice shelves and to a high sea level contribution from the Antarctic Ice Sheet. All models predict a sea level rise of several meters (1–12 m) over 500 a from today. The collapse of the West Antarctic Ice Sheet alone leads to a sea level rise of 2–5 m.

Sainan Sun, Frank Pattyn and Nicholas R. Golledge designed and coordinated the study. Sainan Sun and Frank Pattyn led the writing, and Erika G. Simon and Sainan Sun processed the data. Tanja Schlemm, Torsten Albrecht and Ricarda Winkelmann carried out experiments with the Parallel Ice Sheet Model (PISM). All authors contributed to the experiments, writing and discussion of ideas.

Journal of Glaciology **66**, 260, 891–904 (2020).
DOI: 10.1017/jog.2020.67

1.6.2 A simple stress-based cliff-calving law

Schlemm, T. & Levermann, A.

In this paper, we derive an equation that provides an estimate for the calving rate of tall ice cliffs based on ice thickness and water depth. Stresses in the vicinity of an ice cliff are determined using numerical calculations. If the cliff exceeds a height of approx. 100 m above sea level, the shear stress crosses a critical value at which ice fractures, resulting in an iceberg calving event.

Anders Levermann conceived the study. Tanja Schlemm designed and carried out the numerical experiments. Both authors analysed the data, and Tanja Schlemm wrote the manuscript with input from Anders Levermann.

The Cryosphere **13**, 2475–248 (2019).
DOI: 10.5194/tc-13-2475-2019

1.6.3 A simple parametrization of mélange buttressing for calving glaciers

Schlemm, T. & Levermann, A.

In this paper, we investigate the stabilizing effect of ice mélange on cliff calving rates. Calving laws for ice cliffs can result in very large calving rates of several tens of km/yr. This results in the accumulation of many icebergs in a short time. The fragments of these ice bergs form, together with sea ice, an ice mélange in front of the glacier. This mélange buttresses and stabilizes the ice cliff and thus reduces the calving rate.

Both authors conceived the study and analysed the data. Tanja Schlemm developed the basic equations, carried out the experiments, and wrote the manuscript. Anders Levermann contributed to the writing of the manuscript.

The Cryosphere **15**, 531–545 (2021).
DOI: 10.5194/tc-15-531-2021

1.6.4 Stabilizing effect of mélange buttressing on the Marine Ice Cliff Instability of the West Antarctic Ice Sheet

Schlemm, T.; Feldmann, J.; Winkelmann, W. & Levermann, A.

In this paper, we investigate the Marine Ice Cliff Instability of the West Antarctic Ice Sheet with a numerical ice sheet model. Current observations show that the glaciers of the Amundsen region are exposed to a strongly warming ocean. This suggests that these glaciers may lose their buttressing ice shelves in a few decades. Modelling both processes, the loss of buttressing due to collapsed ice shelves and subsequent calving from exposed ice cliffs, shows that the West Antarctic Ice Sheet may contribute between half a meter and more than three meters to sea level rise within a century. Buttressing from ice mélange increases as the grounding line retreats, which results in a slowdown of ice sheet collapse due to MICI.

Tanja Schlemm and Anders Levermann designed the study with input from Ricarda Winkelmann. Johannes Feldmann created the regional setup of the West Antarctic Ice Sheet and performed the spinup. Tanja Schlemm performed the simulations, analyzed the model results, and wrote the manuscript. All authors commented on the manuscript.

The Cryosphere **16**, 1979–1996 (2022)
DOI: 10.5194/tc-16-1979-2022

Summary of papers

Both marine instabilities of the Antarctic Ice Sheet, MISI and MICI, have the potential for large sea level contributions. While the concept of MISI was first proposed in 1974 by Weertman (1974) and it has since then been thoroughly studied (Schoof, 2007, Joughin and Alley, 2011, Favier et al., 2014, Joughin et al., 2014, Ritz et al., 2015, Feldmann and Levermann, 2015, Scambos et al., 2017, Robel and Banwell, 2019), the concept of MICI has only been proposed recently by Pollard et al. (2015) and was investigated in subsequent studies (DeConto and Pollard, 2016, Edwards et al., 2019).

I investigated both marine instabilites (MISI and MICI) using the Parallel Ice Sheet Model (PISM) with a focus on MICI. First, I contributed to estimating the maximum potential sea level contribution of Antarctica through MISI by participating in a model intercomparison study (Sec. 2.1). I further developed parametrizations for calving processes (Sec. 2.2) and for ice mélange (Sec. 2.3). These were implemented in PISM to simulate the potential sea level rise contribution of the Antarctic Ice Sheet through MICI (Sec. 2.4).

2.1 MISI results in large Antarctic ice loss potential

Antarctica's ice shelves have a buttressing effect on grounded inland ice (Dupont and Alley, 2005, Schoof, 2006). Thinning or complete loss of ice shelves therefore leads to acceleration of ice flow and loss of grounded ice (Rignot et al., 2004, Reese et al., 2018). This loss of buttressing may further lead to ice sheet collapse through the Marine Ice Sheet Instability (MISI) (Weertman, 1974, Scambos et al., 2017). The Antarctic BUttressing Model Intercomparison Project (ABUMIP) investigated how the loss of ice shelves controls Antarctic mass loss by comparing simulations made with 15 different ice sheet models.

In my first paper (Sun et al., 2020), I participated in ABUMIP with the Parallel Ice Sheet Model (PISM). We considered an extreme, although not realistic mass loss scenario by instantaneously removing ice shelves throughout the simulations. Three experiments were made with each model: a control run (ABUC) where ice shelves were retained and forcing conditions kept constant, a floatkill experiment (ABUK) where all ice shelves were removed,

and an extreme melt experiment (ABUM) where an extremely high constant melt rate of 400 m/a was applied underneath the ice shelves. Participating ice sheet models were free to choose the initialization procedure as well as the present-day surface mass balance and basal mass balance. After initialization to the beginning of the 21st century, the experiments were run for 500 years.

The control run experiments (ABUC) were used to determine model drift. Despite the lack of forcing, there is a large variation in the modelled ice sheet mass changes. Overall, the results for ABUC are consistent with those of a previous model intercomparison, initMIP Antarctica (Seroussi et al., 2019). The sudden and sustained loss of ice shelves (ABUK) or an extremely high melt rate beneath the ice shelves (ABUM) results in a significant loss of grounded ice for all ice sheet models. The net mass loss after 500 years corresponds to a sea level rise of 2–10 m for ABUK and 1–12 m for ABUM. In all models, most or all of the West Antarctic Ice Sheet was lost.

Our PISM setup was spun up to an equilibrium state with target values for the ice thickness. With a horizontal resolution of 4 km, it was one of the best resolved models in the study. We also applied a subgrid scheme for the grounding line, which further enhances the model's capability to resolve grounding line dynamics. We used a Coulomb sliding law. With about 2 m of sea level contribution for both ABUM and ABUK, our model results were on the lower end compared to the other models.

Previous ice sheet model intercomparison projects (Pattyn et al., 2013, Bindschadler et al., 2013, Nowicki et al., 2016, Seroussi et al., 2019) related the spread of simulation results to differences in grid resolution, ice dynamics, physical processes included in the models, initialization procedures, and numerical schemes. In the ABUMIP study, the differences between models result mainly from the basal sliding and friction law employed. With the same sliding and friction law, there are further differences in the simulation results due to numerical approaches, in particular the spatial resolution across the grounding line and the way grounding line migration is modeled.

Although the results are highly dependent on the model configurations, this extreme scenario shows that due to MISI, the Antarctic Ice Sheet could make a very large contribution to sea level rise.

2.2 A shear-failure based cliff calving model

Bassis and Walker (2011) were the first to show that ice cliffs exceeding a certain ice thickness threshold are inherently unstable. Pollard et al. (2015) then proposed that this instability of high ice cliffs could lead to MICI. The initial study by Bassis and Walker (2011) considered depth-averaged stresses near the calving front with a shear failure criterion. This depth-

averaged approach makes analytic calculations possible but it neglects the vertical structure of stresses and forces at the calving front. Pollard et al. (2015) transformed this stability limit into a rate by assuming a ramp function: calving fronts below the stability limit do not calve and for calving fronts beyond the stability limit, the calving rate ramps up quickly to a maximum value of 5 km/a. An alternative implementation of the stability limit was used in Bassis et al. (2017), where a constraint at the calving front ensures its thickness never exceeds the stability limit. Other calving parametrisations (Ma et al., 2017, Benn et al., 2017a, Mercenier et al., 2018) were made for glaciers below the stability limit and might not be suitable to model cliff calving. Therefore, in my first paper (Schlemm and Levermann, 2019), I derived a simple stress-based parametrization between the cliff calving rate and ice geometry.

As a first step in parametrizing cliff calving, we solved the stress balance in the vicinity of an ice cliff. The stresses in the ice are determined by the two-dimensional Stokes equations and the continuity equation of the ice flow. At the calving front, we assumed traction continuity to the water pressure and no traction above the waterline. For the bed, two boundary conditions were considered: a slip and a no-slip boundary condition, corresponding to a free-sliding glacier and a glacier frozen to the bed, respectively. This boundary value problem was solved with the finite element package FEniCS (Alnæs et al., 2015) and stabilized with the pressure penalty method (Zhang et al., 2011).

Two invariants of the stress tensor were considered: The largest principal stress and the maximum shear stress (see fig. 2.1). Both can be used to describe calving. Crevasses are a natural candidate as the cause for calving. They can form in the upper part of the ice cliff, where the largest principal stress is tensile (positive). In the lower part of the ice cliff, the largest principal stress becomes compressive (negative) and the propagation of crevasses is suppressed. Surface crevasses, generally, do not penetrate through the whole glacier thickness and so crevasses cannot be the sole cause for calving. We thus did not follow this path to determine a failure region.

Instead, we assumed a shear-failure based mechanism for cliff calving. We defined a failure region as the region close to the calving front where the maximum shear stress exceeds a critical shear stress of 1 MPa (Schulson et al., 1999, Schulson, 2001) anywhere in the ice column. By fitting the size of the failure region L to the ice thickness H and the relative water depth w, an algebraic equation was obtained. A characteristic time to failure τ independent of stress was approximated from data for tensile failure of ice (Pralong et al., 2003) and shear failure of rocks (Brantut et al., 2013). The calving rate, C, was then calculated as the fraction of the size of the failure region and the time to failure:

$$C = \frac{L}{\tau} = C_0 \cdot \left(\frac{F - F_c}{F_s}\right)^s \tag{2.1}$$

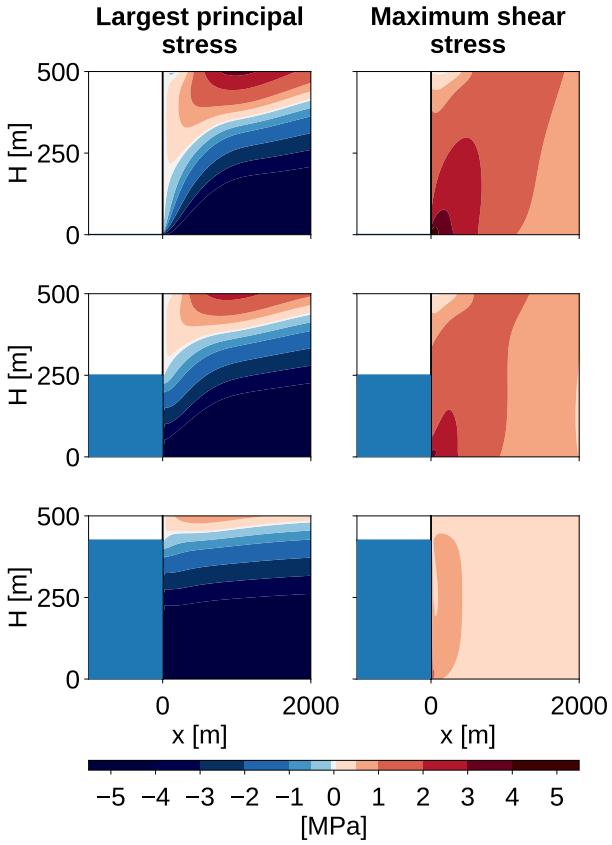

Fig. 2.1. The largest principal and the maximum shear stress at the calving front for a slab of ice that is 500 m thick and 6 km long (only the first 2 km are shown). The top row shows a dry ice cliff, the middle row an ice cliff half-submerged in water and the bottom row shows an ice cliff close to floatation. Stresses in the ice decrease as water depth increases, because the water pressure stabilizes the ice cliff.

with the glacier freeboard $F = H \cdot (1 - w)$, the water-depth-dependent critical freeboard F_c and the water-depth-dependent scaling parameters F_s, s, C_0.

This cliff calving rate increases exponentially with the ice thickness, independently of the topography of individual glaciers. It is valid for glaciers that are frozen to the bed or sliding with a constant velocity and serves as a lower bound for accelerating glaciers. Considering lateral drag that occurs in a three-dimensional setup also increases the calving rate. There is currently no glacier that is clearly in a cliff calving regime and could be used to calibrate the derived cliff calving parametrization. The glacier closest to the cliff calving regime is Jakobshavn glacier in Greenland: a rough comparison suggests that eq. 2.1 does not overestimate cliff calving rates for small freeboards.

This shear-failure based cliff calving parametrization can be implemented in ice sheet models such as PISM and used for large scale simulations (Sec. 2.4).

2.3 Ice mélange buttressing limits calving rates

In the interior of the West Antarctic Ice Sheet, where the bedrock is up to 2 km deep, an ice cliff at floatation has a freeboard of 250 m. According to my cliff calving parametrization (eq. 2.1), this correlates to a calving rate of more than 30 km/a. Thus, in the absence of an upper bound on calving rates, the West Antarctic Ice Sheet could be lost due to cliff calving in under a century. However, there is no evidence that ice loss has been this rapid in the past (Edwards et al., 2019). Therefore, an upper bound on cliff calving rates is needed. Pollard et al. (2015) and DeConto and Pollard (2016) imposed an upper bound of 5 km/a on an ad hoc basis. In contrast, I searched for a physical process which provides this upper limit.

Ice mélange, consisting of fragments of calved icebergs and sea ice, is a natural candidate: it is found in glacial embayments worldwide and is known to buttress calving glaciers. Observations of Greenland glaciers have shown that during the winter season, when the sea ice is especially thick and rigid, ice mélange prevents calving (Walter et al., 2012, Xie et al., 2019). This has been explained in modeling studies of grounded marine glaciers (Krug et al., 2015, Todd et al., 2018, 2019, Crawford et al., 2021): backstresses from the mélange reduce stresses at the glacial terminus, limiting crevasse formation and propagation and thereby reducing calving rates or even preventing calving altogether.

Ice mélange has been modelled as a granualar medium (Robel, 2017, Burton et al., 2018, Amundson and Burton, 2018). These studies found that the mélange backpressure increases with L/W, the ratio between the mélange length and the width of the confining channel. The presence of pinning points at which the mélange is grounded increases the backpressure. The seasonality of basal and surface melting and the resulting thinning of the mélange is another important parameter for mélange buttressing.

In my second paper (Schlemm and Levermann, 2021), I proposed a negative feedback between calving rate and mélange thickness: A glacier terminus with high calving rates produces many icebergs that form the ice mélange in front of the glacier. As the mélange thickens, it provides more buttressing to the glacier terminus, resulting in lower calving rates.

We assumed a linear relationship between mélange thickness and the calving rate. In the absence of mélange, the calving rate is given by the cliff calving parametrization. With increasing mélange thickness, the calving rate decreases. When the mélange thickness reaches a specific fraction of the ice thickness, calving is completely suppressed. There are three processes in our parametrization: mélange production at the calving front, mélange exiting into the ocean, and mélange loss through melting. We assumed a steady state of mélange production and loss resulting in a constant mélange geometry. As a result, the

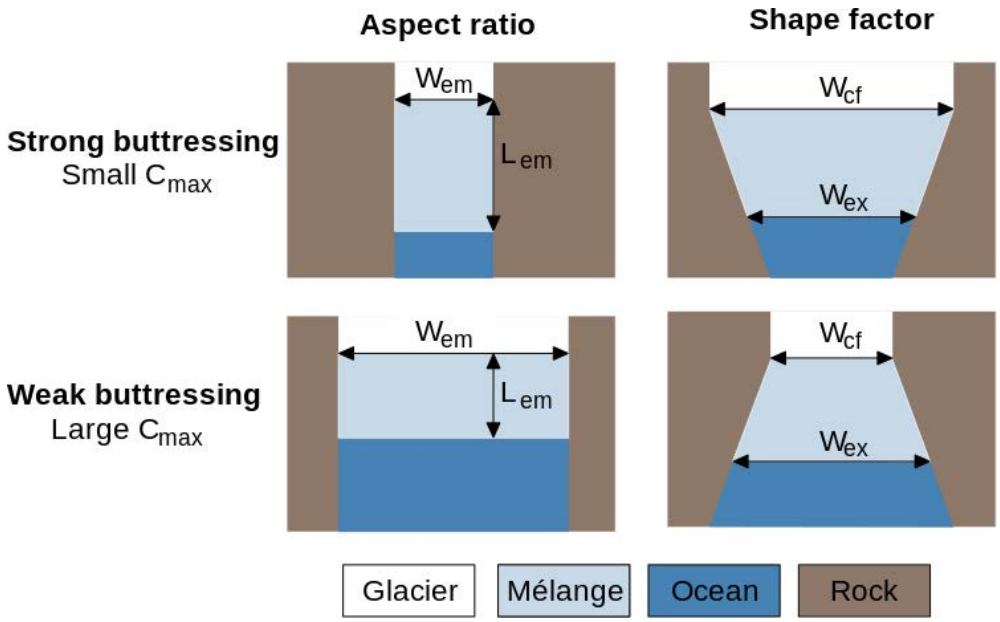

Fig. 2.2. Mélange buttressing strength and the upper limit on calving rates, C_{max}, depend on the embayment geometry. Glaciers terminating in long and narrow embayments experience stronger buttressing than glaciers terminating in wide and short embayments.

mélange-buttressed calving rate C increases with the unbuttressed calving rate C^*, but only up to an upper limit C_{max}:

$$C = \frac{C^*}{1 + C^*/C_{max}} \,. \tag{2.2}$$

The upper limit C_{max} is proportional to the ratio between the width of the embayment at the exit and at the calving front, meaning that embayments that narrow at some distance from the calving front experience stronger mélange buttressing than embayments that widen towards the ocean. The longer the embayment is compared to its average width, the stronger the mélange buttressing (see fig. 2.2). Our research thus shows that the geometry of the embayment plays an important role in determining the susceptibility of glaciers to rapid ice retreat. For example, Thwaites Glacier in Antarctica has a much greater potential for large calving rates and uncontrolled ice retreat (MICI) than the neighboring Pine Island Glacier, even though they face similar ocean conditions.

The steady state assumption used in the parameterization implies a fixed position of the calving front, which is not fulfilled when glacier retreat is considered. Therefore, we also investigated a time-dependent model for mélange buttressing that was solved numerically. If the initial conditions do not correspond to a steady-state solution, the mélange equilibrates to the steady-state solution in less than 6 months of simulation time.

The mélange buttressing parametrization was applied to two stress-based calving parametrizations: the shear-failure based parametrization for glaciers above the cliff calving stability

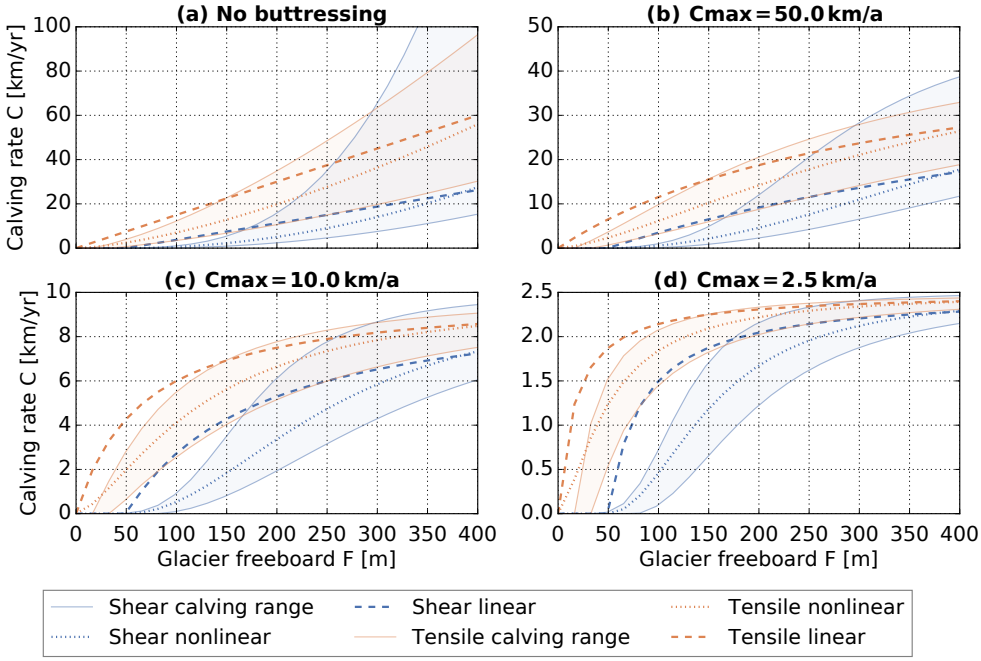

Fig. 2.3. Unbuttressed (a) and buttressed (b-d) calving rates as a function of the glacier freeboard (ice thickness minus water depth) for the shear calving rate parametrization (see Sec. 2.2) and a tensile calving rate parametrization, as well as the nonlinear and linear approximation of these calving parametrizations.

limit described in my paper (Schlemm and Levermann, 2019) and a tensile-failure based parametrization that was derived for glaciers below the cliff calving stability limit (Mercenier et al., 2018) and was extended to higher calving fronts. The calving rates depend on the height of the ice cliff (glacier freeboard) as well as on the water depth (see fig. 2.3). There is no shear calving below the stability limit. Above the stability limit, shear calving rates increase exponentially and exceed tensile calving rates. With mélange buttressing, both tensile and shear calving rates converge to the upper limit C_{max}. Neglecting water depth, we found for each calving parameterization a linear approximation that overestimates small calving rates and a nonlinear approximation that stays within the range of water-depth-dependent calving rates.

Mélange-buttressed calving parametrizations were tested in a simplified glacier setup with retrograde and prograde bed topography using the Parallel Ice Sheet Model (PISM) (Bueler and Brown, 2009, Winkelmann et al., 2011). When all floating ice is removed, MISI is initiated. In addition, the two calving parametrisations were applied with different values for the upper bound C_{max}. In all simulations, there is significant glacier retreat: In the MISI experiment, where no cliff calving is applied, the glacier retreats on the retrograde bed and stabilizes when the glacier terminus reaches the prograde bed. With shear calving, the glacier retreats further until the ice thickness falls below the stability limit. With tensile

calving, the glacier does not stabilize and all ice is lost. In an adaptive approach, where mélange length grows with glacier retreat, the upper bound C_{max} is lowered to 30% of its original value and a complete loss of ice is prevented in the experiments with tensile calving.

Mélange buttressing of calving glaciers may be one mechanism that prevents limitless growth of calving rates. It might therefore slow or even stop the progress of MICI.

2.4 Mélange buttressing can slow down the progress of MICI in the Antarctic ice sheet

Previous studies (DeConto and Pollard, 2016, Pollard et al., 2015) found that in projections considering cliff calving, the Antarctic Ice Sheet could contribute up to 1 m of sea level rise within a century. In my fourth paper (Schlemm et al., 2022), I applied the cliff calving and mélange buttressing parametrisations from Secs. 2.2 and 2.3 (Schlemm and Levermann, 2019, 2021) to estimate the potential ice loss of the West Antarctic Ice Sheet within a century.

Most of the West Antarctic Ice Sheet is grounded on bedrock below sea level and is therefore vulnerable to both MISI and MICI. Observations suggest that MISI may already be in progress in the Amundsen region (Joughin et al., 2014, Mouginot et al., 2014, Rignot et al., 2014). In addition, iceberg plow marks suggest that MICI may have resulted in rapid ice retreat in the Amundsen region during the last deglaciation (Wise et al., 2017). We therefore considered the Amundsen region of the West Antarctic Ice Sheet to be the likely starting point for MICI.

Ice shelf breakup is a necessary precondition for calving of exposed ice cliffs and thus for the onset of MICI. Rapid ice shelf breakup was observed in the Larsen B ice shelf on the Antarctic Peninsula in 2002 (Rack and Rott, 2004): Due to high summer melt rates and the resulting formation of a large number of melt ponds, crevasses deepened rapidly and the ice shelf fragmented (MacAyeal et al., 2003, Glasser and Scambos, 2008). However, the very large surface melt rates required for this hydrofracturing mechanism (Robel and Banwell, 2019) are unlikely to occur in the Amundsen region (Trusel et al., 2015). Nevertheless, warming of the Amundsen Sea (Shepherd et al., 2004) is already causing significant thinning and rifting in all ice shelves in the Amundsen region (Milillo et al., 2019). Therefore, they are likely to disintegrate under global warming conditions (Lhermitte et al., 2020).

We carried out regional simulations of the West Antarctic Ice Sheet with the Parallel Ice Sheet Model (PISM) (Bueler and Brown, 2009, Winkelmann et al., 2011) and assumed that in the near future, the ice shelves in the Amundsen region will break apart and will not be able to regenerate. We performed five types of experiments: first, a reference simulation with current day atmosphere and ocean conditions held constant; second, a basal melt experiment

with a high basal the melt rate in the Amundsen basin; third, a floatkill experiment in which all floating ice in the Amundsen basin was removed; fourth, a cliff-calving experiment with four different values for C_{max}; and finally, a range of adaptive experiments where C_{max} was updated every five model years for the new embayment geometry.

The MISI experiments (basal melt and floatkill experiment) both contribute about 0.6 m of sea level rise within 100 a. This agreement between the melt and the floatkill experiment is consistent with the results of the ABUMIP study (Sun et al., 2020) (Sec. 2.1). Including cliff calving, MICI can more than double or even triple the sea level contribution compared to the MISI experiments. In the adaptive cliff calving experiments, the strength of the mélange buttressing depends on the evolving embayment geometry. As the grounding line retreats into the Amundsen basin, the embayment widens and the calving front lengthens. Therefore, the upper bound on the calving rate decreases and the progress of MICI slows down. This is the most important finding of this paper.

During the winter season, freezing of mélange was observed to stop calving in Greenland glaciers (Medrzycka et al., 2016). We expect similar seasonal effects in Antarctica, where winter freezing of mélange might temporarily stop the progress of MICI. However, in my simplified mélange parameterization, mélange equilibration is too slow and therefore winter freezing of mélange is not sufficient to stop calving.

Finally, we analysed grounding line retreat along the main flow direction of Thwaites and Pine Island glaciers. Whereas the overall speed of MICI is largely determined by the mélange buttressing strength, bed topography has a large influence on the pattern and timing of grounding line retreat. On sections with retrograde bed topography, the grounding line retreats rapidly. At ridges in the bed topography, the grounding line retreat stagnates on the upslope, and accelerates on the downslope.

This study shows that MICI has the potential to double sea level contributions of the Antarctic Ice Sheet compared to projections using only MISI. It is therefore a really important mechanism that needs to be studied more. Mélange buttressing could be one mechanism to slow MICI after its onset.

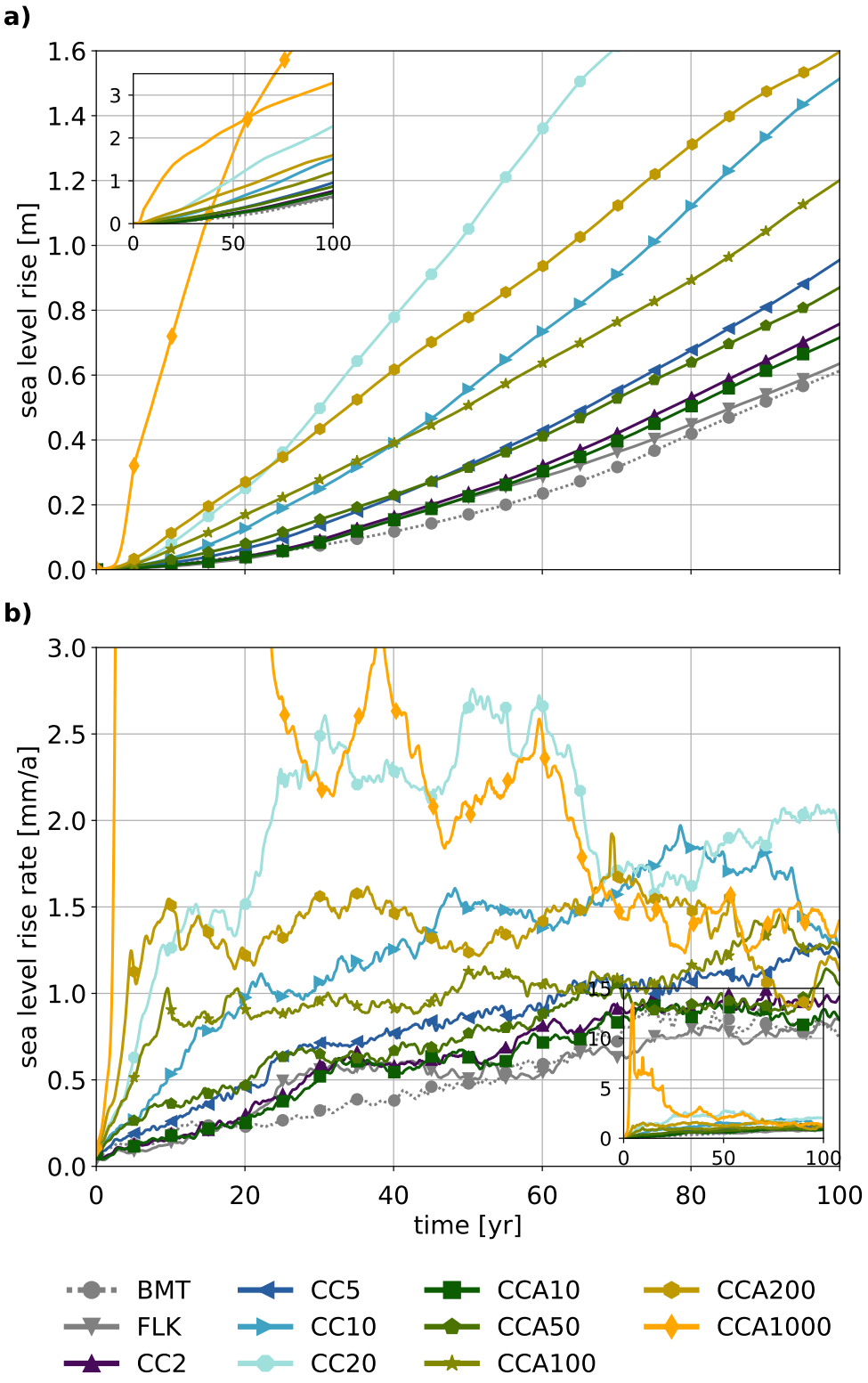

Fig. 2.4. Sea level contributions compared to the reference run (a) and sea level rise rates (b) for the basal melt experiment (BMT), the floatkill experiment (FLK), the cliff calving experiments (CC#) and a range of adaptive cliff calving experiments (CCA#).

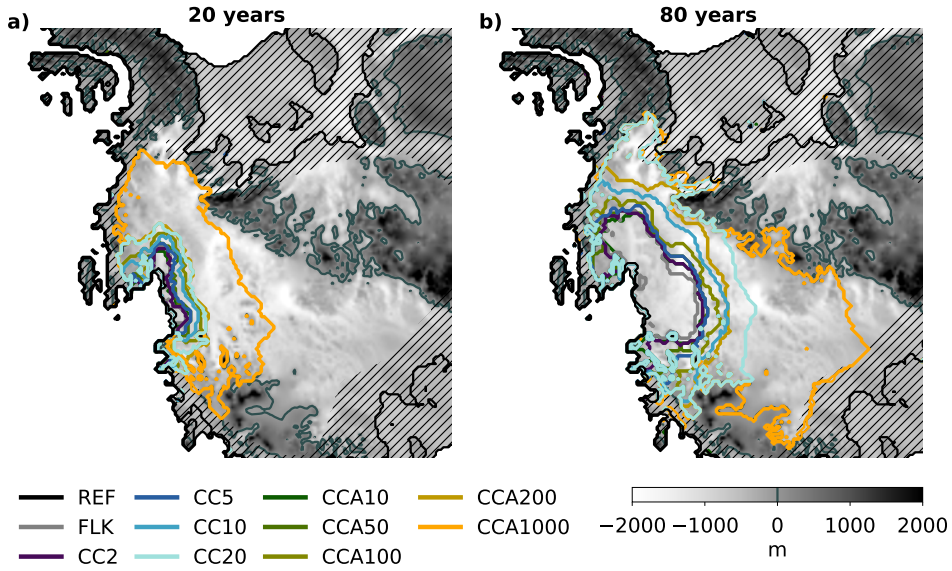

Fig. 2.5. Grounding line retreat after 20 years (a) and 80 years (b) of simulation time for the reference simulation (REF), the floatkill experiment (FLK), the cliff calving experiments (CC#) and a range of adaptive cliff calving experiments (CCA#). Underlaid is the bed topography. Floatkill and cliff calving was only applied to the Amundsen region and the inner West Antarctic Ice Sheet and not in the regions that are shaded.

Discussion

The Antarctic Ice Sheet may be subject to two ice instabilities (MISI and MICI), which could cause a sea level contribution of more than a meter within a century. The *IPCC Special Report on the Ocean and Cryosphere in a Changing Climate* discusses the role of MISI and MICI for sea level projections of the Antarctic Ice Sheet and finds "that unstable retreat and thinning of some Antarctic glaciers, and to a lesser extent Greenland outlet glaciers, may be underway. However, the timescale and future rate of these processes is not well known, casting deep uncertainty on projections of the sea level contributions from the Antarctic Ice Sheet" (IPCC, 2019, p. 246). *The Contribution of Working Group I (The Physical Science Basis) to the Sixth Assessment Report of the IPCC* discusses MICI in more detail and finds that "there is [..] low confidence in simulating mechanisms that have the potential to cause widespread, sustained and very rapid ice loss from Antarctica this century through MICI and low confidence in projecting the driver of ice shelf disintegration" (IPCC, 2021, p. 9-72)

With the publications feeding into this thesis I contributed to a better understanding of both instabilities, but of MICI in particular.

3.1 MISI in the context of an ice sheet model intercomparison study

I first contributed to a collaborative effort to estimate an upper limit of the sea level potential of MISI (ABUMIP, Sun et al. (2020), Sec. 2.1).

Ice sheet models make different modelling choices concerning ice dynamics, which physical processes are included, numerical schemes and initialization procedure. All of these choices are valid, but they can have a large influence on the model results. As a result, projections made with a single model are always uncertain. Ice sheet model intercomparison projects (Pattyn et al., 2013, Bindschadler et al., 2013, Seroussi et al., 2019, Cornford et al., 2020, Seroussi et al., 2020) are therefore used to asses the influence of modelling choices on the model results and to estimate the uncertainety of projections.

The Antarctic BUttressing Model Intercomparison Project (ABUMIP) considered an extreme scenario in which all Antarctic ice shelves were instantaneously removed. A more realistic scenario, in which the ice shelves are lost gradually, would introduce uncertainties related to the forcing and processes of ice shelf thinning and weakening. ABUMIP instead focussed on the response of the grounding line to a complete loss of buttressing.

We thus explored the full potential of MISI and found a possible sea level contribution of 1–12 m over 500 a. These results show that MISI has the potential to contribute significantly to global sea level rise. However, the wide spread of model results indicates that there are still many uncertainties in the modeling decisions and that further developments and improvements are needed.

3.2 Parametrizations for modelling MICI

For the remainder of my thesis I focused on MICI. First I developed tools to model it: I derived a simple parametrisation for cliff calving (Schlemm and Levermann (2019), Sec. 2.2) and for mélange buttressing of calving rates (Schlemm and Levermann (2021), Sec. 2.3).

Both parametrisations rely on very simple models of rather complex processes. As such, they were derived for idealised geometries and don't include details of how ice fractures or how mélange behaves as a granular medium. In addition, there are few observations against which they could be tested. Nevertheless, they are useful both for understanding basic system behavior and for implementation in ice sheet models used for long time and length scales.

3.2.1 Cliff calving parametrization

The calving parametrization I derived in my first paper (Schlemm and Levermann (2019), Sec. 2.2), is a physics-based cliff calving parametrization that gives a rate and can therefore easily be applied in a large scale ice sheet model. I followed the approach of Bassis and Walker (2011) by considering shear failure as the main criterion for cliff failure, but in a 2d numerical model that takes the vertical structure of stresses into account. Unlike previous studies considering the stresses near the calving front (Mercenier et al., 2018), I neglected tensile damage because the crevasses do not reach the full ice thickness and tensile failure therefore needs additional assumptions. A failure region was defined as the region where the maximum shear stress is exceeded anywhere in the ice column. The extend of this failure region, together with a time to failure, gives the calving rate.

This parametrization contains several uncertainties. The first uncertainty lies in the value of the critical shear stress for ice, which laboratory experiments constrain between 0.5–5 MPa (Schulson, 2001). This uncertainty influences the size of the failure region. The

second uncertainety lies in the time to failure for which only a rough estimation has been made because there are no proper observations of the time to failure for shear failure of ice. In addition, an idealized glacier geometry was considered: a rectangular slab of ice, frozen to a flat bed. I also investigated a free slip basal boundary condition and found that this would increase calving rates. I did not consider a possible cliff slope caused by dynamic thinning or an overhang caused by melt-undercut, which would stabilize or destabilize the cliff, respectively, according to other modeling studies (Benn et al., 2017b, Bassis et al., 2021).

The cliff calving parametrization gives no calving for a glacier below the stability limit. However, calving is observed for those glaciers. So for a comprehensive description of calving, the cliff calving parametrization should be combined with another calving law for glaciers below the stabilty limit, such as the one derived by Mercenier et al. (2018). In addition, a comparison with observations of Jakobshavn glacier in Greenland showed that my parametrization gives a lower limit on the calving rate for a glacier, whose glacier freeboard is just a little above the stability limit (Schlemm and Levermann, 2019). This is because it underestimates calving rates when the glacier is just at the beginning of the cliff calving regime. This is in contrast to Ultee and Bassis (2020), where it was shown that a calving model based on a viscoplastic thin-sheet theory provides an upper bound on the calving rates of Greenland glaciers, which depends not only on the ice thickness but also on bed topography and glacier geometry.

Following the publication of my simple cliff calving parametrisation (Schlemm and Levermann, 2019), there have been several studies that analyse the cliff calving process in more detail.

Parizek et al. (2019) gave a more detailed analysis of the slumbing and fracturing processes occuring in an ice cliff by considering how wing cracks caused by shear stresses grow and interact with crevasses caused by tensile stresses. They found that surface melt water and previous damage to the ice increase its susceptibility to cliff failure.

In a different approach, Clerc et al. (2019) used a stress confinement measure to determine which failure mechanism is dominant in different parts of the cliff. They found that tensile failure is confined to the surface area, and shear failure to a thin region below the top of the ice cliff. The middle and bottom part of the cliff are subjected to thermal softening, which has a much larger critical stress for failure than shear and tensile failure. Therefore they concluded, that ice cliffs are stable to much larger cliff heights than previously thought (Bassis and Walker, 2011, Schlemm and Levermann, 2019) unless the buttressing ice shelf is removed very quickly (on a timescale of hours).

Finally, Crawford et al. (2021) used a combination of a particle and a continuum model of ice, which can model tensile and shear failure simultaneously, although not thermal softening.

They found two modes of failure: Viscous deformation leads to surface lowering and bulging at the waterline. This initiates crevassing and calving via forward rotation of an ice block. In addition, pronounced shear bands form up-glacier of the calving front and lead to brittle failure of the ice cliff. From their simulation results, they derived a calving rate, which also grows nonlinearly with the ice thickness. So although their model is much more detailed than my cliff calving parametrisation, their findings support the validity of my parameterization.

3.2.2 Mélange buttressing of calving glaciers

In my third paper (Schlemm and Levermann (2021), Sec. 2.3), I proposed a negative feedback between calving rate and mélange buttressing: Mélange is produced by the calving glacier and lost by mélange drifting away at the embayment exit as well as by melting. With increasing mélange thickness, the calving rate decreases. Assuming a steady state between mélange production and loss, I derived a buttressed calving rate, which is a function of the unbuttressed calving rate and an upper bound C_{max}. This upper bound depends on the embayment geometry and mélange properties.

This mélange parametrisations has several uncertainties in its model parameters. Especially the velocity with which mélange exits the embayment is difficult to constrain: Maximum mélange flow velocities observed off Greenland glaciers are 10–18 km/a (Amundson and Burton, 2018), while velocities of icebergs drifting in the Weddel Sea in Antarctica range from 3000–5500 km/a (Schodlok et al., 2006). The mélange exit velocity is expected to be in the range spanned by these observations. Another uncertain parameter is the internal friction of the mélange, which ranges from about 0.1 to larger than 1 (Amundson and Burton, 2018).

Due to its dependence on an idealized geometry (see fig. 2.2), the mélange parameterization has several limitations when it is applied to realistic embayment geometries. Most importantly, the mapping of a real-world embayment into the idealized geometry is ambiguous. In addition, the position of the mélange margin cannot be determined by the model and must therefore be provided as an external parameter. Finally, the mélange parameterization can neither account for pinning points nor correctly model seasonality.

Nevertheless, it is a simple model of a physical process that has been observed and modeled to bound calving rates. It can be applied to any calving parameterization that provides a rate. In contrast to other parameterizations, the upper bound is not set to a fixed value because the buttressing strength may change as the glacier retreats.

3.3 MICI in the Antarctic Ice Sheet

Finally, in my fourth paper (Sec. 2.4, Schlemm et al. (2022)h), I applied the parameterizations I had developed and tested previously in an idealized glacier system to a regional model of the West Antarctic Ice Sheet. Using this model, I investigated how the loss of ice shelves in the Amundsen region could trigger MICI and how much sea level would rise as a result.

The previous study examining MICI in the Antarctic Ice Sheet by DeConto and Pollard (2016) made sea level projections for a warmer climate in which increased surface melting leads to ice shelf collapse due to hydrofracturing. In contrast, I considered an idealized scenario in which I removed the ice shelves instantaneously, because the processes by which ice shelves break apart are still very uncertain (Robel and Banwell, 2019, Lhermitte et al., 2020). This immediate failure of the ice shelves leads to an immediate onset of MICI. Another difference is that DeConto and Pollard (2016) allowed ice shelf breakup and cliff calving throughout the whole Antarctic Ice Sheet, whereas I restricted both processes to the Amundsen region. This limits the ice loss caused by MICI. Despite these differences, results are similar: using an upper bound of 5 km/a, DeConto and Pollard (2016) get a sea level rise of 1 m by 2100. I considered a range of upper bounds, and setting it to 5 km/a, I also get 1 m of sea level rise within a century of ice shelf removal.

However, the amount of sea level rise is very uncertain because it depends strongly on the upper bound on calving rates, which is difficult to determine. My simulations give a range between 0.7 m for a small upper bound of 2 km/a (where the sea level rise is caused mainly by MISI; the additional effect of MICI is small in this case) and more than 3 m in the nearly unbuttressed case. This illustrates that mélange buttressing is very important and needs to be much better understood and modelled in order to make reliable predictions.

As MICI progresses and the grounding line retreats, a large embayment forms where there was previously grounded ice. Assuming that this entire area is filled with mélange, mélange buttressing increases greatly as the grounding line retreats. As a result, MICI is slowed down significantly. However, this increased buttressing is not sufficient to stop the retreat.

Other processes that may stop or slow MICI are winter freezing of mélange, ridges in the bed topography and dynamic thinning of ice cliffs: Mélange freezing in winter can stop calving temporarily (Walter et al., 2012, Xie et al., 2019). However, my simplified mélange parameterization is not capable of simulating this. During the last deglaciation, retreat of Pine Island Glacier stopped when the grounding line reached a prominent ridge in the bed topography (Wise et al., 2017). In my simulations, however, I observe only temporary stops at bed ridges. Dynamic thinning of the glacier terminus may lower the ice cliff, making it less susceptible to cliff calving (Crawford et al., 2021, Bassis et al., 2021). This process is included in PISM, but since it is only modeled at a resolution of 4 km the dynamics near the terminus cannot be fully resolved. However, as long as the ice shelves cannot reform,

the ice cliff cannot be thinner than flotation thickness. On very deep bedrock, as in the West Antarctic Ice Sheet, this still implies a very high susceptibility to cliff calving.

MICI can only begin after the ice shelves buttressing the ice cliffs have collapsed and continues as long as the ice shelves do not regrow. Therefore, the question under what conditions ice shelves collapse is crucial for a thorough understanding of MICI. Although this question was beyond the scope of my thesis, I will discuss it briefly.

Hydrofracturing has been proposed as the main mechanism for ice shelf breakup (Pollard et al., 2015) based on observations of the collapse of the Larsen B Ice Shelf (MacAyeal et al., 2003, Glasser and Scambos, 2008). However, hydrofracturing requires very large amounts of surface meltwater (Robel and Banwell, 2019), which are unlikely to occur in many regions of the Antarctic Ice Sheet this century (Trusel et al., 2015). In addition, ice cliff instability may depend on the speed of ice shelf collapse (Clerc et al., 2019), and it is likely that hydrofracturing is not fast enough (Robel and Banwell, 2019). Ice shelves can also collapse due to rifting and crevasse formation (Borstad et al., 2012, Jeong et al., 2016, Lhermitte et al., 2020). However, none of these approaches is currently able to predict under what environmental and internal conditions a particular ice shelf will collapse.

If ice shelves can regrow after cliff calving has begun, this could stop MICI after its onset by buttressing ice cliffs and preventing further cliff calving. However, if ice shelves cannot regrow, MICI will continue largely unimpeded because mélange buttressing can only slow, but probably not stop, the progression of MICI. Viscous deformation and ice cliff lowering could prevent the formation of unstable ice cliffs (Clerc et al., 2019, Bassis et al., 2021) and allow ice shelf regrowth. In contrast, a mixed-mode behavior of viscous deformation and fracturing (Crawford et al., 2021) would make ice shelf regrowth unlikely. Understanding these processes is still ongoing work.

Conclusion

The goal of my dissertation was to better understand MISI and MICI, the two marine instabilities that are responsible for the large uncertainty in sea level projections from the Antarctic Ice Sheet.

I contributed to a better understanding of MISI by participating in a model intercomparison study that demonstrated the enormous potential of MISI to contribute to global sea level rise, but also highlighted the large model uncertainties.

To better understand MICI, I developed two simple models that parameterize the main processes that drive MICI: iceberg calving from ice cliffs as well as buttressing of these cliffs by ice mélange formed by calved icebergs. The goal was to find simple parameterizations that, while not providing a complete understanding, were simple enough to be implemented in a large-scale ice sheet model. Both parameterizations are based on idealized scenarios and include uncertainties in the model parameters. Unfortunately, there are few observations against which to test them, but the general results are supported by other modeling studies.

Finally, I implemented both parameterizations in an ice sheet model, PISM, and ran simulations where MICI was triggered in the West Antarctic Ice Sheet by instantaneously removing the ice shelves in the Amundsen region. I found that MISI, which is induced by ice shelf removal, results in a sea level rise of 0.7 m in a century. When cliff calving is added, the contribution of MICI depends on the strength of mélange buttressing: When very strong buttressing is assumed, the additional contribution of MICI to sea level rise is less than 0.1 m. However, in the unbuttressed case, MICI contributes more than 2 m in addition to the sea level rise caused by MISI. This large uncertainty highlights the importance of mélange buttressing. Another important result is that as MICI progresses, mélange buttressing increases and MICI slows down. Winter freezing of mélange and ridges in the bed topography slow or stop MICI only temporarily.

Because of its importance to the speed of MICI, mélange-buttressing of calving glaciers should be observed more thoroughly and across a larger number of glaciers, and be modeled with greater detail. The study of ice shelf failure was beyond the scope of this thesis, but

since it is a prerequisite for cliff failure, it should also be investigated further. A future study simulating MICI in the Antarctic Ice Sheet with an ice sheet model would ideally include a mechanism for ice shelf failure as well as a more advanced mélange model.

Original manuscripts

A.1 Antarctic Ice Sheet response to sudden and sustained ice-shelf collapse (ABUMIP)

Sun, S.; Pattyn, F.; Simon, E. G.; Albrecht, T.; Cornford, S.; Calov, R.; Dumas, C.; Gillet-Chaulet, F.; Goelzer, H.; Golledge, N. R.; Greve, R.; Hoffman, M. J.; Humbert, A.; Kazmierczak, E.; Kleiner, T.; Leguy, G. R.; Lipscomb, W. H.; Martin, D.; Morlighem, M.; Nowicki, S.; Pollard, D.; Price, S.; Quiquet, A.; Seroussi, H.; **Schlemm, T.**; Sutter, J.; van de Wal, R. S. W.; Winkelmann, R. & Zhang, T.

Antarctica's ice shelves modulate the grounded ice flow, and weakening of ice shelves due to climate forcing will decrease their 'buttressing' effect, causing a response in the grounded ice. While the processes governing ice-shelf weakening are complex, uncertainties in the response of the grounded ice sheet are also difficult to assess. The Antarctic BUttressing Model Intercomparison Project (ABUMIP) compares ice-sheet model responses to decrease in buttressing by investigating the 'end-member' scenario of total and sustained loss of ice shelves. Although unrealistic, this scenario enables gauging the sensitivity of an ensemble of 15 ice-sheet models to a total loss of buttressing, hence exhibiting the full potential of marine ice-sheet instability. All models predict that this scenario leads to multi-metre (1–12 m) sea-level rise over 500 years from present day. West Antarctic ice sheet collapse alone leads to a 1.91–5.08 m sea-level rise due to the marine ice-sheet instability. Mass loss rates are a strong function of the sliding/friction law, with plastic laws cause a further destabilization of the Aurora and Wilkes Subglacial Basins, East Antarctica. Improvements to marine ice-sheet models have greatly reduced variability between modelled ice-sheet responses to extreme ice-shelf loss, e.g. compared to the SeaRISE assessments.

Journal of Glaciology **66**, 260, 891–904 (2020).
DOI: 10.1017/jog.2020.67

Journal of Glaciology

Article

Cite this article: Sun S et al. (2020). Antarctic ice sheet response to sudden and sustained ice-shelf collapse (ABUMIP). *Journal of Glaciology* **66**(260), 891–904. https://doi.org/10.1017/jog.2020.67

Received: 31 December 2019
Revised: 17 July 2020
Accepted: 20 July 2020
First published online: 14 September 2020

Keywords:
Antarctic glaciology; ice-sheet modelling; ice shelves

Author for correspondence:
Sainan Sun,
E-mail: sainsun@ulb.ac.be

cambridge.org/jog

Antarctic ice sheet response to sudden and sustained ice-shelf collapse (ABUMIP)

Sainan Sun[1], Frank Pattyn[1], Erika G. Simon[2], Torsten Albrecht[3], Stephen Cornford[4], Reinhard Calov[3], Christophe Dumas[5], Fabien Gillet-Chaulet[6], Heiko Goelzer[1,7], Nicholas R. Golledge[8], Ralf Greve[9,10], Matthew J. Hoffman[11], Angelika Humbert[12,13], Elise Kazmierczak[1], Thomas Kleiner[12], Gunter R. Leguy[14], William H. Lipscomb[14], Daniel Martin[15], Mathieu Morlighem[16], Sophie Nowicki[2], David Pollard[17], Stephen Price[11], Aurélien Quiquet[5], Hélène Seroussi[18], Tanja Schlemm[3,19], Johannes Sutter[12,20], Roderik S. W. van de Wal[7], Ricarda Winkelmann[3,19] and Tong Zhang[11]

[1]Laboratoire de Glaciologie, Université libre de Bruxelles (ULB), Brussels, Belgium; [2]NASA/GSFC, Greenbelt MD, USA; [3]Potsdam Institute for Climate Impact Research (PIK), Member of the Leibniz Association, P.O. Box 601203, 14412, Potsdam, Germany; [4]Department of Geography, Swansea University, Swansea, UK; [5]Laboratoire des Sciences du Climat et de l'Environnement, LSCE/IPSL, CEA-CNRS-UVSQ, Université Paris-Saclay, F-91191 Gif-sur-Yvette, France; [6]Univ. Grenoble Alpes/CNRS/IRD/G-INP, Institut des Géosciences de l'Environnement, 38000 Grenoble, France; [7]Institute for Marine and Atmospheric Research, Utrecht University, The Netherlands; [8]Antarctic Research Centre, Victoria University of Wellington, New Zealand; [9]Institute of Low Temperature Science, Hokkaido University, Sapporo, Japan; [10]Arctic Research Center, Hokkaido University, Sapporo, Japan; [11]Theoretical Division, Los Alamos National Laboratory, Los Alamos NM, USA; [12]Alfred-Wegener-Institut, Helmholz-Zentrum für Polar und Meeresforschung, Bremerhaven, Germany; [13]Department of Geoscience, University of Bremen, Bremen, Germany; [14]Climate and Global Dynamics Laboratory, National Center for Atmospheric Research, Boulder CO, USA; [15]Lawrence Berkeley National Laboratory, Berkeley CA, USA; [16]Department of Earth System Science, University of California Irvine, Irvine, USA; [17]Pennsylvania State University, EMS Earth and Environmental Systems Institute, Pennsylvania, USA; [18]Jet Propulsion Laboratory, California Institute of Technology, Pasadena, USA; [19]University of Potsdam, Institute of Physics and Astronomy, Karl-Liebknecht-Str. 24-25, 14476, Potsdam, Germany and [20]Climate and Environmental Physics, Physics Institute and Oeschger Centre for Climate Change Research, University of Bern, Bern, Switzerland

Abstract

Antarctica's ice shelves modulate the grounded ice flow, and weakening of ice shelves due to climate forcing will decrease their 'buttressing' effect, causing a response in the grounded ice. While the processes governing ice-shelf weakening are complex, uncertainties in the response of the grounded ice sheet are also difficult to assess. The Antarctic BUttressing Model Intercomparison Project (ABUMIP) compares ice-sheet model responses to decrease in buttressing by investigating the 'end-member' scenario of total and sustained loss of ice shelves. Although unrealistic, this scenario enables gauging the sensitivity of an ensemble of 15 ice-sheet models to a total loss of buttressing, hence exhibiting the full potential of marine ice-sheet instability. All models predict that this scenario leads to multi-metre (1–12 m) sea-level rise over 500 years from present day. West Antarctic ice sheet collapse alone leads to a 1.91–5.08 m sea-level rise due to the marine ice-sheet instability. Mass loss rates are a strong function of the sliding/friction law, with plastic laws cause a further destabilization of the Aurora and Wilkes Subglacial Basins, East Antarctica. Improvements to marine ice-sheet models have greatly reduced variability between modelled ice-sheet responses to extreme ice-shelf loss, e.g. compared to the SeaRISE assessments.

Introduction

The vast majority of Earth's freshwater is stored in the Antarctic ice sheet and because of this large volume (>55 m sea-level equivalent (SLE); Nowicki and others, 2013; Albrecht and others, 2020; Morlighem and others, 2020), the loss of even a small fraction of its mass could soon dominate sea-level rise. Reconstructions of past sea level show that the ice sheet could have contributed between 10 and 20 m SLE during the Pliocene, a period stretching between 5.3 and 2.6 million years before present with global mean temperature 2--3°C higher than present-day (Miller and others, 2012; Grant and others, 2019). Current observed mass loss from the Antarctic ice sheet is accelerating and concentrated in the Amundsen Sea area (Mouginot and others, 2014; Rignot and others, 2014; Shepherd and others, 2018) and the Aurora Subglacial Basin, including Totten Glacier (Khazendar and others, 2013). These changes have been attributed to variations in ocean circulation bringing warm, intermediate-depth waters into contact with the base of ice shelves (Payne and others, 2004; Thomas and others, 2004; Jenkins and others, 2010; Pritchard and others, 2012; Paolo and others, 2015; Jenkins and others, 2018).

Despite recent advances in modelling marine ice sheets (Pattyn, 2018), projections of the future contribution of the Antarctic ice sheet to sea level are still hampered by insufficient knowledge of atmospheric and oceanic forcings and the impact of those forcings on critical ice-sheet model physics and dynamics (Pattyn and others, 2018). This is exemplified by the hypothesis of new physical mechanisms, such as the Marine Ice Cliff Instability (MICI; Bassis and Walker, 2012; Pollard and others, 2015), which leads to significantly larger sea-level contributions for the Antarctic ice sheet compared to other studies (DeConto and Pollard, 2016). However, additional studies conclude that major ice loss during the Pliocene Epoch could also be reached without such mechanisms (Bulthuis and others, 2019; Edwards and others, 2019; Golledge and others, 2019). Other uncertainties stem from the timing and processes that govern ice-shelf weakening, disintegration and collapse (Pattyn and others, 2018).

Thinning of ice shelves, and concomitant reduction in ice-shelf buttressing, leads to grounding line retreat, inland ice acceleration and loss of grounded ice mass (Pritchard and others, 2012). Reduction in ice-shelf buttressing has an almost instantaneous effect on ice flow, which implies that this process can result in rapid changes in ice flux over the grounding line (Reese and others, 2018*b*; Gudmundsson and others, 2019). Ice-shelf thinning and weakening due to specific interactions with atmosphere (surface melt, meltwater percolation, refreezing and runoff; Trusel and others, 2015) and ocean (changes in ocean circulation, ocean warming and sub-ice-shelf melting; Alley and others, 2015; Thompson and others, 2018) are parameterized with a large variation in ice-sheet models (Favier and others, 2019).

In this paper, we investigate how changing ice shelves control Antarctic mass loss independent of the triggers for how and when ice shelves weaken. Previous ice-sheet intercomparison efforts (Pattyn and others, 2012, 2013; Bindschadler and others, 2013; Nowicki and others, 2013; Seroussi and others, 2019) highlighted the importance of better assessing the causes of the variation in model results, and separating differences associated with model grid resolution, ice dynamics (e.g. choice of stress balance equation), physical processes included (e.g. calving, hydrofracture and cliff failure), initialization procedure (e.g. data assimilation, spin-up or relaxation) and numerical schemes. We designed a simple experiment that considers an instantaneous and sustained removal of floating ice. This scenario is not realistic, but allows us to investigate how different ice-sheet models cope with the impact of a sudden, complete loss of ice-shelf buttressing. By removing the uncertain causes related to ice-shelf thinning and weakening, we are able to isolate uncertainties in the response of the grounded ice sheet to grounding-line retreat due to loss of ice-shelf buttressing. We analyse 15 simulations from 13 international groups in order to determine the most relevant factors controlling the rate of Antarctic mass changes in an extreme mass loss scenario. Furthermore, the absence of buttressing may lead to ice-sheet collapse through the marine ice-sheet instability (MISI) in areas where the bed deepens towards the interior of the ice sheet. The experiment therefore enables to quantify the MISI potential and associated uncertainties for the Antarctic ice sheet and revises estimates of this potential that have previously been made for the West Antarctic ice sheet (Bamber and others, 2009).

This experiment is coordinated through the Antarctic BUttressing Model Intercomparison Project, ABUMIP (http://www.climate-cryosphere.org/wiki/index.php?title=ABUMIP-Antarctica), endorsed by the Ice Sheet Model Intercomparison Project, ISMIP6 (http://www.climate-cryosphere.org/activities/targeted/ismip6), part of the Coupled Model Intercomparison project, CMIP6 (https://www.wcrp-climate.org/wgcm-cmip/wgcm-cmip6). It builds on the ISMIP6 initialization experiments (http://www.climate-cryosphere.org/wiki/index.php?title=InitMIP-Antarctica) for the Antarctic ice sheet (Seroussi and others, 2019), in which most of the models in this study participated (see Appendix for details on each model). The main purpose of ABUMIP is to gauge the sensitivity of different ice-sheet models with respect to such grounding-line retreat, whether they pertain to numerical methods, physical approximations or boundary conditions. It also enables evaluation of the sensitivity of models that are used for the full Antarctic, for global sea-level rise projections (Seroussi and others, 2019). While similar experiments have been done previously by Cornford and others (2016), Golledge and others (2017, supplementary material) and Pattyn (2017), we are able to put these results into a wider context through a controlled experiment and by examining a large number of diverse models. This will help to better understand the spread in projections of 21st century Antarctic ice sheet contributions to sea level.

Experiments and model setup

Description of the experiments

ABUMIP consisted of three experiments, a control run (ABUC) and two forcing experiments (ABUK and ABUM) that controlled the rate of loss of ice shelves. All experiments started from an initialized present-day state of the Antarctic ice sheet, as defined by the initMIP-Antarctica (Seroussi and others, 2019). All ABUMIP experiments ran for a period of 500 years forward in time.

Control run (ABUC)

Similar to Seroussi and others (2019), atmospheric and oceanic forcings in the control run were assumed to be similar to present-day conditions, without any extra forcing aside from that applied at the end of the initialization.

Ice-shelf removal or 'float-kill' (ABUK)

For the first forcing experiment, all floating ice (ice shelves) surrounding the ice sheet was removed at the start of the run and thereafter any newly-formed floating ice was instantaneously removed (so-called 'float-kill'). In other words, at all times, calving flux was assumed to be larger than the flux across the grounding line to prohibit regrowth of the shelves.

Extreme sub-ice-shelf melt (ABUM)

The second experiment applied an extremely high constant melt rate of 400 m a^{-1} underneath the ice shelves. Similar experiments have been carried out in previous studies with basal melt rates ranging from 200 m a^{-1} in Bindschadler and others (2013) to 400 m a^{-1} in Cornford and others (2016). Such high forcings inevitably lead to rapid loss of ice shelves and hence of buttressing. Preliminary experiments have shown that the actual value within the range found in the literature is of lesser importance.

Model setup

Participating ice-sheet models were free to choose the initialization procedure, which is generally dependent on the given model characteristics and requirements. There were no further constraints on present-day forcing datasets applied (including surface mass balance, surface temperature and sub-shelf melt rates) or on specific physical processes and parameterizations included in the models (e.g. basal sliding and friction laws, ice rheology and stress balance approximation). Isostatic adjustment was not considered. The initialization time varies among models but was near the beginning of the 21st century.

Models were required to represent ice shelves and grounding line dynamics, and the initialization process should include ice shelves. Ice-sheet models applied the present-day surface mass balance

(SMB) and basal mass balance (BMB) of their choice, but without adjusting for the impacts of geometric changes in the forward experiments (i.e. no SMB, surface-elevation feedback). Finally, models used the bed and surface topography of their choice, while bedrock elevation adjustment and processes affecting ice shelves (other than subshelf melting) were not taken into account. Model output was taken in the same format as for the initMIP-Antarctica experiments (Seroussi and others, 2019) but for 500 years instead of 100 years after being initialized to the beginning of the 21st century.

Participating models

A total of 13 modelling groups participated in the experiments and most of these performed all the three experiments (Table 1). Details of the 15 different models, their initialization, their numerical characteristics and which sliding or friction laws are employed are summarized in Table 2. Time steps from 0.4 days to 0.5 years are used by models. Further description of the models can be found in the Appendix.

All models include membrane stresses in their force balance, either corresponding to the so-called Shallow-Shelf Approximation (SSA, Table 2), or by also including vertical shearing and vertically differentiated membrane stresses. The majority of models are hybrid models and heuristically combine the SSA as a sliding or friction law with the Shallow-Ice Approximation (SIA) for inclusion of vertical shearing (Bueler and Brown, 2009). One model includes vertical shear terms in the effective viscosity term (Schoof and Hindmarsh, 2010), which leads to the so-called SSA* approach. One model applies the Blatter–Pattyn approximation (labelled LMLa), which is the hydrostatic approximation of the Stokes equations (Blatter, 1995; Pattyn, 2003), and one model (labelled L1L2) uses a depth-integrated version of this approximation (Goldberg, 2011).

The participating models use several different initialization techniques. A common approach is the paleo spin-up (Sp, Table 2) during which the ice sheet is run through a glacial-interglacial cycle until the present day. In this way, the state includes temperature field and change rates of geometry as cumulative response to past climates. In one case, the spin-up runs with an iterative optimization for basal friction coefficients with target values for ice thickness (SpC). Another common procedure is an equilibrium type spin-up, which also allows for establishing an internal temperature field with equilibrium ice sheet (Eq). In most cases, this equilibrium ice sheet is combined with an iterative optimization of the basal sliding/friction field to obtain an ice-sheet geometry that is close to the observed ice sheet (EqC), with methods described in Pollard and DeConto (2012*b*) and Le clec'h and others (2019), among others. All other models used data assimilation (essentially using the observed surface velocity field) to tune a basal friction field in present day conditions (DA). While models employing paleo spin-up (Sp) or an equilibrium state (Eq) have a present-day ice-sheet geometry that is in poorer agreement with the observed ice sheet (compared to models using assimilation methods), assimilation-based initial conditions generally have noisier and more unrealistic ice thickness transients.

Apart from the wide range of initialization techniques, discussed in more detail in Goelzer and others (2018) and Seroussi and others (2019), major model differences stem primarily from the basal sliding and/or friction law employed. Two commonly used basal conditions are the Weertman sliding (Weertman, 1957) and the Coulomb friction law (Schoof, 2005) (Table 2). Both can be written in the following generic form

$$\tau_b = \beta^2 u_b\,, \tag{1}$$

where τ_b is the basal shear stress (sum of all basal resistance), $\mathbf{u}_b$ is the basal sliding velocity, and β^2 a friction term that in the case of a Weertman sliding law is defined by

$$\beta^2 = C u_b^{1/m-1} N^{p/m}\,, \tag{2}$$

where C is a friction coefficient that can be spatially varying for models that use a SpC, EqC or DA initialization techniques, and N represents the effective pressure at the base of the ice sheet (difference between the ice overburden pressure and subglacial water pressure). For $m = 1$, the friction law becomes viscous and β^2 is solely dependent on the effective pressure. However, most models set $p = 0$ so that N is not considered, except ILTS-PIK-SICOPOLIS that uses $p = 2$. In the case of a Coulomb friction law the friction term is written using the expression as in Schoof (2005) or as in Aschwanden and others (2019)

$$\beta^2 = \frac{N \tan\phi}{|\mathbf{u}_b|^{(1-q)} u_0^q}\,, \tag{3}$$

where ϕ is the till friction angle that is either considered constant or optimized in a similar fashion to the friction term C in Eqn (2). The yield stress τ_c is defined by the numerator in Eqn (3), $0 \le q \le 1$, and u_0 represents a threshold speed for sliding (Aschwanden and others, 2013). The friction law, Eqn (3), includes the case $q = 0$, leading to the purely plastic (Coulomb) relation $\tau_b = \tau_c u_b/|\mathbf{u}_b|$. In the linear case $q = 1$, Eqn (3) becomes $\beta^2 = \tau_c/u_0$ (Bueler and van Pelt, 2015). Most models define the effective pressure N from till dynamics (Bueler and van Pelt, 2015; Aschwanden and others, 2019), which leads to a sharp contrast in effective pressure between saturated till and non-saturated till or hard bedrock. None of the models considered full subglacial hydrology but either define effective pressure from subglacial elevation (submarine basins with saturated till) or from locally generated subglacial melt. The last column of Table 2 lists the values of m and q for the different friction laws employed. One model uses a Weertman law limited by a Coulomb friction law (Table 2), in which the basal shear stress is set to the minimum of the two stresses (Tsai and others, 2015).

Results

ABUC

The standard experiment of the series is the control run (ABUC), where participating models run forward for 500 years starting from the initial conditions without any external forcing. This experiment allows for determining intrinsic model drift. Despite the lack of forcing, there is a large variation in ice-sheet mass changes observed (Fig. 1; expressed in terms of contribution to sea level based on the volume above flotation as defined in Eqn (1) of Bindschadler and others, 2013), depending on the initial dataset used. The method converting ice-sheet mass loss to sea-level contribution results in ~56.7 m SLE based on the Bedmap2 data set, which is lower than the value 58.3 m in Fretwell and others (2013) using the Lambert Azimuthal Equal Area projection for area and volume calculations. For BedMachine Antarctica (Morlighem and others, 2020) the values are ~55.1 and ~57.9 m, respectively. Results for ABUC are in overall agreement with initMIP Antarctica (Seroussi and others, 2019), i.e. models that are using either data assimilation (DA) or target values for ice thickness (SpC, EqC) are closer to the present day volume of the Antarctic Ice Sheet at the start of the model run. Models that use paleo-spinup (Sp; ARC-PISM and AWI-PISMPal) overestimate the initial ice volume above flotation. One model, IMAU-ICE, underestimates the present-day ice

Table 1. List of participating models in the ABUMIP experiment

Contributors	Group ID	Model	Experiments	Affiliation
N. Golledge	ARC	PISM	ABU(C,K,M)	Antarctic Research Centre, Victoria University of Wellington, Wellington, New Zealand
T. Kleiner, J. Sutter, A. Humbert	AWI	PISMPal	ABU(C,K)	Alfred Wegener Institute for Polar and Marine Research, Bremerhaven, Germany
S. Cornford, D. Martin	CPOM	BISICLES	ABU(C,K,M)	Swansea University, Swansea, UK; Lawrence Berkeley National Laboratory, Berkeley, USA
F. Gillet-Chaulet	IGE	Elmer/Ice	ABU(C,K,M)	Institut des Géosciences de l'Environnement, Grenoble, France
R. Greve, R. Calov	ILTS-PIK	SICOPOLIS	ABU(C,K,M)	Institute of Low Temperature Science, Hokkaido University, Sapporo, Japan; Potsdam Institute for Climate Impact Research, Potsdam, Germany
H. Goelzer	IMAU	IMAUICE	ABU(C,K,M)	Institute for Marine and Atmospheric Research, Utrecht, the Netherlands
H. Seroussi, M. Morlighem	JPL	ISSM	ABU(C,M)	University of California, Irvine, USA; Jet Propulsion Laboratory, California Institute of Technology, Pasadena, USA
C. Dumas, A. Quiquet	LSCE	GRISLI	ABU(C,K,M)	Laboratoire des Sciences du Climat et de l'Environnement, Université Paris-Saclay, Gif-sur-Yvette Cedex, France
G. Leguy, W. Lipscomb	NCAR	CISM	ABU(C,K,M)	Climate and Global Dynamics Laboratory, National Center for Atmospheric Research, Boulder, CO, USA
D. Pollard	PSU	PSU3D	ABU(C,K,M)	Earth and Environmental Systems Institute, Pennsylvania State University, University Park, PA, USA
E. Kazmierczak, S. Sun, F. Pattyn	ULB	f.ETISh	ABU(C,K,M)	Université Libre de Bruxelles, Brussels, Belgium
S. Price, M. Hoffman, T. Zhang	DOE	MALI	ABU(C,K)	Los Alamos National Laboratory, NM, USA
T. Albrecht, T. Schlemm, R. Winkelmann	PIK	PISM	ABU(C,K,M)	Potsdam Institute for Climate Impact Research, Potsdam, Germany

Details of the models are given in Table I and Appendix.

Table 2. List of ABUMIP simulations and main model characteristics

Model name	Numerics	Stress balance	Resolution km	Initialization	SMB	Basal sliding/friction
ARC-PISM1	FD	Hybrid	16	Sp	RACMO2.1	Coulomb $q = 0.75$
ARC-PISM2	FD	Hybrid	16	Sp	RACMO2.1	Coulomb $q = 0.75$ with sub-grid melting
AWI-PISMPal	FD	Hybrid	16	Sp	RACMO2.3	Coulomb $q = 0.6$
CPOM-BISICLES	FV	SSA*	0.5–8	DA+	Arthern	Weertman $m = 3$/Coulomb
IGE-Elmer/Ice	FE	SSA	1–50	DA	MAR	Weertman $m = 3$
ILTS-PIK-SICOPOLIS	FD	Hybrid	8	SpC	Arthern	Weertman $m = 3$, $p = 2$
IMAU-ICE	FD	Hybrid	32 (★)	Eq	RACMO2.3	Coulomb $q = 0$
JPL-ISSM	FE	SSA	1–50	DA	RACMO2	Weertman $m = 1$
LSCE-GRISLI	FD	Hybrid	16 (★)	EqC+	RACMO2.3	Coulomb $q = 1$
NCAR-CISM	FE/FV	L1L2	4	EqC	RACMO2.3p2	Weertman $m = 3$/Coulomb
PSU-PSU3D1	FD	Hybrid	16 (★)	EqC	Arthern	Weertman $m = 2$
PSU-PSU3D2	FD	Hybrid	16 (★)	EqC	Arthern	Weertman $m = 2$ without cliff instability
ULB-f.ETISh	FD	Hybrid	16 (★)	EqC+	RACMO2.3	Weertman $m = 2$
DOE-MALI	FE/FV	LMLa	2–20	DA+	RACMO2	Weertman $m = 1$
PIK-PISM	FD	Hybrid	4	EqC+	RACMO2.3p2	Coulomb $q = 0.75$

Numerics rely on the finite-difference (FD), finite-element (FE) or finite-volume (FV) method. Stress balance approximations implemented by models include Shallow-Shelf Approximation (SSA; see MacAyeal, 1989), SSA with vertical shear terms represented in the effective viscosity term (SSA*; see Cornford and others, 2013), combination of SSA and Shallow-Ice Approximation (Hybrid; see Bueler and Brown, 2009; Winkelmann and others, 2011), depth-integrated higher-order approximation (L1L2; see Goldberg, 2011) and Blatter–Pattyn approximation (LMLa; see Pattyn, 2003). Initialization methods are as follows: spin-up (Sp), spin-up with target values for the ice thickness (SpC), data assimilation (DA), equilibrium state (Eq) and equilibrium state with target values for the ice thickness (EqC; see Pollard and DeConto, 2012*a*). (+) Means relaxation after initialization. (★) Marks models that use a grounding line flux parameterization (e.g. Pollard and DeConto, 2012*a*). Initial SMB is derived from the following: RACMO2 (Lenaerts and others, 2012), RACMO2.3 (Van Wessem and others, 2014), RACMO2.3p2 (Van Wessem and others, 2018), MAR (Agosta and others, 2019) and Arthern and others (2006) (Arthern). Ice-sheet geometries are based on Bedmachine (Morlighem and others, 2020) for f.ETISh and Bedmap2 (Fretwell and others, 2013) for all other models. Further details on all the models are given in the Appendix.

volume, as it starts from an equilibrium ice sheet (Eq). All other models are within the range of 55–57 m SLE.

For most models, ABUC leads to a limited model drift between − 0.2 and +0.2 m SLE (Fig. 1). Exceptions are ARC-PISM with a more important mass increase equivalent to 1.5 m SLE. Models that do show a drift of around ±0.5 m SLE are PISM-PIK, DOE-MALI, PSU-PSU3D1, ULB-f.ETISh and JPL-ISSM. Model drift in the control run is generally (but not unequivocally) associated with the initialization scheme, i.e. data assimilation (DA) methods usually match better with observations but exhibit a larger drift, while the opposite is true for models relying on a spin-up or a steady-state solution (Goelzer and others, 2018; Seroussi and others, 2019). However, other processes could be responsible as well. For example, the suspicious mass increase in ARC-PISM could be attributed to the sub-shelf melting scheme (no melting in ABUC), and the higher mass loss (~0.5 m SLE) of PSU-PSU3D1 compared to PSU-PSU3D2 may stem from the inclusion of hydro-fracturing.

ABUK

The sudden and sustained loss of ice shelves (ABUK) or an imposed extreme high sub-shelf melt rate (ABUM) lead to a significant loss of grounded ice over the period of 500 years for all participating ice-sheet models. Net mass loss is between 2 and 10 m SLE for ABUK and between 1 and 12 m SLE for ABUM after 500 years (Fig. 1). Most of the mass loss occurs in the first 100–200 years of the simulations for the majority of models and mass loss rates decrease afterwards to remain more or less steady.

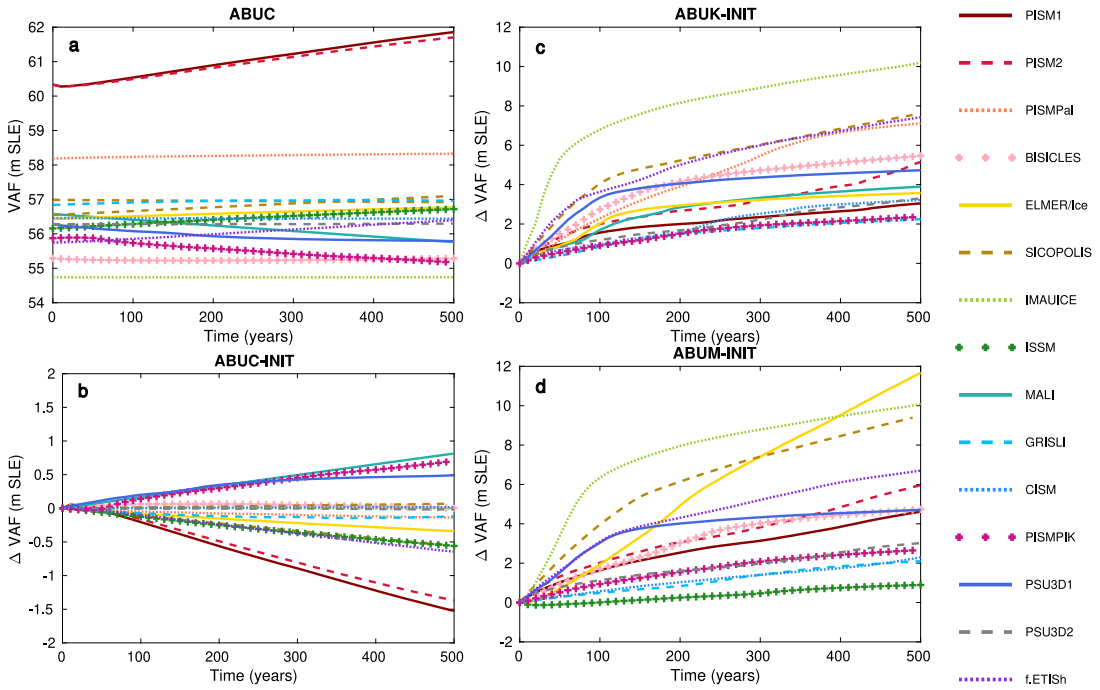

Fig. 1. Volume above flotation (in m SLE) and contribution to sea-level rise (SLR) for ABUC (left) and both ABUK and ABUM experiments (positive means higher sea-level contribution). Subplots b, c and d with title '-INIT' represent the sea-level contribution compared to the initial state.

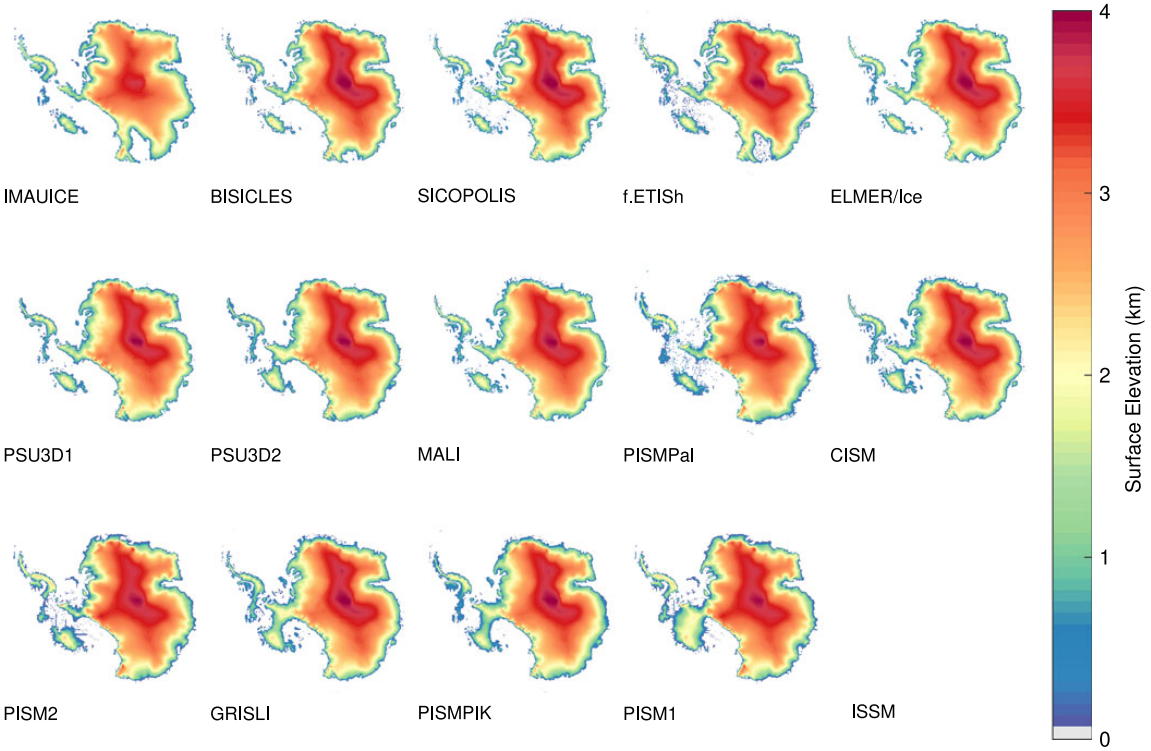

Fig. 2. Surface elevation for the grounded ice sheet after 500 years in ABUK for all participating models. The sequence of models is ordered from lowest to highest grounded area at the end of the simulations. All models effectively lose a large part of WAIS. Some models also lose mass in Recovery Subglacial Basin, Wilkes Subglacial Basin and Aurora Subglacial Basin.

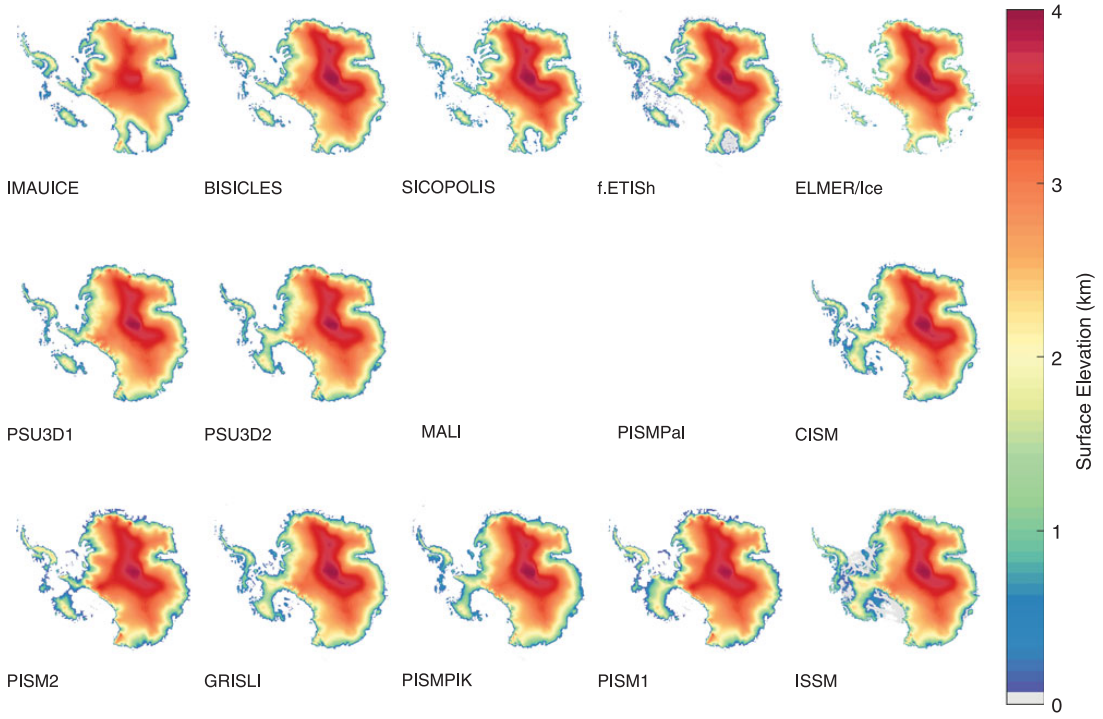

Fig. 3. Surface elevation for the grounded ice sheet after 500 years in experiment ABUM for all participating models. Similar to ABUK results, all models effectively lose a large part of WAIS. Some models also lose mass in Recovery Subglacial Basin, Wilkes Subglacial Basin and Aurora Subglacial Basin. The sequence of the model results is the same as in Figure 2 to facilitate the comparison.

In a spatial context, this implies that all models effectively lose the West Antarctic ice sheet (WAIS) or at least a large part of it (Figs 2 and 3). One exception is ARC-PISM1 with little grounding line retreat in Thwaites glacier, which may be due to a too-coarse spatial resolution across the grounding line (Gladstone and others, 2010, 2012; Pattyn and others, 2013; Leguy and others, 2014). The use of sub-shelf melting underneath grounded parts of the ice-sheet results in higher mass loss with that same model, as shown by the results of ARC-PISM2. PIK-PISM and LSCE-GRISLI conserve an ice bridge in the centre of the WAIS at the end of both experiments, while JPL-ISSM, CISM and PSU3D2 maintain the ice bridge in ABUM experiment.

The ABUK experiment also allows to identify potential mass loss due to MISI. For instance, Bamber and others (2009) calculate the potential contribution to SLR due to WAIS collapse with a simple method: they identify grid cells below sea level on retrograde bed slopes to infer the limit of grounding-line retreat, which leads to a SLR contribution of 3.3 m. However, in order to fully capture the effect of MISI, all dynamical effects need to be taken into account, which is only possible using marine ice-sheet models. ABUK provides such a multi-model experiment in which ice-shelf buttressing is completely removed and the modelled ice sheet evolves through MISI. Most participating models therefore simulate a collapse of the WAIS. In order to make comparison with Bamber and others (2009) possible, we recalculated the mass loss for the same WAIS area. For ABUK, this ranges from 1.91 to 5.08 m, with a mean value of 3.16 m SLE. When considering only those models that are reproducing a full collapse of WAIS, this ranges from 2.86 to 5.08 m, with a mean value of 3.67 m SLE, which is higher than the value given in Bamber and others (2009).

Multi-metre ice mass loss beyond 2–3 m SLE is related to loss of grounded ice in sectors of the East Antarctic ice sheet (EAIS), especially in Recovery Subglacial Basin (location shown in Fig. 4). Some models also lose mass in Wilkes Subglacial Basin and to a lesser extent Aurora Subglacial Basin (locations shown in Fig. 4), i.e. IMAU-ICE, ILTS-PIK-SICOPOLIS, ULB-f.ETISh, IGE-Elmer/Ice and CPOM-BISICLES (Fig. 2).

The overall assessment of the response of the different models is described by the mean value of the average percentage of ice-thickness change against the initial ice thickness over the model ensemble (probability) and its standard deviation among the participating models (Fig. 4). For specific basins, the mean mass loss, the standard deviation of mass loss and the mean proportion of mass loss are listed in Table. 3. The highest values of mass loss occur in the Recovery Subglacial Basin (1.44 m SLE) due to the loss of the Filchner-Ronne ice shelf, in the Siple Coast ice streams (1.16 m SLE) due to the loss of the Ross ice shelf, and in the Amundsen Sea Embayment due to the loss of the Thwaites and Pine Island Glaciers (0.99 m SLE). The standard deviation in the Recovery Subglacial Basin is also high, meaning that models agree less in this basin, while most models agree on the amount of mass loss in the Siple Coast and Amundsen Sea Embayment. The central part of the WAIS has a lower probability of mass loss, since not all models exhibit a complete collapse of the WAIS. The lowest probability and highest standard deviation are seen for the Wilkes and Aurora Subglacial Basins in East Antarctica, as only few models exhibit mass loss in those sectors.

ABUM

The ABUM experiment shows similar characteristics as ABUK, except IGE-Elmer/Ice where ABUM has the most mass loss (up

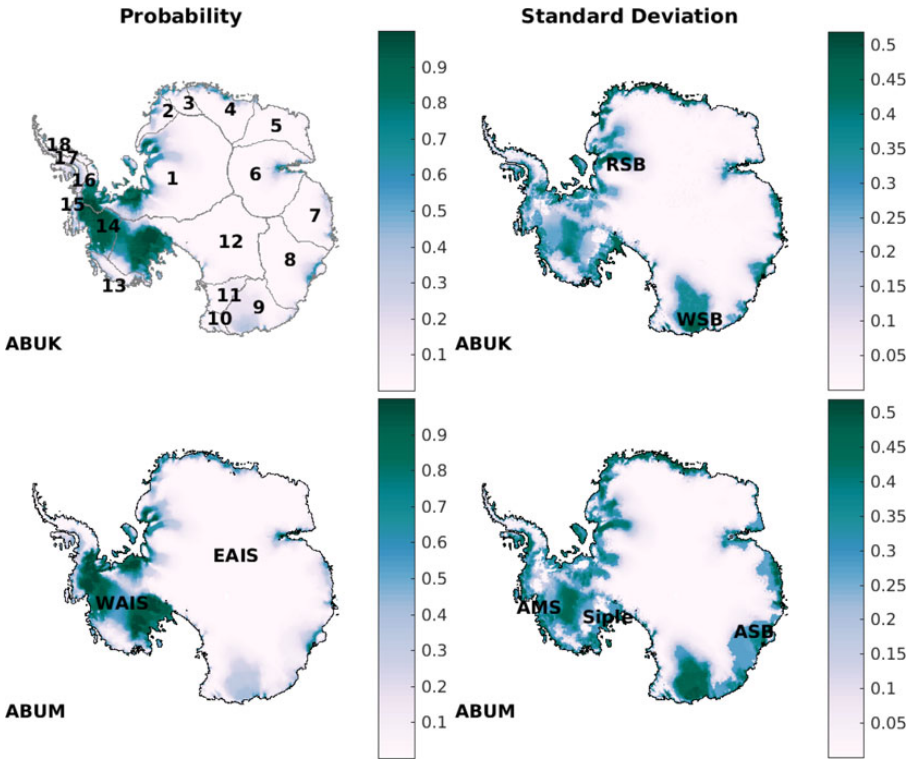

Fig. 4. Average percentage of thickness change against the initial ice thickness over the model ensemble (left column) after 500 years for the ABUK (top) and ABUM (bottom) models. Standard deviation of the percentage of thickness change (right column). Major place names and subglacial basin numbers of Table 3 of the Antarctic Ice Sheet are given in the different panels (AMS, Amundsen Sea Sector; WSB, Wilkes Subglacial Basin; ASB, Aurora Subglacial Basin; RSB, Recovery Subglacial Basin; EAIS, East Antarctic Ice Sheet; WAIS, West Antarctic Ice Sheet).

to 12 m SLE after 500 years). This is likely a mesh resolution issue in the model, as the grounding line migrates beyond the refined grid into the coarser grid areas in ABUM, while the domain was remeshed every 5 years in the ABUK experiment.

It is also interesting to note that PSU3D1 that includes cliff collapse, does not differ that much from the results of PSU3D2, without the cliff collapse mechanism activated. The reason behind the difference with results from Pollard and others (2015); DeConto and Pollard (2016) lies in the fact that surface melt is necessary to provoke hydro-fracturing of the grounded ice sheet to initiate cliff collapse, and this surface melt is not large enough in the current experimental set up. Since the ABUK and ABUM experiment lack any atmospheric forcing, cliff collapse is not invoked by hydro-fracture process.

Discussion

Sensitivity to basal friction

In the ensemble of model results, there seems to be a general tendency of increased mass loss with increased plasticity of the friction law, both Weertman and Coulomb (Fig. 5, where the different models are grouped according to basal friction law). For the ABUK experiment results, models implementing linear Weertman/Coulomb friction law result in 3.07 m SLE ice loss on average, while the value for the pseudo-plastic Coulomb friction law, the Weertman friction law with $m = [2, 3]$, and the plastic Coulomb friction law are 4.41, 5.10, 4.95 and 10.20 m SLE, respectively. The same trend is shown in ABUM experiment results; models implementing the linear Weertman/Coulomb friction law result in 1.49 m SLE ice loss on average, while the value for the pseudo-plastic Coulomb friction law, the Weertman friction law with $m = [2, 3]$, and the plastic Coulomb friction law are respectively 4.41, 4.81, 7.02 and 10.08 m SLE. In the subgroup of pseudo-plastic Coulomb friction law, where different branches of the PISM model are implemented, a 'more' plastic sliding law with $q = 0.6$ results in larger mass loss compared to those with $q = 0.75$. However, this trend is not straightforward for all of the models. This means that other factors influence the model sensitivity as well, and they most likely pertain to differences in numerical approaches of the models, especially the spatial resolution across the grounding line and the way models simulate grounding line migration (Gladstone and others, 2010, 2012; Pattyn and others, 2012, 2013; Pattyn and Durand, 2013; Leguy and others, 2014; Durand and Pattyn, 2015; Brondex and others, 2017). This is further detailed below.

The response to a sudden removal of ice shelves for the different models is not clearly related to the initialization method. However, as also shown in Joughin and others (2009); Parizek and others (2013); Brondex and others (2017); Pattyn (2017); Brondex and others (2019) and Bulthuis and others (2019), plastic sliding/friction law generally lead to more prominent grounding-line migration compared to viscous sliding laws. To demonstrate this, we performed the ABUK experiment with one model (ULB-f.ETISh) for a Weertman sliding law with exponents $m = 1$, 2, 3, 4, and for the Coulomb friction law with $q = 1$ (linear case). Figure 6 demonstrates that a viscous sliding law is the least sensitive to mass loss due to a sudden and sustained loss of ice shelves; the amount of mass loss increases with increasing exponent m. The highest mass loss is encountered for the linear Coulomb

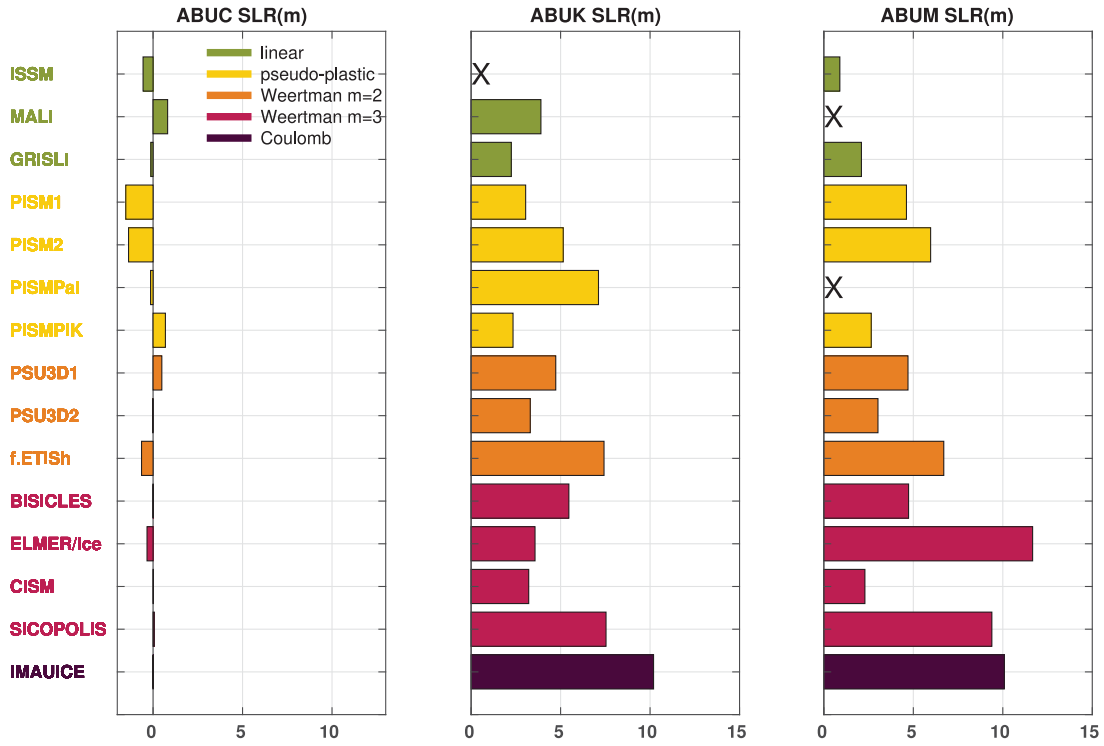

Fig. 5. Overall mass loss (volume above flotation; VAF) for the participating models ordered according to basal friction law characteristics: Weertman and Coulomb linear ($m = 1$, $q = 1$), pseudo-plastic Coulomb ($q = 0.6$–0.75), Weertman $m = 2$, Weertman $m = 3$, Coulomb plastic $q = 0$. Models that did not participate a particular experiment are marked by 'X'.

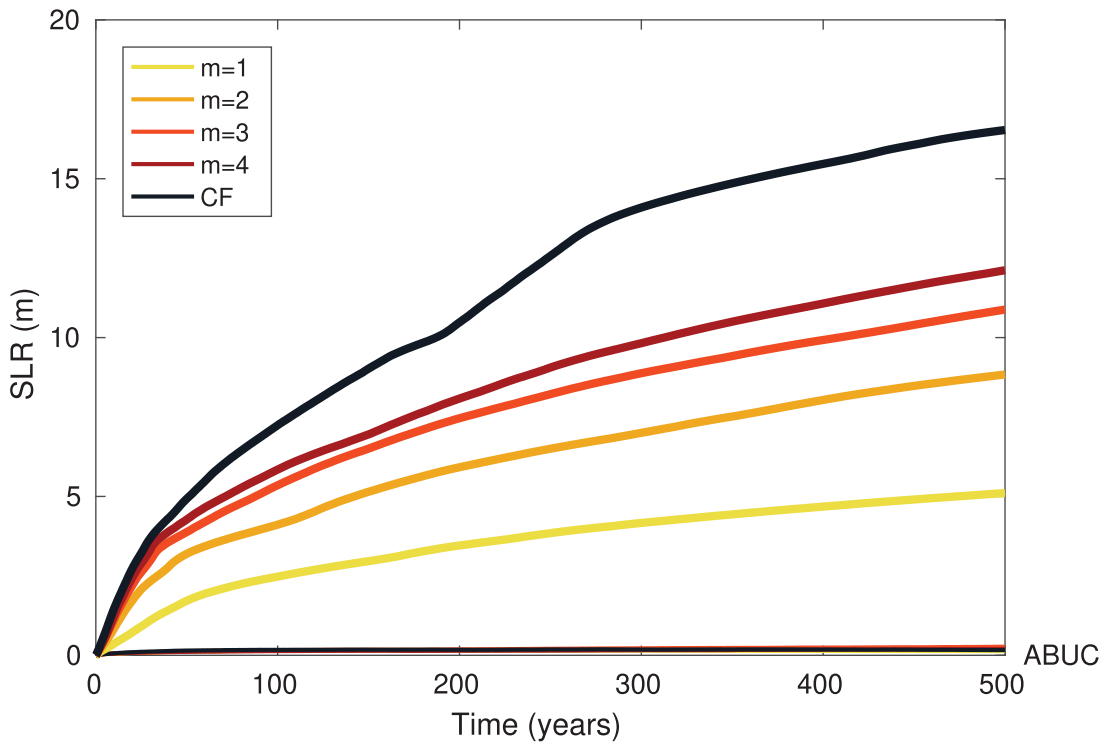

Fig. 6. Ice mass loss for the ABUK and ABUC (labelled) experiments with ULB-f.ETISh for different exponents of the Weertman law ($m = 1, 2, 3, 4$) and the linear Coulomb friction law (CF, $q = 1$). The amount of mass loss increases with increasing exponent m.

Table 3. Model results of mass loss for Antarctic subglacial basins after 500-year simulation of ABUK

Number	Ice shelf (basin)	Mean loss (m SLE)	σ (m SLE)	Probability
1	Filchner-Ronne (RSB)	1.44	1.00	0.10
2	Riiser-Larsen, Stancomb, Brunt	0.053	0.08	0.083
3	Fimbul	0.019	0.015	0.028
4	Baudouin	0.056	0.063	0.024
5	Shirase, Holmes	−0.005	0.06	−0.002
6	Amery	0.18	0.13	0.02
7	Shackleton, West	0.065	0.13	0.02
8	Totten (ASB)	0.15	0.18	0.024
9	Cook, Ninnis, Mertz (WSB)	0.35	0.60	0.11
10	Rennick (WSB)	0.006	0.013	0.024
11	Drygalski (WSB)	0.075	0.19	0.068
12	Ross	1.16	0.52	0.098
13	Getz	0.06	0.05	0.15
14	Pine Island, Thwaites (AMS)	0.99	0.39	0.79
15	Abbot	0.065	0.05	0.41
16	Wilkins, Stange, Bach, George VI	0.08	0.12	0.19
18	Larsen C	−0.003	0.014	−0.13

Basin numbers are in accordance with Reese and others (2018*a*). σ is the standard deviation of mean mass loss in the basin. Probability is the average percentage of mass loss against the initial mass of the basin over the model ensemble. Present-day basin boundaries are used, without consideration of divide migration during the simulation. The abbreviations of the basins are the same with Figure 4.

friction case. However, different grounding line flux parameterizations are implemented in the ULB-f.ETISh model depending on the sliding laws. Indeed, a Coulomb friction law implies a zero effective pressure N at the grounding line (Leguy and others, 2014; Tsai and others, 2015), which leads to a higher sensitivity compared to the parameterization due to Schoof (2007) and demonstrated in Pattyn (2017).

Sensitivity to the forcing scheme

Most models have a slightly higher mass loss after 500 years for the ABUK than for the ABUM experiment (Fig. 5) due to the remaining weak buttressing from ice shelves in the latter. However, some models show a suspiciously stronger sensitivity for ABUM compared to ABUK although the ice-shelf removal should intrinsically have a stronger effect than applying excessive sub-shelf melt rates.

The reason for the more pronounced mass loss in IGE-Elmer/Ice stems from the difference in numerical set up for both experiments. Initially the mesh is much finer mesh around the grounding line and coarser inland. While a new mesh is generated every 5 years to cope with grounding-line retreat in ABUK, the ABUM experiment considers a fixed mesh, so that the grounding line irrevocally retreats from a mesh of 1 to 32 km during the model run.

There are few other models ARC-PISM1, ARC-PISM2, PISM-PIK, ILTS-PIK-SICOPOLIS with higher mass loss for ABUM to a less extent, from 0.82 to 1.9 m SLE. A possible explanation is that the sliding scheme in the vicinity of the grounding line is interpolated as a function of surface gradients and driving stress (Feldmann and others, 2014; Gladstone and others, 2017) so as to have a continuous transition of sliding from the grounding zone to the floating zone. The presence of floating ice in ABUM leads to a gentler surface gradient, and therefore higher sliding at the grounding line compared to ABUK where the grounding line acts as a computational boundary.

Sensitivity to model physics and numerics

The sensitivity of the experimental results to model physics and numerics is more difficult to assess. We considered several essential factors: spatial resolution, initial ice and bedrock geometry, basal sliding law and subglacial hydrology.

Spatial resolution

Spatial resolution may have a profound impact as previous assessments on marine ice-sheet models have demonstrated (Pattyn and others, 2012, 2013; Leguy and others, 2014). Comparing numerical models to theory (Schoof, 2007), Pattyn and others (2012) showed that a spatial resolution of <1 km is necessary to capture the essential dynamics of grounding lines. However, the grid size is also dependent on the basal friction transition across the grounding line, i.e. for a sharp contrast of no slip (grounded ice sheet) to free slip (ice shelf), spatial resolution needs to be high, but smoother transitions – e.g. from a weak till-based ice stream to an ice shelf – are more forgiving with respect to resolution (Pattyn and others, 2006; Gladstone and others, 2010, 2012; Leguy and others, 2014). Moreover, sub-grid grounding line interpolations also relax some resolution requirements (Parizek and others, 2013; Seroussi and others, 2014; Cornford and others, 2016; Hoffman and others, 2018) and such parameterizations are applied in DOE-MALI, NCAR-CISM, ARC-PISM, AWI-PISMPal and PIK-PISM. Some models apply an analytic constraint on the flux across the grounding line based on theoretical derivations for an unbuttressed flow-line setting (e.g. Schoof, 2007). This is the case for IMAU-ICE, LSCE-GRISLI, PSU-PSU3D and ULB-f.ETISh.

High-resolution models without grounding-line parameterizations, interpolations or heuristics, such as DOE-MALI, IGE-Elmer/Ice and CPOM-BISICLES, produce ice mass loss in the range of 3.5–5 m SLE after 500 years. They corroborate results of the other models, i.e. that they lose the complete WAIS and parts of the Recovery and Wilkes Subglacial Basins. However, this sample is too small to confirm whether these mass loss bounds can be considered as being representative of the highest resolution models.

Apart from models with mesh refinement schemes, most of models implement 16 km resolution in the simulations. Models with 4 km resolution (PIK-PISM and CISM) have less mass loss compared to models with similar sliding laws (Fig. 5). IMAU-ICE has the coarsest resolution of 32 km as well as the highest mass loss especially in Wilkes Subglacial Basin. While IMAU-ICE is the only model with 32 km resolution and the only model with Coulomb plastic sliding law, the high mass loss could therefore be a result of the combination of both.

Initial geometry

Other differences may be due to the initial conditions applied in the models, such as the initial surface and bed topography (ULB-f.ETISh used BedMachine Antarctica (Morlighem and others, 2020) while all other models used Bedmap2 (Fretwell and others, 2013)).

Basal sliding law

The tendency for increased model sensitivity to the power of the sliding law, as demonstrated in Figure 6, is only marginally clear when grouping the models in a similar way (Fig. 5). This means that the level of noise, due to different numeric approaches, spatial resolutions, model physics and boundary conditions in the ensemble, is of comparable order of magnitude as the signal.

Subglacial hydrology

A major uncertainty remains in the physical understanding and modelling of subglacial till mechanics that are essential for determining the effective pressure and sliding rate at the base of a marine ice sheet. The few studies that have attempted to tackle this problem (e.g. Bueler and van Pelt, 2015; Gladstone and

others, 2017) are based on seminal work by Tulaczyk and others (2000*a*, 2000*b*), but it is clear that more research in subglacial hydrology and basal mechanics of marine ice sheets is needed.

New techniques have been and will need to be further explored to improve initialization methods using both observed surface elevation and ice velocity changes, allowing for improved understanding of underlying friction laws and rheological conditions of marine-terminating glaciers (Gillet-Chaulet and others, 2016; Gillet-Chaulet, 2020). Observations in regions with large changes can be used to discriminate different parameterizations. Joughin and others (2009), Joughin and others (2019) and Gillet-Chaulet and others (2016) have shown that plastic laws are better suited for fast flowing areas in Pine Island Glacier in the Amundsen Sea Embayment, which in the light of this study makes a strong case for the increased sensitivity of grounding-line retreat and ice-sheet response relative to the commonly used sliding laws. Transient data assimilation (Goldberg and others, 2015; Gillet-Chaulet, 2020) that allow to capture observed rates of change should give better confidence in projections and enable reanalysis to better comprehend processes that drive past changes.

Sensitivity to hydro-fracturing and Marine Ice Cliff Instability

The Marine Ice Cliff Instability (MICI) mechanism (based on Bassis and Walker, 2012; DeConto and Pollard, 2016 and Pollard and others, 2015) leads to SLR projections exceeding 12 m after 500 years for unmitigated climate scenarios. This value is outside the range of most of the projections (Hanna and others, 2020), but not that far out of the range of the upper end model results with the ABUMIP ensemble and without MICI. This demonstrates that other processes besides the MICI may result in large mass loss from the Antarctic ice sheet, including marine basins from the EAIS, and still match values representative of Pliocene sea-level high stands (Edwards and others, 2019). Plastic Coulomb friction laws in particular increase the sensitivity of grounding-line retreat under reduced ice-shelf buttressing. The inclusion of hydro-fracturing in PSU-PSU3D1 results in ∼1.5 m SLE higher mass loss in the ABUK and ABUM experiments compared to the PSU-PSU3D2 model without the extra physics. This lack of considerable mass loss compared to DeConto and Pollard (2016) is mainly due to the absence of atmospheric anomalies in ABUMIP that otherwise would produce substantial surface melt to initiate the hydro-fracturing process.

Comparison to other studies

Three recent studies (Fürst and others, 2016; Reese and others, 2018*b*; Gudmundsson and others, 2019) investigated the sensitivity of ice shelves to buttressing on the inland ice sheet. However, all of them investigated the current and immediate impact of ice shelves on the buttressing potential, not attempting to quantify buttressing importance as a function of potential ice mass loss over time. Martin and others (2019) quantified the vulnerability of present-day Antarctic ice sheet to regional ice-shelf collapse on millennial timescales using BISICLES. ABUMIP therefore offers a unique opportunity to quantify the potential mass loss for the extreme case where all ice shelves are lost and gauges the response of the ice sheet to such dramatic collapse.

The ABUM experiment is comparable to the M3 experiment from the SeaRISE project (Bindschadler and others, 2013; Nowicki and others, 2013) that considered extreme sub-ice-shelf melting with a lower melt rate of 200 m a^{-1}. Despite the higher sub-ice-shelf melting implemented by ABUM, the range of mass loss is significantly decreased from [2–20] m SLE in SeaRISE compared to [1–12] m SLE in ABUM. The better agreement between models here is due to the fact that (i) ice streams are better resolved (in terms of spatial resolution and/or model physics that all include membrane stresses), and (ii) grounding line dynamics are better captured (e.g. Pattyn and others, 2013; Leguy and others, 2014; Durand and Pattyn, 2015). All models now allow for the grounding line to migrate, either through the use of a finer mesh or by means of grounding-line flux parameterizations. Furthermore, ice-sheet models include dynamic ice shelves, which was not the case with the SeaRISE ensemble. Some models in that specific ensemble applied sub-shelf melting spread out across grounded cells, which increases the sensitivity to sub-shelf melt forcing of the model through enhanced grounding-line retreat (Durand and Pattyn, 2015; Seroussi and Morlighem, 2018).

Conclusions

We have presented results of the ISMIP6-ABUMIP experiment that investigate the effects of a sudden loss of ice shelves on Antarctic ice sheet volume change, either through a complete and sustained collapse of ice shelves (ABUK) or an extreme sub-shelf melting rate (ABUM). Results of both experiments exhibit similar responses, i.e. a fast response and high probability of complete collapse of the WAIS and potential gradual mass loss of some EAIS basins, such as Recovery, Wilkes subglacial basins and to a lesser extent Aurora subglacial basin. Previous studies estimated the WAIS collapse due to MISI as 3.3 m SLE (Bamber and others, 2009). Our study shows that WAIS collapse potentially leads to a 1.91–5.08 m sea level rise when ice-dynamical effects are included.

In the absence of ice-shelf buttressing, simulated mass losses are evidently controlled primarily by basal conditions. Basal friction laws with a higher plasticity lead to a more sensitive response to reduced ice-shelf buttressing. The effect of plasticity in a basal friction law ($m = 4$ vs $m = 1$ in a Weertman sliding law) alone causes a ∼7 m SLE difference for the ABUK experiment. Gillet-Chaulet and others (2016) suggest that a more plastic sliding law m≥5 is required to accurately reproduce the observed acceleration in fast flowing regions. If plastic sliding laws are more applicable Antarctic-wide, the ice sheet will have higher sensitivity to ice-shelf loss of buttressing. The range of mass loss indicates that processes other than the Marine Ice Cliff Instability are capable of reproducing large mass losses over centennial time spans, similar to inferred Pliocene sea-level high stands. Given the importance of subglacial processes in guiding the rate of mass loss of marine basins, the inclusion of a more realistic subglacial hydrology will be another challenge for the ice-sheet modelling community.

Uncertainties also stem from numerical approximations, such as spatial and temporal resolutions of the model, as well as parameterization methods for physical processes operating at the grounding line. However, the relatively small ensemble of models with diverse methods make it difficult to quantify the uncertainties from different schemes. Sensitivity tests of different schemes within a single model would therefore be of particular interest. This study will help to better understand the spread in projections of 21st century Antarctic ice sheet contributions to sea level.

Data availability

The model output from the simulations described in this paper and forcing data sets will be made publicly available with digital object identifier https://doi.org/10.5281/zenodo.3932935. In order to document CMIP6's scientific impact and enable ongoing support of CMIP, users are asked to acknowledge CMIP6, ISMIP6 and the participating modelling groups.

Acknowledgments. We thank the Climate and Cryosphere (CliC) effort, which provided support for ISMIP6 through sponsoring of workshops, hosting the ISMIP6 website and wiki, and promoted ISMIP6. We acknowledge the World Climate Research Programme, which, through its Working Group on Coupled Modelling, coordinated and promoted CMIP5 and CMIP6. We thank the climate modelling groups for producing and making available their model output, the Earth System Grid Federation (ESGF) for archiving the CMIP data and providing access, the University at Buffalo for ISMIP6 data distribution and upload, and the multiple funding agencies who support CMIP5 and CMIP6 and ESGF. Support for Matthew Hoffman, Stephen Price and Tong Zhang was provided through the Scientific Discovery through Advanced Computing (SciDAC) programme funded by the US Department of Energy (DOE), Office of Science, Advanced Scientific Computing Research and Biological and Environmental Research Programs. MALI simulations used resources of the National Energy Research Scientific Computing Center, a DOE Office of Science user facility supported by the Office of Science of the US Department of Energy under Contract DE-AC02-05CH11231. Ralf Greve was supported by the Japan Society for the Promotion of Science (JSPS) KAKENHI grant numbers JP16H02224, JP17H06104 and JP17H06323. Support for Mathieu Morlighem was provided by the National Science Foundation (NSF: Grant 1739031). The work of Thomas Kleiner has been conducted in the framework of the PalMod project (FKZ: 01LP1511B), supported by the German Federal Ministry of Education and Research (BMBF) as Research for Sustainability initiative (FONA). Reinhard Calov was funded by the PalMod project (PalMod 1.1 and 1.3 with grants 01LP1502C and 01LP1504D) of the German Federal Ministry of Education and Research (BMBF). Johannes Sutter has been funded via the AWI Strategy Fund and the regional climate initiative REKLIM. Tanja Schlemm is funded by a doctoral stipend granted by the Heinrich Böll Foundation. Torsten Albrecht has been funded by the Deutsche Forschungsgemeinschaft (DFG) in the framework of the priority programme 'Antarctic Research with comparative investigations in Arctic ice areas' by grant WI4556/2-1 and WI4556/4-1. Hélène Seroussi, Erika Simon and Sophie Nowicki were supported by grants from NASA Cryospheric Science and Modeling, Analysis, Predictions Programs. Computing resources supporting ISSM simulations were provided by the NASA High-End Computing Program through the NASA Advanced Supercomputing Division at Ames Research Center. Gunter Leguy and William Lipscomb were supported by the National Center for Atmospheric Research, which is a major facility sponsored by the National Science Foundation under Cooperative Agreement No. 1852977. Computing and data storage resources supporting CISM, including the Cheyenne supercomputer (doi:10.5065/D6RX99HX), were provided by the Computational and Information Systems Laboratory (CISL) at NCAR. Heiko Goelzer has received funding from the programme of the Netherlands Earth System Science Centre (NESSC), financially supported by the Dutch Ministry of Education, Culture and Science (OCW) under grant no. 024.002.001. This research forms part of the MIMO project within the STEREO III programme of the Belgian Science Policy Office, contract SR/00/336. IGE-Elmer/Ice simulations were performed using HPC resources from GENCI-CINES (grant 2018-016066) and using the Froggy platform of the CIMENT infrastructure, which is supported by the Rhone-Alpes region (grant CPER07_13 CIRA), the OSUG@2020 laBex (reference ANR10 LABX56) and the Equip@Meso project (referenceANR-10-EQPX-29-01). Nicholas R. Golledge acknowledges funding from Royal Society of New Zealand grant RDF-VUW1501. This is ISMIP6 contribution 14.

Author contributions.

S.S., F.P. and N.G. designed and coordinated the study, S.S. and F.P. led the writing, E.G.S. and S.S. processed the data and all authors contributed to the experiments, writing and discussion of ideas.

References

Agosta C, Amory C, Kittel C, Orsi A, Favier V and 6 others (2019) Estimation of the Antarctic surface mass balance using the regional climate model MAR (1979–2015) and identification of dominant processes. *The Cryosphere* **13**(1), 281–296. doi: 10.5194/tc-13-281-2019.

Albrecht T, Winkelmann R and Levermann A (2020) Glacial-cycle simulations of the Antarctic Ice Sheet with the Parallel Ice Sheet Model (PISM) – Part 1: boundary conditions and climatic forcing. *The Cryosphere* **14**(2), 599–632. doi: 10.5194/tc-14-599-2020.

Alley RB and 7 others (2015) Oceanic forcing of ice-sheet retreat: West Antarctica and more. *Annual Review of Earth and Planetary Sciences* **43** (1), 207–231. doi: 10.1146/annurev-earth-060614-105344.

Arthern RJ, Winebrenner DP and Vaughan DG (2006) Antarctic snow accumulation mapped using polarization of 4.3-cm wavelength microwave emission. *Journal of Geophysical Research: Atmospheres* **111**, D06107, doi: 10.1029/2004JD005667.

Aschwanden A and 7 others (2019) Contribution of the Greenland Ice Sheet to sea level over the next millennium. *Science Advances* **5**(6), eaav9396, doi: 10.1126/sciadv.aav9396.

Aschwanden A, Adalgeirsdóttir G and Khroulev C (2013) Hindcasting to measure ice sheet model sensitivity to initial states. *The Cryosphere* **7**(4), 1083–1093. doi: 10.5194/tc-7-1083-2013.

Aschwanden A, Bueler E, Khroulev C and Blatter H (2012) An enthalpy formulation for glaciers and ice sheets. *Journal of Glaciology* **58**(209), 441–457. doi: 10.3189/2012JoG11J088.

Bamber JL, Riva REM, Vermeersen BLA and LeBrocq AM (2009) Reassessment of the potential sea-level rise from a collapse of the West Antarctic ice sheet. *Science* **324**(5929), 901–903. doi: 10.1126/science.1169335.

Bassis JN and Walker CC (2012) Upper and lower limits on the stability of calving glaciers from the yield strength envelope of ice. *Proceedings of the Royal Society A: Mathematical, Physical and Engineering Sciences* **468** (2140), 913–931. doi: 10.1098/rspa.2011.0422.

Bernales J, Rogozhina I, Greve R and Thomas M (2017) Comparison of hybrid schemes for the combination of shallow approximations in numerical simulations of the Antarctic Ice Sheet. *The Cryosphere* **11**(1), 247–265. doi: 10.5194/tc-11-247-2017.

Bindschadler RA and 27 others (2013) Ice-sheet model sensitivities to environmental forcing and their use in projecting future sea level (the SeaRISE project). *Journal of Glaciology* **59**(214), 195–224. doi: 10.3189/2013JoG12J125.

Blatter H (1995) Velocity and stress fields in grounded glaciers: a simple algorithm for including deviatoric stress gradients. *Journal of Glaciology* **41** (138), 333–344. doi: 10.3189/S002214300001621X.

Brondex J, Gagliardini O, Gillet-Chaulet F and Durand G (2017) Sensitivity of grounding line dynamics to the choice of the friction law. *Journal of Glaciology* **63**(241), 854–866. doi: 10.1017/jog.2017.51.

Brondex J, Gillet-Chaulet F and Gagliardini O (2019) Sensitivity of centennial mass loss projections of the Amundsen basin to the friction law. *The Cryosphere* **13**(1), 177–195. doi: 10.5194/tc-13-177-2019.

Bueler E and Brown J (2009) Shallow shelf approximation as a 'sliding law' in a thermomechanically coupled ice sheet model. *Journal of Geophysical Research: Earth Surface* **114**(F3), F03008. doi: 10.1029/2008JF001179.

Bueler E and van Pelt W (2015) Mass-conserving subglacial hydrology in the Parallel Ice Sheet Model version 0.6. *Geoscientific Model Development* **8**(6), 1613–1635. doi: 10.5194/gmd-8-1613-2015.

Bulthuis K, Arnst M, Sun S and Pattyn F (2019) Uncertainty quantification of the multi-centennial response of the Antarctic ice sheet to climate change. *The Cryosphere* **13**(4), 1349–1380. doi: 10.5194/tc-13-1349-2019.

Calov R and 8 others (2018) Simulation of the future sea level contribution of Greenland with a new glacial system model. *The Cryosphere* **12**(10), 3097–3121. doi: 10.5194/tc-12-3097-2018.

Cornford SL and 8 others (2013) Adaptive mesh, finite volume modeling of marine ice sheets. *Journal of Computational Physics* **232**, 529–549.

Cornford SL, Martin DF, Lee V, Payne AJ and Ng EG (2016) Adaptive mesh refinement versus subgrid friction interpolation in simulations of Antarctic ice dynamics. *Annals of Glaciology* **57**(73), 1–9. doi: 10.1017/aog.2016.13.

DeConto RM and Pollard D (2016) Contribution of Antarctica to past and future sea-level rise. *Nature* **531**(7596), 591–597. doi: 10.1038/nature17145.

Durand G and Pattyn F (2015) Reducing uncertainties in projections of Antarctic ice mass loss. *The Cryosphere* **9**(6), 2043–2055. doi: 10.5194/tc-9-2043-2015.

Edwards TL and 9 others (2019) Revisiting Antarctic ice loss due to marine ice-cliff instability. *Nature* **566**(7742), 58–64. doi: 10.1038/s41586-019-0901-4.

Favier L and 7 others (2019) Assessment of sub-shelf melting parameterisations using the ocean–ice-sheet coupled model nemo(v3.6)–elmer/ice (v8.3). *Geosci. Model Dev.* **12**, 2255–2283. doi: 10.5194/gmd-12-2255-2019.

Feldmann J, Albrecht T, Khroulev C, Pattyn F and Levermann A (2014) Resolution-dependent performance of grounding line motion in a shallow model compared with a full-Stokes model according to the MISMIP3d

intercomparison. *Journal of Glaciology* **60**(220), 353–360. doi: 10.3189/2014JoG13J093.

Fortuin JPF and Oerlemans J (1990) Parameterization of the annual surface temperature and mass balance of Antarctica. *Annals of Glaciology* **14**, 78–84. doi: 10.3189/S0260305500008302.

Fretwell P and 59 others (2013) Bedmap2: improved ice bed, surface and thickness datasets for Antarctica. *The Cryosphere* **7**(1), 375–393. doi: 10.5194/tc-7-375-2013.

Fürst JJ and 6 others (2016) The safety band of Antarctic ice shelves. *Nature Climate Change* **6**(5), 479–482. doi: 10.1038/nclimate2912.

Gillet-Chaulet F and 6 others (2016) Assimilation of surface velocities acquired between 1996 and 2010 to constrain the form of the basal friction law under Pine Island Glacier. *Geophysical Research Letters* **43**(19), 10311–10321. doi: 10.1002/2016GL069937.

Gillet-Chaulet F (2020) Assimilation of surface observations in a transient marine ice sheet model using an ensemble Kalman filter. *The Cryosphere* **14**(3), 811–832. doi: 10.5194/tc-14-811-2020.

Gladstone RM and 5 others (2017) Marine ice sheet model performance depends on basal sliding physics and sub-shelf melting. *The Cryosphere* **11**(1), 319–329. doi: 10.5194/tc-11-319-2017.

Gladstone RM, Payne AJ and Cornford SL (2010) Parameterising the grounding line in ice sheet models. *The Cryosphere* **4**(4), 605–619. doi: 10.5194/tc-4-605-2010.

Gladstone RM, Payne AJ and Cornford SL (2012) Resolution requirements for grounding-line modelling: sensitivity to basal drag and ice-shelf buttressing. *Annals of Glaciology* **53**(60), 97–105. doi: 10.3189/2012AoG60A148.

Goelzer H and 30 others (2018) Design and results of the ice sheet model initialisation experiments initMIP-Greenland: an ISMIP6 intercomparison. *The Cryosphere* **12**(4), 1433–1460. doi: 10.5194/tc-12-1433-2018.

Goldberg DN (2011) A variationally derived, depth-integrated approximation to a higher-order glaciological flow model. *Journal of Glaciology* **57**(201), 157–170. doi: 10.3189/002214311795306763.

Goldberg DN, Heimbach P, Joughin I and Smith B (2015) Committed retreat of Smith, Pope, and Kohler Glaciers over the next 30 years inferred by transient model calibration. *The Cryosphere* **9**(6), 2429–2446. doi: 10.5194/tc-9-2429-2015.

Golledge NR and 6 others (2019) Global environmental consequences of twenty-first-century ice-sheet melt. *Nature* **566**(7742), 65–72. doi: 10.1038/s41586-019-0889-9.

Golledge NR, Levy RH, McKay RM and Naish TR (2017) East Antarctic ice sheet most vulnerable to Weddell Sea warming. *Geophysical Research Letters* **44**(5), 2343–2351. doi: 10.1002/2016GL072422.

Grant GR and 9 others (2019) The amplitude and origin of sea-level variability during the Pliocene epoch. *Nature* **574**(7777), 237–241. doi: 10.1038/s41586-019-1619-z.

Greve R and SICOPOLIS Developer Team (2019) SICOPOLIS v5.1. Zenodo. doi: 10.5281/zenodo.3727511

Greve R and Blatter H (2016) Comparison of thermodynamics solvers in the polythermal ice sheet model SICOPOLIS. *Polar Science* **10**(1), 11–23. doi: 10.1016/j.polar.2015.12.004.

Gudmundsson GH, Paolo FS, Adusumilli S and Fricker HA (2019) Instantaneous Antarctic ice sheet mass loss driven by thinning ice shelves. *Geophysical Research Letters* **46**(23), 13903–13909. doi: 10.1029/2019GL085027.

Hanna E and 10 others (2020) Mass balance of the ice sheets and glaciers – progress since AR5 and challenges. *Earth-Science Reviews* **201**, 102976. doi: 10.1016/j.earscirev.2019.102976..

Hoffman MJ and 9 others (2018) MPAS-Albany Land Ice (MALI): a variable-resolution ice sheet model for Earth system modeling using Voronoi grids. *Geoscientific Model Development* **11**(9), 3747–3780. doi: 10.5194/gmd-11-3747-2018.

Jenkins A and 6 others (2010) Observations beneath Pine Island Glacier in West Antarctica and implications for its retreat. *Nature Geoscience* **3**(7), 468–472. doi: 10.1038/ngeo890.

Jenkins A and 7 others (2018) West Antarctic Ice Sheet retreat in the Amundsen Sea driven by decadal oceanic variability. *Nature Geoscience* **11**(10), 733–738. doi: 10.1038/s41561-018-0207-4.

Joughin IR and 6 others (2009) Basal conditions for Pine Island and Thwaites Glaciers, West Antarctica, determined using satellite and airborne data. *Journal of Glaciology* **55**(190), 245–257. doi: 10.3189/002214309788608705.

Joughin I, Smith BE and Schoof CG (2019) Regularized coulomb friction laws for ice sheet sliding: application to pine island glacier, antarctica. *Geophysical Research Letters* **46**(9), 4764–4771. doi: 10.1029/2019GL082526.

Jourdain NC and 6 others (2019) A protocol for calculating basal melt rates in the ISMIP6 Antarctic ice sheet projections. *The Cryosphere Discussions* **2019**, 1–33. doi: 10.5194/tc-2019-277.

Khazendar A and 5 others (2013) Observed thinning of Totten Glacier is linked to coastal polynya variability. *Nature Communications* **4**(1), 2857. doi: 10.1038/ncomms3857.

Kleiner T and Humbert A (2014) Numerical simulations of major ice streams in Western Dronning Maud Land, Antarctica, under wet and dry basal conditions. *Journal of Glaciology* **60**(220), 215–232. doi: 10.3189/2014JoG13J006.

Lazeroms WMJ, Jenkins A, Gudmundsson GH and van de Wal RSW (2018) Modelling present-day basal melt rates for Antarctic ice shelves using a parametrization of buoyant meltwater plumes. *The Cryosphere* **12**(1), 49–70. doi: 10.5194/tc-12-49-2018.

Le Brocq AM, Payne AJ and Vieli A (2010) An improved Antarctic dataset for high resolution numerical ice sheet models (ALBMAP v1). *Earth System Science Data* **2**(2), 247–260. doi: 10.5194/essd-2-247-2010.

Le clec'h S and 5 others (2019) A rapidly converging initialisation method to simulate the present-day Greenland ice sheet using the GRISLI ice sheet model (version 1.3). *Geoscientific Model Development* **12**(6), 2481–2499. doi: 10.5194/gmd-12-2481-2019.

Leguy GR, Asay-Davis XS and Lipscomb WH (2014) Parameterization of basal friction near grounding lines in a one-dimensional ice sheet model. *The Cryosphere* **8**(4), 1239–1259. doi: 10.5194/tc-8-1239-2014.

Lenaerts JTM, van den Broeke MR, van de Berg WJ, van Meijgaard E and Kuipers Munneke P (2012) A new, high-resolution surface mass balance map of Antarctica (1979–2010) based on regional atmospheric climate modeling. *Geophysical Research Letters* **39**, L04501. doi: 10.1029/2011GL050713.

Levermann A and 5 others (2012) Kinematic first-order calving law implies potential for abrupt ice-shelf retreat. *The Cryosphere* **6**(2), 273–286. doi: 10.5194/tc-6-273-2012.

Levermann A and 36 others (2020) Projecting Antarctica's contribution to future sea level rise from basal ice shelf melt using linear response functions of 16 ice sheet models (LARMIP-2). *Earth System Dynamics* **11**(1), 35–76. doi: 10.5194/esd-11-35-2020.

MacAyeal DR (1989) Large-scale ice flow over a viscous basal sediment: theory and application to Ice Stream B, Antarctica. *Journal of Geophysical Research* **94**(B4), 4071–4087.

Martin DF, Cornford SL and Payne AJ (2019) Millennial-scale vulnerability of the Antarctic Ice Sheet to regional ice shelf collapse. *Geophysical Research Letters* **46**(3), 1467–1475. doi: 10.1029/2018GL081229.

Martos YM and 6 others (2017) Heat flux distribution of Antarctica unveiled. *Geophysical Research Letters* **44**(22), 11,417–11,426. doi: 10.1002/2017GL075609.

Miller KG and 9 others (2012) High tide of the warm Pliocene: implications of global sea level for Antarctic deglaciation. *Geology* **40**(5), 407–410. doi: 10.1130/G32869.1.

Morlighem M, Rignot E and Binder T, Blankenship D, Drews R and 32 others (2020) Deep glacial troughs and stabilizing ridges unveiled beneath the margins of the Antarctic ice sheet. *Nature Geoscience* **13**(2), 132–137. doi: 10.1038/s41561-019-0510-8.

Mouginot J, Rignot E and Scheuchl B (2014) Sustained increase in ice discharge from the Amundsen Sea Embayment, West Antarctica, from 1973 to 2013. *Geophysical Research Letters* **41**(5), 1576–1584. doi: 10.1002/2013GL059069.

Nowicki S and 30 others (2013) Insights into spatial sensitivities of ice mass response to environmental change from the searise ice sheet modeling project I: Antarctica. *Journal of Geophysical Research: Earth Surface* **118**(2), 1002–1024. doi: 10.1002/jgrf.20081.

Nowicki S and 29 others (2020) Experimental protocol for sea level projections from ISMIP6 standalone ice sheet models. *The Cryosphere* **14**, 2331–2368. doi: 10.5194/tc-14-2331-2020.

Paolo FS, Fricker HA and Padman L (2015) Volume loss from antarctic ice shelves is accelerating. *Science* **348**(6232), 327–331. doi: 10.1126/science.aaa0940.

Parizek BR and 10 others (2013) Dynamic (in)stability of Thwaites Glacier, West Antarctica. *Journal of Geophysical Research: Earth Surface* **118**(2), 638–655. doi: 10.1002/jgrf.20044.

Pattyn F (2003) A new 3D higher-order thermomechanical ice-sheet model: basic sensitivity, ice-stream development and ice flow across subglacial

lakes. *Journal of Geophysical Research: Solid Earth* **108**(B8), 2382. doi: 10.1029/2002JB002329.

Pattyn F, Schoof C, Perichon L, Hindmarsh RCA and Bueler E(2012) Results of the Marine Ice Sheet Model Intercomparison Project, MISMIP. *The Cryosphere* **6**(3), 573–588. doi: 10.5194/tc-6-573-2012.

Pattyn F and 27 others (2013) Grounding-line migration in plan-view marine ice-sheet models: results of the ice2sea MISMIP3d intercomparison. *Journal of Glaciology* **59**(215), 410–422. doi: 10.3189/2013JoG12J129.

Pattyn F (2017) Sea-level response to melting of Antarctic ice shelves on multi-centennial timescales with the fast Elementary Thermomechanical Ice Sheet model (f.ETISh v1.0). *The Cryosphere* **11**(4), 1851–1878. doi: 10.5194/tc-11-1851-2017.

Pattyn F and 17 others (2018) The Greenland and Antarctic ice sheets under 1.5°C global warming. *Nature Climate Change* **8**(12), 1053–1061. doi: 10.1038/s41558-018-0305-8.

Pattyn F (2018) The paradigm shift in Antarctic ice sheet modelling. *Nature Communications* **9**(1), 2728. doi: 10.1038/s41467-018-05003-z.

Pattyn F and Durand G (2013) Why marine ice sheet model predictions may diverge in estimating future sea level rise. *Geophysical Research Letters* **40** (16), 4316–4320. doi: 10.1002/grl.50824.

Pattyn F, Huyghe A, De Brabander S and De Smedt B (2006) Role of transition zones in marine ice sheet dynamics. *Journal of Geophysical Research: Earth Surface* **111**(F2), F02004. doi: 10.1029/2005JF000394.

Payne AJ, Vieli A, Shepherd AP, Wingham DJ and Rignot E (2004) Recent dramatic thinning of largest West Antarctic ice stream triggered by oceans. *Geophysical Research Letters* **31**(23), L23401. doi: 10.1029/2004GL021284.

Petit JR and 18 others (1999) Climate and atmospheric history of the past 420,000 years from the Vostok ice core, Antarctica. *Nature* **399**(6735), 429–436. doi: 10.1038/20859.

Pollard D and DeConto RM (2012*a*) Description of a hybrid ice sheet-shelf model, and application to Antarctica. *Geoscientific Model Development* **5**(5), 1273–1295. doi: 10.5194/gmd-5-1273-2012.

Pollard D and DeConto RM (2012b) A simple inverse method for the distribution of basal sliding coefficients under ice sheets, applied to Antarctica. *The Cryosphere* **6**(5), 953–971. doi: 10.5194/tc-6-953-2012.

Pollard D, DeConto RM and Alley RB (2015) Potential Antarctic Ice Sheet retreat driven by hydrofracturing and ice cliff failure. *Earth and Planetary Science Letters* **412**, 112–121. doi: 10.1016/j.epsl.2014.12.035.

Pritchard HD and 5 others (2012) Antarctic ice-sheet loss driven by basal melting of ice shelves. *Nature* **484**, 502–505. doi: 10.1038/nature10968.

Reese R, Albrecht T, Mengel M, Asay-Davis X and Winkelmann R (2018*a*) Antarctic sub-shelf melt rates via PICO. *The Cryosphere* **12**(6), 1969–1985. doi: 10.5194/tc-12-1969-2018.

Reese R, Gudmundsson GH, Levermann A and Winkelmann R (2018*b*) The far reach of ice-shelf thinning in Antarctica. *Nature Climate Change* **8**(1), 53–57. doi: 10.1038/s41558-017-0020-x.

Rignot E and Mouginot J (2016) Antarctica and Greenland drainage basin and ice sheet definitions. IMBIE 2016. http://imbie.org/imbie-2016/drainage-basins/.

Rignot E, Mouginot J, Morlighem M, Seroussi H and Scheuchl B (2014) Widespread, rapid grounding line retreat of Pine Island, Thwaites, Smith, and Kohler glaciers, West Antarctica, from 1992 to 2011. *Geophysical Research Letters* **41**(10), 3502–3509. doi: 10.1002/2014GL060140.

Rückamp M, Greve R and Humbert A (2019) Comparative simulations of the evolution of the Greenland ice sheet under simplified Paris Agreement scenarios with the models SICOPOLIS and ISSM. *Polar Science* **21**, 14–25. doi: 10.1016/j.polar.2018.12.003.

Sato T and Greve R (2012) Sensitivity experiments for the Antarctic ice sheet with varied sub-ice-shelf melting rates. *Annals of Glaciology* **53**(60), 221–228. doi: 10.3189/2012AoG60A042.

Schmidtko S, Heywood KJ, Thompson AF and Aoki S (2014) Multidecadal warming of Antarctic waters. *Science* **346**(6214), 1227–1231. doi: 10.1126/science.1256117.

Schoof C (2005) The effect of cavitation on glacier sliding. *Proceedings of the Royal Society A* **461**(2055), 609–627. doi: 10.1098/rspa.2004.1350.

Schoof C (2007) Ice sheet grounding line dynamics: steady states, stability, and hysteresis. *Journal of Geophysical Research: Earth Surface* **112**(F3), F03S28. doi: 10.1029/2006JF000664.

Schoof C and Hindmarsh RCA (2010) Thin-film flows with wall slip: an asymptotic analysis of higher order glacier flow models. *The Quarterly Journal of Mechanics and Applied Mathematics* **63**(1), 73–114. doi: 10.1093/qjmam/hbp025.

Seroussi H and 6 others (2014) Sensitivity of the dynamics of Pine Island Glacier, West Antarctica, to climate forcing for the next 50 years. *The Cryosphere* **8**(5), 1699–1710. doi: 10.5194/tc-8-1699-2014.

Seroussi H and 38 others (2019) initMIP-Antarctica: an ice sheet model initialization experiment of ISMIP6. *The Cryosphere* **13**(5), 1441–1471. doi: 10.5194/tc-13-1441-2019.

Seroussi H and 45 others (2020) ISMIP6 Antarctica: a multi-model ensemble of the Antarctic ice sheet evolution over the 21st century. *The Cryosphere Discussions,* in review. doi: 10.5194/tc-2019-324.

Seroussi H and Morlighem M (2018) Representation of basal melting at the grounding line in ice flow models. *The Cryosphere* **12**(10), 3085–3096. doi: 10.5194/tc-12-3085-2018.

Shepherd A and 77 others (2018) Mass balance of the Antarctic ice sheet from 1992 to 2017. *Nature* **558**, 219–222. doi: 10.1038/s41586-018-0179-y.

Thomas R and 17 others (2004) Accelerated sea-level rise from West Antarctica. *Science* **306**(5694), 255–258. doi: 10.1126/science.1099650.

Thompson AF, Stewart AL, Spence P and Heywood KJ (2018) The Antarctic slope current in a changing climate. *Reviews of Geophysics* **56**(4), 741–770. doi: 10.1029/2018RG000624.

Trusel LD and 6 others (2015) Divergent trajectories of Antarctic surface melt under two twenty-first-century climate scenarios. *Nature Geoscience* **8**(12), 927–932. doi: 10.1038/ngeo2563.

Tsai VC, Stewart AL and Thompson AF (2015) Marine ice-sheet profiles and stability under Coulomb basal conditions. *Journal of Glaciology* **61**(226), 205–215. doi: 10.3189/2015JoG14J221.

Tulaczyk SM, Kamb B and Engelhardt HF (2000*a*) Basal mechanics of Ice Stream B, west Antarctica. I. Till mechanics. *Journal of Geophysical Research: Solid Earth* **105**(B1), 463–481. doi: 10.1029/1999JB900329.

Tulaczyk SM, Kamb B and Engelhardt HF (2000*b*) Basal mechanics of Ice Stream B, west Antarctica. II. Undrained plastic bed model. *Journal of Geophysical Research: Solid Earth* **105**(B1), 483–494. doi: 10.1029/1999JB900328.

Van Wessem JM and 13 others (2014) Improved representation of East Antarctic surface mass balance in a regional atmospheric climate model. *Journal of Glaciology* **60**(222), 761–770. doi: 10.3189/2014JoG14J051.

Van Wessem JM and 18 others (2018) Modelling the climate and surface mass balance of polar ice sheets using RACMO2 – Part 2: Antarctica (1979–2016). *The Cryosphere* **12**(4), 1479–1498. doi: 10.5194/tc-12-1479-2018.

Weertman J (1957) On the sliding of glaciers. *Journal of Glaciology* **3**(21), 33–38.

Winkelmann R and 6 others (2011) The Potsdam Parallel Ice Sheet Model (PISM-PIK) Part 1: model description. *The Cryosphere* **5**(3), 715–726. doi: 10.5194/tc-5-715-2011.

Appendix A

Below are descriptions of the ice flow models and the initialization procedure performed by the different groups. For the majority of models, the setup and initialization are similar to Seroussi and others (2019). Only differences with that paper are marked below.

A.1. ARC-PISM

See Appendix B1 in Seroussi and others (2019).

A.2. AWI-PISMpal

See Appendix B2 for PISM1Pal in Seroussi and others (2019).

A.3. CPOM-BISICLES

See Appendix B3 in Seroussi and others (2019).

A.4. IGE-Elmer/Ice

See Appendix B6 in Seroussi and others (2019). For the ABUK experiments, a new mesh is generated every 5 years using the same anisotropic mesh adaptation scheme as for the initial mesh. This allows to keep a fine mesh resolution of approximately 1 km in the grounding line proximity.

A.5. ILTS-PIK-SICOPOLIS

The model SICOPOLIS version 5.1 (Greve and SICOPOLIS Developer Team, 2019; www.sicopolis.net) is applied to the Antarctic ice sheet with hybrid shallow-ice–shelfy-stream dynamics for grounded ice (Bernales and others, 2017) and shallow-shelf dynamics for floating ice. Ice thermodynamics are treated with the melting-CTS enthalpy method (ENTM) by Greve and Blatter (2016). The ice surface is assumed to be traction-free. Basal sliding under grounded ice is described by a Weertman-Budd-type sliding law with sub-melt sliding (Sato and Greve, 2012) and subglacial hydrology (Kleiner and Humbert, 2014; Calov and others, 2018). The model is initialized by a paleoclimatic spin-up over 140,000 years until 1990, forced by Vostok δD converted to ΔT (Petit and others, 1999), in which the topography is nudged towards the present-day topography to enforce a good agreement (Rückamp and others, 2019). Basal sliding coefficients are determined individually for the 18 IMBIE-2016 basins (Rignot and Mouginot, 2016) by minimizing the RMSD between simulated and observed logarithmic surface velocities. For the last 2000 years of the spin-up and the actual ABUMIP experiments, a regular (structured) grid with 8 km resolution is used. In the vertical, terrain-following coordinates with 81 layers in the ice domain and 41 layers in the thermal lithosphere layer below are used. The present-day surface temperature is parameterized (Fortuin and Oerlemans, 1990), the present-day precipitation is due to Arthern and others (2006) and Le Brocq and others (2010), and run-off is modelled by the positive-degree-day method with the parameters by Sato and Greve (2012). The 1960–1989 average SMB correction that results diagnostically from the nudging technique is used as a prescribed SMB correction for the ABUMIP experiments. The bed topography is taken from Bedmap2 (Fretwell and others, 2013), the geothermal heat flux is by Martos and others (2017). Present-day ice-shelf basal melting is parameterized by the non-local quadratic ISMIP6 standard approach (Jourdain and others, 2019; Nowicki and others, 2020). A more detailed description of the set-up (which is consistent with the one used for the ISMIP6 Antarctica projections (Seroussi and others, 2020) and the LARMIP-2 initiative (Levermann and others, 2020)) will be given elsewhere (Greve and others, in preparation).

A.6. IMAU-ICE

See Appendix B8 in Seroussi and others (2019). From the initial state for initMIP-Antarctica, we run 20 kyr with the sub-shelf melt parameterization of Lazeroms and others (2018), forced with sub-surface ocean temperature (375 m) from the World Ocean Atlas to our final steady initial state.

A.7. JPL-ISSM

See Appendix B9 in Seroussi and others (2019).

A.8. LSCE-GRISLI

See Appendix B10 in Seroussi and others (2019). The near-surface air temperature and SMB in ABUMIP are taken from the 1979–2014 climatological annual mean computed by the RACMO2.3p2 regional atmospheric model (Van Wessem and others, 2018) instead of MAR.

A.9. NCAR-CISM

See Appendix B11 in Seroussi and others (2019).

A.10. PSU-ICE3D

See Appendix B13 in Seroussi and others (2019). Addition of PSU-ICE3D1 with the structural failure of large ice cliffs (Pollard and others, 2015; DeConto and Pollard, 2016).

A.11. ULB-f.ETISh

See Appendix B15 in Seroussi and others (2019). Experiments are run with an updated version of the f.ETISh model v1.4, which includes improved calving and sub-shelf melting schemes, which are not used in the ABUMIP setup. Ice sheet geometry is based on Bedmachine (Morlighem and others, 2020).

A.12. DOE-MALI

See Appendix B5 in Seroussi and others (2019).

A.13. PIK-PISM

The Parallel Ice Sheet Model (PISM; Winkelmann and others (2011); http://www.pism-docs.org; dev version c10a3a6e (3 June 2018) based on v1.0) is implemented in ABUMIP. The model domain is discretized on a regular rectangular grid with 4 km horizontal resolution and a vertical resolution between 48 m at the top of the domain at 6000 and 7 m at the base of the ice. The model is initialized from Bedmap2 geometry (Fretwell and others, 2013) with model parameters (e.g. enhancement factors for SIA and SSA, here both equal 1) that minimize dynamic changes over 600 years of constant present-day climatic conditions (not yet in equilibrium). PISM is a thermomechanically coupled (polythermal) model based on the Glen–Paterson–Budd–Lliboutry–Duval flow law (Aschwanden and others, 2012). The three-dimensional enthalpy field can freely evolve for given boundary conditions. Basal melt water is stored in the till. The Mohr–Coulomb criterion relates the yield stress by parameterizations of till material properties to the effective pressure on the saturated till (Bueler and van Pelt, 2015). Till friction angle is a shear strength parameter for the till material property and is optimized iteratively in the grounded region such that mismatch of equilibrium and modern surface elevation (8 km) is minimized (analogous to the friction coefficient in Pollard and DeConto (2012*a*)). We use a pseudo plastic sliding law with $q = 0.75$. The grounding line position is determined using hydrostatic equilibrium, with sub-grid interpolation of the friction Feldmann and others (2014). The melt rate is calculated with the Potsdam Ice-shelf Cavity mOdel (PICO; Reese and others (2018*a*)) which calculates melt patterns underneath the ice shelves (no interpolation applied) for given ocean conditions, taken as mean values over the observational period 1975–2012 (Schmidtko and others, 2014). The basin mean ocean temperature in the Amundsen region of 0.46°C has been corrected to a lower value of -0.37°C, as average from in the neighbouring Getz Ice Shelf basin, assuming that colder conditions have been prevalent in the pre-industrial period. The near-surface climate, surface mass balance and ice surface temperature are from RACMO2.3p2 1986–2005 (Van Wessem and others, 2018). The calving front position can freely evolve using the Eigencalving parameterization (Levermann and others, 2012), with $K = 10^{17}$ m s and a terminal thickness threshold of 200 m.

A.2 A simple stress-based cliff-calving law

Schlemm, T. & Levermann, A.

Over large coastal regions in Greenland and Antarctica the ice sheet calves directly into the ocean. In contrast to ice-shelf calving, an increase in calving from grounded glaciers contributes directly to sea-level rise. Ice cliffs with a glacier freeboard larger than $\approx 100\,\mathrm{m}$ are currently not observed, but it has been shown that such ice cliffs are increasingly unstable with increasing ice thickness. This cliff calving can constitute a self-amplifying ice loss mechanism that may significantly alter sea-level projections both of Greenland and Antarctica. Here we seek to derive a minimalist stress-based parametrization for cliff calving from grounded glaciers whose freeboards exceed the 100 m stability limit derived in previous studies. This will be an extension of existing calving laws for tidewater glaciers to higher ice cliffs.

To this end we compute the stress field for a glacier with a simplified two-dimensional geometry from the two-dimensional Stokes equation. First we assume a constant yield stress to derive the failure region at the glacier front from the stress field within the glacier. Secondly, we assume a constant response time of ice failure due to exceedance of the yield stress. With this strongly constraining but very simple set of assumptions we propose a cliff-calving law where the calving rate follows a power-law dependence on the freeboard of the ice with exponents between 2 and 3, depending on the relative water depth at the calving front. The critical freeboard below which the ice front is stable decreases with increasing relative water depth of the calving front. For a dry water front it is, for example, 75 m The purpose of this study is not to provide a comprehensive calving law but to derive a particularly simple equation with a transparent and minimalist set of assumptions.

The Cryosphere **13**, 2475–248 (2019).
DOI: 10.5194/tc-13-2475-2019

The Cryosphere, 13, 2475–2488, 2019
https://doi.org/10.5194/tc-13-2475-2019

The Cryosphere Open Access EGU

A simple stress-based cliff-calving law

Tanja Schlemm[1,2] **and Anders Levermann**[1,2,3]

[1]Potsdam Institute for Climate Impact Research, Potsdam, Germany
[2]Institute of Physics and Astronomy, University of Potsdam, Potsdam, Germany
[3]Lamont-Doherty Earth Observatory, Columbia University, New York, USA

Correspondence: Anders Levermann (anders.levermann@pik-potsdam.de)

Received: 18 September 2018 – Discussion started: 11 October 2018
Revised: 17 April 2019 – Accepted: 27 August 2019 – Published: 24 September 2019

Abstract. Over large coastal regions in Greenland and Antarctica the ice sheet calves directly into the ocean. In contrast to ice-shelf calving, an increase in calving from grounded glaciers contributes directly to sea-level rise. Ice cliffs with a glacier freeboard larger than ≈ 100 m are currently not observed, but it has been shown that such ice cliffs are increasingly unstable with increasing ice thickness. This cliff calving can constitute a self-amplifying ice loss mechanism that may significantly alter sea-level projections both of Greenland and Antarctica. Here we seek to derive a minimalist stress-based parametrization for cliff calving from grounded glaciers whose freeboards exceed the 100 m stability limit derived in previous studies. This will be an extension of existing calving laws for tidewater glaciers to higher ice cliffs.

To this end we compute the stress field for a glacier with a simplified two-dimensional geometry from the two-dimensional Stokes equation. First we assume a constant yield stress to derive the failure region at the glacier front from the stress field within the glacier. Secondly, we assume a constant response time of ice failure due to exceedance of the yield stress. With this strongly constraining but very simple set of assumptions we propose a cliff-calving law where the calving rate follows a power-law dependence on the freeboard of the ice with exponents between 2 and 3, depending on the relative water depth at the calving front. The critical freeboard below which the ice front is stable decreases with increasing relative water depth of the calving front. For a dry water front it is, for example, 75 m. The purpose of this study is not to provide a comprehensive calving law but to derive a particularly simple equation with a transparent and minimalist set of assumptions.

1 Introduction

Ice loss from Greenland and Antarctica is increasingly contributing to global sea-level rise (Rignot et al., 2014; Shepherd et al., 2018; WCRP Global Sea Level Budget Group, 2018). A possible additional future mass loss from these ice sheets is of crucial importance for future sea-level projections (Slangen et al., 2017; Church et al., 2013; DeConto and Pollard, 2016; Kopp et al., 2017; Mengel et al., 2016; Ritz et al., 2015; Levermann et al., 2014). Ice sheets gain mass by snowfall. The question whether they contribute to changes in sea level is determined by the question how strongly this mass addition is compensated for or overcompensated for by mass loss. Ice sheets in both Greenland and Antarctica currently show a net ice loss. Calving accounts for roughly half the ice loss of the Antarctic ice shelves, the rest is lost by basal melt (Depoorter et al., 2013). For the Greenland ice sheet, calving accounted for two-thirds of the ice loss between 2000 and 2005, the rest is due to enhanced surface melting and runoff (Rignot and Kanagaratnam, 2006). Because surface melt increased faster than glacier speed, calving accounted for one-third of the Greenland ice sheet mass loss between 2009 and 2012 (Enderlin et al., 2014). In the future the melt elevation feedback might further increase surface melt (Levermann and Winkelmann, 2016).

Tidewater glaciers calve vigorously when they are near floatation thickness, producing icebergs with a horizontal extent smaller than the ice thickness. This has been expressed in semiempirical height-above-floatation calving laws (Meier and Post, 1987; van Der Veen, 1996; Vieli et al., 2002). Calving at ice-shelf fronts or floating glacier tongues has long rest periods interrupted by the calving of large tabular ice bergs (Lazzara et al., 1999) and is preceded by the formation of

deep crevasses upstream (Joughin and MacAyeal, 2005). The distinction between these two kinds of calving is not always easy because a tidewater glacier can form or lose a floating tongue; this has for example been observed at the Columbia glacier in Alaska (Walter et al., 2010).

In order to model calving not just for single glaciers but for whole ice sheets, a calving parametrization is needed. Models describing the nucleation and spreading of crevasses in ice (Pralong and Funk, 2005) are computationally very intense and difficult to apply in simulations over long timescales and large spatial dimensions. In order to parametrize calving processes, several approaches have been used.

First, calving can be described as a function of strain rate and crevasse depth. Nye (1957) first described the formation of crevasses as a result of velocity gradients: the depth of the crevasse is determined by the strain rate and overburdening pressure of the ice. Observations show that ice velocities are greater near the calving front than upstream (Meier and Post, 1987); hence, crevasses form mainly at the calving front. When crevasses are deep enough, icebergs are then separated from the glacier and calve off. Benn et al. (2007) proposed a calving law with the assumption that a glacier calves where crevasses reach the water level, Nick et al. (2010) proposed calving when surface and basal crevasses meet. These calving laws have been applied successfully in higher-order flowline models (Nick et al., 2010) and in a 3-D Stokes model (Todd et al., 2018).

Second, a number of approaches have been taken to analyze calving processes via the stress balance. Bassis and Walker (2011) analyzed depth-averaged stresses at the calving front. Considering tensile and shear failure, they found that there is an upper limit for the thickness of stable ice cliffs: an ice cliff is only stable if the glacier's freeboard (ice thickness minus water depth) is lower than 200 m. The limit decreases to 100 m if weakening of the ice through crevasses is also considered. Krug et al. (2014) used damage and fracture mechanics to model calving. This approach, using linear elastic fracture mechanics, has recently been analyzed by Jiménez and Duddu (2018), who found that it can be applied to floating shelves but not to grounded glaciers. Morlighem et al. (2016) give a calving rate in terms of ice velocity and the von Mises stress. Recent works by Ma et al. (2017) and Benn et al. (2017) solved the 2-D full-Stokes equation at the calving front with finite element methods. Ma et al. (2017) found that while sliding glaciers calve through tensile failure, for glaciers frozen to the bed, shear failure dominates. Benn et al. (2017) used finite element models to solve the stress balance and a discrete element model to simulate fracture formation. They modeled a range of calving mechanisms including calving driven by buoyancy and melt-undercutting, but did not give parameterizations of calving rates.

Finally, Mercenier et al. (2018) analyzed tensile failure with a 2-D finite element model and derived a calving law for tidewater glaciers. They analyzed crevasse formation at the glacier terminus, determined the distance of the crevasse to the front and the time to failure until the crevasse penetrates the whole glacier and the iceberg in front of the crevasse calves off. Together this gives an equation for the calving rate as a function of water depth and ice thickness.

All these approaches agree on the basic physics of glacier calving: thicker ice at the terminus leads to higher stresses and larger calving rates. Glaciers terminating in water are stabilized by the water's back-pressure and have smaller calving rates.

The stability limit derived by Bassis and Walker (2011) lead to the formation of the marine ice cliff instability hypothesis. If cliff calving from ice cliffs whose freeboards exceed the stability limit is initiated in an overdeepened basin, e.g., in East Antarctica, it can lead to runaway cliff calving where higher ice cliffs are exposed the further the grounding line retreats, causing even larger cliff-calving rates.

Pollard et al. (2015) and DeConto and Pollard (2016) incorporated cliff calving in Antarctica projections by assuming a linear relation between freeboard exceeding the stability limit and calving rate and showed that the marine ice cliff instability can lead to much faster sea-level rise than found in previous approaches. Bassis et al. (2017) rewrote the condition that the glacier freeboard should not exceed the stability limit as a lower bound on the rate of terminus advance or equivalently an upper bound on the calving rate. More research, and especially a more physically based cliff-calving law, is needed. Studies by Ma et al. (2017), Benn et al. (2017) and Mercenier et al. (2018) were made for tidewater glaciers not exceeding the stability limit and might not be applicable to glaciers exceeding the stability limit.

In this study, we analyze stresses at the calving front by solving the 2-D Stokes equation with a finite element model in order to propose a simple cliff-calving law. The purpose of this study is not to provide a comprehensive analysis. By contrast, we seek a minimalistic set of assumptions that paths the way to a simple stress-based cliff-calving law.

2 Stress balance near the calving front

2.1 Problem setup: 2-D Stokes equation and boundary condition

In this study we consider a plane, flat glacier of constant thickness H terminating in water of depth D in a one-dimensional (flow-line) model with horizontal coordinate x and vertical coordinate z (Fig. 1).

In order to compute the stress field near the calving front we set the glacier to be grounded (relative water depth $w \equiv D/H < 0.9$) and frozen to the bed. The numerical domain has a length of $L = 6 \cdot H \gg H$. The factor 6 was chosen as a compromise to reduce computational effort while ensuring that the upstream boundary does not effect stresses at the glacier terminus. L could have been chosen to be truly "much

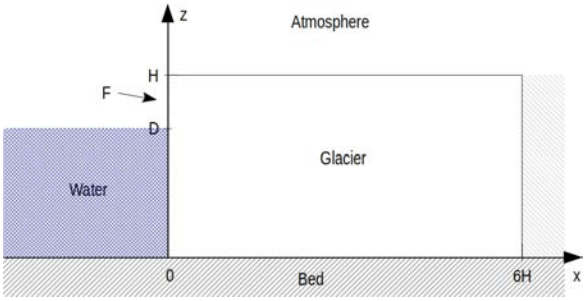

Figure 1. Geometrical setup of the stress computation: two-dimensional plane, flat glacier frozen to the bedrock with a calving front at its terminus. The glacier length L is 6 times as large as the glacier height H in order to ensure that the boundary condition on the right does not significantly influence the stress field at the terminus on the left. The ice thickness is denoted H, ice thickness below the water level is D and the free-board is denoted F.

larger" than H, but that would have required a lot of computation time without significantly benefiting the precision of the calculation. The flow-line assumption is justified, for example, in situations where the glacier is wide in comparison to its length and thickness. In these cases lateral stresses can often be neglected. The flow-line assumption is a strong constraint that neglects, for example, any buttressing effects within the ice sheet. However, the considered geometry with the width of the glacier much larger than the horizontal extent in the flow-line direction $L = 6 \cdot H$ is internally consistent and applicable to a number of situations observed both in Greenland and Antarctica. The assumption of a flat ice thickness is justifiable on a horizontal scale of several hundred meters to a few kilometers.

The ice flow and the stresses within the ice are governed by the Stokes equations,

$$\partial_x \sigma_{xx} + \partial_z \sigma_{xz} = 0, \tag{1}$$

$$\partial_x \sigma_{zx} + \partial_z \sigma_{zz} = f, \tag{2}$$

and the continuity equation,

$$\nabla \cdot \boldsymbol{u} = \partial_x u_x + \partial_z u_z = 0, \tag{3}$$

with the Cauchy stress tensor $\boldsymbol{\sigma}$ and the gravitational force f. The Cauchy stress tensor can be split into an isotropic pressure P (also called cryostatic pressure) and the deviatoric stress tensor $\mathbf{S}$, such that

$$\sigma_{ij} = -P \cdot \delta_{ij} + S_{ij}, \tag{4}$$

where δ_{ij} is the Kronecker delta. Ice rheology is assumed to be given by Glen's flow law (van der Veen, 1999),

$$\dot{\epsilon}_{ij} = A S_{\mathrm{e}}^{n-1} S_{ij}, \tag{5}$$

with the strain rate tensor $\dot{\epsilon}_{ij} = \frac{1}{2}\left(\partial_i u_j + \partial_j u_i\right)$ and the effective stress $S_{\mathrm{e}} = \sqrt{\frac{1}{2}S_{xx}^2 + \frac{1}{2}S_{zz}^2 + S_{xz}^2}$.

The surface boundary is assumed to be traction-free. At the calving front boundary, we assume traction continuity to the water pressure and no traction above the water line. At the glacier bed, a no-slip boundary condition is assumed, which corresponds to a glacier frozen to its bed. No inflow is assumed at the upstream boundary.

$$\text{Ice top:} \quad \boldsymbol{\sigma} \cdot \boldsymbol{n} = \begin{pmatrix} \sigma_{xz} \\ \sigma_{zz} \end{pmatrix} = \mathbf{0} \tag{6}$$

$$\text{Ice base:} \quad \boldsymbol{u} = \mathbf{0} \tag{7}$$

$$\text{Ice front:} \quad \boldsymbol{\sigma} \cdot \boldsymbol{n} = \begin{pmatrix} -\sigma_{xx} \\ -\sigma_{xz} \end{pmatrix} = \begin{cases} (-\rho_w g z, 0), & z < D \\ (0,0), & z > D \end{cases} \tag{8}$$

$$\text{Upstream:} \quad u_x = 0 \tag{9}$$

2.2 Numerical solution of the stress field

The boundary value problem was solved with the Finite Element package FEniCS (Alnæs et al., 2015) and stabilized with the Pressure Penalty method (Zhang et al., 2011). The numerical domain was divided into a regular triangular mesh with 100 vertical and 600 horizontal divisions.

Since the Stokes equations are linear in the stresses and the terminus boundary condition is linear in the ice thickness, the equations can be solved on a dimensionless domain and the stresses scaled to arbitrary ice thickness. Velocities do not scale linearly but can be obtained from the scaled stresses through the ice rheology equation. The water depth at the calving front was incorporated via the relative (dimensionless) water depth $w = D/H$.

In order to determine a suitable stress criterion for cliff calving we consider a number of commonly used stresses that have a clear physical role (Fig. 2). Generally, stresses increase with ice thickness, while the presence of water at the glacier terminus decreases the stresses and stabilizes the calving front.

The deviatoric normal stress, S_{xx}, corresponds to an outwards force at the calving front that has two maxima, one at the waterline and one at the foot of the terminus. The deviatoric shear stress, or Cauchy shear stress, ($S_{xz} = \sigma_{xz}$), translates to a bending moment that bends the top of the calving front forward and downward.

The different components of the deviatoric stress tensor are not invariants of the stress tensor, i.e., they depend on the coordinate system in which they are computed, and therefore they are not suitable as failure criteria. The largest principal stress,

$$\sigma_1 = \frac{\sigma_{xx} + \sigma_{zz}}{2} + \sqrt{\left(\frac{\sigma_{xx} - \sigma_{zz}}{2}\right)^2 + \sigma_{xz}^2}, \tag{10}$$

is calculated as the largest eigenvalue of the Cauchy stress tensor and corresponds to the largest normal stress in a given point. When σ_1 is positive, it is tensile and crevasses can

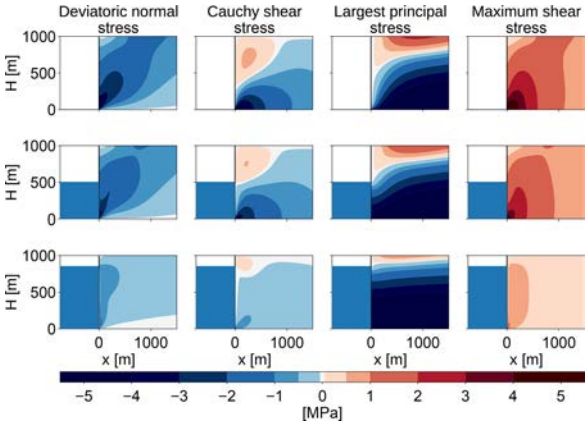

Figure 2. Stress configurations at the calving front for different relative water depths ($w = 0$, 0.5, 0.85) for a fixed ice thickness of 1000 m. The first column shows the deviatoric normal stress in the x direction, S_{xx}, the second column shows the Cauchy shear stress, $\sigma_{xz} = S_{xz}$, the third column shows the largest principal stress, σ_i, and the last column shows the maximum shear stress, $\tau_{\max}$.

form. The maximum shear stress,

$$\tau_{\max} = \sqrt{\left(\frac{\sigma_{xx} - \sigma_{zz}}{2}\right)^2 + \sigma_{xz}^2}, \tag{11}$$

acts on a plane at an angle 45° to the plane where the largest principal stress acts. It has its maximum at the foot of the calving front. The maximum shear stress can be related to brittle compressive failure (Schulson, 2001) and is therefore of particular interest for cliff failure.

The von Mises stress is the second invariant J_2 of the deviatoric stress tensor,

$$\sigma_{\text{Mises}} = \sqrt{\frac{3}{2}\left(S_{xx}^2 + S_{zz}^2 + 2S_{xz}^2\right)}, \tag{12}$$

and is used as a measure of deviatoric strain energy. It can also be related to material failure (Ford and Alexander, 1963) and has been used as a calving criterion by Morlighem et al. (2016). Since $S_{xx} = -S_{zz}$ due to the incompressibility of ice, the von Mises stress and the maximum shear stress differ by only a single factor: $\sigma_{\text{Mises}} = \sqrt{3}\tau_{\max}$.

3 Cliff failure criterion

As a first step we select a failure criterion, which then yields a failure region based on the computed stress fields. As a second step we decide on a timescale for the failure in order to derive a simple calving law.

3.1 Partial thickness failure through crevasses

Crevasses are a natural candidate for ice front failure. In the case of glaciers that are frozen to the ground, crevasses, generally, do not form from the base upward (Ma et al., 2017). Instead, surface crevasses can form in the upper part of the glacier down to the depth where the principal stress becomes compressive, i.e., attains negative values (Nye, 1957). The presence of water at the calving front reduces the stresses in the ice and decreases the depth to which surface crevasses can penetrate. Surface crevasses, generally, do not penetrate through the whole glacier thickness and so crevasses cannot be the sole cause for calving. We thus do not follow this path to determine a failure region.

Surface meltwater filling surface crevasses can increase their depth (hydrofracturing) (Weertman, 1973; Das et al., 2008; Pollard et al., 2015), but this is also not considered here. The presence of crevasses weakens the ice and is expected to enable failure even when the critical shear stress is not yet exceeded but also this is not further considered here.

3.2 Full thickness shear failure

Instead, we assume shear faulting to be the dominant process in ice-cliff failure. We could use the von Mises stress as a failure criterion instead and reach qualitatively the same result because they differ only by a factor of $\sqrt{3}$.

The failure region is defined as the region close to the calving front where the maximum shear stress exceeds a critical shear stress of $\tau_c = 1$ MPa (Schulson et al., 1999; Schulson, 2001). While the specific value of the critical shear stress may be subject to uncertainties (values might be between 0.5 and 5 MPa), it is mainly a constant that will not alter the calving rate dependence on the freeboard and the water depth. The specific choice of the value is motivated by laboratory experiments and can only provide an order of magnitude of the calving rate. However, the uncertainty resulting from this choice is smaller than the uncertainty arising from the estimate of the failure time (see below).

3.3 Comparison to Coulomb failure

In general, brittle compressive failure happens through shear faulting (Schulson et al., 1999) and can be described with the Coulomb law (Weiss and Schulson, 2009): the shear stress τ acting on the future fault plane is resisted by material cohesion S_0 and by friction $\mu\sigma$ with the friction coefficient μ and the normal stress across the failure plane σ. Failure happens when

$$\tau \geq S_0 + \mu\sigma. \tag{13}$$

This expression depends on the direction of the fault plane. The failure condition can be expressed more generally in terms of the maximum shear stress $\tau_{\max}$ and the isotropic pressure P as

$$\sqrt{\mu^2 + 1}\,\tau_{\max} = \tau_0 + \mu P, \tag{14}$$

where τ_0 is another measure of cohesive strength related to S_0 (Weiss and Schulson, 2009).

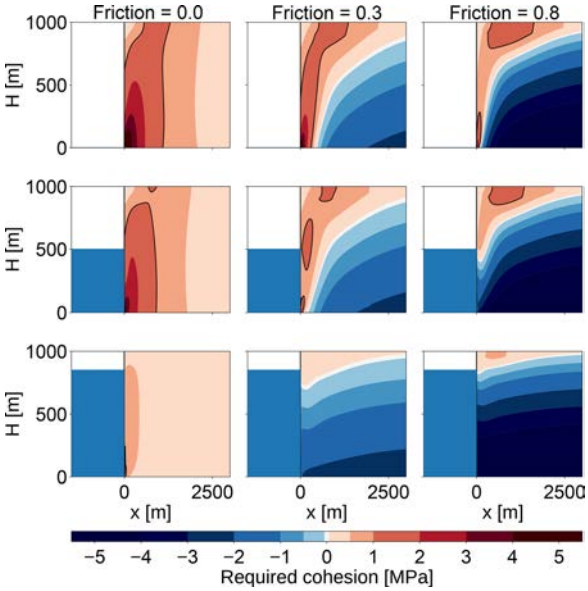

Figure 3. Assuming Coulomb failure, the required cohesion, $\tau_0 = \sqrt{\mu^2+1}\tau_{\max} - \mu P$, is shown for different friction parameters ($\mu = 0, 0.3, 0.8$). The failure region for a maximum cohesion of $\tau_{\max} = 1$ MPa is encased by the black line.

Weiss and Schulson (2009) provide values of $\mu = 0.3\ldots0.8$, depending on the temperature of the ice. Since friction increases the strength of the ice, this could stabilize rather large ice cliffs. Bassis and Walker (2011) looked at upper bounds of glacier stability with a depth-averaged shear stress for different values of μ (0.65, 0.4, 0) and a cohesion of $\tau_0 = 1$ MPa. With a large friction coefficient, ice cliffs would be stable for freeboards of up to 600 m (see Fig. 3) Since this is not observed in nature, they concluded that the best model is the one without friction, which only allows freeboards of up to 200 m. Thus, with vanishing friction, the Coulomb failure criterion is equal to the maximum shear stress criterion used here.

4 Failure region

We define the failure region as the region close to the calving front where the maximum shear stress exceeds the critical shear stress τ_c anywhere in the ice column. The failure distance L is the maximum distance of the failure region to the front and was determined for a range of ice thicknesses H and relative water depths w by solving the 2-D Stokes equation numerically and tracing the contour line where the maximum shear stress $\tau_{\max}$ equals the critical shear stress τ_c (see Fig. 4).

For a given water depth, the failure distance L increases with the ice thickness H or the glacier freeboard $F = H - D$

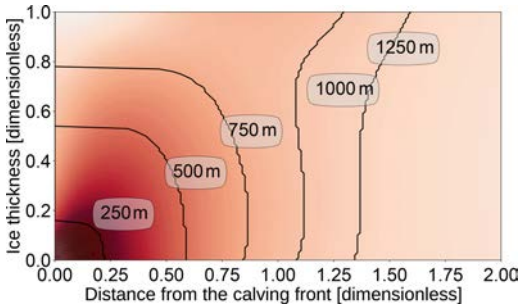

Figure 4. Outline of the failure region for different ice thicknesses on a dimensionless domain and without water stabilizing the front (ice thickness = glacier freeboard). The background color shows the maximum shear stress on a dimensionless scale with darker areas signifying larger stress. The failure region is defined as the region close to the calving front where the maximum shear stress exceeds the critical shear stress τ_c anywhere in the ice column. The outline for $H = 1000$ m is also shown in Fig. 3 in the top-left panel.

(Fig. 5). For glacier freeboards smaller than approximately 100 m, the failure region vanishes: the critical shear stress is not exceeded anywhere in the ice and no shear failure takes place. This confirms results by Bassis and Walker (2011), which were derived analytically with some simplifications (see Appendix A1 for more details). The relative water depths influences the slope of the freeboard–failure distance relation: for large relative water depths, the failure distance grows more quickly with increasing freeboard. This is because, for a large relative water depth, the overall ice thickness is much larger than for a similar freeboard with a smaller relative water depth and so the failure region is larger.

Above a critical freeboard of about 1000 m (see Fig. 4 for $w = 0$ and $F = H$), the failure region encompasses the whole ice thickness. Below this critical value the failure region contains only the lower part of the ice thickness, but once the lower part of the ice column fails the upper part lacks support and fails as well. The freeboard–failure distance relation has a steeper slope for large freeboards when the whole ice thickness fails. This leads to a bend at the critical freeboard, and hence the two parts require separate analytical fits. Here, we only consider values below the critical freeboard because that is the range of values most likely to occur in nature.

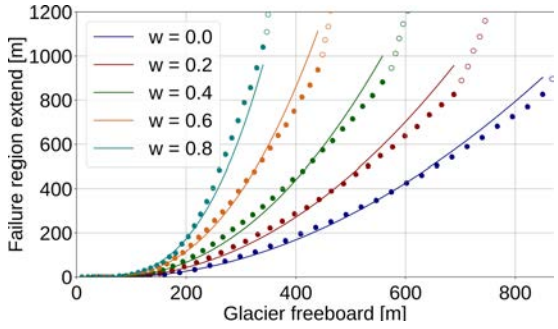

Figure 5. Size of shear failure region L as a function of glacier freeboard $F = H - D$ and relative water depth $w = D/H$. Numerical results are shown for smaller freeboards where the failure region does not encompass the whole ice thickness (filled dots) and for large freeboards, where the failure region contains the whole ice thickness (empty circles). A power law has been fitted to the numerical results for small freeboards (continuous line), which is given by Eq. (15). The fit has been optimized for relative error in order to get the onset of cliff calving right.

In Fig. 5 we provide an analytical fit with a power-law function of the form

$$L = \left(\frac{F - F_c}{F_s}\right)^s \text{m}, \tag{15}$$

$$F_s = \left(115 \cdot (w - 0.356)^4 + 21\right) \text{m}, \tag{16}$$

$$F_c = (75 - w \cdot 49) \text{ m}, \tag{17}$$

$$s = 0.17 \cdot 9.1^w + 1.76, \tag{18}$$

with $w \equiv D/H < 0.9$ and $F \equiv H - D = H \cdot (1 - w)$. At first L was fitted as a function of F for each value of w. Then the parameter functions F_s, F_c and s were fitted as functions of w.

Figure 5 shows the numerical results and the fit. Note that the fit has been optimized for relative error, so for large freeboards the fit is a little off, but it was considered more important to fit the onset of cliff calving correctly.

5 Failure time

There is a theory for damage evolution in ice for tensile damage (Pralong et al., 2003), from which the time to failure is derived as follows (Mercenier et al., 2018):

$$T_f = \frac{(1 - D_0)^{k+r+1} - (1 - D_c)^{k+r+1}}{(k + r + 1)B(\sigma_0 - \sigma_{\text{th}})^r}, \tag{19}$$

with the rate factor for damage evolution B, material constants r and k, initial damage D_0, critical damage D_c, stress threshold for damage creation σ_{th}, and the working stress σ_0, which we assume to be the maximum shear stress $\tau_{\max}$. With these assumptions Eq. (19) can be written as

$$T_f = (\sigma_0 - \sigma_{\text{th}})^{-r} / B^*, \tag{20}$$

with $\sigma_{\text{th}} = 0.17$ MPa, $r = 0.43$ and $B^* = 65\text{MPa}^{-r}\text{a}^{-1}$, as given in Mercenier et al. (2018). These parameters have been determined by calibrating a tensile failure calving model with data on calving rate, water depth and ice thickness for a variety of tidewater glaciers in the Arctic.

However, Eq. (20) is valid only for damages created through tensile creep. The difference between tensile and compressive damage is that under tension a single crack grows in an unstable fashion to cause failure, while in compression a large number of small cracks grow in a stable fashion until their interaction causes failure (Ashby and Sammis, 1990).

There is plenty of literature about compressive creep and failure in rocks (Brantut et al., 2013). Fatigue failure happens when a material is loaded with stresses below the failure stress and fails with a time delay due to the development of micro-cracks. There is an exponential law as well as a power law for the time to failure:

$$t_f = t_0 \exp\left(-b\frac{\sigma}{\sigma_0}\right), \tag{21}$$

$$t_f = t_0'\left(\frac{\sigma}{\sigma_0}\right)^{-b'}. \tag{22}$$

The power-law exponent is usually large, $b' \approx 20$, so the power law is very similar to the exponential law. Once the major stress σ exceeds the instantaneous strength σ_0, immediate failure is assumed ($t_f = 0$). Both time to failure relations fit the experimental data for rock well (Amitrano and Helmstetter, 2006). However, the constants depend on material properties, and there are to our knowledge no studies for time dependence of compressive creep failure in ice.

This leaves us with a dilemma: there have been no studies that determined the material properties of ice under time-dependent brittle compressive failure. Also, we cannot determine those material properties ourselves by fitting the resulting calving law to observations because, so far, cliff calving has not been observed as the major calving process in any glacier. That makes it impossible to estimate the time to failure using Eq. (21) or (22). Equation (20) and the value of its constants have been determined for tensile failure, which is microscopically very different from brittle compressive failure. So there is little reason to expect it to describe the timescale of shear failure well.

Nevertheless, we will use it as a starting point for our further analysis. For the stresses above the shear failure threshold, $\sigma_0 > 1$ MPa, the time to failure for tensile failure (given by Eq. 20) changes by only a factor of 2 (see Fig. 6). Hence, the calving relation can be further simplified by assuming that there is a characteristic time to failure, T_c, that is the same for all stresses and sizes of failure regions, $T_c \approx 4$ d. This characteristic time has been derived from parameters determined for tensile failure, so its application to shear failure comes with an uncertainty that is difficult to quantify.

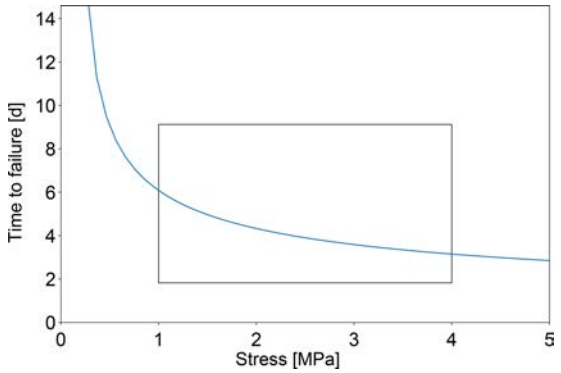

Figure 6. Time to failure given by Eq. (20). For stresses above the shear failure threshold, $\sigma_0 > 1$ MPa, the time to failure changes only little (box).

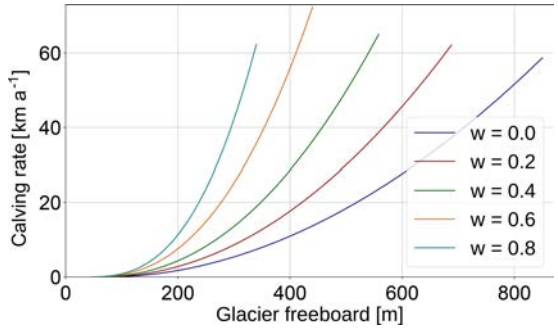

Figure 7. Cliff-calving rates C as a function of glacier freeboard $F = H - D$ and relative water depth $w = D/H$, as given by Eq. (23).

6 Calving law

With a constant failure time, the calving rate is proportional to the size of the failure region

$$C = C_0 \cdot \left(\frac{F - F_c}{F_s}\right)^s, \tag{23}$$

$$F_s = \left(115 \cdot (w - 0.356)^4 + 21\right) \text{ m}, \tag{24}$$

$$F_c = (75 - w \cdot 49) \text{ m}, \tag{25}$$

$$s = 0.17 \cdot 9.1^w + 1.76, \tag{26}$$

$$C_0 = \frac{1\,\text{m}}{4\,\text{d}} = 91.25\,\text{m}\,\text{a}^{-1}, \tag{27}$$

with $w \equiv D/H < 0.9$ and $F \equiv H - D = H \cdot (1 - w)$.
A dry cliff ($w = 0$) reaches calving rates of $C = 50\,\text{km}\,\text{a}^{-1}$ at an ice thickness of $F = H \approx 800$ m, while an ice cliff that is close to floatation ($w = 0.8$) reaches the same calving rate at a freeboard of $F \approx 300$ m, which corresponds to an ice thickness of $H \approx 1500$ m (see Fig. 7).

Table 1. Table of parameters in the cliff-calving relation (Eq. 23), giving the exponent s, critical freeboard F_c and scaling factor F_s for a range of relative water depth values w.

w	s	F_c (m)	F_s
0	1.93	75.0	22.85
0.1	1.97	70.1	21.49
0.2	2.02	65.2	21.07
0.3	2.09	60.3	21.00
0.4	2.17	55.4	21.00
0.5	2.27	50.5	21.05
0.6	2.40	45.6	21.41
0.7	2.56	40.7	22.61
0.8	2.75	35.8	25.47
0.9	3.00	30.9	31.07

How do cliff-calving rates given by Eq. (23) compare to currently observed calving rates? A glacier enters the cliff-calving regime when its freeboard is larger than the critical freeboard F_c and the cliff-calving rate given by Eq. (23) becomes nonzero. Obviously, glaciers calve through tensile failure before and after they reach the cliff-calving regime, so we expect the overall calving rate to be larger than the cliff-calving rate, especially for glaciers that just entered the cliff-calving regime and are heavily crevassed.

Jakobshavn glacier in Greenland is one of the few glaciers that are currently in a cliff-calving mode. Jakobshavn glacier terminates in water with a depth of 800 m (Morlighem et al., 2014) and has a glacier freeboard of 100 m (Xie et al., 2018). Therefore, it can be considered to be at the beginning of the cliff-calving regime. Since the terminus is also heavily crevassed, we expect tensile calving to be the main contribution to the overall calving rate. Hence, this example can only give an upper bound on the possible cliff-calving rate.

It is difficult to determine calving rates directly. The ice flow velocity to the front of Jakobshavn is up to $12\,\text{km}\,\text{a}^{-1}$ (Joughin et al., 2012). The grounding line of Jakobshavn glacier retreats and advances seasonally about 6 km each year, but the maximum grounding line position has not changed much between 2012 and 2015 (Xie et al., 2018). Assuming a fixed grounding line, the calving rate plus frontal melt rate would equal the flow velocity. Hence, the averaged yearly calving rate is smaller than $12\,\text{km}\,\text{a}^{-1}$.

Inserting values of glacier freeboard and water depth given above into Eq. (23) gives a cliff-calving rate of $C = 750\,\text{m}\,\text{a}^{-1}$, which is well below the overall calving rate.

7 Discussion and conclusion

We solved the 2-D Stokes equation numerically for a flat glacier frozen to its bed in a flow-line model and investigated the stresses at the calving front.

The following four simplifications were made.

1. The model was solved in one horizontal direction, neglecting lateral shear effects. Without lateral shear effects, the result is independent of the topography of individual glaciers.

2. We assumed a basal boundary condition corresponding to a glacier frozen to its bed. Sliding was not considered.

3. The main failure mechanism was assumed to be shear faulting. We assumed brittle compressive failure according to the Coulomb law without friction stabilizing the ice cliff. Friction would allow glaciers with larger freeboards than observed to be stable.

4. A constant time to failure has been assumed.

Under these assumptions, crevasses cannot penetrate the whole glacier depth and shear failure was chosen as the main failure mechanism. The region where shear stresses exceed a critical shear stress of 1 MPa is called the failure region. The extent of this failure region, the failure distance, was determined for a range of glacier freeboards and relative water depths. For freeboards small enough for the failure region not to encompass the whole ice thickness, an analytical fit was made. Assuming a constant time to failure, a cliff-calving rate was derived. Resulting cliff-calving rates seem large compared to currently observed calving rates. Comparison with Jakobshavn glacier in Greenland shows that the cliff-calving rate is smaller than the overall calving rate; hence, we conclude that Eq. (23) probably does not overestimate cliff-calving rates.

7.1 Idealized setup vs. realistic conditions

The cliff-calving rate was derived using an idealized setup, given by the first two of the four assumptions described above. Realistic glaciers that might experience cliff calving sit in valleys where they experience lateral drag and may be sliding. The calving front may have a slope rather than a vertical cliff and there might be an undercut caused by frontal melt.

7.1.1 Sliding glaciers

First consider sliding with a constant velocity v (i.e., vanishing strain rate) for which the upstream boundary condition is an influx with velocity v, so $u = v$. The basal boundary conditions become $u = v$, $w = 0$. Solving the Stokes' equations with these boundary conditions numerically with FeniCS gives the exact same stress fields as in the frozen case and the velocity field is simply shifted by the sliding velocity v. This is not surprising: a simple Galilean transformation takes this sliding glacier back to the frozen glacier previously considered without changing any of the physics.

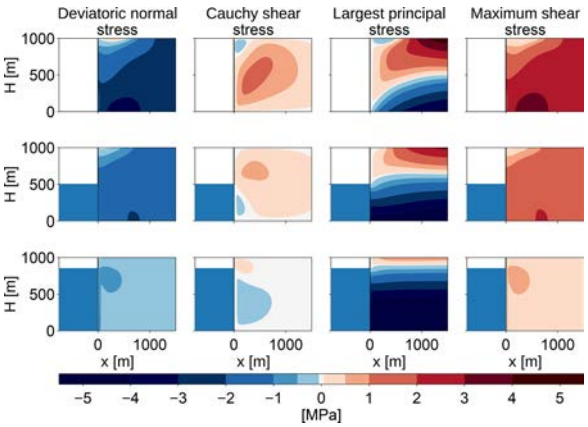

Figure 8. Stress configurations at the calving front for different relative water depths ($w = 0$, 0.5, 0.85) for a fixed ice thickness of 1000 m with a free-slip basal boundary condition, instead of the no-slip boundary condition used in the previous analysis (compare Fig. 2). The first column shows the deviatoric normal stress in the x direction, S_{xx}, the second column shows the Cauchy shear stress, $\sigma_{xz} = S_{xz}$, the third column shows the largest principal stress, σ_i, and the last column shows the maximum shear stress, $\tau_{\max}$. In contrast with the no-slip case, there is no definite failure region, as the maximum shear stress is large throughout the whole numerical domain.

In general, sliding velocities increase towards the glacier terminus. The steepest possible velocity gradient can be obtained with a free-slip basal boundary condition: we assume no influx at the upstream boundary, $u = 0$, and at the bed we assume free slip in the horizontal direction, which only leaves a boundary condition for the vertical velocity, $w = 0$. The basal velocity is zero at the upstream boundary and takes its maximum at the calving front. Due to this velocity gradient, the maximum shear stress is large throughout the whole numerical domain (see Fig. 8). For increasing ice thickness it becomes difficult to define a meaningful failure region because the critical shear stress is exceeded in the whole numerical domain – one must assume that the whole numerical domain will fail. Thus, in the case of a sliding glacier, the failure region is larger than in the case of a glacier frozen to its bed. Hence, the derived cliff-calving rate can serve as a lower bound for this kind of calving front.

To summarize, the derived cliff-calving law is valid for glaciers that are frozen to the bed or sliding with a constant velocity and vanishing strain rate. It serves as a lower bound on the calving rate for glaciers in which velocities increase towards the calving front.

7.1.2 Lateral drag

In order to investigate how lateral drag influences cliff calving, we will assume ice flow in a channel with a flow-line in the x direction. Ice is assumed to flow only in the x di-

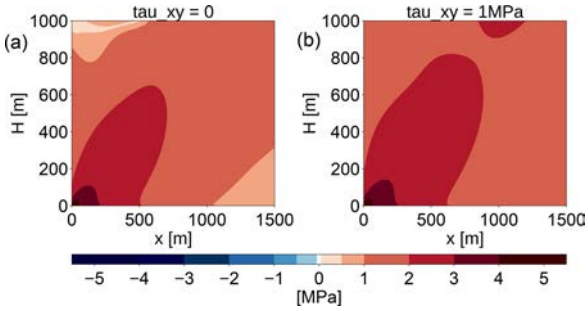

Figure 9. Maximum shear stress $\tau_{\max}$ in the vicinity of the calving front in the case without lateral drag **(a)** and with a constant lateral drag of $\tau_{xy} = 1$ MPa **(b)**.

rection with a flow maximum in the middle of the channel. Since deviatoric stresses are connected to the strain rate, $\tau_{ij} = B\dot{\epsilon}_e\dot{\epsilon}_{ij}$, and the strain rate is given by the velocity gradients, $\dot{\epsilon}_{ij} = \frac{1}{2}\left(\partial_i u_j + \partial_i u_j\right)$, we get an additional deviatoric shear stress in the x–y plane, τ_{xy}. The other stress components in y vanish, $\tau_{yz} = \tau_{yy} = 0$, because the respective velocity gradients vanish. The Cauchy stress tensor becomes

$$\boldsymbol{\sigma} = \begin{pmatrix} P + \tau_{xx} & \tau_{xy} & \tau_{xz} \\ \tau_{xy} & P & 0 \\ \tau_{xz} & 0 & P - \tau_{xx} \end{pmatrix}. \tag{28}$$

The principal stresses σ_i are defined as eigenvalues of σ, and the maximum shear stress $\tau_{\max}$ is defined as the difference between the maximum and minimum principal stress. In 3-D, there is no simple analytical formula for the eigenvalues of a matrix, and therefore it is not feasible to get an analytical estimate on whether the introduction of nonzero τ_{xy} makes $\tau_{\max}$ smaller or larger.

Assuming $P(x, z)$, $\tau_{xx}(x, z)$ and $\tau_{xz}(x, z)$, as given by the FeniCS simulation with a constant $\tau_{xy} = 1$ MPa, we calculate the principal stresses and the maximum shear stress numerically. This shows that $\tau_{\max}$ increases with increasing absolute value of τ_{xy} (see Fig. 9).

Hence, lateral shear increases the maximum shear, therefore increasing the size of the failure region and the cliff-calving rate. The derived cliff-calving rate can serve as a lower bound if lateral drag is present.

7.1.3 Calving front slope

Other studies have shown that a calving front with a slope has significantly reduced stresses compared to a calving front with a vertical cliff (Benn et al., 2017; Mercenier et al., 2018). It is clear that a calving front slope also reduces the cliff-calving rate.

We have not analyzed this effect here because once cliff calving has been initiated, the full thickness calving probably prevents calving front slopes from forming. We aim to find a parametrization that can be implemented in ice sheet models capable of simulating the Antarctic ice sheet. These simulations are done on resolutions of several kilometers and cannot resolve calving front slopes on length scales of several tens or hundreds of meters.

7.1.4 Melt undercut

Undercut from melt would increase the stresses near the calving front (Benn et al., 2017) and hence increase the calving rate.

7.2 Uncertainties

Cliff calving is still a rather hypothetical process with a very limited scope of observations. Since there are currently no glaciers that are clearly in a cliff-calving regime, the calving rate cannot be fitted to observed calving rates. There is uncertainty in the maximum shear stress used to determine the failure distance as well as the time to failure.

Laboratory studies give a range of values between 0.5 and 5 MPa for the critical shear stress (Schulson et al., 1999; Schulson, 2001). A much larger uncertainty arises from the time to failure. There are studies that give time to failure relations and parameters for brittle compressive failure of rocks but none for ice. Time to failure of ice has only been studied for tensile failure. We use the time to failure relation used by Mercenier et al. (2018) as a first guess. Applying this time to failure for tensile failure to a process of shear failure is very uncertain. We guess that the time to failure could be up to an order of magnitude smaller or larger.

The scaling parameter C_0 in Eq. (23) should therefore be considered a free parameter. In any implementation of this cliff-calving relation, a range of values for C_0 should be tested for plausibility.

7.3 Comparison with other calving parametrizations

7.3.1 Other cliff-calving approaches

Bassis and Walker (2011) derived a stability limit for ice cliffs considering shear and tensile failure (their assumptions are analyzed further in the appendix). According to Eq. (23), cliff calving starts when the freeboard exceeds $F \approx 75$ m, this is close to the stability limit of $F \approx 100$ m given by Bassis and Walker (2011).

Pollard et al. (2015) and DeConto and Pollard (2016) implemented cliff calving in their ice sheet model by assuming a cliff-calving rate that is zero until the freeboard has reached ≈ 100 m, increases linearly up to 3 km a^{-1} for a freeboard of about 150 m and stays constant after that. The calving relation is modified by factors representing back stress and additional wet crevasse deepening. Edwards et al. (2019) did an ensemble study with a range of values for the maximum cliff-calving rate from 0 km a^{-1} (no cliff calving) up to 5 km a^{-1}. Depending on the scaling constant C_0, cliff-calving rates given by Eq. (23) have an equal range of mag-

nitude but increase with a power-law dependence and have no upper bound.

Bassis et al. (2017) implemented cliff calving by requiring that ice cliffs cannot exceed the stability limit. This becomes a condition for the speed of grounding line retreat and advance. Equation (23) is easier to implement in ice sheet models because it can be implemented just like other calving parameterizations and does not need to be rewritten as a condition for the grounding line.

7.3.2 Other stress-based calving laws

Mercenier et al. (2018) derived a cliff-calving law for tidewater glaciers below the stability limit by solving the stresses in the vicinity of the front and assuming tensile failure through the formation of a large crevasse. In contrast, we assume shear failure (also called brittle compressive failure). The calving rate given by Mercenier et al. (2018) increases approximately linearly with the freeboard and has no lower bound, while the calving rate given by Eq. (23) grows with a power $s(w) > 1$ for freeboards larger than the critical freeboard $F_c(w)$ (see Fig. 10). Hence, we expect tensile failure to dominate for small freeboards and shear failure to dominate for large freeboards.

It is difficult to say at which glacier freeboard the tensile failure regime ends and the shear failure regime begins, not only due to uncertainty in the scaling parameter C_0. In practice, both failure modes will interact, with tensile stress damaging the ice through a few large crevasses originating from the surface of the ice and shear stress damaging the ice through a large number of small crevasses in the lower part of the cliff. This likely interaction of failure modes cannot be analyzed by assuming ice to be a continuous medium (like the approach used here and by Mercenier et al., 2018) but should be done with damage theory or a discrete element approach.

7.4 Conclusion

The calving law proposed here was derived under a number of constraining assumptions. First, it was assumed that friction plays no role in shear failure. Second, it was assumed that once the critical shear stress is exceeded, ice fails after a constant time to failure. An improved cliff-calving model might include friction and allow a stress-dependent time to failure.

If the Coulomb law with a friction component is used, the immediate failure region is smaller than in the no-friction case. Time to failure relations for compressive failure, as given by Eqs. (21) and (22), are valid for stresses below the critical shear stress. Failure is assumed to be instantaneous as soon as the critical shear stress is reached. Regions where the stress is below the failure stress would be assigned a stress-dependent failure time leading to a spatially distributed time to failure. Since friction is smaller at the top of the ice cliff, the top would fail earlier than the base, leaving a foot that would subsequently fail due to buoyant forces. There is no simple way to find a parametrization of the cliff-calving rate for these processes.

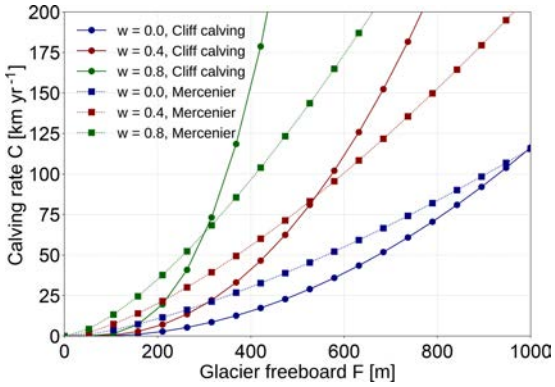

Figure 10. Comparison of the cliff-calving law given by Eq. (23) (continuous line) with the calving law for tidewater glaciers given by Mercenier et al. (2018), Eq. (22) (dotted line). Note that the cliff-calving rate could be scaled differently due to the uncertainty in C_0.

Another problem is that there are no laboratory studies on the parameters in the time to failure relations for ice. It is also not possible to calibrate the calving relation using observed calving rates because there are no glaciers currently available where cliff calving is the primary failure mechanism. Paleorecords might provide some means to calibrate cliff-calving rates as attempted in Pollard et al. (2015) and DeConto and Pollard (2016).

Paleorecords might not be constraining enough to provide a useful limit for the Antarctic sea-level contribution of the next 85 years. But even if it is difficult to constrain the rate of cliff-calving there are important qualitative consequences of a monotonously increasing cliff-calving dependence on ice thickness. The most important is the potential of a self-amplifying ice loss mechanism, which is not constrained by the reduction in calving but must be constrained by other processes. Without some kind of cliff-calving mechanism it is likely that ice sheet models are lacking an important ice loss mechanism.

Code availability. FeniCS can be downloaded from the project website https://fenicsproject.org/download/ (last access: 1 September 2018). The script used for the FeniCS simulation in this paper is available on request from the authors.

Appendix A: Simplified stress balance

It is possible to solve the stress balance at the calving front analytically in a depth-averaged model with a simplifying assumption for the isotropic pressure. This has been used by Bassis and Walker (2011) and Pollard et al. (2015). It is interesting to compare this with the numerical stress field solution obtained above.

Bassis and Walker (2011) and Pollard et al. (2015) assumed the isotropic pressure is given by the gravitational pressure

$$P(x,z) = \rho_i g(H-z), \tag{A1}$$

where ρ_i is the density of ice. This assumption is actually only true over length scales that are large compared with the ice thickness and far from the ice margins (MacAyeal, 1989), which is not the case when stresses close to the calving front are analyzed. But making this assumption allows for an analytical solution of the depth-averaged stresses and does not require any ice rheology.

Together with incompressibility, which means that the trace of the strain rate disappears ($\dot\epsilon_{kk}=0$) and implies $S_{xx}+S_{zz}=0$, the 2-D Stokes equations become

$$0 = \frac{\partial S_{xx}}{\partial x} + \frac{\partial S_{xz}}{\partial z}, \tag{A2}$$

$$0 = \frac{\partial S_{xz}}{\partial x} - \frac{\partial S_{xx}}{\partial z}. \tag{A3}$$

Assuming a traction-free surface boundary, traction-continuity at the terminus boundary and vanishing deviatoric stresses at the upstream boundary, as well as the bed boundary, a boundary value problem arises that can be solved numerically.

The resulting stresses are smaller than the stresses obtained in Sect. 2 for the 2-D Stokes equation with nonlinear ice rheology (Fig. A1). A failure region can be defined as in Sect. 3 and its size shows a very similar dependence on glacier freeboard and water depth, though it is smaller by about a factor of 3.

The biggest difference between the two approaches lies in the largest principal stress: in this simplified problem, the largest principal stress is negative in the whole ice volume; there is no region of tensile stresses, so no crevasses form. This is due to the assumption that the isotropic pressure is equal to the gravitational pressure, which is not actually the case in the vicinity of the glacier terminus.

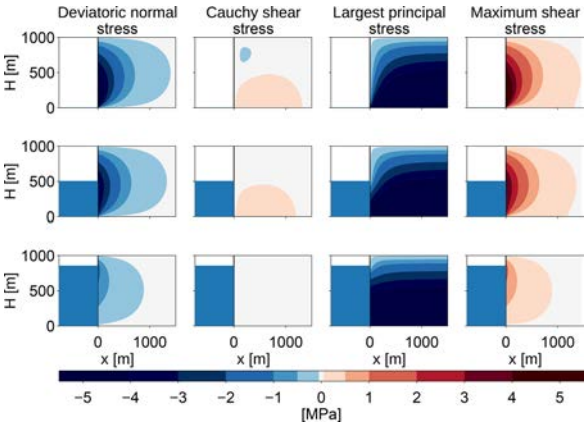

Figure A1. Stress configurations at the calving front for different relative water depths ($w = 0$, 0.5, 0.85) for a fixed ice thickness of 1000 m. The first column shows the deviatoric normal stress in the x direction, S_{xx}, the second column shows the Cauchy shear stress, $\sigma_{xz} = S_{xz}$, the third column shows the largest principal stress, σ_i, and the last column shows the maximum shear stress, τ_max.

Author contributions. AL conceived the study, TS designed and carried out the numerical experiments, both authors analysed the data, and TS wrote the manuscript with input from AL.

Competing interests. The authors declare that they have no conflict of interest.

Acknowledgements. Tanja Schlemm would like to thank Yue Ma and Christian Helanow for their valuable help with FeniCS. We would like to thank Andy Aschwanden and two anonymous reviewers for their very useful comments on earlier versions of the manuscript.

Financial support. As a doctoral student, Tanja Schlemm is funded by a doctoral stipend granted by the Heinrich Böll Foundation.

The publication of this article was funded by the Open Access Fund of the Leibniz Association.

Review statement. This paper was edited by Eric Larour and reviewed by Andy Aschwanden and two anonymous referees.

References

Alnæs, M. S., Blechta, J., Hake, J., Johansson, A., Kehlet, B., Logg, A., Richardson, C., Ring, J., Rognes, M. E., and Wells, G. N.: The FEniCS Project Version 1.5, Archive of Numerical Software, 3, 9–23, https://doi.org/10.11588/ans.2015.100.20553, 2015.

Amitrano, D. and Helmstetter, A.: Brittle creep, damage, and time to failure in rocks, J. Geophys. Res.-Solid , 111, B11201, https://doi.org/10.1029/2005JB004252, 2006.

Ashby, M. F. and Sammis, C. G.: The damage mechanics of brittle solids in compression, Pure Appl. Geophys., 133, 489–521, https://doi.org/10.1007/BF00878002, 1990.

Bassis, J. N. and Walker, C. C.: Upper and lower limits on the stability of calving glaciers from the yield strength envelope of ice, Philos. T. R. Soc. Lond., 468, 913–931, https://doi.org/10.1098/rspa.2011.0422, 2011.

Bassis, J. N., Petersen, S. V., and Mac Cathles, L.: Heinrich events triggered by ocean forcing and modulated by isostatic adjustment, Nature, 542, 332–334, https://doi.org/10.1038/nature21069, 2017.

Benn, D., Astrom, J., Zwinger, T., Todd, J., Nick, F., Cook, S., Hulton, N., and Luckmann, A.: Melt-under-cutting and buoyancy-driven calving from tidewater glaciers: new insights from discrete element and continuum model simulations, J. Glaciol., 63, 691–702, https://doi.org/10.1017/jog.2017.41, 2017.

Benn, D. I., Warren, C. R., and Mottram, R. H.: Calving processes and the dynamics of calving glaciers, Earth-Sci. Rev., 82, 143–179, https://doi.org/10.1016/j.earscirev.2007.02.002, 2007.

Brantut, N., Heap, M., Meredith, P., and Baud, P.: Time-dependent cracking and brittle creep in crustal rocks: A review, J. Struct. Geol., 52, 17–43, https://doi.org/10.1016/j.jsg.2013.03.007, 2013.

Church, J. A., Clark, P. U., Cazenave, A., Gregory, J. M., Jevrejeva, S., Levermann, A., Merrifield, M. A., Milne, G. A., Nerem, R. S., Nunn, P. D., Payne, A. J., Pfeffer, W. T., Stammer, D., and Unnikrishnan, A. S.: Sea-Level Rise by 2100, Science, 342, 1445–1445, https://doi.org/10.1126/science.342.6165.1445-a, 2013.

Das, S. B., Joughin, I., Behn, M. D., Howat, I. M., King, M. A., Lizarralde, D., and Bhatia, M. P.: Fracture Propagation to the Base of the Greenland Ice Sheet During Supraglacial Lake Drainage, Science, 320, 778–781, https://doi.org/10.1126/science.1153360, 2008.

DeConto, R. M. and Pollard, D.: Contribution of Antarctica to past and future sea-level rise, Nature, 531, 591–597, https://doi.org/10.1038/nature17145, 2016.

Depoorter, M. A., Bamber, J. L., Griggs, J. A., Lenaerts, J. T. M., Ligtenberg, S. R. M., van den Broeke, M. R., and Moholdt, G.: Calving fluxes and basal melt rates of Antarctic ice shelves, Nature, 502, 89–92, https://doi.org/10.1038/nature12567, 2013.

Edwards, T. L., Brandon, M. A., Durand, G., Edwards, N. R., Golledge, N. R., Holden, P. B., Nias, I. J., Payne, A. J., Ritz, C., and Wernecke, A.: Revisiting Antarctic ice loss due to marine ice-cliff instability, Nature, 566, 58–64, https://doi.org/10.1038/s41586-019-0901-4, 2019.

Enderlin, E. M., Howat, I. M., Jeong, S., Noh, M.-J., Angelen, J. H., and Broeke, M. R.: An improved mass budget for the Greenland ice sheet, Geophys. Res. Lett., 41, 866–872, https://doi.org/10.1002/2013GL059010, 2014.

Ford, H. and Alexander, J. M.: Advanced mechanics of materials, Wiley, 672 pp., 1963.

Jiménez, S. and Duddu, R.: On the evaluation of the stress intensity factor in calving models using linear elastic fracture mechanics, J. Glaciol., 64, 759–770, https://doi.org/10.1017/jog.2018.64, 2018.

Joughin, I. and MacAyeal, D. R.: Calving of large tabular icebergs from ice shelf rift systems, Geophys. Res. Lett., 32, L02501, https://doi.org/10.1029/2004GL020978, 2005.

Joughin, I., Smith, B. E., Howat, I. M., Floricioiu, D., Alley, R. B., Truffer, M., and Fahnestock, M.: Seasonal to decadal scale variations in the surface velocity of Jakobshavn Isbrae, Greenland: Observation and model-based analysis, J. Geophys. Res.-Earth Surface, 117, F02030, https://doi.org/10.1029/2011JF002110, 2012.

Kopp, R. E., DeConto, R. M., Bader, D. A., Hay, C. C., Horton, R. M., Kulp, S., Oppenheimer, M., Pollard, D., and Strauss, B. H.: Evolving Understanding of Antarctic Ice-Sheet Physics and Ambiguity in Probabilistic Sea-Level Projections, Earth's Future, 5, 1217–1233, https://doi.org/10.1002/2017EF000663, 2017.

Krug, J., Weiss, J., Gagliardini, O., and Durand, G.: Combining damage and fracture mechanics to model calving, The Cryosphere, 8, 2101–2117, https://doi.org/10.5194/tc-8-2101-2014, 2014.

Lazzara, M. A., Jezek, K. C., Scambos, T. A., MacAyeal, D. R., and van der Veen, C. J.: On the recent calving of icebergs from the Ross Ice Shelf, Polar Geogr., 23, 201–212, https://doi.org/10.1080/10889379909377676, 1999.

Levermann, A. and Winkelmann, R.: A simple equation for the melt elevation feedback of ice sheets, The Cryosphere, 10, 1799–1807, https://doi.org/10.5194/tc-10-1799-2016, 2016.

Levermann, A., Winkelmann, R., Nowicki, S., Fastook, J. L., Frieler, K., Greve, R., Hellmer, H. H., Martin, M. A., Meinshausen, M., Mengel, M., Payne, A. J., Pollard, D., Sato, T., Timmermann, R., Wang, W. L., and Bindschadler, R. A.: Projecting Antarctic ice discharge using response functions from SeaRISE ice-sheet models, Earth Syst. Dynam., 5, 271–293, https://doi.org/10.5194/esd-5-271-2014, 2014.

Ma, Y., Tripathy, C. S., and Bassis, J. N.: Bounds on the calving cliff height of marine terminating glaciers, Geophys. Res. Lett., 44, 1369–1375, https://doi.org/10.1002/2016GL071560, 2017.

MacAyeal, D. R.: Large-scale ice flow over a viscous basal sediment: Theory and application to ice stream B, Antarctica, J. Geophys. Res.-Sol. Ea., 94, 4071–4087, https://doi.org/10.1029/JB094iB04p04071, 1989.

Meier, M. F. and Post, A.: Fast tidewater glaciers, J. Geophys. Res.-Sol. Ea., 92, 9051–9058, https://doi.org/10.1029/JB092iB09p09051, 1987.

Mengel, M., Feldmann, J., and Levermann, A.: Linear sea-level response to abrupt ocean warming of major West Antarctic ice basin, Nat. Clim. Change, 6, 71–74, https://doi.org/10.1038/nclimate2808, 2016.

Mercenier, R., Lüthi, M. P., and Vieli, A.: Calving relation for tidewater glaciers based on detailed stress field analysis, The Cryosphere, 12, 721–739, https://doi.org/10.5194/tc-12-721-2018, 2018.

Morlighem, M., Rignot, E., Mouginot, J., Seroussi, H., and Larour, E.: Deeply incised submarine glacial valleys beneath the Greenland ice sheet, Nat. Geosci., 7, 418–422, https://doi.org/10.1038/ngeo2167, 2014.

Morlighem, M., Bondzio, J., Seroussi, H., Rignot, E., Larour, E., Humbert, A., and Rebuffi, S.: Modeling of Store Gletscher's calving dynamics, West Greenland, in response to ocean thermal forcing, Geophys. Res. Lett., 43, 2659–2666, https://doi.org/10.1002/2016GL067695, 2016.

Nick, F., van der Veen, C., Vieli, A., and Benn, D.: A physically based calving model applied to marine outlet glaciers and implications for the glacier dynamics, J. Glaciol., 56, 781–794, https://doi.org/10.3189/002214310794457344, 2010.

Nye, J. F.: The Distribution of Stress and Velocity in Glaciers and Ice-Sheets, Philos. T. R. Soc. Lond., 239, 113–133, https://doi.org/10.1098/rspa.1957.0026, 1957.

Pollard, D., DeConto, R. M., and Alley, R. B.: Potential Antarctic Ice Sheet retreat driven by hydrofracturing and ice cliff failure, Earth Planet. Sci. Lett., 412, 112–121, https://doi.org/10.1016/j.epsl.2014.12.035, 2015.

Pralong, A. and Funk, M.: Dynamic damage model of crevasse opening and application to glacier calving, J. Geophys. Res.-Sol. Ea., 110, B01309, https://doi.org/10.1029/2004JB003104, 2005.

Pralong, A., Funk, M., and Lüthi, M. P.: A description of crevasse formation using continuum damage mechanics, Ann. Glaciol., 37, 77–82, 2003.

Rignot, E. and Kanagaratnam, P.: Changes in the Velocity Structure of the Greenland Ice Sheet, Science, 311, 986–990, https://doi.org/10.1126/science.1121381, 2006.

Rignot, E., Mouginot, J., Morlighem, M., Seroussi, H., and Scheuchl, B.: Widespread, rapid grounding line retreat of Pine Island, Thwaites, Smith, and Kohler glaciers, West Antarctica, from 1992 to 2011, Geophys. Res. Lett., 41, 3502–3509, https://doi.org/10.1002/2014GL060140,2014.

Ritz, C., Edwards, T. L., Durand, G., Payne, A. J., Peyaud, V., and Hindmarsh, Richard C. A.: Potential sea-level rise from Antarctic ice-sheet instability constrained by observations, Nature, 528, 115–118, https://doi.org/10.1038/nature16147, 2015.

Schulson, E. M.: Brittle failure of ice, Eng. Fract. Mech., 68, 1839–1887, https://doi.org/10.1016/S0013-7944(01)00037-6, 2001.

Schulson, E. M., Iliescu, D., and Renshaw, C. E.: On the initiation of shear faults during brittle compressive failure: A new mechanism, J. Geophys. Res.-Sol. Ea., 104, 695–705, https://doi.org/10.1029/1998JB900017, 1999.

Shepherd, A., Ivins, E., Rignot, E., Smith, B., van den Broeke, M., Velicogna, I., Whitehouse, P., Briggs, K., Joughin, I., Krinner, G., Nowicki, S., Payne, T., Scambos, T., Schlegel, N., Geruo, A., Agosta, C., Ahlstrøm, A., Babonis, G., Barletta, V., Blazquez, A., Bonin, J., Csatho, B., Cullather, R., Felikson, D., Fettweis, X., Forsberg, R., Gallee, H., Gardner, A., Gilbert, L., Groh, A., Gunter, B., Hanna, E., Harig, C., Helm, V., Horvath, A., Horwath, M., Khan, S., Kjeldsen, K. K., Konrad, H., Langen, P., Lecavalier, B., Loomis, B., Luthcke, S., McMillan, M., Melini, D., Mernild, S., Mohajerani, Y., Moore, P., Mouginot, J., Moyano, G., Muir, A., Nagler, T., Nield, G., Nilsson, J., Noel, B., Otosaka, I., Pattle, M. E., Peltier, W. R., Pie, N., Rietbroek, R., Rott, H., Sandberg-Sørensen, L., Sasgen, I., Save, H., Scheuchl, B., Schrama, E., Schröder, L., Seo, K.-W., Simonsen, S., Slater, T., Spada, G., Sutterley, T., Talpe, M., Tarasov, L., van de Berg, W. J., van der Wal, W., van Wessem, M., Vishwakarma, B. D., Wiese, D., Wouters, B., and the IMBIE team.: Mass balance of the Antarctic Ice Sheet from 1992 to 2017, Nature, 558, 219–222, https://doi.org/10.1038/s41586-018-0179-y, 2018.

Slangen, A. B. A., Adloff, F., Jevrejeva, S., Leclercq, P. W., Marzeion, B., Wada, Y., and Winkelmann, R.: A Review of Recent Updates of Sea-Level Projections at Global and Regional Scales, in: Integrative Study of the Mean Sea Level and Its Components, edited by: Cazenave, A., Champollion, N., Paul F., and Benveniste, J., Space Sciences Series of ISSI, Springer, Cham, 58, 395–416, https://doi.org/10.1007/978-3-319-56490-6_17, 2017.

Todd, J., Christoffersen, P., Zwinger, T., Råback, P., Chauché, N., Benn, D., Luckman, A., Ryan, J., Toberg, N., Slater, D., and Hubbard, A.: A Full-Stokes 3-D Calving Model Applied to a Large Greenlandic Glacier, J. Geophys. Res.-Earth, 123, 410–432, https://doi.org/10.1002/2017JF004349, 2018.

van der Veen, C. J.: Fundamentals of Glacier Dynamics, A. A. Balkema, CRC Press, 403 pp., 1999.

van Der Veen, J.: Tidewater calving, J. Glaciol., 42, 375–385, https://doi.org/10.3198/1996JoG42-141-375-385, 1996.

Vieli, A., Jania, J., and Kolondra, L.: The retreat of a tidewater glacier: observations and model calculations on Hansbreen, Spitsbergen, J. Glaciol., 48, 592–600, https://doi.org/10.3189/172756502781831089, 2002.

Walter, F., O'Neel, S., McNamara, D., Pfeffer, W. T., Bassis, J. N., and Fricker, H. A.: Iceberg calving during transition from grounded to floating ice: Columbia Glacier, Alaska, Geophys. Res. Lett., 37, L15501, https://doi.org/10.1029/2010GL043201, 2010.

WCRP Global Sea Level Budget Group: Global sea-level budget 1993–present, Earth Syst. Sci. Data, 10, 1551–1590, https://doi.org/10.5194/essd-10-1551-2018, 2018.

Weertman, J.: Can a water-filled crevasse reach the bottom surface of a glacier, IASH Publ., 95, 139–145, 1973.

Weiss, J. and Schulson, E. M.: Coulombic faulting from the grain scale to the geophysical scale: lessons from ice, J. Phys. D, 42, 214017, https://doi.org/10.1088/0022-3727/42/21/214017, 2009.

Xie, S., Dixon, T. H., Voytenko, D., Deng, F., and Holland, D. M.: Grounding line migration through the calving season at Jakobshavn Isbræ, Greenland, observed with terrestrial radar interferometry, The Cryosphere, 12, 1387–1400, https://doi.org/10.5194/tc-12-1387-2018, 2018.

Zhang, H., Ju, L., Gunzburger, M., Ringler, T., and Price, S.: Coupled Models and Parallel Simulations for Three-Dimensional Full-Stokes Ice Sheet Modeling, Numer. Math.-Theory Me., 4, 396–418, https://doi.org/10.1017/S1004897900000416, 2011.

A.3 A simple parametrization of mélange buttressing for calving glaciers

Schlemm, T. & Levermann, A.

Both ice sheets in Greenland and Antarctica are discharging ice into the ocean. In many regions along the coast of the ice sheets, the icebergs calve into a bay. If the addition of icebergs through calving is faster than their transport out of the embayment, the icebergs will be frozen into a mélange with surrounding sea ice in winter. In this case, the buttressing effect of the ice mélange can be considerably stronger than any buttressing by mere sea ice would be. This in turn stabilizes the glacier terminus and leads to a reduction in calving rates. Here we propose a simple parametrization of ice mélange buttressing which leads to an upper bound on calving rates and can be used in numerical and analytical modelling.

The Cryosphere **15**, 531–545 (2021).
DOI: 10.5194/tc-15-531-2021

The Cryosphere, 15, 531–545, 2021
https://doi.org/10.5194/tc-15-531-2021

The Cryosphere Open Access EGU

A simple parametrization of mélange buttressing for calving glaciers

Tanja Schlemm[1,2] **and Anders Levermann**[1,2,3]

[1]Potsdam Institute for Climate Impact Research, Potsdam, Germany
[2]Institute of Physics and Astronomy, University of Potsdam, Potsdam, Germany
[3]Lamont-Doherty Earth Observatory, Columbia University, New York, USA

Correspondence: Anders Levermann (anders.levermann@pik-potsdam.de)

Received: 12 February 2020 – Discussion started: 17 February 2020
Revised: 1 December 2020 – Accepted: 14 December 2020 – Published: 3 February 2021

Abstract. Both ice sheets in Greenland and Antarctica are discharging ice into the ocean. In many regions along the coast of the ice sheets, the icebergs calve into a bay. If the addition of icebergs through calving is faster than their transport out of the embayment, the icebergs will be frozen into a mélange with surrounding sea ice in winter. In this case, the buttressing effect of the ice mélange can be considerably stronger than any buttressing by mere sea ice would be. This in turn stabilizes the glacier terminus and leads to a reduction in calving rates. Here we propose a simple parametrization of ice mélange buttressing which leads to an upper bound on calving rates and can be used in numerical and analytical modelling.

1 Introduction

Ice sheets gain mass by snowfall and freezing of seawater and lose mass through calving of icebergs and melting at the surface and the bed. Currently the ice sheets in Antarctica and Greenland have a net mass loss and contribute increasingly to sea level rise (Rignot et al., 2014; Shepherd et al., 2018b; WCRP Global Sea Level Budget Group, 2018; Rignot et al., 2019; Mouginot et al., 2019). The ice sheet's future mass loss is important for sea level projections (Church et al., 2013; Ritz et al., 2015; Golledge et al., 2015; DeConto and Pollard, 2016; Mengel et al., 2016; Kopp et al., 2017; Slangen et al., 2017; Golledge et al., 2019; Levermann et al., 2020). For the Greenland ice sheet, calving accounted for two-thirds of the ice loss between 2000 and 2005, while the rest was lost due to enhanced surface melting (Rignot and Kanagaratnam, 2006). Because surface melt increased faster than glacier speed, calving was responsible for a third of the mass loss of the Greenland ice sheet between 2009 and 2012 (Enderlin et al., 2014). In the future, enhanced warming (Franco et al., 2013) and the melt elevation feedback (Weertman, 1961; Levermann and Winkelmann, 2016) will further increase surface melt but also intensify the flow of ice into the ocean. Calving accounts for roughly half the ice loss of the Antarctic ice shelves; the rest is lost by basal melt (Depoorter et al., 2013).

It is clear that calving plays an important role in past and present ice loss and is therefore very likely to play an important role for future ice loss. However, by just calving off icebergs into the ocean and considering them eliminated from the stress field of the ice sheet–ice shelf system, most studies neglect the buttressing effect of a possible ice mélange, which can form within the embayment into which the glacier is calving. This study provides a simple parametrization that accounts for the buttressing effect of ice mélange on calving on a large spatial scale and that can be used for continental-scale ice sheet modelling. Such simulations are typically run on resolutions of several kilometres and over decadal to millennial timescales. Any mélange parameterization needs to be combined with a large-scale calving parameterization, of which there are some. Benn et al. (2007) proposed a crevasse-depth calving criterion assuming that once a surface crevasse reaches the water level, an iceberg calves off. This does not give a calving rate but rather the position of the calving front. It has been implemented in a flow-line model by Nick et al. (2010). Further calving parametrizations are a strain-rate-dependent calving rate for ice shelves (Levermann et al.,

2012), a calving rate parametrization based on von Mises stress and glacier flow velocity (Morlighem et al., 2016), and a calving rate for a grounded glacier based on tensile failure (Mercenier et al., 2018). In addition to calving caused by crevasses, another calving mechanism called cliff calving has first been proposed by Bassis and Walker (2011), who found that ice cliffs with a freeboard (ice thickness minus water depth) larger than 100 m are inherently unstable due to shear failure. Cliff calving was implemented as an almost step-like calving rate by Pollard et al. (2015) and DeConto and Pollard (2016), while Bassis et al. (2017) implemented cliff calving as a criterion for the calving front position. Finally, Schlemm and Levermann (2019) derived a cliff calving rate dependent on glacier freeboard and water depth by analysing stresses close to the glacier terminus and using a Coulomb failure criterion.

Mélange buttressing is likely to have a stabilizing effect on possible ice sheet instabilities. First, the so-called marine ice sheet instability (MISI; Mercer, 1978; Schoof, 2007; Favier et al., 2014) can unfold if the grounding line is situated on a reverse-sloping bed. Secondly, if the ice shelves buttressing the grounding line have disintegrated due to calving or melting, and large ice cliffs become exposed, runaway cliff calving might lead to the marine ice cliff instability (MICI; Pollard et al., 2015). DeConto and Pollard (2016) carried out past and future simulations of the Antarctic ice sheet with cliff calving implemented as a step function with a discussed but rather ad hoc upper limit of $5\,\mathrm{km\,a^{-1}}$ as well as an additional hydrofracturing process that attacks the ice shelves. Edwards et al. (2019) did further analysis and compared the simulations of mid-Pliocene ice retreat (about 3 million years ago), where sea level was 5–20 m higher than present day, to observations. Given the uncertainty in many ice sheet parameters, uncertainties in air and ocean temperature forcing as well as uncertainty in determining Pliocene sea level, agreement between simulations and observations could be achieved even without MICI. Calving rates larger than $5\,\mathrm{km\,a^{-1}}$ were not considered, but it is clear that using one of the recently derived calving parametrizations with calving rates up to at least $65\,\mathrm{km\,a^{-1}}$ (see Fig. 1) would result in too much and too fast ice retreat. An upper limit on the calving rates appears to be necessary.

So far, the calving rate cut-off has been an ad hoc assumption. However, this upper limit should correspond to some physical process that is responsible for limiting calving rates. We propose that ice mélange, a mix of icebergs and sea ice that is found in many glacial embayments, gives rise to a negative feedback on calving rates.

Observations in Store Glacier and Jakobshavn Glacier in Greenland have shown that in the winter, when sea ice is thick, ice mélange prevents calving (Walter et al., 2012; Xie et al., 2019). This has also been reproduced in modelling studies of grounded marine glaciers (Krug et al., 2015; Todd et al., 2018, 2019): back stresses from the mélange reduce the stresses in the glacier terminus, thereby limiting crevasse propagation and reducing calving rates or preventing calving completely. There is a large uncertainty in the value of mélange back stresses; values given in the literature range between 0.02–3 MPa (Walter et al., 2012; Krug et al., 2015; Todd et al., 2018). Mélange back stress increases with L/W, the ratio of mélange length to the width of the confining channel (Robel, 2017; Burton et al., 2018; Amundson and Burton, 2018). The presence of pinning points where the mélange grounds can also increase the back pressure. Seasonality of basal and surface melting and resulting thinning of the ice mélange are other important parameters for mélange back stress. In addition to the reduced stresses caused by the back stress of the mélange, the presence of mélange may prevent a full-thickness iceberg from rotating away from the terminus, especially if the glacier is thicker than floatation thickness (Amundson et al., 2010). Tensile-failure-based calving (Mercenier et al., 2018) is likely to produce full-thickness icebergs and may be hindered significantly by mélange. Shear-failure-based calving (Schlemm and Levermann, 2019) is more likely to produce many smaller icebergs (break-up occurs through many small, interacting fractures at the foot of the terminus) and might be less influenced by mélange. Ice mélange is also relevant for calving from ice shelves in Antarctica: the presence of mélange stabilizes rifts in the ice shelf and can prevent tabular icebergs from separating from the ice shelf (Rignot and MacAyeal, 1998; Khazendar et al., 2009; Jeong et al., 2016).

We propose a negative feedback between calving rate and mélange thickness: a glacier terminus with high calving rates produces a lot of icebergs, which become part of the ice

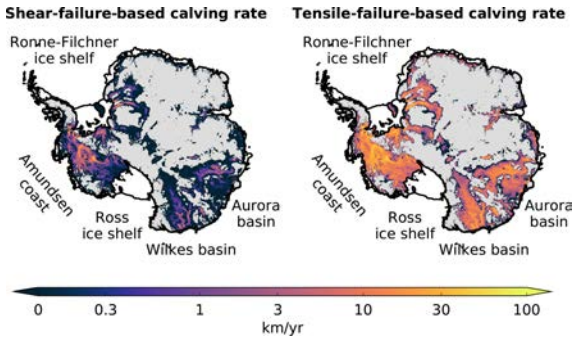

Figure 1. Potential shear-failure-based calving rates (Eq. 16) and tensile-failure-based calving rates (Eq. 15) in the grounded, marine regions of the Antarctic ice sheet. Floating ice is shown in white and grounded ice above sea level in grey. In the marine regions, ice is assumed to be at floatation thickness, which gives a minimal estimate of the potential calving rates. Estimates for shear calving rates go up to $65\,\mathrm{km\,a^{-1}}$, and estimates for tensile calving rates go up to $75\,\mathrm{km\,a^{-1}}$. If the grounding line retreat is faster than the speed with which the glacier terminus thins to floatation, calving rates could be even larger. Imposing an upper bound on the calving rates is necessary to prevent unrealistic, runaway ice loss.

mélange in front of the glacier. The thicker the mélange is, the stronger it buttresses the glacier terminus, leading to reduced calving rates. In Sect. 2, we show that with a few simple assumptions, this negative feedback between calving rate and mélange thickness leads to an upper limit on the calving rates. Section 3 shows that the model can extend beyond the steady state. Application to two calving parametrizations and possible simplifications are discussed in Sect. 4, and in Sect. 5 the mélange-buttressed calving rates are applied in an idealized glacier set-up.

2 Derivation of an upper limit to calving rates due to mélange buttressing

Mélange can prevent calving in two ways: first, in the winter, additional sea ice stiffens and fortifies the mélange and can thus inhibit calving, for example of Greenland glaciers (Amundson et al., 2010; Todd and Christoffersen, 2014; Krug et al., 2015). Secondly, a weaker mélange can still prevent a full-thickness iceberg from rotating out (Amundson et al., 2010) and thus prevent further calving. Ice sheet models capable of simulating the whole Greenland or Antarctic ice sheet over decadal to millennial timescales cannot resolve the stresses at individual calving glacier termini and often do not resolve seasonal variations in forcing. Therefore, we need a model of mélange-buttressed calving that is dependent on the geometries of the embayment and the ice sheet averaged over the year.

To this end, we start by assuming a linear relationship between mélange thickness and the reduction in the calving rate:

$$C = \left(1 - \frac{d_{\mathrm{cf}}}{\gamma H}\right) C^*, \tag{1}$$

where C^* is a calving rate derived for an unbuttressed glacier terminus (Morlighem et al., 2016; Mercenier et al., 2018; Schlemm and Levermann, 2019), and C is the reduced calving rate caused by mélange buttressing. H is the ice thickness at the glacier terminus, and d_{cf} is the mélange thickness at the calving front. In the absence of mélange, $d_{\mathrm{cf}} = 0$, the calving rate is not affected. As the mélange thickness increases, the calving rate is reduced, and when the mélange thickness equals a specific fraction γ of the ice thickness H, calving is completely suppressed. The value of γ may depend on the stiffness and compactness of the mélange and on how fractured the calving front is.

In order to estimate the mélange thickness at the calving front, d_{cf}, we assume a glacier terminating in an embayment already filled with ice mélange, where the mélange does not necessarily need to extend all the way to the embayment exit. Furthermore, we assume that the mélange properties are constant over the entire embayment and that the mélange thickness thins linearly along the flow direction (Fig. 2). The embayment area is given by A_{em}, its width at the calving front by W_{cf}, and its width at the exit by W_{ex}. The calving rate C is assumed to be equal to the ice flow u_{cf} so that the calving front remains at a fixed position. As the mélange thins on its way to the embayment exit, it has an exit thickness d_{ex} and an exit velocity u_{ex} at which mélange and icebergs are transported away by ocean currents (see also Appendix B). We consider a mélange volume $V = A_{\mathrm{em}}\overline{d}$, where $\overline{d}$ is the average mélange thickness. The overall rate of change in the mélange volume is given by

$$\frac{\mathrm{d}V}{\mathrm{d}t} = W_{\mathrm{cf}} H C - W_{\mathrm{ex}} d_{\mathrm{ex}} u_{\mathrm{ex}} - m A_{\mathrm{em}}, \tag{2}$$

where the first term corresponds to mélange production at the calving front, the second term corresponds to mélange exiting into the ocean, and the third term corresponds to mélange loss through melting (assuming an average melt rate m). Assuming a steady state of mélange production and loss resulting in a constant mélange geometry ($\mathrm{d}V/\mathrm{d}t = 0$), we can solve Eq. (2) for d_{ex}:

$$d_{\mathrm{ex}} = \frac{W_{\mathrm{cf}} H C - m A_{\mathrm{em}}}{W_{\mathrm{ex}} u_{\mathrm{ex}}}. \tag{3}$$

This equation only has a physical solution if $m A_{\mathrm{em}} < W_{\mathrm{cf}} H C$, which implies that melting is small enough that mélange actually reaches the embayment exit. If this is not given, mélange may still exist, but it will not reach the embayment exit, and the above inequality becomes a condition on the mélange length. Assuming a viscoplastic rheology and quasi-static flow of ice mélange, Amundson and Burton (2018) found that mélange thinning along the embayment length is given by an implicit exponential function. A linear approximation gives

$$d_{\mathrm{cf}} = \beta d_{\mathrm{ex}}, \quad \beta = b_0 + b_1 \mu_0 L_{\mathrm{em}} / \overline{W}, \tag{4}$$

where μ_0 is the internal friction of the mélange, b_0 and b_1 are constants slightly larger than 1, and $\overline{W}$ is the average embayment width (for more details see Appendix A). Then the mélange thickness at the calving front is given as

$$d_{\mathrm{cf}} = a C H - d_{\mathrm{m}}, \quad \text{with } a = \frac{W_{\mathrm{cf}}}{W_{\mathrm{ex}}} \frac{\beta}{u_{\mathrm{ex}}}, \quad d_{\mathrm{m}} = \beta \frac{m A_{\mathrm{em}}}{W_{\mathrm{ex}} u_{\mathrm{ex}}}, \tag{5}$$

where d_{m} is the mélange thickness lost to melting; a has the units of an inverse calving rate and is related to the upper bound on calving rates in Eq. (7). Inserting Eq. (5) into Eq. (1), we get

$$C = \left(1 + \frac{d_{\mathrm{m}}}{\gamma H}\right) \frac{C^*}{1 + \widetilde{a}\, C^*}, \quad \text{with } \widetilde{a} = a \gamma^{-1}. \tag{6}$$

Neglecting melting for simplicity, we get

$$C = \frac{C^*}{1 + \widetilde{a}\, C^*} = \frac{C^*}{1 + C^*/C_{\max}}. \tag{7}$$

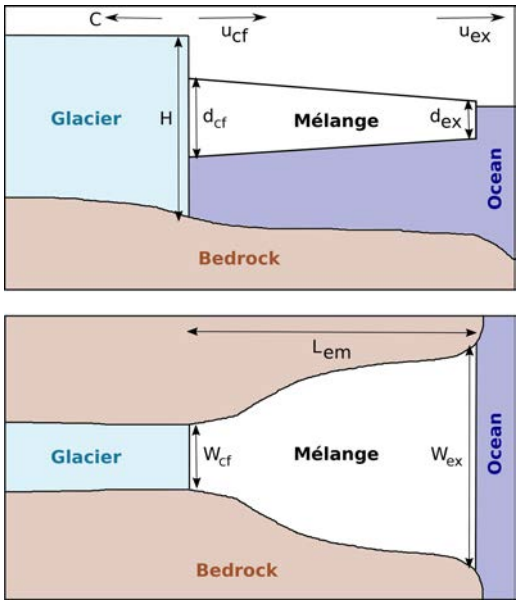

Figure 2. Geometry of the glacier terminus, ice mélange, and embayment as a side view and a top view. The side view shows the ice thickness H, the calving front thickness d_{cf}, and exit thickness d_{ex} of the ice mélange as well as the calving rate C and the mélange exit velocity u_{ex}. The plan view shows the embayment width at the calving front W_{cf} and the embayment exit width W_{ex} as well as the length of the embayment L_{em}. The mélange does not necessarily need to extend all the way to the embayment exit: if it is shorter, then L_{em} donates the mélange length and W_{ex} the width of the embayment at the position where the mélange ends.

This function is linear, $C \approx C^*$, for small unbuttressed calving rates ($C^* \ll C_{max} = \widetilde{a}^{-1}$), and the buttressed calving rate C saturates at an upper limit $C_{max} = \widetilde{a}^{-1}$ for large unbuttressed calving rates ($C^* \gg C_{max} = \widetilde{a}^{-1}$). This means that the parameter $\widetilde{a}$ can be considered to be the inverse maximum calving rate, $C_{max} = \widetilde{a}^{-1}$, which is dependent on the embayment geometry, mélange flow properties, and the embayment exit velocity. If the unbuttressed calving rate, C^*, is small compared to the upper bound C_{max}, there is little buttressing. If C^* is of the same order of magnitude or larger than C_{max}, there is significant buttressing (see Fig. 5). Including melt of the mélange leads to higher calving rates because melting thins the mélange and weakens the buttressing it provides to the calving front.

Rather than imposing an upper bound on the calving rates as an ad hoc cut-off as done by DeConto and Pollard (2016) and Edwards et al. (2019), mélange buttressing gives a natural upper bound on the calving rate, which is reached smoothly. The value of the upper bound can be different for each glacier depending on the embayment geometry and may change seasonally in accord with mélange properties.

According to Eqs. (5) and (7), the limit on calving rates is a function of embayment geometry and mélange properties:

$$C_{max} = \frac{W_{ex}}{W_{cf}} \left(b_0 + b_1 \mu_0 \frac{L_{em}}{\overline{W}} \right)^{-1} \gamma u_{ex}. \tag{8}$$

Since C_{max} is proportional to W_{ex}/W_{cf}, embayments that become narrower at some distance from the calving front experience stronger mélange buttressing and consequently have smaller upper limits than embayments that are widening towards the ocean. Also the longer the embayment is compared to the average embayment width ($L_{em}/\overline{W}$), the smaller the upper limit is, even though friction between the mélange and the embayment walls has not been taken explicitly into account. Previous studies have already shown this for the mélange back stress (Burton et al., 2018; Amundson and Burton, 2018). Fast ocean currents or strong wind forcing at the embayment exit may lead to fast export of mélange (fast exiting velocities u_{ex}) and hence reduced mélange buttressing. Melting of the mélange from below will also reduce mélange buttressing and hence increase C_{max}. The stronger the internal friction of the mélange (μ_0), the larger the buttressing effect.

It can be instructive to consider the force per unit width at the calving front as given by Eq. (10) in Amundson and Burton (2018) with the mélange thickness given by Eq. (5) derived above:

$$\begin{aligned} \frac{F}{W} &= \frac{1}{2}\rho_i \left(1 - \frac{\rho_i}{\rho_w}\right)\left(1 - \frac{d_{ex}}{d_{cf}}\right) d_{cf}^2 \\ &= \frac{1}{2}\rho_i \left(1 - \frac{\rho_i}{\rho_w}\right)\left(b_0 + b_1\mu_0 \frac{L_{em}}{\overline{W}} - 1\right) \\ &\quad \left(\frac{HC^*}{1 + C^* \frac{W_{cf}}{W_{ex}\gamma\, u_{ex}} \left(b_0 + b_1\mu_0 \frac{L_{em}}{\overline{W}}\right)} \frac{W_{cf}}{W_{ex}u_{ex}} - \frac{mA_{em}}{W_{ex}u_{ex}} \right)^2. \end{aligned} \tag{9}$$

3 Beyond a steady-state solution

The mélange buttressing model derived in Sect. 2 assumes mélange to be in a steady state with a fixed mélange geometry. This implies a fixed calving front position. This assumption is not fulfilled if glacier retreat is considered. Therefore it is worthwhile to go beyond the steady-state solution. If the mélange geometry changes in time, the change in the mélange volume can be expressed as

$$\frac{dV}{dt} = \frac{d}{dt} \int_0^{L(t)} dx\ W(x)\, d(x,t), \tag{10}$$

where $L(t)$ is the distance between the embayment exit and the calving front, $W(x)$ is the width of the embayment at a distance x from the embayment exit, $d(x,t)$ is the mélange thickness, and the embayment exit is fixed at $x = 0$. This expression is equal to the sum of mélange production and loss

terms given in Eq. (2). By applying the Leibniz integral rule to the volume integral of Eq. (10) as rewriting the mélange production and loss terms as functions of time and calving front position, Eq. (2) becomes

$$W_{\mathrm{L}}HC - W_0 d_0 u_{\mathrm{ex}} - m\int_0^{\mathrm{L}} \mathrm{d}x\ W(x) = W_{\mathrm{L}}\beta d_0 \cdot \frac{\mathrm{d}}{\mathrm{d}t}L + \left(\int_0^{\mathrm{L}} \mathrm{d}x\ W(x)\right) \cdot \frac{\mathrm{d}}{\mathrm{d}t}\left(\beta d_0\right), \tag{11}$$

with $L = L(t)$, $H = H(L(t))$, $C = C(t)$, $d_0 = \mathrm{d}(0,t)$, $W_0 = W(0)$, $W_{\mathrm{L}} = W(L(t))$, and $\beta = \beta(L(t))$. The first three terms on the left-hand side are the mélange production through calving, the mélange loss at the embayment exit, and the mélange melting, respectively, and the right-hand side is the rewritten volume integral. If the embayment geometry $W(x)$ and the ice thickness at the calving front $H(L(t))$ are known, the calving rate $C(t)$ is given by

$$C(t) = \left(1 - \frac{\beta(L(t))\mathrm{d}(0,t)}{\gamma H(L(t))}\right) C^*, \tag{12}$$

and if an equation for the evolution of the mélange length $L(t)$ is assumed, this differential equation for $d(0,t)$ can be solved. We consider two cases for the evolution of $L(t)$: first, a constant mélange length where the mélange retreats with the calving front, and second, mélange pinned to the embayment exit so that the mélange length grows with the rate of the glacier retreat. We now consider an idealized set-up with constant ice thickness, $H(x) = H$, as well as constant embayment width, $W(x) = W$. Equations (11)–(14) are solved numerically for the parameter values $H = 1000\,\mathrm{m}$, $W = 10\,\mathrm{km}$, $\mu = 0.3$, $\gamma = 0.2$, $C^* = 3\,\mathrm{km\,a^{-1}}$, $u_{\mathrm{ex}} = 100\,\mathrm{km\,a^{-1}}$, $b_0 = 1.11$, and $b_1 = 1.21$ and the initial conditions $L(0) = 10\,\mathrm{km}$ and $d(0) = 10\,\mathrm{m}$. We consider a scenario without mélange melting, $m = 0$, and a scenario with mélange melting, where the melt rate is set to $m = 10\,\mathrm{m\,a^{-1}}$.

3.1 Constant mélange length

First, we assume a constant mélange length:

$$\frac{\mathrm{d}}{\mathrm{d}t}L(t) = 0. \tag{13}$$

This might be either because the calving front does not move (ice flow equals calving rate) or because the mélange is not pinned to the embayment exit and retreats with the calving front, keeping a constant length.

The solutions for the force per unit width at the calving front ($F(t)/W$), mélange thickness at the embayment exit ($d(0,t)$), mélange thickness at the calving front ($d(L(t),t)$), and the resulting buttressed calving rate ($C(t)$) are shown in Fig. 3. The initial conditions chosen do not correspond to a steady-state solution, but the mélange equilibrates quickly, with the free-evolution solution reaching the constant steady-state solution in less than 6 months of simulation time. If melting is included, the mélange is thinner, and hence the final calving rate is slightly larger. The force per unit width is small compared to other mélange models (Amundson and Burton, 2018; Burton et al., 2018), but it is not an integral part of the model, rather only a diagnostic. A force of about $10^7\,\mathrm{N\,m^{-1}}$ (Amundson et al., 2010) prevents icebergs from rotating out and would inhibit calving. A weaker mélange merely reduces calving rates as seen here. Also the set-up here is of a rather short mélange ($L/W = 1$), and hence the mélange is not very thick.

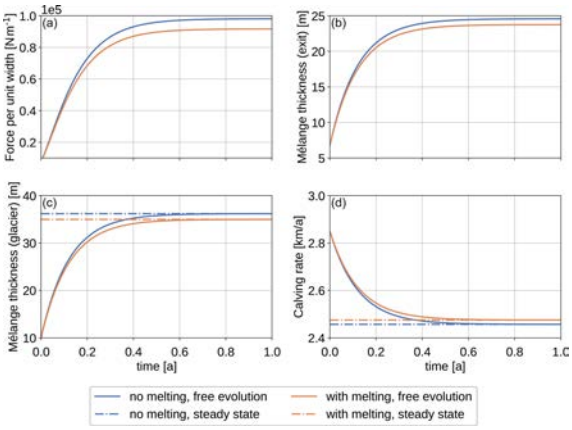

Figure 3. Panels **(a)** and **(b)** show the numerical solutions of force per unit width, $F(t)/W$, and mélange thickness at the embayment exit, $d(0,t)$, given by Eqs. (11)–(14) if mélange length is assumed to be constant. Two scenarios are considered: without melting (blue line) and with melting (orange). Panels **(c)** and **(d)** show the mélange thickness at the calving front, $d(L(t),t)$, and the resulting buttressed calving rate, $C(t)$. The solution with free evolution of the mélange geometry (continuous line) is contrasted with the steady-state solution obtained by plugging the mélange length, $L(t)$, into Eqs. (5) and (6), respectively (dashed line), showing equilibration of the mélange in less than a year.

3.2 Mélange pinned to embayment exit

Second, we assume that the mélange is pinned to the embayment exit; hence the mélange length grows with the rate of glacier retreat:

$$\frac{\mathrm{d}}{\mathrm{d}t}L(t) = C(t) - u_{\mathrm{cf}}(t), \tag{14}$$

where the ice flow velocity at the calving front, $u_{\mathrm{cf}}(t)$, depends on the bed topography and the ice dynamics. In this simplified set-up, we neglect ice flow by setting $u_{\mathrm{cf}} = 0$. The solutions for mélange length ($L(t)$), mélange thickness at the embayment exit ($d(0,t)$), mélange thickness at the calving front ($d(L(t),t)$), and the resulting buttressed calving rate

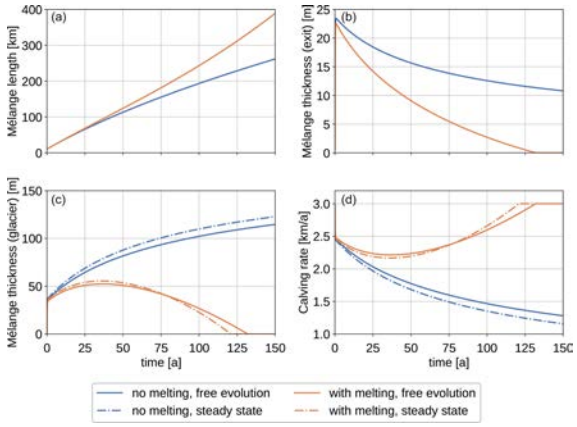

Figure 4. Panels **(a)** and **(b)** show the numerical solutions of mélange length, $L(t)$, and mélange thickness at the embayment exit, $d(0,t)$, given by Eqs. (11)–(14). Two scenarios are considered: without melting (blue line) and with melting (orange). Panels **(c)** and **(d)** show the mélange thickness at the calving front, $d(L(t),t)$, and the resulting buttressed calving rate, $C(t)$. The solution with free evolution of the mélange geometry (continuous line) is contrasted with the steady-state solution obtained by plugging the mélange length, $L(t)$, into Eqs. (5) and (6), respectively, (dashed line).

($C(t)$) are shown in Fig. 4. In the scenario without melting, mélange length and thickness at the calving front increase, while mélange thickness at the embayment exit and buttressed calving rate decrease. If melting of mélange is considered, the mélange thickness at the calving front increases initially and then decreases until the embayment is mélange-free since the volume of mélange melted increases with mélange area. A comparison between these solutions, where the mélange geometry is free to evolve, and the corresponding steady-state solution for mélange thickness at the calving front and the calving front, obtained by plugging the mélange length, $L(t)$, into Eqs. (5) and (6), respectively, shows good agreement (see Fig. 4c and d). As in the previous example the mélange equilibrates quickly, and the free-evolution solution follows the steady-state solution closely in the remaining time. This justifies the adaptive approach discussed in Sect. 5.2.

4 Application to stress-based calving parametrizations

Bassis and Walker (2011) showed that ice cliffs with a glacier freeboard (ice thickness minus water depth) exceeding $\approx$ 100 m are inherently unstable due to shear failure. However, smaller ice cliffs calve off icebergs as well. Mercenier et al. (2018) derived a tensile-failure-based calving parametrization for calving fronts with freeboards below this stability limit, while Schlemm and Levermann (2019) derived a shear-failure-based calving parametrization for calving fronts with freeboards exceeding the stability limit.

4.1 Tensile-failure-based calving

A calving relation based on tensile failure was derived by Mercenier et al. (2018), who used the Hayhurst stress as a failure criterion to determine the position of a large crevasse that would separate an iceberg from the glacier terminus and calculated the timescale of failure using damage propagation. The resulting tensile calving rate is given by

$$C_{\mathrm{t}}^{*} = B \cdot \left(1 - w^{2.8}\right) \cdot \left((0.4 - 0.45(w - 0.065)^2) \cdot \rho_{\mathrm{i}} g H - \sigma_{\mathrm{th}}\right)^{\mathrm{r}} \cdot H, \qquad (15)$$

with effective damage rate $B = 65\,\mathrm{MPa}^{-\mathrm{r}}\,\mathrm{a}^{-1}$, stress threshold for damage creation $\sigma_{\mathrm{th}} = 0.17\,\mathrm{MPa}$, constant exponent $r = 0.43$, ice density $\rho_{\mathrm{i}} = 1020\,\mathrm{kg\,m}^{-3}$, gravitational constant $g = 9.81\,\mathrm{m\,s}^{-2}$, and the relative water depth $w = D/H$. This calving relation was derived for glacier fronts with a glacier freeboard smaller than the stability limit.

4.2 Shear-failure-based calving

An alternative calving relation based on shear failure of an ice cliff was derived in Schlemm and Levermann (2019), where shear failure was assumed in the lower part of an ice cliff with a freeboard larger than the stability limit. The resulting shear calving rate is given by

$$C_{\mathrm{s}}^{*} = C_0 \cdot \left(\frac{F - F_{\mathrm{c}}}{F_{\mathrm{s}}}\right)^{\mathrm{s}} \qquad (16)$$

$$F_{\mathrm{s}} = \left(114.3(w - 0.3556)^4 + 20.94\right)\,\mathrm{m} \qquad (17)$$

$$F_{\mathrm{c}} = (75.58 - 49.18\,w)\,\mathrm{m} \qquad (18)$$

$$s = 0.1722 \cdot \exp(2.210\,w) + 1.757, \qquad (19)$$

with relative water depth $w \equiv D/H < 0.9$ and glacier freeboard $F \equiv H - D = H \cdot (1 - w)$. F_{c} is the critical freeboard above which calving occurs, F_{s} is a scaling parameter, and s is a nonlinear exponent. The scaling parameter C_0 is given as $C_0 = 90\,\mathrm{m\,a}^{-1}$, but this value is badly constrained, and therefore C_0 can be considered a free parameter which parametrizes the uncertainty in the time to failure. This calving law assumes that there is no calving for freeboards smaller than the critical freeboard $F < F_{\mathrm{c}}$.

Plugging the calving relation, Eq. (16), into the mélange-buttressed calving rate given by Eq. (7) and expanding, it can be shown that the value of the upper bound $C_{\max}$ has a greater influence on the resulting calving rates than the scaling parameter C_0: let us call the dimensionless freeboard-dependent part of the cliff calving relation

$$\widetilde{C}_{\mathrm{s}} = \left(\frac{F - F_{\mathrm{c}}}{F_{\mathrm{s}}}\right)^{\mathrm{s}}; \qquad (20)$$

then the buttressed calving rate is

$$C_s = \frac{\widetilde{C}_s}{\frac{1}{C_0} + \frac{\widetilde{C}}{C_{max}}}. \quad (21)$$

Then if $1 \ll \widetilde{C}$,

$$C_s = C_{max} - \frac{C_{max}^2}{\widetilde{C} C_0}. \quad (22)$$

For small $\widetilde{C}$ the choice of scaling parameter C_0 influences the final calving rate C, but for large $\widetilde{C}$, the upper bound C_{max} determines the resulting calving rate. Since the scaling parameter C_0 is difficult to constrain and has little influence on the mélange-buttressed calving rate, it makes sense to use a fixed value, e.g. $C_0 = 90\,\mathrm{m\,a^{-1}}$, and treat only the upper bound C_{max} as a free parameter (which is dependent on the embayment geometry and mélange properties).

4.3 Comparison of the calving parametrizations

A comparison of the two stress-based calving rates can be divided into four parts (see Fig. 5a):

1. According to the calving parametrizations considered here (Eqs. 15 and 16), glacier fronts with very small freeboards ($< \approx 20\,\mathrm{m}$) do not calve.

2. For glacier freeboards below the stability limit of $\approx 100\,\mathrm{m}$, there is only tensile calving with calving rates up to $\approx 10\,\mathrm{km\,a^{-1}}$ and no shear calving.

3. Above the stability limit, shear calving rates increase slowly at first but speed up exponentially and equal the tensile calving rates at freeboards between 200–300 m and calving rates between 15–60 $\mathrm{km\,a^{-1}}$. There is a spread in these values because both calving rates depend on the water depth as well as the freeboard.

4. For even larger freeboards, shear calving rates have a larger spread than tensile calving rates and much larger values for cliffs at floatation.

A comparison of the buttressed calving rates can be classified in the same way (see Fig. 5b–d), where the only difference is that large calving rates converge to a value just below the upper limit C_{max}, and hence the difference between tensile and shear calving rates for large freeboards is smaller.

Summarizing, there are two different calving parametrizations based on tensile and shear failure and derived for glacier freeboards below and above the stability limit, respectively. It might seem obvious that one should simply use each calving law in the range for which it was derived. However, that would lead to a large discontinuity in the resulting calving rate because the tensile calving rate is much larger at the stability limit than the shear calving rate. Another possibility is to use each parametrization in the range for which it gives the larger calving rate. Since it is likely that in nature large ice cliffs fail due to a combination of failure modes, it also seems reasonable to use a combination of tensile and shear calving rates.

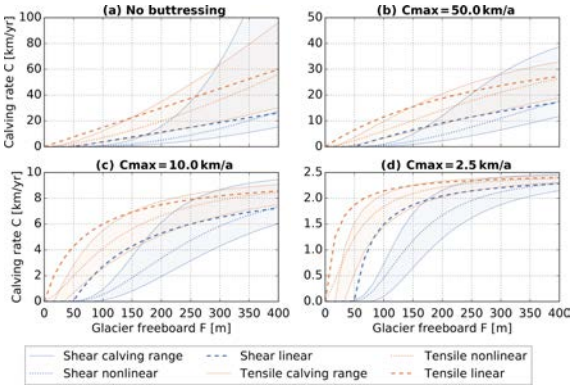

Figure 5. Calving rates as a function of glacier freeboard (ice thickness – water depth) in the unbuttressed case and for a range of upper bounds C_{max}. Shear calving and tensile calving rates depend also on the water depth: two lines are shown for each configuration, the lower line for a dry cliff ($w = 0.0$) and the upper line for a cliff at floatation ($w = 0.8$). This spans the range of possible calving rates for a given freeboard. Also shown are the nonlinear (dotted line) and linear (dashed lines) approximations to these calving laws. In the tensile case, calving commences with freeboard $F = 0$, while shear calving only happens for freeboards larger $F_c \approx 50\,\mathrm{m}$.

In the context of the Marine Ice Cliff Instability (MICI) hypothesis, one would expect a sudden and large increase in calving rates for ice cliffs higher than the stability limit. Despite a nonlinear increase in calving rates in the unbuttressed case, neither of the two stress-based calving parametrizations (Mercenier et al., 2018; Schlemm and Levermann, 2019) nor a combination of them shows discontinuous behaviour at the stability limit.

4.4 Simplified calving relations

There are uncertainties in both calving laws because a dominating failure mode is assumed (shear and tensile failure, respectively), while in reality failure modes are likely to interact. Also, in the calving laws ice is assumed to be previously undamaged, whereas a glacier is usually heavily crevassed and therefore weakened near the terminus. In addition, shear calving has a large uncertainty with respect to the time to failure, which leads to uncertainty in the scaling parameter C_0. These uncertainties, together with the observation that the upper limit C_{max} seems to have a stronger influence on resulting calving rates than the choice of calving law, provide a good reason to consider simplifying these calving laws. The important distinction between shear and tensile calving is that shear calving has a much larger critical freeboard: for small freeboards ($F < 100\,\mathrm{m}$), we have tensile calving but no

shear calving. Since the mélange-buttressed calving rate is linear in the calving rates for small calving rates, this distinction remains in the buttressed calving rates (see Fig. 5). However, for larger freeboards the calving rates approach the upper limit no matter which calving law was chosen. This distinction should be conserved in the simplified calving relations. The dependence of the calving rate on water depth is important in the unbuttressed case (see Fig. 5a): there is a large range between calving rates for the same freeboard and different relative water depths because larger relative water depth implies a larger overall depth. For the same glacier freeboard, this means a larger ice thickness and therefore larger stresses in the ice column, implying a larger calving rate. But in the mélange-buttressed case, large calving rates are more strongly buttressed than small calving rates. Thus the large range of possible calving rates for a given glacier freeboard is transformed into a much smaller range so that water depth becomes less important (see Fig. 5b–d). Therefore we consider simplifications of the calving relations where we average over the water depth and further simplify. This is done mostly for illustrative purposes.

Take the shear calving relation:

$$C_{\mathrm{s}}^{*} = C_0 \cdot \left(\frac{F - F_{\mathrm{c}}}{F_{\mathrm{s}}}\right)^{\mathrm{s}}, \tag{23}$$

where $C_0 = 90\,\mathrm{m\,a^{-1}}$, $s(w) \in [1.93, 3.00]$, $F_{\mathrm{c}}(w) \in [30.9, 75.0]\,\mathrm{m}$, and $F_{\mathrm{s}}(w) \in [21.0, 31.1]\,\mathrm{m}$. In choosing round values within these intervals, we can simplify the relation.

$$C_{\mathrm{s,\ nonlin}}^{*} = 90\ \mathrm{m\,a^{-1}} \cdot \left(\frac{F - 50\,\mathrm{m}}{20\,\mathrm{m}}\right)^{2} \tag{24}$$

Because the exponent s is on the smaller end of the possible values, we chose a smaller value for F_{s} to get an approximation that lies well within the range of the full-cliff calving relation, though it lies at the lower end (see Fig. 5). An even simpler linear approximation

$$C_{\mathrm{s,\ lin}}^{*} = 75\,\mathrm{a^{-1}} \cdot (F - 50\,\mathrm{m}) \tag{25}$$

overestimates the calving rates for small freeboards ($F < 200\,\mathrm{m}$) and underestimates for large freeboards ($F > 600\,\mathrm{m}$).

The tensile calving relation can be written as

$$C_{\mathrm{t}}^{*} = a(w)(b(w)F - \sigma_{\mathrm{th}})^{0.43} \cdot F \approx c \cdot F^{1.5} \tag{26}$$

and can be fitted with a power function

$$C_{\mathrm{t,\ nonlin}}^{*} = 7\,\mathrm{m^{-0.5}a^{-1}} \cdot F^{1.5} \tag{27}$$

or a linear function

$$C_{\mathrm{t,\ lin}}^{*} = 150\,\mathrm{a^{-1}} \cdot F. \tag{28}$$

Here we neglect the small offset in freeboard that tensile calving has. This gives us two kinds of simplified calving relations to compare: one that begins calving immediately and one that only calves off cliffs larger than a certain critical freeboard. For both we have a linear approximation that overestimates small calving rates and a nonlinear approximation that lies well within the original spread of calving rates (see Fig. 5).

5 Mélange-buttressed calving in an idealized glacier set-up

We consider a Marine Ice Sheet Model Intercomparison Project (MISMIP+)-like glacier set-up (Cornford et al., 2020) that is symmetric about $x = 0$ and has periodic boundary conditions on the fjord walls. The glacial valley has an average bedrock depth of 200 m and a width of 40 km and experiences a constant accumulation of $1.5\,\mathrm{m\,a^{-1}}$ (see Fig. 6). The set-up has rocky fjord walls, and where the bedrock wall is below sea level, there is grounded ice resting on it. This grounded ice does not retreat during the calving experiments and forms the embayment. Ice flow is concentrated in the middle of the channel, where the bedrock is significantly deeper. Since there is no ice reservoir at the top of the glacier, this set-up can also be considered to be a model for a mountain glacier. The experiments were done with the Parallel Ice Sheet Model (PISM; Bueler and Brown, 2009; Winkelmann et al., 2011), which uses the shallow ice approximation (Hutter, 1983) and the shallow shelf approximation (Weis et al., 1999). We use Glen's flow law in the isothermal case and a pseudoplastic basal friction law (the PISM authors, 2018). A spin-up simulation was run until it reached a steady-state configuration with an attached ice shelf. During the experiment phase of the simulation, all floating ice is removed at each time step. When the ice shelf is removed, the marine ice sheet instability (MISI) kicks in because of the slightly retrograde bed topography, and the glacier retreats. Calving accelerates this retreat. Experiments were made with no calving (MISI only), mélange-buttressed shear calving, and its nonlinear and linear approximation as well as mélange-buttressed tensile calving and its two approximations. The initial upper bound was varied, $C_{\max} = [2.5, 10.0, 50.0, 500.0]\,\mathrm{km\,a^{-1}}$, where the last upper bound was chosen to be large enough that the calving rates nearly match the unbuttressed calving rates.

5.1 Constant upper bound on calving rates

In this experiment, the upper bound was kept constant even though the glacier retreated and embayment length increased. The buttressing Eq. (7) was derived assuming a steady-state mélange geometry, which implies a fixed mélange geometry. This is the case in this idealized set-up if we assume that mélange length is fixed, and mélange retreats with the calving front, as in Sect. 3.1.

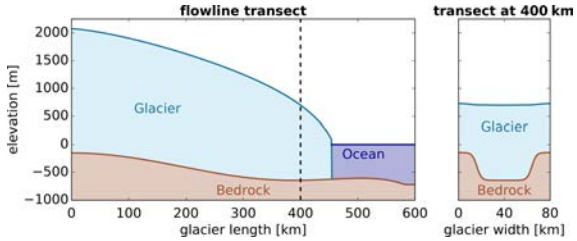

Figure 6. Set-up of the idealized glacier experiments. Only half of the set-up is shown; the glacier is connected to an identical copy on the left to ensure periodic boundary conditions at the ice divide.

Figure 7 shows the simulated glacier retreat. Even without calving in the MISI-only experiment, there is a significant retreat after removing the ice shelves because of the buttressing loss and slightly retrograde bed of the glacier. The glacier retreats from a front position at 440 to 200 km in the first 100 years, after which the retreat decelerates, and the glacier stabilizes at a length of about 130 km. Adding calving leads to additional retreat: the higher the upper bound on the calving rates, the faster the retreat. Shear calving causes less additional retreat than tensile calving because it has small calving rates for freeboards below 150 m. Since the channel is rather shallow, the freeboards are generally small. Only the linear approximation of shear calving has a significant ice retreat because even though it starts only with a freeboard of 50 m, it grows much faster than the actual shear calving or the nonlinear approximation. But it also reaches a stable glacier position when the ice thickness is smaller than the critical freeboard condition. The assumption of tensile calving causes the glacier to retreat much faster. The linear approximation, which has higher calving rates for small freeboards, leads to a faster retreat. For the nonlinear approximation the glacier is close to floatation for most of its retreat, which corresponds to the upper half of the tensile calving range. This approximation gives smaller calving rates and hence slower retreat. None of the tensile calving relations allow the glacier to stabilize. That is to say the minimum freeboard below which an ice front is stable for shear calving is ultimately the stabilizing factor in these simulations.

Figure 8 shows that the effect of mélange buttressing becomes relevant for small values of the export of ice out of the embayment, i.e. for small values of $C_{\max}$. In this limit of strong buttressing, i.e. where the parameterization of Eq. (7) is relevant, the glacier retreat becomes almost independent of the specific calving parameterization.

5.2 An adaptive upper limit on calving rates

Assuming that mélange equilibration is faster than glacier retreat, the upper bound $C_{\max}$ can be calculated as a function of mélange length L_{em}. This is further justified by the discussion in Sect. 3. Here we assume that the position of the embayment exit remains fixed so that the mélange length grows with the same rate with which the glacier retreats. We assume an initial upper bound $C_{\max 0} = [2.5, 10.0, 50.0, 500.0]\,\mathrm{km\,a^{-1}}$ at $t = 0$ and update $C_{\max}$ each simulation year. We perform the same experiments as described above. This adaptive approach leads to much smaller calving rates and slows down the glacier retreat significantly (compare Fig. 9 to Fig. 7). In the case with $C_{\max 0} = 10\,\mathrm{km\,a^{-1}}$ and $C_{\max 0} = 2.5\,\mathrm{km\,a^{-1}}$, the adaptive approach prevents the complete loss of ice. Due to the increase in embayment length, the upper bound in calving rate is reduced down to 30 % of its original value (see Fig. 10).

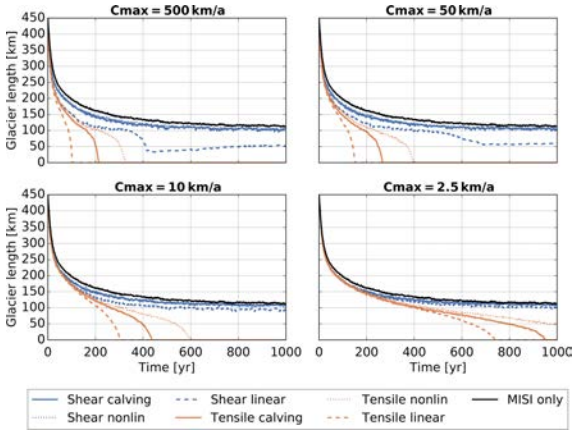

Figure 7. Glacier length time series. Upper left panel shows runs with an upper limit of $C_{\max} = 500\,\mathrm{km\,a^{-1}}$, which is essentially equivalent to the unbuttressed calving rates. Then we have decreasing upper limits, and consequently the glacier retreat slows down.

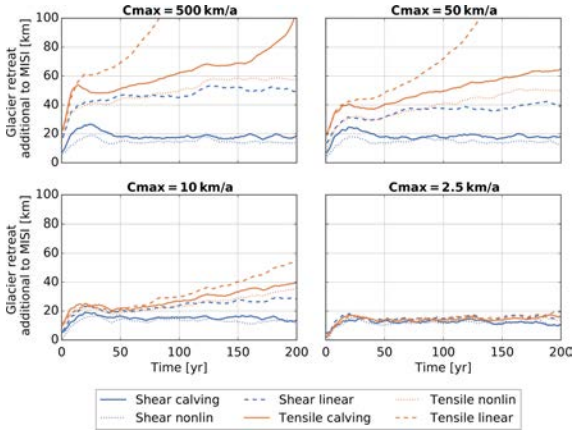

Figure 8. Time series of glacier retreat in addition to the MISI retreat, i.e. retreat caused by calving.

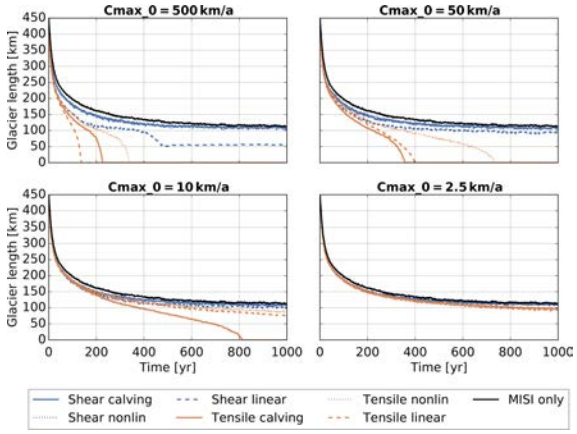

Figure 9. Glacier length time series with an adaptive calving limit.

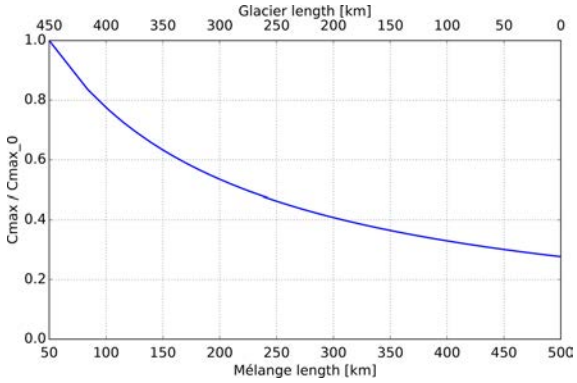

Figure 10. Reduction in the upper limit on calving rates as a function of mélange length and glacier length.

6 Conclusions

We considered mélange buttressing of calving glaciers to be a complement to previously derived calving relations. These calving relations can lead to unrealistically large calving rates. This is a problem with the calving relations and should be further investigated. Backed by evidence for mélange buttressing in observations and numerical simulations, we propose that mélange buttressing may be one mechanism that prevents calving rates from growing too large. The approach here is to provide an equation that uses simple and transparent assumptions to yield a non-trivial relation. The central assumption is that the reduction in calving rates is linear with mélange thickness. Other important factors determining the mélange buttressing are the strength of the sea ice bonding the icebergs together (Robel, 2017) and possibly also iceberg size distribution. The continuum rheology model (Amundson and Burton, 2018) adapted here agrees with discrete models (Burton et al., 2018; Robel, 2017) that mélange buttressing increases with the length-to-width ratio, and that is also a feature found here in Eq. (8). The buttressing is described in the form of a reduced calving rate which is a function of the maximum calving rate as it is derived for the ice front without mélange buttressing. First, we assumed that calving rates decrease linearly with the mélange thickness. Secondly, we assume a steady state between mélange production through calving and mélange loss through melting and exit from the embayment. This implies a fixed calving front position. Using these two assumptions, we derived a mélange-buttressed calving rate, Eq. (7), that is linear for small calving rates and converges to an upper limit $C_{\max}$, which depends on the embayment geometry, mélange flow properties, and the embayment exit velocity. We also went beyond the steady-state solution of mélange buttressing and considered an evolving mélange geometry. We found that mélange equilibration is faster than glacier retreat, which justifies the use of an adaptive approach in which the upper limit $C_{\max}$ is dependent on the mélange geometry.

This framework can be applied to any calving parametrization that gives a calving rate rather than the position of the calving front. We investigated its application to a tensile-failure-based calving rate and to a shear-failure-based calving rate. For small calving rates, the differences between the parametrizations persist in the buttressed case. However, large calving rates converge to the upper limit, and the choice of calving parametrization becomes less important. This suggest that it is possible to simplify the calving parametrizations further, but we show that the simplifications differ for small calving rates, and those differences persist. We illustrated this with a simulation of an idealized glacier. Choice of calving parametrization and choice of upper limit determine the retreat velocity. Following the adaptive approach, glacier retreat leads to a larger embayment and hence larger mélange buttressing and smaller calving rates.

Embayment geometry plays an important role in determining how susceptible glaciers facing similar ocean conditions are to rapid ice retreat: Pine Island Glacier and Thwaites Glacier in West Antarctica face similar ocean conditions in the Amundsen Sea, where the warming ocean (Shepherd et al., 2004, 2018a) leads to the retreat and rifting of their buttressing ice shelves (Jeong et al., 2016; Milillo et al., 2019), and might be susceptible to both MISI and MICI. Pine Island terminates in an embayment about 45 km wide, currently filled by an ice shelf of roughly 60 km length. The upper part of the glacier lies in a straight narrow valley with a width of about 35 km (distances measured on topography and ice thickness maps provided by Fretwell et al., 2013). If Pine Island Glacier lost its current shelf, it would have a long and narrow embayment holding the ice mélange and would therefore experience strong mélange buttressing. In contrast, Thwaites Glacier is more than 70 km wide, and its ice shelf spreads into the open ocean. It has currently no embayment at all, and once it retreats, it lies in a wide basin that can provide little mélange buttressing. Hence, Thwaites Glacier has

a much larger potential for large calving rates and runaway ice retreat (MICI) than Pine Island Glacier.

Ocean temperatures off the coast of Antarctica are mostly sub-zero, with 0.5–0.6 °C warming expected by 2100, while the ocean temperatures off the coast of Greenland are sub-zero in the north but up to 4 °C in the south, with an expected 1.7–2.0 °C warming by 2200 (Yin et al., 2011). This leads to increased mélange melting in Greenland compared to Antarctica and therefore higher upper limits on calving rates in Greenland glaciers that have geometries comparable to Antarctic glaciers. Future ocean warming and intrusion of warm ocean water under the ice mélange increase melting rates and the upper limit on calving rates. This could be another mechanism by which ocean warming increases calving rates.

The concept of cliff calving and a cliff calving instability is not without criticism. According to Clerc et al. (2019), the lower part of the glacier terminus, where shear failure is assumed to occur (Bassis and Walker, 2011; Schlemm and Levermann, 2019), is actually in a regime of thermal softening with a much higher critical stress and thus remains stable for large ice thicknesses. Tensile failure may occur in the shallow upper part of the cliff and initiate failure in the lower part of the cliff (Parizek et al., 2019). The critical subaerial cliff height at which failure occurs depends on the timescale of the ice shelf collapse: for collapse times longer than 1 d, the critical cliff height lies between 170–700 m (Clerc et al., 2019).

The mélange buttressing model proposed here does not depend on the specific calving mechanism, and it is not comprehensive, especially since it is not derived from first principles but from a macroscopic perspective. The advantage of the equation proposed here is the very limited number of parameters.

Appendix A: Mélange thickness gradient

In Sect. 2, the mélange thickness was assumed to thin linearly along the embayment length with $d_{cf} = \beta d_{ex}$. Amundson and Burton (2018) give an implicit exponential relation for the mélange thickness:

$$d_{cf} = d_{ex} \exp\left(\mu_0 \frac{L_{em}}{W} + \frac{d_{cf} - d_{ex}}{2d_{cf}}\right), \tag{A1}$$

where μ_0 is the coefficient of internal friction of the mélange and ranges from about 0.1 to larger than 1. The embayment width, W, is assumed to be constant along the embayment in Amundson and Burton (2018); here we can replace it with the average embayment width. In a linear approximation, Eq. (A1) becomes

$$d_{cf} = d_{ex}\left(1 + \mu_0 \frac{L_{em}}{W} + \frac{d_{cf} - d_{ex}}{2d_{cf}}\right). \tag{A2}$$

This equation has one physical solution for d_{cf}:

$$\begin{aligned} d_{cf} &= d_{ex} \cdot \frac{1}{4} \\ &\left(3 + 2\mu_0 \frac{L_{em}}{W} + \sqrt{1 + 12\mu_0 \frac{L_{em}}{W} + 4\left(\mu_0 \frac{L_{em}}{W}\right)^2}\right) \\ &\approx \beta d_{ex}. \end{aligned} \tag{A3}$$

The parameter β can be linearized to take the form given in Eq. (4), where the parameters b_0 and b_1 are determined by the way of obtaining the linear approximation: completing the square under the square root gives the asymptotic upper limit with $b_0 = 1.5$, $b_1 = 1.0$. Taylor expansion can be used to get a more accurate approximation around a specific value of $\mu_0 L/W$: expansion around $\mu_0 L/W = 0.5$ gives $b_0 = 1.11, b_1 = 1.21$, while expansion around $\mu_0 L/W = 1.0$ gives $b_0 = 1.17$, $b_1 = 1.11$. The choice of linearization parameters b_0 and b_1 should depend on the expected range of values for $\mu_0 L/W$. Figure A1 shows that each of the linear approximations given in the text overestimates β slightly but that it is possible to achieve a small error (<5 %) over a rather large range of values for L/W.

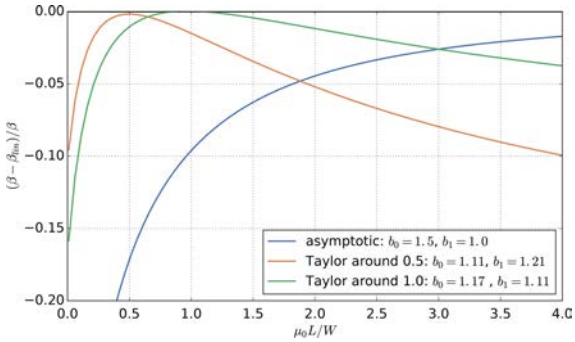

Figure A1. The relative difference between β given by Eq. (A3) and different linear approximations of β.

Appendix B

Overview of the variables used in Sect. 2. The embayment and mélange geometry is illustrated in Fig. 2.

H	ice thickness
C^*, C	unbuttressed and buttressed calving rates
γ	fraction of the ice thickness
d_{cf}	mélange thickness at the calving front
d_{ex}	mélange thickness at the embayment exit
$\overline{d}$	average mélange thickness
V	mélange volume
W_{cf}	embayment width at the calving front
W_{ex}	embayment width at the embayment exit
$\overline{W}$	average embayment width
L_{em}	embayment (mélange) length
A_{em}	embayment (mélange) area
u_{cf}	ice flow velocity at the calving front
u_{ex}	mélange exit velocity
m	average mélange melt rate
β	mélange thinning gradient
μ_0	mélange internal friction
d_m	mélange thickness lost due to melting
a	mélange buttressing parameter
$\widetilde{a}$	inverse of C_{max}
C_{max}	upper limit on calving rates

Code and data availability. Data and code are available from the authors upon request.

Author contributions. Both authors conceived the study and analysed the data. TS developed the basic equations, carried out the experiments, and wrote the manuscript. AL contributed to the writing of the manuscript.

Competing interests. The authors declare that they have no conflict of interest.

Financial support. Tanja Schlemm was funded by a doctoral scholarship of the Heinrich Böll foundation.

The publication of this article was funded by the Open Access Fund of the Leibniz Association.

Review statement. This paper was edited by Kerim Nisancioglu and reviewed by Douglas Benn and two anonymous referees.

References

Amundson, J. M. and Burton, J. C.: Quasi-Static Granular Flow of Ice Mélange, J. Geophys. Res.-Earth, 123, 2243–2257, https://doi.org/10.1029/2018JF004685, 2018.

Amundson, J. M., Fahnestock, M., Truffer, M., Brown, J., Lüthi, M. P., and Motyka, R. J.: Ice mélange dynamics and implications for terminus stability, Jakobshavn Isbræ, Greenland, J. Geophys. Res.-Earth, 115, F01005, https://doi.org/10.1029/2009JF001405, 2010.

Bassis, J. N. and Walker, C. C.: Upper and lower limits on the stability of calving glaciers from the yield strength envelope of ice, P. Roy. Soc. Lond. A. Mat., 468, 913–931, https://doi.org/10.1098/rspa.2011.0422, 2011.

Bassis, J. N., Petersen, S. V., and Mac Cathles, L.: Heinrich events triggered by ocean forcing and modulated by isostatic adjustment, Nature, 542, 332–334, https://doi.org/10.1038/nature21069, 2017.

Benn, D. I., Hulton, N. R., and Mottram, R. H.: "Calving laws", "sliding laws" and the stability of tidewater glaciers, Ann. Glaciol., 46, 123–130, https://doi.org/10.3189/172756407782871161, 2007.

Bueler, E. and Brown, J.: Shallow shelf approximation as a "sliding law" in a thermomechanically coupled ice sheet model, J. Geophys. Res.-Earth, 114, F03008, https://doi.org/10.1029/2008JF001179, 2009.

Burton, J. C., Amundson, J. M., Cassotto, R., Kuo, C.-C., and Dennin, M.: Quantifying flow and stress in ice mélange, the world's largest granular material, P. Natl. Acad. Sci. USA, 115, 5105–5110, https://doi.org/10.1073/pnas.1715136115, 2018.

Church, J. A., Clark, P. U., Cazenave, A., Gregory, J. M., Jevrejeva, S., Levermann, A., Merrifield, M. A., Milne, G. A., Nerem, R. S., Nunn, P. D., Payne, A. J., Pfeffer, W. T., Stammer, D., and Unnikrishnan, A. S.: Sea-Level Rise by 2100, Science, 342, 1445, https://doi.org/10.1126/science.342.6165.1445-a, 2013.

Clerc, F., Minchew, B. M., and Behn, M. D.: Marine Ice Cliff Instability Mitigated by Slow Removal of Ice Shelves, Geophys. Res. Lett., 46, 12108–12116, https://doi.org/10.1029/2019GL084183, 2019.

Cornford, S. L., Seroussi, H., Asay-Davis, X. S., Gudmundsson, G. H., Arthern, R., Borstad, C., Christmann, J., Dias dos Santos, T., Feldmann, J., Goldberg, D., Hoffman, M. J., Humbert, A., Kleiner, T., Leguy, G., Lipscomb, W. H., Merino, N., Durand, G., Morlighem, M., Pollard, D., Rückamp, M., Williams, C. R., and Yu, H.: Results of the third Marine Ice Sheet Model Intercomparison Project (MISMIP+), The Cryosphere, 14, 2283–2301, https://doi.org/10.5194/tc-14-2283-2020, 2020.

DeConto, R. M. and Pollard, D.: Contribution of Antarctica to past and future sea-level rise, Nature, 531, 591–597, https://doi.org/10.1038/nature17145, 2016.

Depoorter, M. A., Bamber, J. L., Griggs, J. A., Lenaerts, J. T. M., Ligtenberg, S. R. M., van den Broeke, M. R., and Moholdt, G.: Calving fluxes and basal melt rates of Antarctic ice shelves, Nature, 502, 89–92, https://doi.org/10.1038/nature12567, 2013.

Edwards, T. L., Brandon, M. A., Durand, G., Edwards, N. R., Golledge, N. R., Holden, P. B., Nias, I. J., Payne, A. J., Ritz, C., and Wernecke, A.: Revisiting Antarctic ice loss due to marine ice-cliff instability, Nature, 566, 58–64, https://doi.org/10.1038/s41586-019-0901-4, 2019.

Enderlin, E. M., Howat, I. M., Jeong, S., Noh, M.-J., Angelen, J. H., and Broeke, M. R.: An improved mass budget for the Greenland ice sheet, Geophys. Res. Lett., 41, 866–872, https://doi.org/10.1002/2013GL059010, 2014.

Favier, L., Durand, G., Cornford, S. L., Gudmundsson, G. H., Gagliardini, O., Gillet-Chaulet, F., Zwinger, T., Payne, A. J., and Le Brocq, A. M.: Retreat of Pine Island Glacier controlled by marine ice-sheet instability, Nat. Clim. Change, 4, 117–121, https://doi.org/10.1038/nclimate2094, 2014.

Franco, B., Fettweis, X., and Erpicum, M.: Future projections of the Greenland ice sheet energy balance driving the surface melt, The Cryosphere, 7, 1–18, https://doi.org/10.5194/tc-7-1-2013, 2013.

Fretwell, P., Pritchard, H. D., Vaughan, D. G., Bamber, J. L., Barrand, N. E., Bell, R., Bianchi, C., Bingham, R. G., Blankenship, D. D., Casassa, G., Catania, G., Callens, D., Conway, H., Cook, A. J., Corr, H. F. J., Damaske, D., Damm, V., Ferraccioli, F., Forsberg, R., Fujita, S., Gim, Y., Gogineni, P., Griggs, J. A., Hindmarsh, R. C. A., Holmlund, P., Holt, J. W., Jacobel, R. W., Jenkins, A., Jokat, W., Jordan, T., King, E. C., Kohler, J., Krabill, W., Riger-Kusk, M., Langley, K. A., Leitchenkov, G., Leuschen, C., Luyendyk, B. P., Matsuoka, K., Mouginot, J., Nitsche, F. O., Nogi, Y., Nost, O. A., Popov, S. V., Rignot, E., Rippin, D. M., Rivera, A., Roberts, J., Ross, N., Siegert, M. J., Smith, A. M., Steinhage, D., Studinger, M., Sun, B., Tinto, B. K., Welch, B. C., Wilson, D., Young, D. A., Xiangbin, C., and Zirizzotti, A.: Bedmap2: improved ice bed, surface and thickness datasets for Antarctica, The Cryosphere, 7, 375–393, https://doi.org/10.5194/tc-7-375-2013, 2013.

Golledge, N. R., Kowalewski, D. E., Naish, T. R., Levy, R. H., Fogwill, C. J., and Gasson, E. G. W.: The multi-millennial Antarctic commitment to future sea-level rise, Nature, 526, 421–425, https://doi.org/10.1038/nature15706, 2015.

Golledge, N. R., Keller, E. D., Gomez, N., Naughten, K. A., Bernales, J., Trusel, L. D., and Edwards, T. L.: Global environmental consequences of twenty-first-century ice-sheet melt, Nature, 566, 65–72, https://doi.org/10.1038/s41586-019-0889-9, 2019.

Hutter, K.: Theoretical Glaciology, D. Reidel Publishing Company/Terra Scientific Publishing Company, https://doi.org/10.1007/978-94-015-1167-4, 1983.

Jeong, S., Howat, I. M., and Bassis, J. N.: Accelerated ice shelf rifting and retreat at Pine Island Glacier, West Antarctica, Geophys. Res. Lett., 43, 11720–11725, https://doi.org/10.1002/2016GL071360, 2016.

Khazendar, A., Rignot, E., and Larour, E.: Roles of marine ice, rheology, and fracture in the flow and stability of the Brunt/Stancomb-Wills Ice Shelf, J. Geophys. Res.-Earth, 114, F04007, https://doi.org/10.1029/2008JF001124, 2009.

Kopp, R. E., DeConto, R. M., Bader, D. A., Hay, C. C., Horton, R. M., Kulp, S., Oppenheimer, M., Pollard, D., and Strauss, B. H.: Evolving Understanding of Antarctic Ice-Sheet Physics and Ambiguity in Probabilistic Sea-Level Projections, Earth's Future, 5, 1217–1233, https://doi.org/10.1002/2017EF000663, 2017.

Krug, J., Durand, G., Gagliardini, O., and Weiss, J.: Modelling the impact of submarine frontal melting and ice mélange on glacier dynamics, The Cryosphere, 9, 989–1003, https://doi.org/10.5194/tc-9-989-2015, 2015.

Levermann, A. and Winkelmann, R.: A simple equation for the melt elevation feedback of ice sheets, The Cryosphere, 10, 1799–1807, https://doi.org/10.5194/tc-10-1799-2016, 2016.

Levermann, A., Albrecht, T., Winkelmann, R., Martin, M. A., Haseloff, M., and Joughin, I.: Kinematic first-order calving law implies potential for abrupt ice-shelf retreat, The Cryosphere, 6, 273–286, https://doi.org/10.5194/tc-6-273-2012, 2012.

Levermann, A., Winkelmann, R., Albrecht, T., Goelzer, H., Golledge, N. R., Greve, R., Huybrechts, P., Jordan, J., Leguy, G., Martin, D., Morlighem, M., Pattyn, F., Pollard, D., Quiquet, A., Rodehacke, C., Seroussi, H., Sutter, J., Zhang, T., Van Breedam, J., Calov, R., DeConto, R., Dumas, C., Garbe, J., Gudmundsson, G. H., Hoffman, M. J., Humbert, A., Kleiner, T., Lipscomb, W. H., Meinshausen, M., Ng, E., Nowicki, S. M. J., Perego, M., Price, S. F., Saito, F., Schlegel, N.-J., Sun, S., and van de Wal, R. S. W.: Projecting Antarctica's contribution to future sea level rise from basal ice shelf melt using linear response functions of 16 ice sheet models (LARMIP-2), Earth Syst. Dynam., 11, 35–76, https://doi.org/10.5194/esd-11-35-2020, 2020.

Mengel, M., Feldmann, J., and Levermann, A.: Linear sea-level response to abrupt ocean warming of major West Antarctic ice basin, Nat. Clim. Change, 6, 71–74, https://doi.org/10.1038/nclimate2808, 2016.

Mercenier, R., Lüthi, M. P., and Vieli, A.: Calving relation for tidewater glaciers based on detailed stress field analysis, The Cryosphere, 12, 721–739, https://doi.org/10.5194/tc-12-721-2018, 2018.

Mercer, J. H.: West Antarctic ice sheet and CO_2 greenhouse effect: a threat of disaster, Nature, 271, 321–325, https://doi.org/10.1038/271321a0, 1978.

Milillo, P., Rignot, E., Rizzoli, P., Scheuchl, B., Mouginot, J., Bueso-Bello, J., and Prats-Iraola, P.: Heterogeneous retreat and ice melt of Thwaites Glacier, West Antarctica, Science Advances, 5, eaau3433, https://doi.org/10.1126/sciadv.aau3433, 2019.

Morlighem, M., Bondzio, J., Seroussi, H., Rignot, E., Larour, E., Humbert, A., and Rebuffi, S.: Modeling of Store Gletscher's calving dynamics, West Greenland, in response to ocean thermal forcing, Geophys. Res. Lett., 43, 2659–2666, https://doi.org/10.1002/2016GL067695, 2016.

Mouginot, J., Rignot, E., Bjørk, A. A., van den Broeke, M., Millan, R., Morlighem, M., Noël, B., Scheuchl, B., and Wood, M.: Forty-six years of Greenland Ice Sheet mass balance from 1972 to 2018, P. Natl. Acad. Sci. USA, 116, 9239–9244, https://doi.org/10.1073/pnas.1904242116, 2019.

Nick, F., van der Veen, C., Vieli, A., and Benn, D.: A physically based calving model applied to marine outlet glaciers and implications for the glacier dynamics, J. Glaciol., 56, 781–794, https://doi.org/10.3189/002214310794457344, 2010.

Parizek, B. R., Christianson, K., Alley, R. B., Voytenko, D., Vaňková, I., Dixon, T. H., Walker, R. T., and Holland, D. M.: Ice-cliff failure via retrogressive slumping, Geology, 47, 449–452, https://doi.org/10.1130/G45880.1, 2019.

PISM: PISM, a Parallel Ice Sheet Model, available at: https://pism-docs.org (last access: 13 June 2020), 2018.

Pollard, D., DeConto, R. M., and Alley, R. B.: Potential Antarctic Ice Sheet retreat driven by hydrofracturing and ice cliff failure, Earth. Planet. Sc. Lett., 412, 112–121, https://doi.org/10.1016/j.epsl.2014.12.035, 2015.

Rignot, E. and MacAyeal, D. R.: Ice-shelf dynamics near the front of the Filchner-Ronne Ice Shelf, Antarctica, revealed by SAR interferometry, J. Glaciol., 44, 405–418, https://doi.org/10.3189/S0022143000002732, 1998.

Rignot, E. and Kanagaratnam, P.: Changes in the Velocity Structure of the Greenland Ice Sheet, Science, 311, 986–990, https://doi.org/10.1126/science.1121381, 2006.

Rignot, E., Mouginot, J., Morlighem, M., Seroussi, H., and Scheuchl, B.: Widespread, rapid grounding line retreat of Pine Island, Thwaites, Smith and Kohler glaciers, West Antarctica, from 1992 to 2011, Geophys. Res. Lett., 41, 3502–3509, https://doi.org/10.1002/2014GL060140, 2014.

Rignot, E. Mouginot, J., Scheuchl, B., van den Broeke, M., van Wessem, M. J., and Morlighem, M.: Four decades of Antarctic Ice Sheet mass balance from 1979–2017, P. Natl. Acad. Sci. USA, 116, 1095–1103, https://doi.org/10.1073/pnas.1812883116, 2019.

Ritz, C., Edwards, T. L., Durand, G., Payne, A. J., Peyaud, V., and Hindmarsh, R. C. A.: Potential sea-level rise from Antarctic ice-sheet instability constrained by observations, Nature, 528, 115–118, https://doi.org/10.1038/nature16147, 2015.

Robel, A. A.: Thinning sea ice weakens buttressing force of iceberg mélange and promotes calving, Nat. Commun., 8, 14596, https://doi.org/10.1038/ncomms14596, 2017.

Schlemm, T. and Levermann, A.: A simple stress-based cliff-calving law, The Cryosphere, 13, 2475–2488, https://doi.org/10.5194/tc-13-2475-2019, 2019.

Schoof, C.: Ice sheet grounding line dynamics: Steady states, stability, and hysteresis, J. Geophys. Res.-Earth, 112, F03S28, https://doi.org/10.1029/2006JF000664, 2007.

Shepherd, A., Wingham, D., and Rignot, E.: Warm ocean is eroding West Antarctic Ice Sheet, Geophys. Res. Lett., 31, L23402, https://doi.org/10.1029/2004GL021106, 2004.

Shepherd, A., Fricker, H. A., and Farrell, S. L.: Trends and connections across the Antarctic cryosphere, Nature, 558, 223–232, https://doi.org/10.1038/s41586-018-0171-6, 2018a.

Shepherd, A., Ivins, E., Rignot, E., Smith, B., van den Broeke, M., Velicogna, I., Whitehouse, P., Briggs, K., Joughin, I., Krinner, G., Nowicki, S., Payne, T., Scambos, T., Schlegel, N., Geruo, A., Agosta, C., Ahlstrøm, A., Babonis, G., Barletta, V., Blazquez, A., Bonin, J., Csatho, B., Cullather, R., Felikson, D., Fettweis, X., Forsberg, R., Gallee, H., Gardner, A., Gilbert, L., Groh, A., Gunter, B., Hanna, E., Harig, C., Helm, V., Horvath, A., Horwath, M., Khan, S., Kjeldsen, K. K., Konrad, H., Langen, P., Lecavalier, B., Loomis, B., Luthcke, S., McMillan, M., Melini, D., Mernild, S., Mohajerani, Y., Moore, P., Mouginot, J., Moyano, G., Muir, A., Nagler, T., Nield, G., Nilsson, J., Noel, B., Otosaka, I., Pattle, M. E., Peltier, W. R., Pie, N., Rietbroek, R., Rott, H., Sandberg-Sørensen, L., Sasgen, I., Save, H., Scheuchl, B., Schrama, E., Schröder, L., Seo, K.-W., Simonsen, S., Slater, T., Spada, G., Sutterley, T., Talpe, M., Tarasov, L., van de Berg, W. J., van der Wal, W., van Wessem, M., Vishwakarma, B. D., Wiese, D., Wouters, B., and the T.I.M.B.I.E. team: Mass balance of the Antarctic Ice Sheet from 1992 to 2017, Nature, 558, 219–222, https://doi.org/10.1038/s41586-018-0179-y, 2018b.

Slangen, A. B. A., Adloff, F., Jevrejeva, S., Leclercq, P. W., Marzeion, B., Wada, Y., and Winkelmann, R.: A Review of Recent Updates of Sea-Level Projections at Global and Regional Scales, in: Integrative Study of the Mean Sea Level and Its Components, edited by: Cazenave, A., Champollion, N., Paul, F., and Benveniste, J., Springer International Publishing, Cham, Switzerland, 395–416 pp., https://doi.org/10.1007/978-3-319-56490-6_17, 2017.

Todd, J. and Christoffersen, P.: Are seasonal calving dynamics forced by buttressing from ice mélange or undercutting by melting? Outcomes from full-Stokes simulations of Store Glacier, West Greenland, The Cryosphere, 8, 2353–2365, https://doi.org/10.5194/tc-8-2353-2014, 2014.

Todd, J., Christoffersen, P., Zwinger, T., Råback, P., Chauché, N., Benn, D., Luckman, A., Ryan, J., Toberg, N., Slater, D., and Hubbard, A.: A Full-Stokes 3D Calving Model Applied to a Large Greenlandic Glacier, J. Geophys. Res.-Earth, 123, 410–432, https://doi.org/10.1002/2017JF004349, 2018.

Todd, J., Christoffersen, P., Zwinger, T., Råback, P., and Benn, D. I.: Sensitivity of a calving glacier to ice–ocean interactions under climate change: new insights from a 3-D full-Stokes model, The Cryosphere, 13, 1681–1694, https://doi.org/10.5194/tc-13-1681-2019, 2019.

Walter, J. I., Box, J. E., Tulaczyk, S., Brodsky, E. E., Howat, I. M., Ahn, Y., and Brown, A.: Oceanic mechanical forcing of a marine-terminating Greenland glacier, Ann. Glaciol., 53, 181–192, https://doi.org/10.3189/2012AoG60A083, 2012.

WCRP Global Sea Level Budget Group: Global sea-level budget 1993–present, Earth Syst. Sci. Data, 10, 1551–1590, https://doi.org/10.5194/essd-10-1551-2018, 2018.

Weertman, J.: Stability of ice-age ice sheets, J. Geophys. Res., 66, 3783–3792, https://doi.org/10.1029/JZ066i011p03783, 1961.

Weis, M., Greve, R., and Hutter, K.: Theory of shallow ice shelves, Continuum Mech. Therm., 11, 15–50, https://doi.org/10.1007/s001610050102, 1999.

Winkelmann, R., Martin, M. A., Haseloff, M., Albrecht, T., Bueler, E., Khroulev, C., and Levermann, A.: The Potsdam Parallel Ice Sheet Model (PISM-PIK) – Part 1: Model description, The Cryosphere, 5, 715–726, https://doi.org/10.5194/tc-5-715-2011, 2011.

Xie, S., Dixon, T. H., Holland, D. M., Voytenko, D., and Vaňková, I.: Rapid iceberg calving following removal of tightly packed pro-glacial mélange, Nat. Commun., 10, 3250, https://doi.org/10.1038/s41467-019-10908-4, 2019.

Yin, J., Overpeck, J. T., Griffies, S. M., Hu, A., Russell, J. L., and Stouffer, R. J.: Different magnitudes of projected subsurface ocean warming around Greenland and Antarctica, Nat. Geosci., 4, 524–528, https://doi.org/10.1038/ngeo1189, 2011.

A.4 Mélange buttressing can slow down the progress of MICI in the Antarctic ice sheet

Schlemm, T.; Feldmann, J.; Winkelmann, W. & Levermann, A.

Owing to global warming and particularly high regional ocean warming, both Thwaites and Pine Island Glaciers in the Amundsen region of the Antarctic Ice Sheet could lose their buttressing ice shelves over time. We analyse the possible consequences using the parallel ice sheet model (PISM), applying a simple cliff-calving parameterization and an ice mélange-buttressing model. We find that the instantaneous loss of ice-shelf buttressing, due to enforced ice-shelf melting, initiates grounding-line retreat and triggers marine ice sheet instability (MISI). As a consequence, the grounding line progresses into the interior of the West Antarctic Ice Sheet and leads to a sea level contribution of 0.6 m within 100 years. By subjecting the exposed ice cliffs to cliff calving using our simplified parameterization, we also analyse marine ice cliff instability (MICI). In our simulations it can double or even triple the sea level contribution depending on the only loosely constrained parameter that determines the maximum cliff-calving rate. The speed of MICI depends on this upper bound of the calving rate, which is given by the ice mélange buttressing the glacier. However, stabilization of MICI may occur for geometric reasons. Because the embayment geometry changes as MICI advances into the interior of the ice sheet, the upper bound on calving rates is reduced and the progress of MICI is slowed down. Although we cannot claim that our simulations bear relevant quantitative estimates of the effect of ice-mélange buttressing on MICI, the mechanism has the potential to stop the instability. Further research is needed to evaluate its role for the past and future evolution of the Antarctic Ice Sheet.

The Cryosphere **16**, 1979–1996 (2022)
DOI: 10.5194/tc-16-1979-2022

The Cryosphere, 16, 1979–1996, 2022
https://doi.org/10.5194/tc-16-1979-2022

The Cryosphere Open Access EGU

Stabilizing effect of mélange buttressing on the marine ice-cliff instability of the West Antarctic Ice Sheet

Tanja Schlemm[1,2], **Johannes Feldmann**[1], **Ricarda Winkelmann**[1,2], **and Anders Levermann**[1,2,3]

[1]Earth System Dynamics, Potsdam Institute for Climate Impact Research, Potsdam, Germany
[2]Institute of Physics and Astronomy, University of Potsdam, Potsdam, Germany
[3]Lamont-Doherty Earth Observatory, Columbia University, New York, USA

Correspondence: Anders Levermann (anders.levermann@pik-potsdam.de)

Received: 30 July 2021 – Discussion started: 12 August 2021
Revised: 19 April 2022 – Accepted: 25 April 2022 – Published: 24 May 2022

Abstract. Owing to global warming and particularly high regional ocean warming, both Thwaites and Pine Island Glaciers in the Amundsen region of the Antarctic Ice Sheet could lose their buttressing ice shelves over time. We analyse the possible consequences using the parallel ice sheet model (PISM), applying a simple cliff-calving parameterization and an ice mélange-buttressing model. We find that the instantaneous loss of ice-shelf buttressing, due to enforced ice-shelf melting, initiates grounding-line retreat and triggers marine ice sheet instability (MISI). As a consequence, the grounding line progresses into the interior of the West Antarctic Ice Sheet and leads to a sea level contribution of 0.6 m within 100 a. By subjecting the exposed ice cliffs to cliff calving using our simplified parameterization, we also analyse marine ice cliff instability (MICI). In our simulations it can double or even triple the sea level contribution depending on the only loosely constrained parameter that determines the maximum cliff-calving rate. The speed of MICI depends on this upper bound of the calving rate, which is given by the ice mélange buttressing the glacier. However, stabilization of MICI may occur for geometric reasons. Because the embayment geometry changes as MICI advances into the interior of the ice sheet, the upper bound on calving rates is reduced and the progress of MICI is slowed down. Although we cannot claim that our simulations bear relevant quantitative estimates of the effect of ice-mélange buttressing on MICI, the mechanism has the potential to stop the instability. Further research is needed to evaluate its role for the past and future evolution of the Antarctic Ice Sheet.

1 Introduction

Ice loss from the Greenland and Antarctic Ice Sheets is contributing increasingly to global sea level rise (Rignot et al., 2014; Shepherd et al., 2018b; WCRP Global Sea Level Budget Group, 2018). Ice sheets gain mass through accumulation of snowfall. Whether they contribute to sea level changes depends on how much this mass gain is offset or overcompensated for by mass losses due to surface and basal melting as well as iceberg calving. Ice sheets in both Greenland and Antarctica are currently losing ice (Enderlin et al., 2014; Shepherd et al., 2018b; Mouginot et al., 2019; Larour et al., 2019; Bell and Seroussi, 2020). Estimating the additional future mass loss of these ice sheets is critical for future sea level projections (Church et al., 2013; Ritz et al., 2015; DeConto and Pollard, 2016; Mengel et al., 2016; Kopp et al., 2017; Slangen et al., 2017; Golledge et al., 2019; Levermann et al., 2020; Edwards et al., 2021). Uncertainties in modelling the physics of the Antarctic Ice Sheet (AIS) lead to large uncertainties in sea level projections (Noble et al., 2020; Pattyn and Morlighem, 2020).

One such uncertainty is the potential collapse and the calving of large ice cliffs after the ice shelves buttressing them have disintegrated. The concept of cliff calving was motivated by an analysis of depth-averaged stresses near an ice cliff, which showed that ice cliffs exceeding an ice thickness stability limit are inherently unstable (Bassis and Walker, 2011). Cliff calving could lead to uncontrolled ice retreat: grounding-line retreat caused by cliff calving may expose even higher ice cliffs further inland, which in turn are more susceptible to collapse, resulting in self-reinforcing ice re-

treat. This is referred to as Marine Ice Cliff Instability (MICI) (DeConto and Pollard, 2016).

A study by DeConto and Pollard (2016) found that the AIS could contribute up to 1 m of sea level rise within a century, if cliff calving is taken into account. This is substantially more than all other projections that do not include MICI. However, this study has been criticized as over-estimating sea level contribution (Edwards et al., 2019) owing to a lack of observationally constrained models of the cliff-calving process. DeConto and Pollard (2016) parameterized cliff calving with a step-like function that is zero for ice cliffs below the stability limit and ramps up rapidly to an upper limit for all ice cliffs exceeding the stability limit. We revisit the question of MICI in the AIS using a more complex parameterization of cliff calving, which is based on the shear failure of an ice cliff and gives the cliff-calving rate as an exponential function of ice thickness and water depth (Schlemm and Levermann, 2019). A recent, more detailed modelling study of ice cliff failure, incorporating different structural failure modes as well as surface lowering due to viscous deformation, supports the findings that calving rates increase exponentially with ice thickness (Crawford et al., 2021). In our model, we further assume that calved icebergs form an ice mélange that buttresses the ice cliffs, providing an upper bound on calving rates (Schlemm and Levermann, 2021).

We consider the Amundsen region of the West Antarctic Ice Sheet (WAIS) as the likely initiator of MICI. Iceberg plough marks on the seafloor indicate that large full thickness icebergs calved from Pine Island Glacier and that MICI was active in this area during the last deglaciation (Wise et al., 2017). Additionally, the WAIS is grounded largely on bedrock below sea level and is therefore vulnerable to both the marine ice sheet instability (MISI) and MICI. MISI is caused by grounding-line retreat on a retrograde bed: retreat into deeper bed regions increases the flux across the grounding line and therefore accelerates grounding-line retreat, resulting in self-reinforcing ice loss (Mercer, 1978; Schoof, 2007; Favier et al., 2014). Observations show that MISI is possibly already underway in the Amundsen region (Joughin et al., 2014; Mouginot et al., 2014; Rignot et al., 2014). Once MISI is initiated, the entire WAIS could collapse on a millennial time scale, resulting in a sea- level rise of 3 m (Feldmann and Levermann, 2015). With the addition of cliff calving (MICI), the WAIS collapse would occur much more rapidly.

The breakup of ice shelves is a necessary precondition for the calving of exposed ice cliffs and thus for the onset of MICI. Hydrofracturing, in which the deepening of ice crevasses due to extensive surface meltwater leads to the catastrophic failure of an entire ice shelf, has been proposed by DeConto and Pollard (2016) as the main mechanism for ice-shelf breakup and the consequent exposure of ice cliffs.

In 2002, the Larsen B Ice Shelf on the Antarctic Peninsula collapsed within a week after having thinned in previous years owing to high summer melt rates (Rack and Rott, 2004; Glasser and Scambos, 2008). As a result of the ice-shelf collapse, glaciers flowing into the shelf have permanently accelerated (Scambos et al., 2004; Berthier et al., 2012). These are small glaciers with little impact on the overall Antarctic mass balance. Based on the observation of numerous surface meltwater ponds prior to ice-shelf collapse, it has been suggested that hydrofracturing owing to intense surface melting was the primary cause of this sudden collapse (MacAyeal et al., 2003). However, anomalously large surface melt rates are required for an ice shelf to break up as rapidly as the Larsen B Ice Shelf did (Robel and Banwell, 2019). Thus, hydrofracturing would probably not be the main mechanism leading to ice-shelf failure in the Amundsen region: even under the RCP 8.5 scenario, surface meltwater production on the Pine Island Ice Shelf is projected to remain far below a threshold of $300\,\mathrm{mm\,a^{-1}}$ at the end of the century (Trusel et al., 2015). This threshold is equivalent to current surface meltwater production on the remaining Larsen C Ice Shelf and less than half of the pre-collapse surface meltwater production on the Larsen B Ice Shelf (Trusel et al., 2015). Therefore, it is unlikely that the ice shelves in the Amundsen region will fail owing to hydrofracturing.

Nevertheless, it is likely that the ice shelves in the Amundsen region will break apart under persisting global warming conditions. The Amundsen Sea is warming (Shepherd et al., 2004, 2018a), leading to increased basal melting of ice shelves. This is already causing thinning and grounding-line retreat in all the glaciers in the Amundsen region (MacGregor et al., 2012; Mouginot et al., 2014; Milillo et al., 2019).

The destabilizing effect of basal melt on ice shelves can be further amplified by basal and surface crevasses: satellite observations show a trend of widespread surface rifting at the shear margins of all glaciers in the Amundsen region (MacGregor et al., 2012) as well as an increase in rifts originating from basal crevasses in the centre of the Pine Island Ice Shelf (Jeong et al., 2016). Ocean warming may be the cause of the observed expansion of basal crevasses (Jeong et al., 2016). Rifting and crevassing accelerates grounding-line retreat: damage feedback modelling showed that a basal melt rate of $20\,\mathrm{m\,a^{-1}}$ combined with a 20-m-deep surface crevasse in the shear zone at the grounding line causes a faster grounding-line retreat than a basal melt rate of $100\,\mathrm{m\,a^{-1}}$ on an undamaged shelf (Lhermitte et al., 2020).

In addition, calving front retreat of small ice shelves may be self-reinforcing: a linear elastic fracture mechanics model of calving at Thwaites Glacier showed a positive feedback, i.e. if calving results in a shorter ice shelf, this shorter ice shelf is more likely to calve (Yu et al., 2017). It is also possible that weakened buttressing due to ice-shelf thinning at Pine Island and Thwaites Glaciers could amplify the development of damage in their shear zones. Lhermitte et al. (2020) suggest that this damage feedback might predispose the ice shelves at Pine Island and Thwaites Glaciers to disintegration. This would remove buttressing from glaciers terminating in the Amundsen Sea and expose large ice cliffs, triggering MISI and MICI.

We perform a series of simulations using the parallel ice sheet model (PISM) in a regional setup of the WAIS, where we initiate MISI and MICI by removing the ice shelves in the Amundsen region. The ice sheet model and calving parameterizations are described in more detail in Sect. 2. We present the resulting sea-level contributions in Sect. 3. In Sect. 4, we discuss how the strength of mélange buttressing changes with grounding-line retreat and show that as a result MICI slows down as it progresses.

2 Methods

2.1 Mélange-buttressed cliff calving

2.1.1 Model description

The model for mélange-buttressed cliff calving consists of two parts: cliff-calving parameterization (Schlemm and Levermann, 2019) and mélange-buttressing parameterization (Schlemm and Levermann, 2021).

For the ice cliffs, i.e. grounded ice sheet at the coast, we use a cliff-calving relation based on shear failure of an ice cliff (Schlemm and Levermann, 2019). If the difference between ice thickness and water depths lies below a water depth-dependent threshold (≈ 100 m), the cliff is assumed to be stable. For larger ice cliffs, the calving rate grows exponentially with ice thickness and water depth. This assumed exponential relation and the fact that in many regions in West Antarctica the bed topography is down-sloping inland, can lead to very large calving rates ($> 30\,\mathrm{km\,a^{-1}}$, see Fig. 1a).

In addition to the recently discussed stabilizing effect of dynamic thinning (Bassis et al., 2021; Golledge and Lowry, 2021), a mélange of icebergs and sea ice, may have a stabilizing effect on MICI. Here we apply a very simple mélange-buttressing parameterization (Schlemm and Levermann, 2021): larger calving rates lead to the production of more icebergs, which together with sea ice form a stiff ice mélange. This mélange buttresses the ice cliff, thereby stabilizing it. As a result of this negative feedback between calving rate and mélange buttressing, there is an upper limit to the calving rate, $C_{\max}$ (see Fig. 1b). This threshold, derived in Schlemm and Levermann (2021), is a function of embayment geometry and mélange properties,

$$C_{\max} = \frac{W_{\mathrm{ex}}}{W_{\mathrm{cf}}}\left(b_0 + b_1\mu_0\frac{L_{\mathrm{em}}}{W_{\mathrm{em}}}\right)^{-1}\gamma\, u_{\mathrm{ex}}, \tag{1}$$

where the mélange length is denoted by L_{em}, the mélange width at the calving front by W_{cf}, the mélange exit width by W_{ex} and the average mélange width by W_{em} (see Fig. 2). γ is the fraction of the ice thickness H beyond which calving is completely suppressed, and u_{ex} is the exit velocity, with which mélange drifts out of the embayment. Finally, the internal friction of the mélange, μ_0, has values between 0.1 and 1 (Amundson and Burton, 2018), and the linearization parameters are given by $b_0 = 1.17$ and $b_1 = 1.11$.

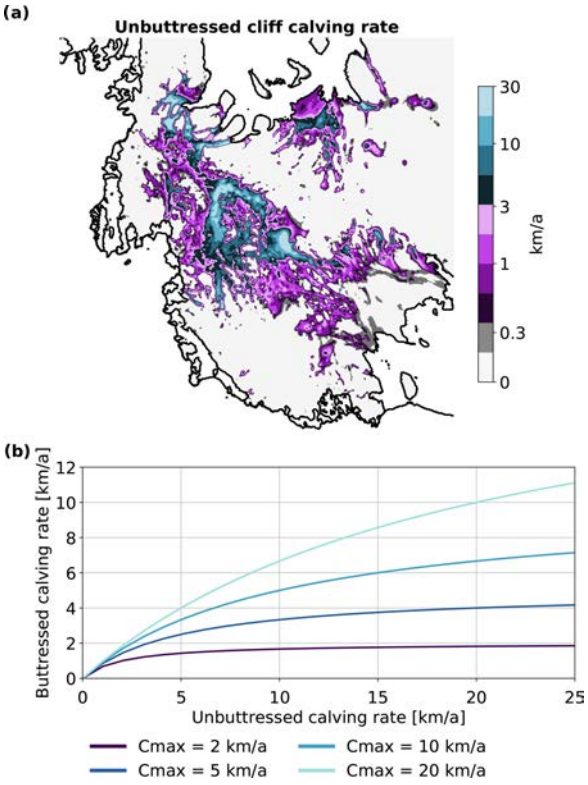

Figure 1. (a) Potential unbuttressed cliff-calving rates in the WAIS. For this estimate we assume the ice cliff to be at flotation thickness, making the calving rate a function of bed topography. In the case of very fast grounding-line retreat, the ice cliff may not have thinned to flotation and calving rates may be larger. **(b)** The mélange-buttressed calving rates as a function of the unbuttressed calving rates for the values of $C_{\max}$ considered in this study.

2.1.2 Uncertainties in the model parameters

The scaling parameter in the cliff-calving parameterization, C_0, is poorly constrained because it depends on the time scale of shear failure and there are no experimental or observational studies on this for ice (Schlemm and Levermann, 2019). However, in the mélange-buttressed case, $C_{\max}$ plays a much larger role in determining the overall calving rate, so the uncertainty of C_0 is not a major concern (Schlemm and Levermann, 2021).

In the mélange-buttressing parameterization, we chose $\mu_0 = 0.3$ and $\gamma = 0.2$ as in Schlemm and Levermann (2021). $C_{\max}$ depends linearly on the embayment exit velocity u_{ex} (see Eq. 1). Therefore, constraining its range is important for estimating $C_{\max}$: maximum mélange flow speeds observed in front of Greenland glaciers are 30–50 $\mathrm{m\,d^{-1}} \approx 10$–

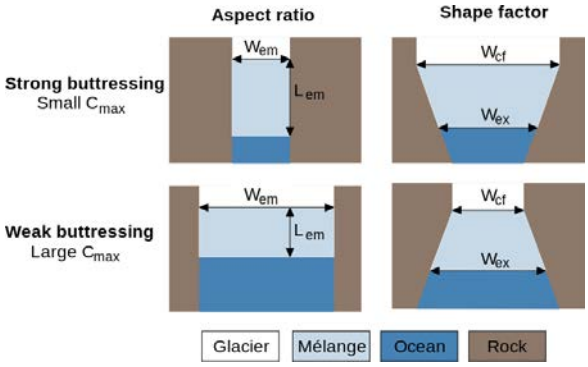

Figure 2. Illustration of how embayment geometry determines buttressing strength in Eq. (1): aspect ratio $L_{\mathrm{em}}/W_{\mathrm{em}}$ and shape factor $W_{\mathrm{ex}}/W_{\mathrm{cf}}$ determine the strength of mélange buttressing.

$18\,\mathrm{km\,a^{-1}}$ (Amundson and Burton, 2018). The velocities of icebergs drifting in the Weddel Sea in Antarctica are within the range 9–15 $\mathrm{km\,d^{-1}} \approx 3000$–$5500\,\mathrm{km\,a^{-1}}$ (Schodlok et al., 2006). We assume that the mélange exit velocity lies within the range covered by these observations. The value of $C_{\max}$ then depends solely on the embayment geometry (Fig. 2).

2.1.3 Mélange buttressing depends on embayment geometry

In order to estimate $C_{\max}$ for a given grounding-line configuration, we assume that the entire embayment is filled with mélange. Note that the calving rate would be larger if the embayment were initially free of mélange. However, as the mélange parameterization cannot evolve the mélange margin, we must assume its position. The evolution of the mélange thickness can be modelled, though: when the entire embayment is filled with a very thin, spread-out mélange, the calving rate is high and many icebergs are produced. As a result, the mélange thickness grows rapidly and reaches its equilibrium thickness within a few years (Schlemm and Levermann, 2021). Therefore, it can be assumed that within a few years after the onset of calving, the entire embayment is filled with mélange.

We estimate the width of the mélange exit, W_{ex}, and the length of the calving front, W_{cf}, by measuring the embayment manually. The average mélange width, W_{em}, is calculated as the average of W_{ex} and W_{cf}. The mélange length, L_{em}, is calculated as the average distance between the embayment exit and the calving front (the resulting trapezoids are shown in Fig. 11b). Table 1 shows estimates of $C_{\max}$ for Thwaites and Pine Island Glaciers as well as for two extreme cases of mélange geometry: a narrow and long mélange strongly buttresses the calving front, resulting in a small $C_{\max}$, while a wide and short mélange provides little buttressing at the calving front, resulting in a large $C_{\max}$.

2.2 PISM

2.2.1 Model description

We carry out regional simulations of the WAIS with PISM (Bueler and Brown, 2009; Winkelmann et al., 2011) at a horizontal resolution of 4 km and a minimum vertical resolution of 7 m. At this resolution, the reversibility of the grounding line is similar to that of higher-order models (Feldmann et al., 2014). The model setup is similar to the one used and described in Feldmann et al. (2019).

PISM is a thermomechanically coupled model based on the Glen—Paterson—Budd—Lliboutry—Duval flow law (Aschwanden et al., 2012). It uses a superposition of the shallow ice approximation (Hutter, 1983) and the shallow shelf approximation (Morland, 1987; MacAyeal, 1989), allowing for a smooth transition between different ice-sheet flow regimes. Basal friction is calculated using a nonlinear Weertman-type sliding law with a sliding exponent of 3/4 combined with a Mohr-Coulomb model for plastic till (Bueler and van Pelt, 2015) that accounts for the effect of evolving ice thickness and the associated change in overburden pressure on the basal till. The till friction angle is parameterized with bed elevation (see Martin et al., 2011, Eqs. 8–12). This friction scheme ensures a continuous transition from quasi–non-slip regimes in elevated regions to the marine areas where basal resistance is low. The grounding-line position is free to evolve using hydrostatic equilibrium. Grounding-line movement has been evaluated in the model intercomparison projects MISMIP3d (Pattyn et al., 2013; Feldmann et al., 2014) and MISMIP+ (Cornford et al., 2020). Basal friction at the grounding line is interpolated according to a sub-grid, linear interpolation of the grounding-line position (Feldmann et al., 2014).

2.2.2 Breakup of ice shelves

In our simulations, we assume that in the near future the ice shelves in the Amundsen region will break apart and will not be able to regenerate. This is a very strong assumption and is implemented in PISM with what we call a "floatkill" mechanism, which removes all floating ice in the Amundsen region at each time step. The ice front, which is now identical to the grounding line, is free to evolve. For the remaining ice shelves, mainly the Ross and Ronne–Filchner ice shelves, but also small ice shelves along the Antarctic Peninsula, the so-called eigencalving parameterization is applied (Levermann et al., 2012).

2.2.3 Mélange-buttressed cliff calving

Mélange-buttressed cliff calving is applied to ice cliffs, i.e. grounded ice sheet at the coast. Similar to the floatkill parameterization, it is not applied to the entire model domain, but only to the coast of the Amundsen region and the interior of the WAIS. The shaded region in Fig. 5 shows the region

Table 1. Upper bounds on calving rates given by Eq. (1) with $\mu_0 = 0.3$, $\gamma = 0.2$ and $u_{ex} = 100\,\mathrm{km\,a^{-1}}$. We first consider two extremes of a narrow and long as well as a wide and short buttressing mélange, while assuming a rectangular mélange geometry with constant mélange width, $W_{ex} = W_{cf} = W_{em}$. For Thwaites and Pine Island Glaciers, we assume mélange geometry similar to the current ice shelf. The smaller the upper bound C_{max}, the stronger the buttressing effect caused by the ice mélange.

	W_{em} [km]	L_{em} [km]	W_{ex}/W_{cf}	C_{max} [km a^{-1}]
Narrow and long	5	100	1	2.6
Wide and short	200	5	1	17.0
Thwaites Glacier	93	14	1.19	19.6
Pine Island Glacier	48	58	1.14	15.5

where the floatkill parameterization and mélange-buttressed cliff calving are not applied. This implementation prevents MISI and MICI from starting in other regions of the AIS, such as the Antarctic Peninsula.

2.3 MISI and MICI in the WAIS with PISM

2.3.1 Boundary conditions

Basal melt rates under ice shelves are calculated using the Potsdam Ice-shelf Cavity mOdel (PICO) (Reese et al., 2018a), where ocean conditions are determined by mean values over the observational period 1975–2012 (Schmidtko et al., 2014). The surface mass balance and ice surface temperature are averaged from RACMO2.3p2 1986–2005 (van Wessem et al., 2018). The model domain includes the West Antarctic Ice Sheet, the Antarctic Peninsula and parts of the East Antarctic Ice Sheet, in particular, the drainage basins towards the Ross and Ronne–Filchner ice shelves (Zwally et al., 2012). The bed topography and initial ice configuration were taken from Bedmap2 (Fretwell et al., 2013). For more details see Feldmann et al. (2019), where the same setup was used.

2.3.2 Initialization and experiments

The ice sheet was spun up into thermal equilibrium with fixed bed and ice geometry for 100 000 model years (Feldmann et al., 2019). A further 10-year run with evolving ice geometry was performed to remove short-lived floating regions in the WAIS (such as in the middle of Smith Glacier, west of Thwaites Glacier). Five types of experiments were carried out:

REF: a reference simulation with the current-day atmosphere and ocean conditions held constant (see Sect. 2.3.1)

BMT: the "basal melt experiment" is a melt experiment with current-day atmospheric conditions and the melt rate in the Amundsen Basin set to $200\,\mathrm{m\,a^{-1}}$. This assumed basal melt rate is higher than the current and projected average melt rates of the Amundsen region ice shelves (Naughten et al., 2018). However, close to the grounding line of Thwaites Glacier, basal melt rates of up to $200\,\mathrm{m\,a^{-1}}$ were found (Milillo et al., 2019). In the melt experiment, this rate was applied to the whole of the ice shelves in the Amundsen region. The ice front is free to evolve.

FLK: the floatkill-parameterization experiment with current-day atmospheric and ocean conditions, in which all floating ice in the Amundsen Basin and the interior of the WAIS was removed. The grounding line is now the ice front and is free to evolve.

CC#: four cliff-calving experiments, which were performed in the same way as the floatkill-parameterization experiment, with the addition of exposing grounded glacier margins to cliff calving with different upper limits. The upper bound range is $C_{max} = [2, 5, 10, 20]\,\mathrm{km\,a^{-1}}$ (CC2, CC5, CC10, CC20).

CCA#: five adaptive cliff-calving experiments, where the upper bound C_{max} was updated every 5 model years for the new embayment geometry. The mélange exit velocity range is $u_{ex} = [10, 50, 100, 200, 1000]\,\mathrm{km\,a^{-1}}$ (CCA10, CCA50, CCA100, CCA200, CCA1000).

Each experiment was run for 100 a. Some experiments (FLK, CC2, CC5, CC10, CCA10, CCA50, CCA100, CCA200) were extended until they reached a retreat comparable with the fastest cliff-calving experiment (CC20).

2.4 Seasonal mélange freezing with the stand-alone mélange model

Finally, we investigated whether mélange freezing can stop MICI after its onset. Mélange freezing and thereby stopping of calving has been observed in Greenland glaciers in the winter season (Medrzycka et al., 2016). In the summer season, the sea ice in the mélange breaks up, the mélange becomes mobile, and calving sets in again.

The mélange-buttressing parameterization can model melting of mélange as a loss of mélange volume and therefore mélange-buttressing strength. However it cannot explicitly model mélange freezing. We used the exit velocity as a tool to simulate mélange freezing: in the steady-state

model of mélange buttressing (see Sect. 2.1), calving is completely suppressed if no mélange leaves the embayment exit ($u_{ex} = 0 \Rightarrow C_{max} = 0$, according to Eq. 1). However, starting with a very thin mélange and solving the non-steady-state equations of the mélange-buttressing model as described in Schlemm and Levermann (2021), calving is allowed until the mélange thickness has reached its steady-state value.

We started from a very thin mélange (10 m) and modelled seasonality with a time-dependent mélange exit velocity of the form

$$u_{ex}(t) = u_0 \cdot \Big(1 + \arctan\left(k \cdot \sin\left(t \cdot 2\pi\right)\right)\Big) \Big/ \arctan(k) \quad \text{with} \quad k = 20 \quad , \qquad (2)$$

with a winter minimum of $u_{winter} = 0$, a summer maximum of $u_{summer} = 2u_0$ and an average of u_0.

The mélange geometry was assumed to be rectangular with $W = 30$ km, $L = 60$ km, the initial mélange thickness at the calving front was $d_0 = 10$m and the unbuttressed calving rate was $C_0 = 5\,\mathrm{km\,a^{-1}}$.

3 Results

3.1 MISI discharge caused by floatkill is similar to that caused by basal melt

In our setup, the two MISI experiments (FLK and BMT) contribute about 0.6 m of sea-level rise within 100 a (see Fig. 3 and Table 2). This corresponds to the upper limit of the sea-level contribution from the Amundsen sector found in LARMIP-2 (Levermann et al., 2020), where a basal melt anomaly of up to $16\,\mathrm{m\,a^{-1}}$ was applied to currently observed melt rates. It is at the upper end of the 16 models that participated in LARMIP-2, but is not the highest.

The sea-level contributions resulting from the FLK and BMT experiments are very similar. This agrees with results from the ABUMIP intercomparison study (Sun et al., 2020), which showed that Antarctic-wide ice loss due to large basal melt rates is comparable with ice loss due to the floatkill parameterization.

3.2 MICI discharge is controlled by an upper bound on calving rates

When comparing the speed of the instabilities, we use two measures: the sea- level contribution and the calving discharge. In the experiments with cliff calving (CC# and CCA#), MISI and MICI occur simultaneously. Therefore, the sea-level contribution in these experiments is caused by both instabilities. Calving discharge is a better parameter to compare the contribution of MISI and MICI in each experiment because the discharge caused by the floatkill mechanism and the discharge caused by cliff calving are reported separately.

For the two lowest upper bounds on cliff calving (CC2 and CC5), MICI contributes a factor of up to 1.5 in addition

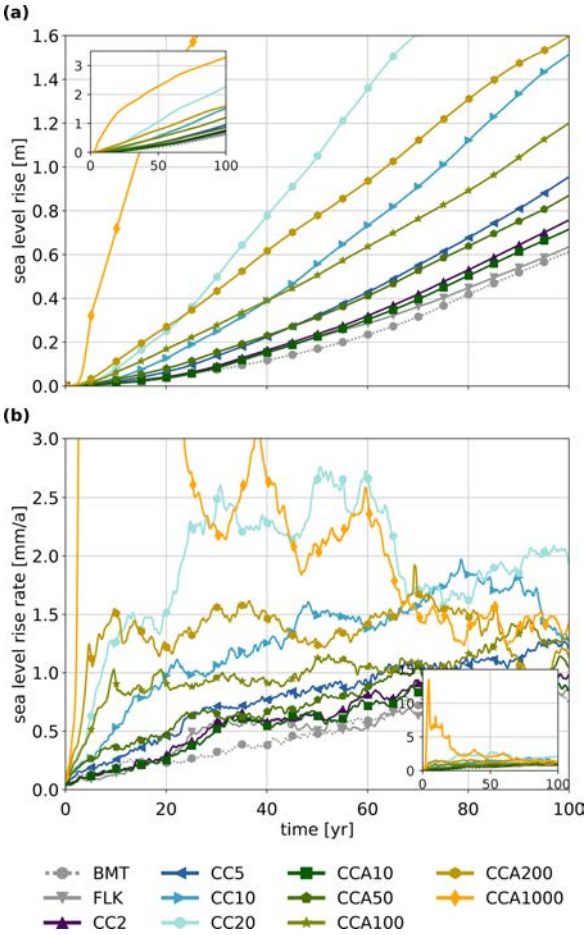

Figure 3. Cumulative sea-level contribution **(a)** and rate of sea-level rise **(b)** relative to the reference run for all experiments carried out. The insets shows the same plot but with a larger range so that the curve of the CCA1000 experiment is shown completely.

to sea-level rise from the MISI experiments. For larger upper bounds, MICI can more than double (CC10) or even triple (CC20) the sea-level contribution compared with the MISI experiments (FLK, BMT). The sea-level contributions of the first four adaptive experiments (CCA10, CCA50, CCA100, CCA200) are similar to those of the first three cliff-calving experiments (CC2, CC5, CC10). The adaptive experiment with the largest exit velocity (CCA1000) has more than five times the sea-level contribution of the MISI experiments (FLK and BMT) (see Fig. 3 and Table 2).

Ice-retreat rates increase with time, with sea-level rates for the FLK and CC2 experiments reaching about $1\,\mathrm{mm\,a^{-1}}$ after 100 a, whereas the CC20 experiment reaches its maximum sea-level rate of $2.5\,\mathrm{mm\,a^{-1}}$ as early as after 50 a. The sea-level rate of the CC20 experiment decreases after 60 a of runtime because the grounding-line retreat along the

Table 2. Sea- level contribution after 50 and 100 a is computed as the difference to the REF simulation. Cumulative calving discharge from the Amundsen region is given after 100 a. Average calving amplification is calculated as fraction between overall calving discharge (including cliff calving) and calving discharge only due to the floatkill parameterization.

		Sea level contribution [m]		Cumulative discharge [10^6 Gt]	Average calving amplification
		50 a	100 a		
MISI	BMT	0.17	0.61	–	–
	FLK	0.22	0.64	4.00	1
MISI + MICI	CC2	0.24	0.76	4.72	1.34
	CC5	0.32	0.95	6.00	1.86
	CC10	0.56	1.51	9.68	2.39
	CC20	1.05	2.28	14.53	3.15
	CCA10	0.23	0.72	4.34	1.22
	CCA50	0.31	0.87	5.43	1.63
	CCA100	0.51	1.20	7.64	2.02
	CCA200	0.78	1.60	10.14	2.38
	CCA1000	2.27	3.27	21.53	7.90

Pine Island Glacier towards the Ronne Ice Shelf has reached the boundary of the inner WAIS region, beyond which cliff calving and the floatkill parameterization are not applied (see Fig. 5). In the adaptive experiments (CCA10, CCA50, CCA100, CCA200), the sea-level rise rate increases initially and then levels off. This corresponds to the reduction of the adaptive upper bound on calving rates (see Table 3 and Fig. 6). In the CCA1000 experiment, the sea-level rise rate initially goes up to 13 mm a^{-1} and decreases sharply after 20 a when the retreat along the Pine Island Glacier reaches the boundary of the inner WAIS region where cliff calving and floatkill parameterization are applied. The sea-level rate decreases again after 45 a when the retreat reaches bedrock above sea level and after 65 a when it reaches the boundary of the inner WAIS region close to the Siple coast (see Fig. 5).

Calving is the main cause of sea-level rise: for experiments CC2, CC5, CCA10 and CCA50 the cumulative calving discharge is only slightly larger than for the FLK experiments; for experiments CC10 and CCA100 as well as CC20 and CCA200 the calving discharge doubles and triples, respectively. The slowdown of the CC20 experiment after 60 a is also visible in the reduced calving discharge. Similar to the sea-level rise rate, the calving discharge of the adaptive experiments (CCA10, CCA50, CCA100, CCA200) increases initially and then levels off (see Fig. 4 and Table 2).

For each cliff-calving experiment (CC# and CCA#), PISM reports ice discharge due to the floatkill mechanism and due to cliff calving separately. We use this to calculate the calving amplification as the ratio between the total calving discharge and the discharge only due to floatkill (Table 2). It reveals a doubling or tripling in the calving discharge for the highest values of $C_{\max}$, similar to the increase in the sea-level contributions mentioned above.

The cliff-calving experiments with a small upper bound (CC2, CCA10) show only a modestly faster ice retreat than the floatkill experiment. This is because PISM uses a subgrid scheme for the ice margin, involving partially filled cells that are not affected by either the ice dynamics or the floatkill mechanism (Albrecht et al., 2011). Cliff calving with a small value of $C_{\max}$ can prevent partially filled cells from filling up and thus reduce the ice loss due to the floatkill parameterization. This may result in a slightly lower overall calving discharge than floatkill with no cliff calving. Cliff calving with a large value of $C_{\max}$ is much more likely to completely remove partially filled cells, so the floatkill parameterization mechanism is not hindered in this case. This issue depends on the resolution of the domain: previously unpublished sensitivity tests in a channel setup showed that for a resolution of x km, this problem occurs for calving rates smaller than x km a^{-1}.

3.3 Mélange buttressing increases as MICI progresses, slowing MICI speed

In the adaptive cliff-calving experiments (CCA#), mélange-buttressing strength depends on the embayment geometry (see Eq. 1 and Fig. 2). Because the calving front becomes longer and its distance to the embayment exit increases, the upper bound on calving rate decreases with grounding-line retreat into the Amundsen Basin. The development of the upper bound with simulation time is given in Table 3. In Fig. 6, the upper bound is shown as a function of the sea-level contribution of the corresponding embayment geometry. Initially, Thwaites and Pine Island Glaciers have separate embayments with different values for $C_{\max}$. After some time, depending on the mélange exit velocity, the embayments merge, leading to one value of $C_{\max}$ for the whole Amundsen Basin. As the grounding-line retreats deeper into the Amundsen Basin, $C_{\max}$ decreases to about one third of its initial value. The relation between calving rate and sea-level

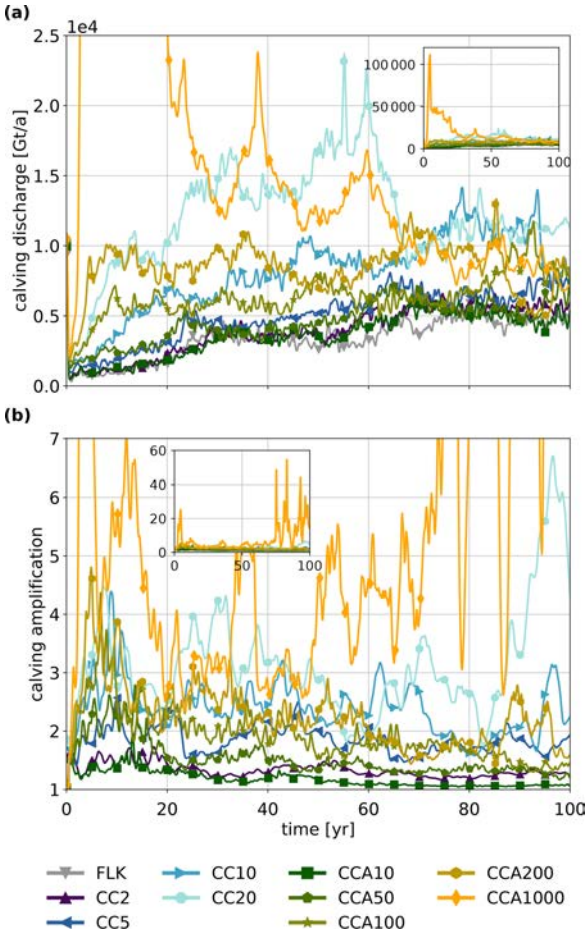

Figure 4. (a) Overall calving discharge from the Amundsen region. PISM uses a subgrid scheme at the ice margin with partially filled cells (Albrecht et al., 2011). At each time step, calving removes some of the ice in such a cell, whereas floatkill removes whole cells if they float. This removed ice volume is summed up in the calving discharge variable. **(b)** The calving amplification calculated as the fraction between overall calving discharge and calving discharge due to the floatkill parameterization only. Note that no calving amplification has been calculated for the floatkill-only experiment because no cliff calving takes place. The calving amplification of the CC20 and the CCA1000 experiments increases toward the end of the simulation time because parts of the grounding line have reached the margin of the inner WAIS region, beyond which cliff calving and the floatkill mechanism are not applied.

contribution can be fitted with:

$$\frac{C_{\max}}{C^0_{\max}} \approx 0.19 \cdot \exp\left(\frac{0.17\,\mathrm{m}}{\mathrm{SLR} + 0.11\,\mathrm{m}}\right), \tag{3}$$

with $C^0_{\max}$ the average of the initial upper bounds for Thwaites and Pine Island Glaciers.

As MICI progresses and the grounding-line retreats, the area covered by ice mélange grows, which increases the strength of mélange buttressing. This in turn lowers the upper limit on calving rates and slows further progression of MICI. Thus, as a consequence of mélange buttressing, MICI cannot be arbitrarily fast and even decelerates as it progresses.

3.4 Bed topography controls the rate of grounding-line retreat

The grounding-line retreat initially follows the main flow directions of Pine Island and Thwaites Glaciers, but after some time (depending on $C_{\max}$) it involves the entire interior of the WAIS (see Fig. 5). The retreat reaches the Ronne Basin earlier than the Ross Basin. The CC20 experiment reaches the Ronne Ice Shelf after 70 a of runtime, where the retreat ends as no further floatkill parameterization and cliff calving are allowed there. The retreat towards the Ross Ice Shelf continues. The experiments with smaller $C_{\max}$ as well as the FLK experiment take longer to reach the Ronne Ice Shelf, with the FLK experiment being the slowest, arriving there after 150 a (not shown here).

We examine the retreat along two flowlines, leading from Thwaites Glacier across to the Ross Ice Shelf and from Pine Island Glacier across to the Ronne Ice Shelf, respectively (see Fig. 7). These are the same 2-dimensional experiments discussed in the rest of the paper, except that they are analysed along the trajectory of the flowlines. As the ice divides are free to move, it may be that their lateral movement changes the actual flowline, i.e. the main direction of the ice flow. This has not been taken into account.

Both glaciers have retrograde beds, with Thwaites Glacier having a steeper slope than Pine Island Glacier. After the flowlines cross the initial ice divide, the bed topography changes: the retreating grounding line of Thwaites Glacier meets the Bindschadler Ice Stream, which has a rather shallow and slightly prograde bed topography (in the direction of grounding-line retreat). In contrast, the retreating grounding line of Pine Island Glacier reaches the Evans Ice Stream, which has a deep bed depression. Figure 8 shows the retreat of the grounding line and ice divide along these flowlines over time. For Thwaites Glacier, all experiments show some inertia to the retreat initially, which is followed by rapid retreat along the first 150 km of the flowline. Retreat then levels off, with experiments with larger $C_{\max}$ showing faster retreat. Pine Island Glacier shows steady initial retreat over the first 300 km, after which the retreat stalls for 25 to 50 a, depending on the experiment. This is followed by a rapid retreat that is stopped only when the grounding line reaches the Ronne Ice Shelf, where no further retreat is possible. As the grounding-line retreats, so does the ice divide, but with a considerable delay.

An explanation for this retreat pattern can be found by a more detailed analysis that compares the grounding-line retreat rates with the slope of the bed topography (see Fig. 9).

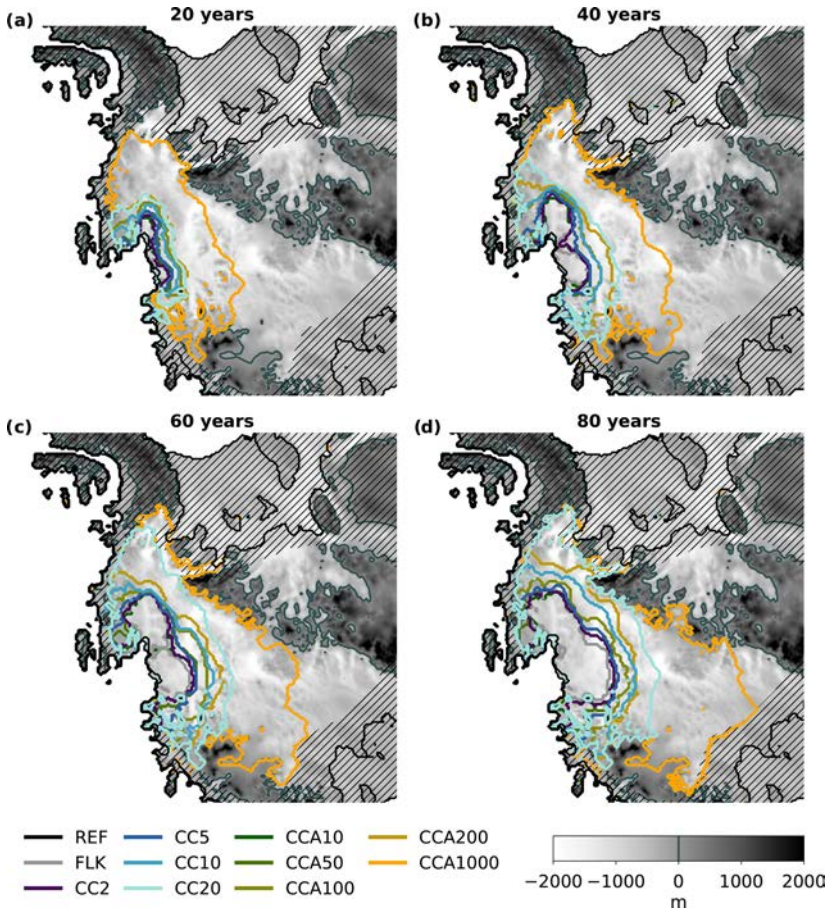

Figure 5. Maps of grounding-line retreat in the WAIS, underlaid with the bed topography. In the shaded region, neither the floatkill parameterization nor cliff calving is applied (see Sect. 2.2.3). Grounding-line retreat of CCA1000, the fastest experiment, halts when it reaches bed topography above sea level (in which case cliff calving is no longer applied) or the margin of the interior Amundsen region domain (beyond which neither floatkill nor cliff calving is applied).

Table 3. Upper bound on calving rates for the adaptive cliff-calving experiments (CCA#) in km a^{-1}. Where two values are given, the first is for Thwaites Glacier and the second for Pine Island Glacier. Where only one value is given, both glaciers share one embayment.

	0 a	20 a	40 a	60 a	80 a	100 a
CCA10	1.96/1.55	1.51/1.85	1.48/1.26	0.60	0.54	0.50
CCA50	9.78/7.75	4.09	2.97	2.77	2.67	2.30
CCA100	19.6/15.5	7.72	5.90	5.32	4.98	4.57
CCA200	39.1/31.0	12.6	9.23	8.61	7.28	6.78
CCA1000	195/155	32.2	25.5	21.3	22.3	21.4

Grounding-line retreat along Thwaites flow line is rapid at first, with retreat rates up to 18 km a^{-1} (depending on C_{max}) along a steep retrograde bed, and slows down once the grounding line reaches a more even bed topography segment beginning at 150 km. In this segment, retreat rates fluctuate below 10 km a^{-1}. Ridges in the bed topography at 220 and 430 km cause stagnation of grounding-line retreat on the upslope, followed by acceleration on the downslope. A steady retrograde slope between 500 and 630 km causes grounding-line retreat rates to increase up to 10 km a^{-1}. The steep prograde slope between 630 and 700 km causes the retreat to slow down significantly.

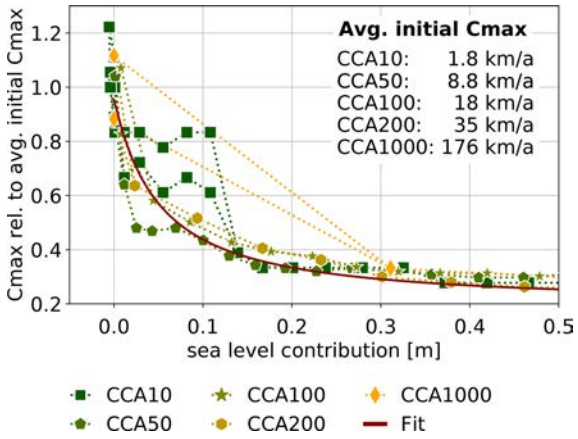

Figure 6. The upper bound on calving rates, $C_{\max}$ of the adaptive cliff-calving experiments (CCA#) as a function of the sea-level contribution of the corresponding embayment geometry. Initially, Thwaites and Pine Island Glaciers have separate embayments, which merge after several model years. The upper bound decreases with sea-level contribution and with the corresponding simulation time (see Table 3).

The retreat along the Pine Island flow line has a steady rate between 5 and 15 km a^{-1} for the first 300 km until the grounding line approaches a bathymetric ridge, where the retreat slows temporarily. A short 20-km-long depression following this ridge causes an acceleration of up to 10 km a^{-1}, followed by a slowdown as the bed rises again. Grounding-line retreat accelerates sharply up to values between 15 and 33 km a^{-1} once it reaches a steep bed depression beneath the Evans Ice Stream, which begins at 450 km.

The CCA1000 experiment has much larger calving rates than the other experiments (see Table 3) and therefore also much larger retreat rates. Its retreat depends more on the mélange buttressing than the bed topography.

We expect bed topography to control grounding-line retreat for two reasons: analytical calculations in a depth-averaged flowline model show that the flux across the grounding-line scales superlinearly with ice thickness (Schoof, 2007). The cliff-calving rate also scales superlinearly with ice thickness (Schlemm and Levermann, 2019). Assuming that the glacier terminus is at flotation, this means that there should also be a relationship between the grounding-line retreat rate and the bed depth.

However, a correlation analysis using the Spearman correlation coefficient of determination between the grounding-line retreat rate and bed topography shows only a minimal correlation for Pine Island Glacier and no correlation at all for Thwaites Glacier (see Table 4). There are two main reasons for this: first, we analyse flow along a 1-dimensional flowline embedded in a more complex 2-dimensional flow. The retreat of the grounding line in neighbouring flowlines, where the bed topography can be different, may drag on the grounding line and either accelerate or decelerate it, in comparison to the result of the 1-dimensional analysis. In addition, the analysed flowlines may not lie exactly along the flow direction, especially in the vicinity of bed-topography disturbances that are only a few grid cells in size. Second, ice flow has inertia, which means that the grounding line takes some time to accelerate when it reaches a steep retrograde bed. Inertia can also drive it over bumps in the bed that would be expected to slow it down, especially in the case of large $C_{\max}$.

Table 4. Spearman correlation coefficients of determination between bed depth and grounding-line retreat rate.

		Thwaites Glacier	Pine Island Glacier
MISI	FLK	0.06	0.79
MISI + MICI	CC2	0.04	0.80
	CC5	0.07	0.76
	CC10	0.04	0.77
	CC20	0.01	0.64
	CCA10	0.08	0.73
	CCA50	0.07	0.52
	CCA100	0.01	0.62
	CCA200	0.13	0.50
	CCA1000	0.01	0.37

In summary, we find no clear statistical correlation between the bed topography and the grounding-line retreat rate. Nevertheless, we observe an acceleration of the grounding line when the bed is retrograde and a deceleration when it is prograde. In addition, bathymetric ridges temporarily halt grounding-line retreat. So we can conclude that bed topography is a major control of the rate of grounding-line retreat.

3.5 Winter freezing of mélange is not sufficient to stop MICI

Assuming that no mélange exits the embayment, mélange buildup can prevent calving almost completely within 10 a (see Fig. 10a, grey lines). Also, assuming a seasonal exit velocity leads to seasonal variations in the strength of mélange buttressing (see Fig. 10, orange and blue lines): after an initial equilibration period, mélange volume and backstress decrease in the summer and the calving rate increases, whereas in the winter mélange volume and backstress increase and the calving rate decreases. The minimum and maximum mélange properties fluctuate around the equilibrium value calculated by using the averaged exit velocity u_0. Contrary to observations, in this simplified mélange parameterization, winter freezing of mélange is not sufficient to stop calving. The reason is that the equilibration of the mélange is too slow and takes several years rather than months or weeks.

Studies explicitly analysing the influence of the mélange backpressure on the stress balance of the glacier terminus fo-

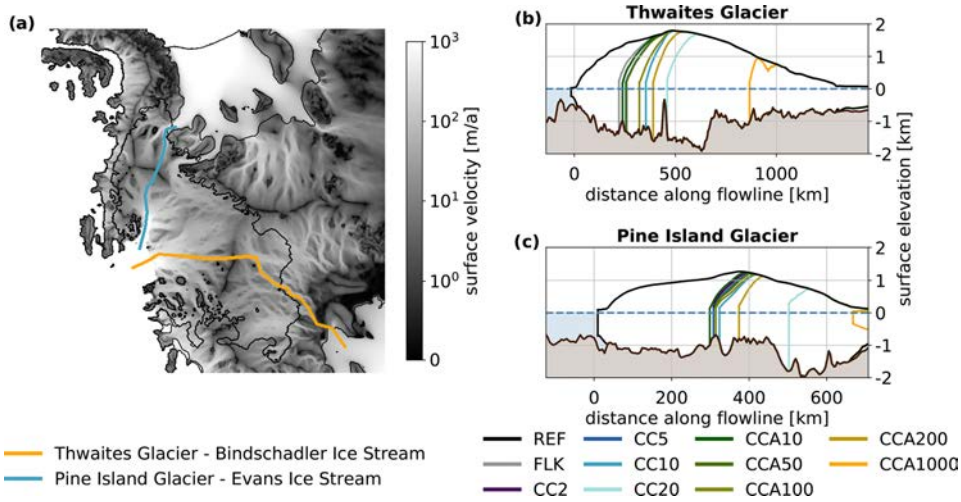

Figure 7. **(a)** Map of flowlines from Pine Island Glacier through Evans ice stream to the Ronne Ice Shelf and from Thwaites Glacier through the Bindschadler Ice Stream to the Ross Ice Shelf. **(b, c)** Bed topography and ice surface profiles after 60 a runtime for Thwaites Glacier and Pine Island Glacier respectively. The distance along the flowline has its zero at the initial grounding-line position. Note that for Pine Island Glacier, the reference run also shows some grounding-line retreat.

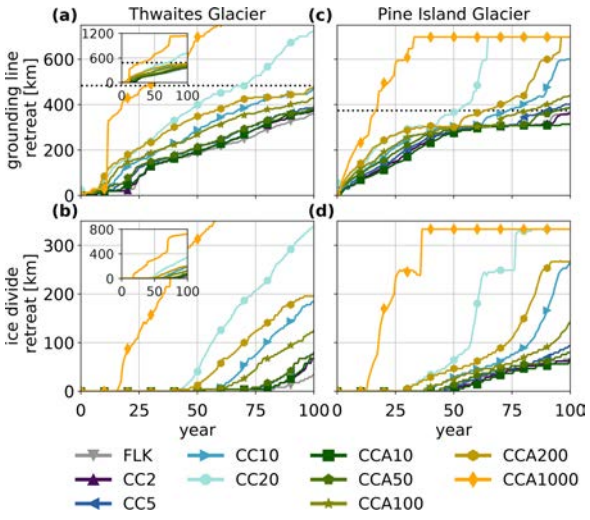

Figure 8. Grounding-line retreat **(a, c)** and ice-divide retreat **(b, d)** along the flowlines in Thwaites **(a, b)** and Pine Island Glaciers **(c, d)** as a function of simulated time. The dotted line shows the initial ice-divide position.

cus on the force per unit width exerted by the mélange at the calving front (Amundson et al., 2010; Todd and Christoffersen, 2014; Crawford et al., 2021). Therefore, the force per unit width was calculated as a diagnostic variable. A mélange backpressure of $6.66 \times 10^6\,\mathrm{N\,m^{-1}}$ is sufficient to prevent cliff calving of an ice cliff with $H = 1000\,\mathrm{m}$ (Crawford et al., 2021). In our solution of the non-steady-state equation, a similar force per unit width was found when calving is suppressed (see Fig. 10c, grey lines after > 5 a).

In conclusion, assuming that no mélange is lost by drifting off at the mélange exit, a very thick and strong mélange is built up within a period of several years, which completely prevents further calving and would thus stop the progression of MICI. However, this is only likely to happen in the winter season and would therefore halt MICI only temporarily.

4 Discussion

In this section we discuss our results in the light of mechanisms and conditions that may be important in limiting the speed of MICI evolution, including the influence of mélange properties, climatic variations, and the ice or bed geometry.

4.1 Limitations of the idealized mélange-buttressing parameterization

Owing to its reliance on an idealized geometry, the mélange parameterization has several limitations when applied to realistic embayment geometries (see Fig. 11a and b):

- The conversion of the realistic geometry into the idealized geometry is not unique: it is difficult to specify exactly where each parameter of the idealized geometry should be measured.

- The mélange parameterization assumes a constant calving rate along the entire length of the calving front. This may be valid when considering a single glacier, but is

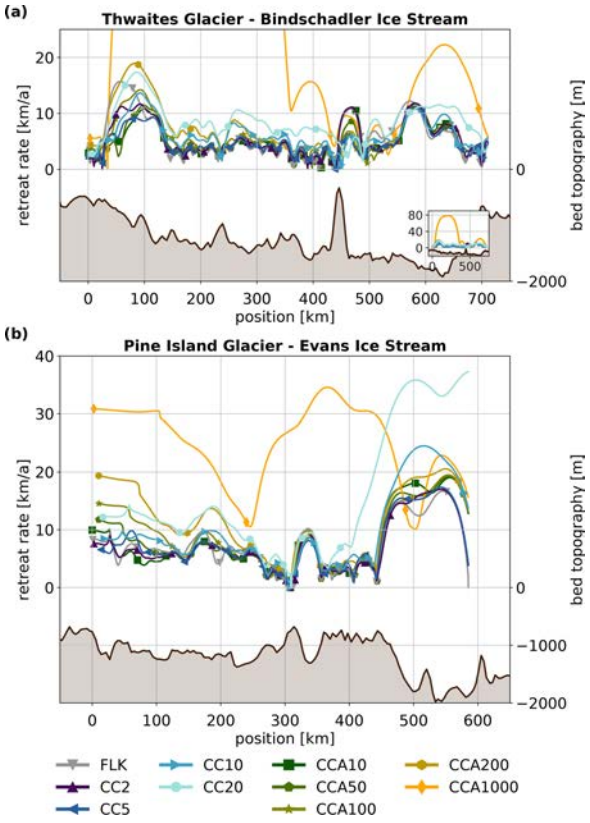

Figure 9. Grounding-line retreat rates along the flowlines in Thwaites **(a)** and Pine Island Glaciers **(b)** as a function of grounding-line position, together with bed topography. Markers are set every 10 a.

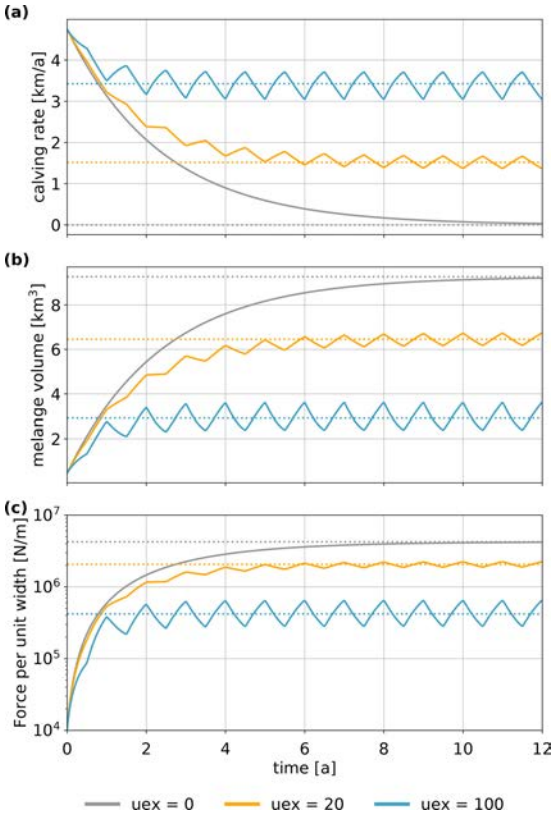

Figure 10. Evolution of the buttressed calving rate **(a)**, the mélange volume **(b)**, and the force per unit width at the calving front **(c)** in the case of no mélange exiting the embayment ($u_{ex} = 0$, grey lines) and for a seasonal variation in mélange exit velocity (orange and blue lines). The dotted lines show the corresponding equilibrium solution. For an equilibrated ice mélange, if no mélange exits the embayment ($u_{ex} = 0$), calving is completely suppressed ($C_{max} = 0$). However, in the time-dependent case and starting with a thin initial mélange, calving is possible for some years. Seasonal variations in the exit velocity lead to seasonal variations of the mélange-buttressing strength.

no longer the case when several glaciers calve into the same embayment.

- On the west side of the Amundsen embayment, ice resting on bedrock above sea-level forms pinning points that provide additional support to the ice mélange. This effect is neglected in the parameterization.
- The mélange margin cannot be inferred from the model and must therefore be provided as an external parameter.
- Mélange freezing cannot be modelled explicitly and has been modelled using the mélange exit velocity. This allows mélange buildup, but its effect takes too long to transmit to the calving front (several years).

To get a better understanding of how mélange buttressing impacts calving rates in a realistic setup, it would be beneficial to use a spatially resolved mélange model. It should be able to handle realistic embayment geometries, including pinning points, as well as spatially resolved calving rates, and have a criterion for where mélange stops being mélange, which would enable it to model the mélange margin (see for example Pollard et al., 2018). However, such a model introduces additional mélange parameters, which are difficult to constrain.

4.2 The role of ice shelves for MICI

Understanding the processes by which ice shelves fracture rapidly and disintegrate is still ongoing work (Yu et al., 2017; Robel and Banwell, 2019; Lhermitte et al., 2020) and difficult to implement in an ice-sheet model.

One way of removing ice shelves is by highly elevated basal melting. In PISM, this approach leaves small ice-shelf remnants that are only a few grid cells in size. The result-

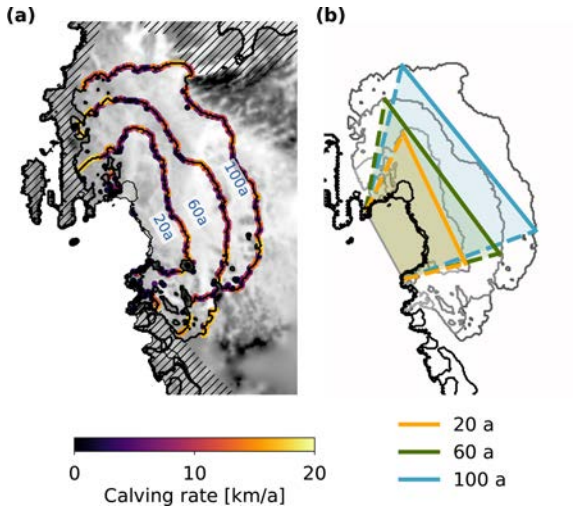

Figure 11. **(a)** Different grounding-line configurations of the adaptive cliff-calving experiment CCA100 with unbuttressed calving rates. **(b)** Idealized embayment geometry derived from the grounding lines.

ing buttressing loss induces MISI. However, because we assume that cliff calving only occurs at exposed, grounded ice cliffs, the ice-shelf remnants prevent the onset of MICI. This is in contrast to the implementation in Pollard et al. (2015): they assumed that a small ice-shelf remnant with vanishing buttressing strength does not prevent cliff calving, basing their reasoning on the Schoof flux across the grounding line (Schoof, 2007) and depth-averaged stresses in the vicinity of the ice cliff (Bassis and Walker, 2011). However, the Schoof flux may not be applicable beyond a flowline setup (Reese et al., 2018b). Additionally, a small ice shelf may impact the stress balance at the ice cliff in a 3d setup. Therefore, we assume that cliff calving only occurs at exposed grounded ice cliffs.

In our model setup, we remove all floating ice in the Amundsen Basin and inner WAIS. This floatkill parameterization mechanism eliminates all existing ice shelves at once in the first-time step and prevents re-growth of ice shelves during the retreat. The removal of ice shelves initiates both MISI and MICI.

Two questions of vital importance for the onset and progress of MICI need further research:

1. Under which conditions do ice shelves collapse completely? As ice-shelf collapse is the prerequisite for the onset of MICI, the answer to this question determines when and if at all MICI will play a role in the future of the Antarctic Ice Sheet. There has been a lot of observational and theoretical work on hydrofracturing (MacAyeal et al., 2003; Robel and Banwell, 2019) as well as rifting and crevassing (Borstad et al., 2012; Jeong et al., 2016; Lhermitte et al., 2020), but so far it is impossible to predict under which environmental and internal conditions a specific ice shelf will collapse.

2. Can ice shelves regrow after MICI has set in? If ice shelves can regrow after cliff calving has begun, this could stop MICI after its onset by buttressing the ice cliffs and preventing further cliff calving. However, if ice shelves cannot regrow, then MICI will continue mostly unhindered, because mélange buttressing can only slow the progress of MICI, but not stop it. Viscous deformation could prevent the formation of unstable ice cliffs (Clerc et al., 2019; Bassis et al., 2021) and allow ice shelves to regrow, whereas a mixed-mode behaviour of viscous deformation and fracture (Crawford et al., 2021) would make ice-shelf regrowth unlikely.

4.3 Influence of regional climatic conditions on the progress of MICI

So far there are few observations of cliff-calving glaciers. The retreat of Sermeq Kujalleq, also known as Jakobshavn Glacier (Bjørk et al., 2015), in Greenland since 1998 (Joughin et al., 2008) was regarded as an indication that Sermeq Kujalleq may be at the beginning of a cliff-calving regime (Bassis and Walker, 2011; DeConto and Pollard, 2016; Schlemm and Levermann, 2019). However, since 2016, Sermeq Kujalleq has re-advanced as a result of regional ocean cooling (Khazendar et al., 2019). The cooling of the Fjord water has led to a decrease in frontal melt (Khazendar et al., 2019) as well as increased mélange buttressing at the glacier terminus (Joughin et al., 2020), thereby stopping its retreat. This suggests that changes in regional climatic conditions may slow or prevent grounding-line retreat caused by cliff calving.

4.4 Slowdown of MICI at bathymetric ridges

During the last deglaciation, MICI was probably active for approximately 1000 a in the Amundsen region of the WAIS and then stopped, when the grounding line re-stabilized on a prominent bathymetric ridge (Wise et al., 2017). This is an indication that MICI can be stopped after its onset by features of the bed topography. However, our simulations show only temporary halts in grounding-line retreat at bathymetric ridges in the interior of the WAIS (see Fig. 9).

5 Conclusions

We performed PISM simulations of the WAIS to investigate the potential speeds of the two marine instabilities, MISI and MICI. We choose the Amundsen region as the starting point of the instabilities because observations show that MISI is possibly already in progress there. Owing to ocean warming and increased crevassing, glaciers in the Amundsen re-

gion may lose their ice shelves in the future, which would set MICI in motion. We applied a floatkill parameterization to remove the ice shelves in the Amundsen region, a cliff-calving parameterization depending on ice thickness, and a mélange-buttressing parameterization, which limits calving rates.

We found that MISI, whether forced by the floatkill parameterization or by high subshelf melt rates, has the potential to contribute 0.6 m of sea- level rise within 100 a. The sea-level potential of MICI depends on the upper limit of calving: if the cliff-calving rate is limited below $2\,\mathrm{km\,a^{-1}}$ or $5\,\mathrm{km\,a^{-1}}$, MICI has a smaller contribution to sea-level rise than MISI. If the upper limit is $10\,\mathrm{km\,a^{-1}}$ or $20\,\mathrm{km\,a^{-1}}$, MICI doubles or even triples the sea-level contribution of MISI.

We also showed that grounding-line retreat is regulated by bed topography for both MISI and MICI. Although there is no clear statistical correlation between the retreat rate and the bed depth, we observe an accelerated retreat of the grounding line on retrograde beds and a slowdown on prograde beds.

Finally, we investigated how the upper limit for calving from mélange buttressing depends on the embayment geometry and the mélange exit velocity. Seasonal effects cause mélange build-up, which slows the progress of MICI temporarily under winter conditions. We also showed that as MICI progresses and the grounding-line retreats, the calving front becomes longer whereas the width of the embayment exit remains the same. This leads to an increase in mélange buttressing, a decrease in the upper bound on calving rates, and consequently a slowdown in the progress of MICI. It is unlikely that mélange alone can completely stop MICI, but it could provide enough buttressing to enable ice-shelf regrowth, which would then stop further MICI progress.

Future research is needed to gain a better understanding of the conditions under which MICI kicks off and to further constrain its potential sea-level contribution.

The applied mélange parameterization assumes an idealized geometry and is therefore of limited applicability when extended to realistic embayment geometries. A spatially resolved mélange model might be a better choice. However, such a model would require more parameters describing mélange properties, which are difficult to constrain.

Two important unresolved questions about ice-shelf collapse are beyond the scope of this study. First, under which conditions do ice shelves collapse? This determines the onset of MICI and is therefore crucially important in constraining at what degree of warming MICI becomes a concern. Second, can ice shelves regrow after MICI has started? This seems to be the only way to stop MICI. These two important questions control if and when MICI sets in and if it can be not only slowed down but stopped completely after its onset.

Code and data availability. The PISM code used for these simulations is available at https://doi.org/10.5281/zenodo.6325006 (Schlemm and PISM authors, 2022). The model output data and Python scripts for running the experiments and generating the figures shown in the paper are stored in a band archive at the Potsdam Institute for Climate Impact Research and indexed in a metadata archive; they are available upon request.

Author contributions. TS and AL designed the study with input from RW. JF created the regional setup of the WAIS and performed the spinup. TS performed the simulations, analysed the model results, and wrote the paper. All authors commented on the paper.

Competing interests. The contact author has declared that neither they nor their co-authors has any competing interests.

Disclaimer. Publisher's note: Copernicus Publications remains neutral with regard to jurisdictional claims in published maps and institutional affiliations.

Acknowledgements. This paper is supported by the European Union's Horizon 2020 research and innovation programme under grant agreement no. 869304 (PROTECT). This paper is supported by the European Union's Horizon 2020 research and innovation programme under grant agreement no. 820575 (TiPACCs). Johannes Feldmann and Ricarda Winkelmann acknowledge support by the Deutsche Forschungsgemeinschaft (DFG) through grants WI4556/4-1 and WI4556/6-1. RW is grateful for support by the European Union's Horizon 2020 research and innovation programme under grant agreements no. 820575 (TiPACCs) and no. 869304 (PROTECT), and by the PalMod project (FKZ: 01LP1925D), supported by the German Federal Ministry of Education and Research (BMBF) as a Research for Sustainability initiative (FONA). Tanja Schlemm acknowledges support by the Heinrich Böll Stiftung.

Financial support. This research has been supported by the Heinrich Böll Stiftung.

The publication of this article was funded by the Open Access Fund of the Leibniz Association.

Review statement. This paper was edited by Ginny Catania and reviewed by Lizz Ultee and two anonymous referees.

References

Albrecht, T., Martin, M., Haseloff, M., Winkelmann, R., and Levermann, A.: Parameterization for subgrid-scale motion of ice-shelf calving fronts, The Cryosphere, 5, 35–44, https://doi.org/10.5194/tc-5-35-2011, 2011.

Amundson, J. M. and Burton, J. C.: Quasi-Static Granular Flow of Ice Mélange, J. Geophys. Res.-Earth, 123, 2243–2257, https://doi.org/10.1029/2018JF004685, 2018.

Amundson, J. M., Fahnestock, M., Truffer, M., Brown, J., Lüthi, M. P., and Motyka, R. J.: Ice mélange dynamics and implications for terminus stability, Jakobshavn Isbræ, Greenland, J. Geophys. Res.-Earth, 115, F01005, https://doi.org/10.1029/2009JF001405, 2010.

Aschwanden, A., Bueler, E., Khroulev, C., and Blatter, H.: An enthalpy formulation for glaciers and ice sheets, J. Glaciol., 58, 441–457, https://doi.org/10.3189/2012JoG11J088, 2012.

Bassis, J. N. and Walker, C. C.: Upper and lower limits on the stability of calving glaciers from the yield strength envelope of ice, P. Roy. Soc. Lond. A, 468, 913–931, https://doi.org/10.1098/rspa.2011.0422, 2011.

Bassis, J. N., Berg, B., Crawford, A. J., and Benn, D. I.: Transition to marine ice cliff instability controlled by ice thickness gradients and velocity, Science, 372, 1342–1344, https://doi.org/10.1126/science.abf6271, 2021.

Bell, R. E. and Seroussi, H.: History, mass loss, structure, and dynamic behavior of the Antarctic Ice Sheet, Science, 367, 1321–1325, https://doi.org/10.1126/science.aaz5489, 2020.

Berthier, E., Scambos, T. A., and Shuman, C. A.: Mass loss of Larsen B tributary glaciers (Antarctic Peninsula) unabated since 2002, Geophys. Res. Lett., 39, L13501, https://doi.org/10.1029/2012GL051755, 2012.

Bjørk, A. A., Kruse, L. M., and Michaelsen, P. B.: Brief communication: Getting Greenland's glaciers right – a new data set of all official Greenlandic glacier names, The Cryosphere, 9, 2215–2218, https://doi.org/10.5194/tc-9-2215-2015, 2015.

Borstad, C. P., Khazendar, A., Larour, E., Morlighem, M., Rignot, E., Schodlok, M. P., and Seroussi, H.: A damage mechanics assessment of the Larsen B ice shelf prior to collapse: Toward a physically-based calving law, Geophys. Res. Lett., 39, l18502, https://doi.org/10.1029/2012GL053317, 2012.

Bueler, E. and Brown, J.: Shallow shelf approximation as a "sliding law" in a thermomechanically coupled ice sheet model, J. Geophys. Res.-Earth, 114, F03008, https://doi.org/10.1029/2008JF001179, 2009.

Bueler, E. and van Pelt, W.: Mass-conserving subglacial hydrology in the Parallel Ice Sheet Model version 0.6, Geosci. Model Dev., 8, 1613–1635, https://doi.org/10.5194/gmd-8-1613-2015, 2015.

Church, J. A., Clark, P. U., Cazenave, A., Gregory, J. M., Jevrejeva, S., Levermann, A., Merrifield, M. A., Milne, G. A., Nerem, R. S., Nunn, P. D., Payne, A. J., Pfeffer, W. T., Stammer, D., and Unnikrishnan, A. S.: Sea-Level Rise by 2100, Science, 342, 1445–1445, https://doi.org/10.1126/science.342.6165.1445-a, 2013.

Clerc, F., Minchew, B. M., and Behn, M. D.: Marine Ice Cliff Instability Mitigated by Slow Removal of Ice Shelves, Geophys. Res. Lett., 46, 12108–12116, https://doi.org/10.1029/2019GL084183, 2019.

Cornford, S. L., Seroussi, H., Asay-Davis, X. S., Gudmundsson, G. H., Arthern, R., Borstad, C., Christmann, J., Dias dos Santos, T., Feldmann, J., Goldberg, D., Hoffman, M. J., Humbert, A., Kleiner, T., Leguy, G., Lipscomb, W. H., Merino, N., Durand, G., Morlighem, M., Pollard, D., Rückamp, M., Williams, C. R., and Yu, H.: Results of the third Marine Ice Sheet Model Intercomparison Project (MISMIP+), The Cryosphere, 14, 2283–2301, https://doi.org/10.5194/tc-14-2283-2020, 2020.

Crawford, A. J., Benn, D. I., Todd, J., Åström, J. A., Bassis, J. N., and Zwinger, T.: Marine ice-cliff instability modeling shows mixed-mode ice-cliff failure and yields calving rate parameterization, Nat. Commun., 12, 2701, https://doi.org/10.1038/s41467-021-23070-7, 2021.

DeConto, R. M. and Pollard, D.: Contribution of Antarctica to past and future sea-level rise, Nature, 531, 591–597, https://doi.org/10.1038/nature17145, 2016.

Edwards, T. L., Brandon, M. A., Durand, G., Edwards, N. R., Golledge, N. R., Holden, P. B., Nias, I. J., Payne, A. J., Ritz, C., and Wernecke, A.: Revisiting Antarctic ice loss due to marine ice-cliff instability, Nature, 566, 58–64, https://doi.org/10.1038/s41586-019-0901-4, 2019.

Edwards, T. L., Nowicki, S., Marzeion, B., Hock, R., Goelzer, H., Seroussi, H., Jourdain, N. C., Slater, D. A., Turner, F. E., Smith, C. J., McKenna, C. M., Simon, E., Abe-Ouchi, A., Gregory, J. M., Larour, E., Lipscomb, W. H., Payne, A. J., Shepherd, A., Agosta, C., Alexander, P., Albrecht, T., Anderson, B., Asay-Davis, X., Aschwanden, A., Barthel, A., Bliss, A., Calov, R., Chambers, C., Champollion, N., Choi, Y., Cullather, R., Cuzzone, J., Dumas, C., Felikson, D., Fettweis, X., Fujita, K., Galton-Fenzi, B. K., Gladstone, R., Golledge, N. R., Greve, R., Hattermann, T., Hoffman, M. J., Humbert, A., Huss, M., Huybrechts, P., Immerzeel, W., Kleiner, T., Kraaijenbrink, P., Le clec'h, S., Lee, V., Leguy, G. R., Little, C. M., Lowry, D. P., Malles, J.-H., Martin, D. F., Maussion, F., Morlighem, M., O'Neill, J. F., Nias, I., Pattyn, F., Pelle, T., Price, S. F., Quiquet, A., Radić, V., Reese, R., Rounce, D. R., Rückamp, M., Sakai, A., Shafer, C., Schlegel, N.-J., Shannon, S., Smith, R. S., Straneo, F., Sun, S., Tarasov, L., Trusel, L. D., Van Breedam, J., van de Wal, R., van den Broeke, M., Winkelmann, R., Zekollari, H., Zhao, C., Zhang, T., and Zwinger, T.: Projected land ice contributions to twenty-first-century sea level rise, Nature, 593, 74–82, https://doi.org/10.1038/s41586-021-03302-y, 2021.

Enderlin, E. M., Howat, I. M., Jeong, S., Noh, M.-J., Angelen, J. H., and Broeke, M. R.: An improved mass budget for the Greenland ice sheet, Geophys. Res. Lett., 41, 866–872, https://doi.org/10.1002/2013GL059010, 2014.

Favier, L., Durand, G., Cornford, S. L., Gudmundsson, G. H., Gagliardini, O., Gillet-Chaulet, F., Zwinger, T., Payne, A. J., and Le Brocq, A. M.: Retreat of Pine Island Glacier controlled by marine ice-sheet instability, Nat. Clim. Change, 4, 117–121, https://doi.org/10.1038/nclimate2094, 2014.

Feldmann, J. and Levermann, A.: Collapse of the West Antarctic Ice Sheet after local destabilization of the Amundsen Basin, P. Natl. Acad. Sci. USA, 112, 14191–14196, https://doi.org/10.1073/pnas.1512482112, 2015.

Feldmann, J., Albrecht, T., Khroulev, C., Pattyn, F., and Levermann, A.: Resolution-dependent performance of grounding line motion in a shallow model compared with a full-Stokes model according to the MISMIP3d intercomparison, J. Glaciol., 60, 353–360, https://doi.org/10.3189/2014JoG13J093, 2014.

Feldmann, J., Levermann, A., and Mengel, M.: Stabilizing the West Antarctic Ice Sheet by surface mass deposition, Sci. Adv., 5, eaaw4132, https://doi.org/10.1126/sciadv.aaw4132, 2019.

Fretwell, P., Pritchard, H. D., Vaughan, D. G., Bamber, J. L., Barrand, N. E., Bell, R., Bianchi, C., Bingham, R. G., Blankenship, D. D., Casassa, G., Catania, G., Callens, D., Conway, H., Cook, A. J., Corr, H. F. J., Damaske, D., Damm, V., Ferraccioli, F., Forsberg, R., Fujita, S., Gim, Y., Gogineni, P., Griggs, J. A., Hindmarsh, R. C. A., Holmlund, P., Holt, J. W., Jacobel, R. W., Jenkins, A., Jokat, W., Jordan, T., King, E. C., Kohler,

J., Krabill, W., Riger-Kusk, M., Langley, K. A., Leitchenkov, G., Leuschen, C., Luyendyk, B. P., Matsuoka, K., Mouginot, J., Nitsche, F. O., Nogi, Y., Nost, O. A., Popov, S. V., Rignot, E., Rippin, D. M., Rivera, A., Roberts, J., Ross, N., Siegert, M. J., Smith, A. M., Steinhage, D., Studinger, M., Sun, B., Tinto, B. K., Welch, B. C., Wilson, D., Young, D. A., Xiangbin, C., and Zirizzotti, A.: Bedmap2: improved ice bed, surface and thickness datasets for Antarctica, The Cryosphere, 7, 375–393, https://doi.org/10.5194/tc-7-375-2013, 2013.

Glasser, N. and Scambos, T.: A structural glaciological analysis of the 2002 Larsen B ice-shelf collapse, J. Glaciol., 54, 3–16, https://doi.org/10.3189/002214308784409017, 2008.

Golledge, N. R. and Lowry, D. P.: Is the marine ice cliff hypothesis collapsing?, Science, 372, 1266–1267, https://doi.org/10.1126/science.abj3266, 2021.

Golledge, N. R., Keller, E. D., Gomez, N., Naughten, K. A., Bernales, J., Trusel, L. D., and Edwards, T. L.: Global environmental consequences of twenty-first-century ice-sheet melt, Nature, 566, 65–72, https://doi.org/10.1038/s41586-019-0889-9, 2019.

Hutter, K.: Theoretical Glaciology, D. Reidel Publishing Company/Terra Scientific Publishing Company, https://doi.org/10.1007/978-94-015-1167-4, 1983.

Jeong, S., Howat, I. M., and Bassis, J. N.: Accelerated ice shelf rifting and retreat at Pine Island Glacier, West Antarctica, Geophys. Res. Lett., 43, 11720–11725, https://doi.org/10.1002/2016GL071360, 2016.

Joughin, I., Howat, I. M., Fahnestock, M., Smith, B., Krabill, W., Alley, R. B., Stern, H., and Truffer, M.: Continued evolution of Jakobshavn Isbrae following its rapid speedup, J. Geophys. Res.-Earth, 113, F04006, https://doi.org/10.1029/2008JF001023, f04006, 2008.

Joughin, I., Smith, B. E., and Medley, B.: Marine Ice Sheet Collapse Potentially Under Way for the Thwaites Glacier Basin, West Antarctica, Science, 344, 735–738, https://doi.org/10.1126/science.1249055, 2014.

Joughin, I., Shean, D. E., Smith, B. E., and Floricioiu, D.: A decade of variability on Jakobshavn Isbræ: ocean temperatures pace speed through influence on mélange rigidity, The Cryosphere, 14, 211–227, https://doi.org/10.5194/tc-14-211-2020, 2020.

Khazendar, A., Fenty, I. G., Carroll, D., Gardner, A., Lee, C. M., Fukumori, I., Wang, O., Zhang, H., Seroussi, H., Moller, D., Noël, B. P. Y., van den Broeke, M. R., Dinardo, S., and Willis, J.: Interruption of two decades of Jakobshavn Isbrae acceleration and thinning as regional ocean cools, Nature Geoscience, 12, 277–283, https://doi.org/10.1038/s41561-019-0329-3, 2019.

Kopp, R. E., DeConto, R. M., Bader, D. A., Hay, C. C., Horton, R. M., Kulp, S., Oppenheimer, M., Pollard, D., and Strauss, B. H.: Evolving Understanding of Antarctic Ice-Sheet Physics and Ambiguity in Probabilistic Sea-Level Projections, Earth's Future, 5, 1217–1233, https://doi.org/10.1002/2017EF000663, 2017.

Larour, E., Seroussi, H., Adhikari, S., Ivins, E., Caron, L., Morlighem, M., and Schlegel, N.: Slowdown in Antarctic mass loss from solid Earth and sea-level feedbacks, Science, 364, eaav7908, https://doi.org/10.1126/science.aav7908, 2019.

Levermann, A., Albrecht, T., Winkelmann, R., Martin, M. A., Haseloff, M., and Joughin, I.: Kinematic first-order calving law implies potential for abrupt ice-shelf retreat, The Cryosphere, 6, 273–286, https://doi.org/10.5194/tc-6-273-2012, 2012.

Levermann, A., Winkelmann, R., Albrecht, T., Goelzer, H., Golledge, N. R., Greve, R., Huybrechts, P., Jordan, J., Leguy, G., Martin, D., Morlighem, M., Pattyn, F., Pollard, D., Quiquet, A., Rodehacke, C., Seroussi, H., Sutter, J., Zhang, T., Van Breedam, J., Calov, R., DeConto, R., Dumas, C., Garbe, J., Gudmundsson, G. H., Hoffman, M. J., Humbert, A., Kleiner, T., Lipscomb, W. H., Meinshausen, M., Ng, E., Nowicki, S. M. J., Perego, M., Price, S. F., Saito, F., Schlegel, N.-J., Sun, S., and van de Wal, R. S. W.: Projecting Antarctica's contribution to future sea level rise from basal ice shelf melt using linear response functions of 16 ice sheet models (LARMIP-2), Earth Syst. Dynam., 11, 35–76, https://doi.org/10.5194/esd-11-35-2020, 2020.

Lhermitte, S., Sun, S., Shuman, C., Wouters, B., Pattyn, F., Wuite, J., Berthier, E., and Nagler, T.: Damage accelerates ice shelf instability and mass loss in Amundsen Sea Embayment, P. Natl. Acad. Sci. USA, 117, 24735–24741, https://doi.org/10.1073/pnas.1912890117, 2020.

MacAyeal, D. R.: Large-scale ice flow over a viscous basal sediment: Theory and application to ice stream B, Antarctica, J. Geophys. Res.-Sol. Ea., 94, 4071–4087, https://doi.org/10.1029/JB094iB04p04071, 1989.

MacAyeal, D. R., Scambos, T. A., Hulbe, C. L., and Fahnestock, M. A.: Catastrophic ice-shelf break-up by an ice-shelf-fragment-capsize mechanism, J. Glaciol., 49, 22–36, https://doi.org/10.3189/172756503781830863, 2003.

MacGregor, J. A., Catania, G. A., Markowski, M. S., and Andrews, A. G.: Widespread rifting and retreat of ice-shelf margins in the eastern Amundsen Sea Embayment between 1972 and 2011, J. Glaciol., 58, 458–466, https://doi.org/10.3189/2012JoG11J262, 2012.

Martin, M. A., Winkelmann, R., Haseloff, M., Albrecht, T., Bueler, E., Khroulev, C., and Levermann, A.: The Potsdam Parallel Ice Sheet Model (PISM-PIK) – Part 2: Dynamic equilibrium simulation of the Antarctic ice sheet, The Cryosphere, 5, 727–740, https://doi.org/10.5194/tc-5-727-2011, 2011.

Medrzycka, D., Benn, D. I., Box, J. E., Copland, L., and Balog, J.: Calving Behavior at Rink Isbræ, West Greenland, from Time-Lapse Photos, Arct. Antarct. Alp. Res., 48, 263–277, https://doi.org/10.1657/aaar0015-059, 2016.

Mengel, M., Feldmann, J., and Levermann, A.: Linear sea-level response to abrupt ocean warming of major West Antarctic ice basin, Nat. Clim. Change, 6, 71–74, https://doi.org/10.1038/nclimate2808, 2016.

Mercer, J. H.: West Antarctic ice sheet and CO_2 greenhouse effect: a threat of disaster, Nature, 271, 321–325, https://doi.org/10.1038/271321a0, 1978.

Milillo, P., Rignot, E., Rizzoli, P., Scheuchl, B., Mouginot, J., Bueso-Bello, J., and Prats-Iraola, P.: Heterogeneous retreat and ice melt of Thwaites Glacier, West Antarctica, Sci. Adv., 5, aau3433, https://doi.org/10.1126/sciadv.aau3433, 2019.

Morland, L. W.: Unconfined Ice-Shelf Flow, in: Dynamics of the West Antarctic Ice Sheet, edited by: Van der Veen, C. J. and Oerlemans, J., Springer Netherlands, Dordrecht, 99–116, https://doi.org/10.1007/978-94-009-3745-1_6, 1987.

Mouginot, J., Rignot, E., and Scheuchl, B.: Sustained increase in ice discharge from the Amundsen Sea Embayment, West Antarc-

tica, from 1973 to 2013, Geophys. Res. Lett., 41, 1576–1584, https://doi.org/10.1002/2013GL059069, 2014.

Mouginot, J., Rignot, E., Bjørk, A. A., van den Broeke, M., Millan, R., Morlighem, M., Noël, B., Scheuchl, B., and Wood, M.: Forty-six years of Greenland Ice Sheet mass balance from 1972 to 2018, P. Natl. Acad. Sci. USA, 116, 9239–9244, https://doi.org/10.1073/pnas.1904242116, 2019.

Naughten, K. A., Meissner, K. J., Galton-Fenzi, B. K., England, M. H., Timmermann, R., and Hellmer, H. H.: Future projections of Antarctic ice shelf melting based on CMIP5 scenarios, J. Clim., 31, 5243–5261, 2018.

Noble, T. L., Rohling, E. J., Aitken, A. R. A., Bostock, H. C., Chase, Z., Gomez, N., Jong, L. M., King, M. A., Mackintosh, A. N., McCormack, F. S., McKay, R. M., Menviel, L., Phipps, S. J., Weber, M. E., Fogwill, C. J., Gayen, B., Golledge, N. R., Gwyther, D. E., Hogg, A. M., Martos, Y. M., Pena-Molino, B., Roberts, J., van de Flierdt, T., and Williams, T.: The Sensitivity of the Antarctic Ice Sheet to a Changing Climate: Past, Present, and Future, Rev. Geophys., 58, e2019RG000663, https://doi.org/10.1029/2019RG000663, 2020.

Pattyn, F. and Morlighem, M.: The uncertain future of the Antarctic Ice Sheet, Science, 367, 1331–1335, https://doi.org/10.1126/science.aaz5487, 2020.

Pattyn, F., Perichon, L., Durand, G., Favier, L., Gagliardini, O., Hindmarsh, R. C., Zwinger, T., Albrecht, T., Cornford, S., Docquier, D., Fürst, J. J., Goldberg, D., Gudmundsson, G. H., Humbert, A., Hütten, M., Huybrechts, P., Jouvet, G., Kleiner, T., Larour, E., Martin, D., Morlighem, M., Payne, A. J., Pollard, D., Rückamp, M., Rybak, O., Seroussi, H., Thoma, M., and Wilkens, N.: Grounding-line migration in plan-view marine ice-sheet models: results of the ice2sea MISMIP3d intercomparison, J. Glaciol., 59, 410–422, https://doi.org/10.3189/2013JoG12J129, 2013.

Pollard, D., DeConto, R. M., and Alley, R. B.: Potential Antarctic Ice Sheet retreat driven by hydrofracturing and ice cliff failure, Earth Planet. Sc. Lett., 412, 112–121, https://doi.org/10.1016/j.epsl.2014.12.035, 2015.

Pollard, D., DeConto, R. M., and Alley, R. B.: A continuum model (PSUMEL1) of ice mélange and its role during retreat of the Antarctic Ice Sheet, Geosci. Model Dev., 11, 5149–5172, https://doi.org/10.5194/gmd-11-5149-2018, 2018.

Rack, W. and Rott, H.: Pattern of retreat and disintegration of the Larsen B ice shelf, Antarctic Peninsula, Ann. Glaciol., 39, 505–510, https://doi.org/10.3189/172756404781814005, 2004.

Reese, R., Albrecht, T., Mengel, M., Asay-Davis, X., and Winkelmann, R.: Antarctic sub-shelf melt rates via PICO, The Cryosphere, 12, 1969–1985, https://doi.org/10.5194/tc-12-1969-2018, 2018a.

Reese, R., Winkelmann, R., and Gudmundsson, G. H.: Grounding-line flux formula applied as a flux condition in numerical simulations fails for buttressed Antarctic ice streams, The Cryosphere, 12, 3229–3242, https://doi.org/10.5194/tc-12-3229-2018, 2018b.

Rignot, E., Mouginot, J., Morlighem, M., Seroussi, H., and Scheuchl, B.: Widespread, rapid grounding line retreat of Pine Island, Thwaites, Smith, and Kohler glaciers, West Antarctica, from 1992 to 2011, Geophys. Res. Lett., 41, 3502–3509, https://doi.org/10.1002/2014GL060140, 2014.

Ritz, C., Edwards, T. L., Durand, G., Payne, A. J., Peyaud, V., and Hindmarsh, R. C. A.: Potential sea-level rise from Antarctic ice-sheet instability constrained by observations, Nature, 528, 115–118, https://doi.org/10.1038/nature16147, 2015.

Robel, A. A. and Banwell, A. F.: A Speed Limit on Ice Shelf Collapse Through Hydrofracture, Geophys. Res. Lett., 46, 12092–12100, https://doi.org/10.1029/2019GL084397, 2019.

Scambos, T. A., Bohlander, J. A., Shuman, C. A., and Skvarca, P.: Glacier acceleration and thinning after ice shelf collapse in the Larsen B embayment, Antarctica, Geophys. Res. Lett., 31, L18402, https://doi.org/10.1029/2004GL020670, l18402, 2004.

Schlemm, T. and Levermann, A.: A simple stress-based cliff-calving law, The Cryosphere, 13, 2475–2488, https://doi.org/10.5194/tc-13-2475-2019, 2019.

Schlemm, T. and Levermann, A.: A simple parametrization of mélange buttressing for calving glaciers, The Cryosphere, 15, 531–545, https://doi.org/10.5194/tc-15-531-2021, 2021.

Schlemm, T. and PISM authors: PISM for MICI: PISM version as used in Schlemm et al. The Cryosphere publication, Zenodo [data set], https://doi.org/10.5281/zenodo.6325006, 2022.

Schmidtko, S., Heywood, K. J., Thompson, A. F., and Aoki, S.: Multidecadal warming of Antarctic waters, Science, 346, 1227–1231, https://doi.org/10.1126/science.1256117, 2014.

Schodlok, M. P., Hellmer, H. H., Rohardt, G., and Fahrbach, E.: Weddell Sea iceberg drift: Five years of observations, J. Geophys. Res.-Ocean., 111, C06018, https://doi.org/10.1029/2004JC002661, 2006.

Schoof, C.: Ice sheet grounding line dynamics: Steady states, stability, and hysteresis, J. Geophys. Res.-Earth, 112, F03S28, https://doi.org/10.1029/2006JF000664, f03S28, 2007.

Shepherd, A., Wingham, D., and Rignot, E.: Warm ocean is eroding West Antarctic Ice Sheet, Geophys. Res. Lett., 31, L23402, https://doi.org/10.1029/2004GL021106, l23402, 2004.

Shepherd, A., Fricker, H. A., and Farrell, S. L.: Trends and connections across the Antarctic cryosphere, Nature, 558, 223–232, https://doi.org/10.1038/s41586-018-0171-6, 2018a.

Shepherd, A., Ivins, E., Rignot, E., Smith, B., van den Broeke, M., Velicogna, I., Whitehouse, P., Briggs, K., Joughin, I., Krinner, G., Nowicki, S., Payne, T., Scambos, T., Schlegel, N., Geruo, A., Agosta, C., Ahlstrøm, A., Babonis, G., Barletta, V., Blazquez, A., Bonin, J., Csatho, B., Cullather, R., Felikson, D., Fettweis, X., Forsberg, R., Gallee, H., Gardner, A., Gilbert, L., Groh, A., Gunter, B., Hanna, E., Harig, C., Helm, V., Horvath, A., Horwath, M., Khan, S., Kjeldsen, K. K., Konrad, H., Langen, P., Lecavalier, B., Loomis, B., Luthcke, S., McMillan, M., Melini, D., Mernild, S., Mohajerani, Y., Moore, P., Mouginot, J., Moyano, G., Muir, A., Nagler, T., Nield, G., Nilsson, J., Noel, B., Otosaka, I., Pattle, M. E., Peltier, W. R., Pie, N., Rietbroek, R., Rott, H., Sandberg-Sørensen, L., Sasgen, I., Save, H., Scheuchl, B., Schrama, E., Schröder, L., Seo, K.-W., Simonsen, S., Slater, T., Spada, G., Sutterley, T., Talpe, M., Tarasov, L., van de Berg, W. J., van der Wal, W., van Wessem, M., Vishwakarma, B. D., Wiese, D., Wouters, B., and the IMBIE team: Mass balance of the Antarctic Ice Sheet from 1992 to 2017, Nature, 558, 219–222, https://doi.org/10.1038/s41586-018-0179-y, 2018b.

Slangen, A. B. A., Adloff, F., Jevrejeva, S., Leclercq, P. W., Marzeion, B., Wada, Y., and Winkelmann, R.: A Review of Recent Updates of Sea-Level Projections at Global and Regional Scales, Springer International Publishing, Cham, 395–416, https://doi.org/10.1007/978-3-319-56490-6_17, 2017.

Sun, S., Pattyn, F., Simon, E. G., Albrecht, T., Cornford, S., Calov, R., Dumas, C., Gillet-Chaulet, F., Goelzer, H., Golledge, N. R., Greve, R., Hoffman, M. J., Humbert, A., Kazmierczak, E., Kleiner, T., Leguy, G. R., Lipscomb, W. H., Martin, D., Morlighem, M., Nowicki, S., Pollard, D., Price, S., Quiquet, A., Seroussi, H., Schlemm, T., Sutter, J., van de Wal, R. S. W., Winkelmann, R., and Zhang, T.: Antarctic ice sheet response to sudden and sustained ice-shelf collapse (ABUMIP), J. Glaciol., 66, 891–904, https://doi.org/10.1017/jog.2020.67, 2020.

Todd, J. and Christoffersen, P.: Are seasonal calving dynamics forced by buttressing from ice mélange or undercutting by melting? Outcomes from full-Stokes simulations of Store Glacier, West Greenland, The Cryosphere, 8, 2353–2365, https://doi.org/10.5194/tc-8-2353-2014, 2014.

Trusel, L. D., Frey, K. E., Das, S. B., Karnauskas, K. B., Kuipers Munneke, P., van Meijgaard, E., and van den Broeke, M. R.: Divergent trajectories of Antarctic surface melt under two twenty-first-century climate scenarios, Nat. Geosci., 8, 927–932, https://doi.org/10.1038/ngeo2563, 2015.

van Wessem, J. M., van de Berg, W. J., Noël, B. P. Y., van Meijgaard, E., Amory, C., Birnbaum, G., Jakobs, C. L., Krüger, K., Lenaerts, J. T. M., Lhermitte, S., Ligtenberg, S. R. M., Medley, B., Reijmer, C. H., van Tricht, K., Trusel, L. D., van Ulft, L. H., Wouters, B., Wuite, J., and van den Broeke, M. R.: Modelling the climate and surface mass balance of polar ice sheets using RACMO2 – Part 2: Antarctica (1979–2016), The Cryosphere, 12, 1479–1498, https://doi.org/10.5194/tc-12-1479-2018, 2018.

WCRP Global Sea Level Budget Group: Global sea-level budget 1993–present, Earth Syst. Sci. Data, 10, 1551–1590, https://doi.org/10.5194/essd-10-1551-2018, 2018.

Winkelmann, R., Martin, M. A., Haseloff, M., Albrecht, T., Bueler, E., Khroulev, C., and Levermann, A.: The Potsdam Parallel Ice Sheet Model (PISM-PIK) – Part 1: Model description, The Cryosphere, 5, 715–726, https://doi.org/10.5194/tc-5-715-2011, 2011.

Wise, M. G., Dowdeswell, J. A., Jakobsson, M., and Larter, R. D.: Evidence of marine ice-cliff instability in Pine Island Bay from iceberg-keel plough marks, Nature, 550, 506–510, https://doi.org/10.1038/nature24458, 2017.

Yu, H., Rignot, E., Morlighem, M., and Seroussi, H.: Iceberg calving of Thwaites Glacier, West Antarctica: full-Stokes modeling combined with linear elastic fracture mechanics, The Cryosphere, 11, 1283–1296, https://doi.org/10.5194/tc-11-1283-2017, 2017.

Zwally, H. J., Giovinetto, M. B., Beckley, M. A., and Sab, J. L.: Antarctic and Greenland Drainage Systems, https://earth.gsfc.nasa.gov/cryo/data/polar-altimetry/antarctic-and-greenland-drainage-systems (last access: 15 May 2022), 2012.

References

M. S. Alnæs, J. Blechta, J. Hake, A. Johansson, B. Kehlet, A. Logg, C. Richardson, J. Ring, M. E. Rognes, and G. N. Wells. The fenics project version 1.5. *Archive of Numerical Software*, 3(100), 2015. doi: 10.11588/ans.2015.100.20553.

J. M. Amundson and J. C. Burton. Quasi-static granular flow of ice mélange. *Journal of Geophysical Research: Earth Surface*, 123(9):2243–2257, 2018. doi: 10.1029/2018JF004685. URL https://agupubs.onlinelibrary.wiley.com/doi/abs/10.1029/2018JF004685.

J. N. Bassis and C. C. Walker. Upper and lower limits on the stability of calving glaciers from the yield strength envelope of ice. *Proceedings of the Royal Society of London A: Mathematical, Physical and Engineering Sciences*, 468:913–931, 2011. ISSN 1364-5021. doi: 10.1098/rspa.2011.0422. URL http://rspa.royalsocietypublishing.org/content/early/2011/11/17/rspa.2011.0422.

J. N. Bassis, S. V. Petersen, and L. Mac Cathles. Heinrich events triggered by ocean forcing and modulated by isostatic adjustment. *Nature*, 542:332, Feb. 2017. URL https://doi.org/10.1038/nature21069.

J. N. Bassis, B. Berg, A. J. Crawford, and D. I. Benn. Transition to marine ice cliff instability controlled by ice thickness gradients and velocity. *Science*, 372(6548):1342–1344, 2021. ISSN 0036-8075. doi: 10.1126/science.abf6271. URL https://science.sciencemag.org/content/372/6548/1342.

D. Benn, J. Astrom, T. Zwinger, J. Todd, F. Nick, S. Cook, N. Hulton, and A. Luckmann. Melt-under-cutting and buoyancy-driven calving from tidewater glaciers: new insights from discrete element and continuum model simulations. *Journal of Glaciology*, 63(240): 691–702, 2017a. doi: 10.1017/jog.2017.41.

D. I. Benn, C. R. Warren, and R. H. Mottram. Calving processes and the dynamics of calving glaciers. *Earth-Science Reviews*, 82(3–4):143–179, 2007. ISSN 0012-8252. doi: 10.1016/j.earscirev.2007.02.002. URL http://www.sciencedirect.com/science/article/pii/S0012825207000396.

D. I. Benn, T. Cowton, J. Todd, and A. Luckman. Glacier calving in greenland. *Current Climate Change Reports*, 3(4):282–290, 2017b. ISSN 2198-6061. doi: 10.1007/s40641-017-0070-1. URL https://doi.org/10.1007/s40641-017-0070-1.

R. A. Bindschadler, S. Nowicki, A. Abe-Ouchi, A. Aschwanden, H. Choi, J. Fastook, G. Granzow, R. Greve, G. Gutowski, U. Herzfeld, C. Jackson, J. Johnson, C. Khroulev,

A. Levermann, W. H. Lipscomb, M. A. Martin, M. Morlighem, B. R. Parizek, D. Pollard, S. F. Price, D. Ren, F. Saito, T. Sato, H. Seddik, H. Seroussi, K. Takahashi, R. Walker, and W. L. Wang. Ice-sheet model sensitivities to environmental forcing and their use in projecting future sea level (the searise project). *Journal of Glaciology*, 59(214):195–224, 2013. doi: doi:10.3189/2013JoG12J125. URL http://www.ingentaconnect.com/content/igsoc/jog/2013/00000059/00000214/art00001.

C. P. Borstad, A. Khazendar, E. Larour, M. Morlighem, E. Rignot, M. P. Schodlok, and H. Seroussi. A damage mechanics assessment of the larsen b ice shelf prior to collapse: Toward a physically-based calving law. *Geophysical Research Letters*, 39(18), 2012. ISSN 1944-8007. doi: 10.1029/2012GL053317. URL http://dx.doi.org/10.1029/2012GL053317. L18502.

N. Brantut, M. J. Heap, P. G. Meredith, and P. Baud. Time-dependent cracking and brittle creep in crustal rocks: A review. *Journal of Structural Geology*, 52:17–43, 2013. ISSN 0191-8141. doi: https://doi.org/10.1016/j.jsg.2013.03.007. URL http://www.sciencedirect.com/science/article/pii/S0191814113000473.

N. Brooks, R. Nicholls, and J. Hall. Sea level rise: Coastal impacts and responses, 2006. URL http://www.wbgu.de/wbgu_sn2006_ex03.pdf.

E. Bueler and J. Brown. Shallow shelf approximation as a "sliding law" in a thermomechanically coupled ice sheet model. *Journal of Geophysical Research: Earth Surface*, 114(F3), 2009. ISSN 2156-2202. doi: 10.1029/2008JF001179. URL http://dx.doi.org/10.1029/2008JF001179.

J. C. Burton, J. M. Amundson, R. Cassotto, C.-C. Kuo, and M. Dennin. Quantifying flow and stress in ice mélange, the world's largest granular material. *Proceedings of the National Academy of Sciences*, 115(20):5105–5110, 2018. ISSN 0027-8424. doi: 10.1073/pnas.1715136115. URL http://www.pnas.org/content/115/20/5105.

A. Chapuis and T. Tetzlaff. The variability of tidewater-glacier calving: Origin of event-size and interval distributions. *Journal of Glaciology*, 60(222):622–634, 2014. doi: 10.3189/2014JoG13J215.

J. A. Church, P. U. Clark, A. Cazenave, J. M. Gregory, S. Jevrejeva, A. Levermann, M. A. Merrifield, G. A. Milne, R. S. Nerem, P. D. Nunn, A. J. Payne, W. T. Pfeffer, D. Stammer, and A. S. Unnikrishnan. Sea-level rise by 2100. *Science*, 342 (6165):1445–1445, 2013a. ISSN 0036-8075. doi: 10.1126/science.342.6165.1445-a. URL http://science.sciencemag.org/content/342/6165/1445.1.

J. A. Church, P. U. Clark, A. Cazenave, J. M. Gregory, S. Jevrejeva, A. Levermann, M. A. Merrifield, G. A. Milne, R. S. Nerem, P. D. Nunn, A. J. Payne, W. T. Pfeffer, D. Stammer, and A. S. Unnikrishnan. *Sea Level Change*, book section 13, page 1137–1216. Cambridge University Press, Cambridge, United Kingdom and New York, NY, USA, 2013b. ISBN ISBN 978-1-107-66182-0. doi: 10.1017/CBO9781107415324.026. URL http://www.climatechange2013.org.

F. Clerc, B. M. Minchew, and M. D. Behn. Marine ice cliff instability mitigated by slow removal of ice shelves. *Geophysical Research Letters*, 46(ja):12108–12116, 2019. doi:

10.1029/2019GL084183. URL https://agupubs.onlinelibrary.wiley.com/doi/abs/10.1029/2019GL084183.

S. L. Cornford, H. Seroussi, X. S. Asay-Davis, G. H. Gudmundsson, R. Arthern, C. Borstad, J. Christmann, T. Dias dos Santos, J. Feldmann, D. Goldberg, M. J. Hoffman, A. Humbert, T. Kleiner, G. Leguy, W. H. Lipscomb, N. Merino, G. Durand, M. Morlighem, D. Pollard, M. Rückamp, C. R. Williams, and H. Yu. Results of the third marine ice sheet model intercomparison project (mismip+). *The Cryosphere*, 14(7):2283–2301, 2020. doi: 10.5194/tc-14-2283-2020. URL https://tc.copernicus.org/articles/14/2283/2020/.

A. J. Crawford, D. I. Benn, J. Todd, J. A. Åström, J. N. Bassis, and T. Zwinger. Marine ice-cliff instability modeling shows mixed-mode ice-cliff failure and yields calving rate parameterization. *Nature Communications*, 12(1):2701, May 2021. ISSN 2041-1723. URL https://doi.org/10.1038/s41467-021-23070-7.

R. M. DeConto and D. Pollard. Contribution of Antarctica to past and future sea-level rise. *Nature*, 531(7596):591–597, 2016. ISSN 0028-0836. doi: http://dx.doi.org/10.1038/nature1714510.1038/nature17145. URL http://www.nature.com/nature/journal/v531/n7596/abs/nature17145.html#supplementary-information.

R. M. DeConto, D. Pollard, R. B. Alley, I. Velicogna, E. Gasson, N. Gomez, S. Sadai, A. Condron, D. M. Gilford, E. L. Ashe, R. E. Kopp, D. Li, and A. Dutton. The paris climate agreement and future sea-level rise from antarctica. *Nature*, 593(7857):83–89, May 2021. ISSN 1476-4687. URL https://doi.org/10.1038/s41586-021-03427-0.

M. A. Depoorter, J. L. Bamber, J. A. Griggs, J. T. M. Lenaerts, S. R. M. Ligtenberg, M. R. van den Broeke, and G. Moholdt. Calving fluxes and basal melt rates of antarctic ice shelves. *Nature*, 502:89, Sept. 2013. URL http://dx.doi.org/10.1038/nature12567.

T. K. Dupont and R. B. Alley. Assessment of the importance of ice-shelf buttressing to ice-sheet flow. *Geophysical Research Letters*, 32(4), 2005. ISSN 1944-8007. doi: 10.1029/2004GL022024. URL http://dx.doi.org/10.1029/2004GL022024. L04503.

T. L. Edwards, M. A. Brandon, G. Durand, N. R. Edwards, N. R. Golledge, P. B. Holden, I. J. Nias, A. J. Payne, C. Ritz, and A. Wernecke. Revisiting antarctic ice loss due to marine ice-cliff instability. *Nature*, 566(7742):58–64, Feb. 2019. ISSN 1476-4687. URL https://doi.org/10.1038/s41586-019-0901-4.

T. L. Edwards, S. Nowicki, B. Marzeion, R. Hock, H. Goelzer, H. Seroussi, N. C. Jourdain, D. A. Slater, F. E. Turner, C. J. Smith, C. M. McKenna, E. Simon, A. Abe-Ouchi, J. M. Gregory, E. Larour, W. H. Lipscomb, A. J. Payne, A. Shepherd, C. Agosta, P. Alexander, T. Albrecht, B. Anderson, X. Asay-Davis, A. Aschwanden, A. Barthel, A. Bliss, R. Calov, C. Chambers, N. Champollion, Y. Choi, R. Cullather, J. Cuzzone, C. Dumas, D. Felikson, X. Fettweis, K. Fujita, B. K. Galton-Fenzi, R. Gladstone, N. R. Golledge, R. Greve, T. Hattermann, M. J. Hoffman, A. Humbert, M. Huss, P. Huybrechts, W. Immerzeel, T. Kleiner, P. Kraaijenbrink, S. Le clec'h, V. Lee, G. R. Leguy, C. M. Little, D. P. Lowry, J.-H. Malles, D. F. Martin, F. Maussion, M. Morlighem, J. F. O'Neill, I. Nias, F. Pattyn, T. Pelle, S. F. Price, A. Quiquet, V. Radić, R. Reese, D. R. Rounce, M. Rückamp, A. Sakai, C. Shafer, N.-J. Schlegel, S. Shannon, R. S. Smith, F. Straneo, S. Sun, L. Tarasov, L. D. Trusel, J. Van Breedam, R. van de Wal, M. van den

Broeke, R. Winkelmann, H. Zekollari, C. Zhao, T. Zhang, and T. Zwinger. Projected land ice contributions to twenty-first-century sea level rise. *Nature*, 593(7857):74–82, May 2021. ISSN 1476-4687. URL https://doi.org/10.1038/s41586-021-03302-y.

L. Favier, G. Durand, S. L. Cornford, G. H. Gudmundsson, O. Gagliardini, F. Gillet-Chaulet, T. Zwinger, A. J. Payne, and A. M. Le Brocq. Retreat of pine island glacier controlled by marine ice-sheet instability. *Nature Climate Change*, 4(2):117–121, Feb. 2014. ISSN 1758-6798. URL https://doi.org/10.1038/nclimate2094.

J. Feldmann and A. Levermann. Collapse of the west antarctic ice sheet after local destabilization of the amundsen basin. *Proceedings of the National Academy of Sciences*, 112(46):14191–14196, 2015. ISSN 0027-8424. doi: 10.1073/pnas.1512482112. URL https://www.pnas.org/content/112/46/14191.

T. Frederikse, F. Landerer, L. Caron, S. Adhikari, D. Parkes, V. W. Humphrey, S. Dangendorf, P. Hogarth, L. Zanna, L. Cheng, and Y.-H. Wu. The causes of sea-level rise since 1900. *Nature*, 584(7821):393–397, Aug. 2020. ISSN 1476-4687. URL https://doi.org/10.1038/s41586-020-2591-3.

P. Fretwell, H. D. Pritchard, D. G. Vaughan, J. L. Bamber, N. E. Barrand, R. Bell, C. Bianchi, R. G. Bingham, D. D. Blankenship, G. Casassa, G. Catania, D. Callens, H. Conway, A. J. Cook, H. F. J. Corr, D. Damaske, V. Damm, F. Ferraccioli, R. Forsberg, S. Fujita, Y. Gim, P. Gogineni, J. A. Griggs, R. C. A. Hindmarsh, P. Holmlund, J. W. Holt, R. W. Jacobel, A. Jenkins, W. Jokat, T. Jordan, E. C. King, J. Kohler, W. Krabill, M. Riger-Kusk, K. A. Langley, G. Leitchenkov, C. Leuschen, B. P. Luyendyk, K. Matsuoka, J. Mouginot, F. O. Nitsche, Y. Nogi, O. A. Nost, S. V. Popov, E. Rignot, D. M. Rippin, A. Rivera, J. Roberts, N. Ross, M. J. Siegert, A. M. Smith, D. Steinhage, M. Studinger, B. Sun, B. K. Tinto, B. C. Welch, D. Wilson, D. A. Young, C. Xiangbin, and A. Zirizzotti. Bedmap2: improved ice bed, surface and thickness datasets for antarctica. *The Cryosphere*, 7(1):375–393, 2013. doi: 10.5194/tc-7-375-2013. URL http://www.the-cryosphere.net/7/375/2013/.

K. Frieler, P. U. Clark, F. He, C. Buizert, R. Reese, S. R. M. Ligtenberg, M. R. van den Broeke, R. Winkelmann, and A. Levermann. Consistent evidence of increasing antarctic accumulation with warming. *Nature Climate Change*, 5(4):348–352, Apr. 2015. ISSN 1758-6798. URL https://doi.org/10.1038/nclimate2574.

N. F. Glasser and T. A. Scambos. A structural glaciological analysis of the 2002 larsen b ice-shelf collapse. *Journal of Glaciology*, 54(184):3–16, 2008. doi: 10.3189/002214308784409017.

N. R. Golledge, E. D. Keller, N. Gomez, K. A. Naughten, J. Bernales, L. D. Trusel, and T. L. Edwards. Global environmental consequences of twenty-first-century ice-sheet melt. *Nature*, 566(7742):65–72, Feb. 2019. ISSN 1476-4687. URL https://doi.org/10.1038/s41586-019-0889-9.

M. E. Hauer, E. Fussell, V. Mueller, M. Burkett, M. Call, K. Abel, R. McLeman, and D. Wrathall. Sea-level rise and human migration. *Nature Reviews Earth & Environment*, 1(1):28–39, Jan. 2020. ISSN 2662-138X. URL https://doi.org/10.1038/s43017-019-0002-9.

T. Hughes. Theoretical calving rates from glaciers along ice walls grounded in water of variable depths. *Journal of Glaciology*, 38(129):282–294, 1992. ISSN 0022-1430. doi: 10.3198/1992JoG38-129-282-294. URL http://www.ingentaconnect.com/content/igsoc/jog/1992/00000038/00000129/art00008.

IPCC. Ipcc special report on the ocean and cryosphere in a changing climate. Technical report, IPCC, 2019.

IPCC. Climate change 2021: The physical science basis. contribution of working group i to the sixthassessment report of the intergovernmental panel on climate change. Technical report, IPCC, 2021.

M. Jakobsson, K. A. Hogan, L. A. Mayer, A. Mix, A. Jennings, J. Stoner, B. Eriksson, K. Jerram, R. Mohammad, C. Pearce, B. Reilly, and C. Stranne. The holocene retreat dynamics and stability of petermann glacier in northwest greenland. *Nature Communications*, 9(1):2104, May 2018. ISSN 2041-1723. URL https://doi.org/10.1038/s41467-018-04573-2.

S. Jeong, I. M. Howat, and J. N. Bassis. Accelerated ice shelf rifting and retreat at pine island glacier, west antarctica. *Geophysical Research Letters*, 43(22):11,720–11,725, 2016. doi: 10.1002/2016GL071360. URL https://agupubs.onlinelibrary.wiley.com/doi/abs/10.1002/2016GL071360.

S. Jiménez and R. Duddu. On the evaluation of the stress intensity factor in calving models using linear elastic fracture mechanics. *Journal of Glaciology*, 64(247):759–770, 2018. doi: 10.1017/jog.2018.64.

I. Joughin and R. B. Alley. Stability of the West Antarctic ice sheet in a warming world. *Nature Geosci*, 4(8):506–513, 2011. ISSN 1752-0894. doi: http://dx.doi.org/10.1038/ngeo1194. 10.1038/ngeo1194.

I. Joughin and D. R. MacAyeal. Calving of large tabular icebergs from ice shelf rift systems. *Geophysical Research Letters*, 32(2), 2005. ISSN 1944-8007. doi: 10.1029/2004GL020978. URL http://dx.doi.org/10.1029/2004GL020978. L02501.

I. Joughin, I. M. Howat, M. Fahnestock, B. Smith, W. Krabill, R. B. Alley, H. Stern, and M. Truffer. Continued evolution of jakobshavn isbrae following its rapid speedup. *Journal of Geophysical Research: Earth Surface*, 113(F4), 2008. ISSN 2156-2202. doi: 10.1029/2008JF001023. URL http://dx.doi.org/10.1029/2008JF001023. F04006.

I. Joughin, B. E. Smith, and B. Medley. Marine ice sheet collapse potentially under way for the thwaites glacier basin, west antarctica. *Science*, 344(6185):735–738, 2014. ISSN 0036-8075. doi: 10.1126/science.1249055. URL https://science.sciencemag.org/content/344/6185/735.

A. Khazendar, I. G. Fenty, D. Carroll, A. Gardner, C. M. Lee, I. Fukumori, O. Wang, H. Zhang, H. Seroussi, D. Moller, B. P. Y. Noël, M. R. van den Broeke, S. Dinardo, and J. Willis. Interruption of two decades of jakobshavn isbrae acceleration and thinning as regional ocean cools. *Nature Geoscience*, 12(4):277–283, Apr. 2019. ISSN 1752-0908. URL https://doi.org/10.1038/s41561-019-0329-3.

R. E. Kopp, R. M. Horton, C. M. Little, J. X. Mitrovica, M. Oppenheimer, D. J. Rasmussen, B. H. Strauss, and C. Tebaldi. Probabilistic 21st and 22nd century sea-level

projections at a global network of tide-gauge sites. *Earth's Future*, 2(8):383–406, 2014. doi: https://doi.org/10.1002/2014EF000239. URL https://agupubs.onlinelibrary.wiley.com/doi/abs/10.1002/2014EF000239.

R. E. Kopp, R. M. DeConto, D. A. Bader, C. C. Hay, R. M. Horton, S. Kulp, M. Oppenheimer, D. Pollard, and B. H. Strauss. Evolving understanding of antarctic ice-sheet physics and ambiguity in probabilistic sea-level projections. *Earth's Future*, 5(12):1217–1233, 2017. doi: 10.1002/2017EF000663. URL https://agupubs.onlinelibrary.wiley.com/doi/abs/10.1002/2017EF000663.

J. Krug, J. Weiss, O. Gagliardini, and G. Durand. Combining damage and fracture mechanics to model calving. *The Cryosphere*, 8(6):2101–2117, 2014.

J. Krug, G. Durand, O. Gagliardini, and J. Weiss. Modelling the impact of submarine frontal melting and ice mélange on glacier dynamics. *The Cryosphere*, 9(3):989–1003, 2015. doi: 10.5194/tc-9-989-2015. URL https://www.the-cryosphere.net/9/989/2015/.

M. A. Lazzara, K. C. Jezek, T. A. Scambos, D. R. MacAyeal, and C. J. van der Veen. On the recent calving of icebergs from the ross ice shelf. *Polar Geography*, 23(3):201–212, 1999. doi: 10.1080/10889379909377676. URL http://dx.doi.org/10.1080/10889379909377676.

A. Levermann, R. Winkelmann, T. Albrecht, H. Goelzer, N. R. Golledge, R. Greve, P. Huybrechts, J. Jordan, G. Leguy, D. Martin, M. Morlighem, F. Pattyn, D. Pollard, A. Quiquet, C. Rodehacke, H. Seroussi, J. Sutter, T. Zhang, J. Van Breedam, R. Calov, R. DeConto, C. Dumas, J. Garbe, G. H. Gudmundsson, M. J. Hoffman, A. Humbert, T. Kleiner, W. H. Lipscomb, M. Meinshausen, E. Ng, S. M. J. Nowicki, M. Perego, S. F. Price, F. Saito, N.-J. Schlegel, S. Sun, and R. S. W. van de Wal. Projecting antarctica's contribution to future sea level rise from basal ice shelf melt using linear response functions of 16 ice sheet models (larmip-2). *Earth System Dynamics*, 11(1):35–76, 2020. doi: 10.5194/esd-11-35-2020. URL https://www.earth-syst-dynam.net/11/35/2020/.

S. Lhermitte, S. Sun, C. Shuman, B. Wouters, F. Pattyn, J. Wuite, E. Berthier, and T. Nagler. Damage accelerates ice shelf instability and mass loss in amundsen sea embayment. *Proceedings of the National Academy of Sciences*, 117(40):24735–24741, 2020. ISSN 0027-8424. doi: 10.1073/pnas.1912890117. URL https://www.pnas.org/content/early/2020/09/08/1912890117.

Y. Ma, C. S. Tripathy, and J. N. Bassis. Bounds on the calving cliff height of marine terminating glaciers. *Geophysical Research Letters*, 44(3):1369–1375, 2017. ISSN 1944-8007. doi: 10.1002/2016GL071560. URL http://dx.doi.org/10.1002/2016GL071560. 2016GL071560.

D. R. MacAyeal, T. A. Scambos, C. L. Hulbe, and M. A. Fahnestock. Catastrophic ice-shelf break-up by an ice-shelf-fragment-capsize mechanism. *Journal of Glaciology*, 49(164):22–36, 2003. ISSN 0022-1430. doi: doi:10.3189/172756503781830863. URL http://www.ingentaconnect.com/content/igsoc/jog/2003/00000049/00000164/art00004.

G. McGranahan, D. Balk, and B. Anderson. The rising tide: assessing the risks of climate change and human settlements in low elevation coastal zones. *Environment and Urbanization*, 19(1):17–37, 2007. doi: 10.1177/0956247807076960. URL https://doi.org/10.1177/0956247807076960.

D. Medrzycka, D. I. Benn, J. E. Box, L. Copland, and J. Balog. Calving behavior at rink isbræ, west greenland, from time-lapse photos. *Arctic, Antarctic, and Alpine Research*, 48(2):263–277, May 2016. ISSN 1523-0430. doi: 10.1657/aaar0015-059. URL https://doi.org/10.1657/AAAR0015-059.

M. F. Meier and A. Post. Fast tidewater glaciers. *Journal of Geophysical Research: Solid Earth*, 92(B9):9051–9058, 1987. ISSN 2156-2202. doi: 10.1029/JB092iB09p09051. URL http://dx.doi.org/10.1029/JB092iB09p09051.

M. Mengel, J. Feldmann, and A. Levermann. Linear sea-level response to abrupt ocean warming of major west antarctic ice basin. *Nature Climate Change*, 6:71–74, Oct. 2016. URL http://dx.doi.org/10.1038/nclimate2808.

M. Mengel, A. Nauels, J. Rogelj, and C.-F. Schleussner. Committed sea-level rise under the paris agreement and the legacy of delayed mitigation action. *Nature Communications*, 9 (1):601, Feb. 2018. ISSN 2041-1723. URL https://doi.org/10.1038/s41467-018-02985-8.

R. Mercenier, M. P. Lüthi, and A. Vieli. Calving relation for tidewater glaciers based on detailed stress field analysis. *The Cryosphere*, 12(2):721–739, 2018. doi: 10.5194/tc-12-721-2018. URL https://www.the-cryosphere.net/12/721/2018/.

S. H. Mernild, T. L. Mote, and G. E. Liston. Greenland ice sheet surface melt extent and trends: 1960–2010. *Journal of Glaciology*, 57(204):621–628, 2011. doi: 10.3189/002214311797409712.

P. Milillo, E. Rignot, P. Rizzoli, B. Scheuchl, J. Mouginot, J. Bueso-Bello, and P. Prats-Iraola. Heterogeneous retreat and ice melt of thwaites glacier, west antarctica. *Science Advances*, 5(1), 2019. doi: 10.1126/sciadv.aau3433. URL http://advances.sciencemag.org/content/5/1/eaau3433.

M. Morlighem, J. Bondzio, H. Seroussi, E. Rignot, E. Larour, A. Humbert, and S. Rebuffi. Modeling of store gletscher's calving dynamics, west greenland, in response to ocean thermal forcing. *Geophysical Research Letters*, 43(6):2659–2666, 2016. ISSN 1944-8007. doi: 10.1002/2016GL067695. URL http://dx.doi.org/10.1002/2016GL067695. 2016GL067695.

M. Morlighem, C. N. Williams, E. Rignot, L. An, J. E. Arndt, J. L. Bamber, G. Catania, N. Chauché, J. A. Dowdeswell, B. Dorschel, I. Fenty, K. Hogan, I. Howat, A. Hubbard, M. Jakobsson, T. M. Jordan, K. K. Kjeldsen, R. Millan, L. Mayer, J. Mouginot, B. P. Y. Noël, C. O'Cofaigh, S. Palmer, S. Rysgaard, H. Seroussi, M. J. Siegert, P. Slabon, F. Straneo, M. R. van den Broeke, W. Weinrebe, M. Wood, and K. B. Zinglersen. Bedmachine v3: Complete bed topography and ocean bathymetry mapping of greenland from multibeam echo sounding combined with mass conservation. *Geophysical Research Letters*, 44(21):11,051–11,061, 2017. doi: https://doi.org/10.1002/2017GL074954. URL https://agupubs.onlinelibrary.wiley.com/doi/abs/10.1002/2017GL074954.

J. Mouginot, E. Rignot, and B. Scheuchl. Sustained increase in ice discharge from the amundsen sea embayment, west antarctica, from 1973 to 2013. *Geophysical Research Letters*, 41(5):1576–1584, 2014. doi: https://doi.org/10.1002/2013GL059069. URL https://agupubs.onlinelibrary.wiley.com/doi/abs/10.1002/2013GL059069.

K. A. Naughten, K. J. Meissner, B. K. Galton-Fenzi, M. H. England, R. Timmermann, and H. H. Hellmer. Future projections of antarctic ice shelf melting based on cmip5 scenarios. *Journal of Climate*, 31(13):5243–5261, 2018.

S. V. Nghiem, D. K. Hall, T. L. Mote, M. Tedesco, M. R. Albert, K. Keegan, C. A. Shuman, N. E. DiGirolamo, and G. Neumann. The extreme melt across the greenland ice sheet in 2012. *Geophysical Research Letters*, 39(20), 2012. doi: https://doi.org/10.1029/2012GL053611. URL https://agupubs.onlinelibrary.wiley.com/doi/abs/10.1029/2012GL053611.

F. M. Nick, C. J. van der Veen, A. Vieli, and D. I. Benn. A physically based calving model applied to marine outlet glaciers and implications for the glacier dynamics. *Journal of Glaciology*, 56(199):781–794, 2010. ISSN 0022-1430. doi: doi:10.3189/002214310794457344. URL http://www.ingentaconnect.com/content/igsoc/jog/2010/00000056/00000199/art00004.

T. L. Noble, E. J. Rohling, A. R. A. Aitken, H. C. Bostock, Z. Chase, N. Gomez, L. M. Jong, M. A. King, A. N. Mackintosh, F. S. McCormack, R. M. McKay, L. Menviel, S. J. Phipps, M. E. Weber, C. J. Fogwill, B. Gayen, N. R. Golledge, D. E. Gwyther, A. M. Hogg, Y. M. Martos, B. Pena-Molino, J. Roberts, T. van de Flierdt, and T. Williams. The sensitivity of the antarctic ice sheet to a changing climate: Past, present, and future. *Reviews of Geophysics*, 58(4):e2019RG000663, 2020. doi: https://doi.org/10.1029/2019RG000663. URL https://agupubs.onlinelibrary.wiley.com/doi/abs/10.1029/2019RG000663. e2019RG000663 2019RG000663.

S. M. J. Nowicki, A. Payne, E. Larour, H. Seroussi, H. Goelzer, W. Lipscomb, J. Gregory, A. Abe-Ouchi, and A. Shepherd. Ice sheet model intercomparison project (ismip6) contribution to cmip6. *Geoscientific Model Development*, 9(12):4521–4545, 2016. doi: 10.5194/gmd-9-4521-2016. URL https://gmd.copernicus.org/articles/9/4521/2016/.

J. F. Nye. The distribution of stress and velocity in glaciers and ice-sheets. *Proceedings of the Royal Society of London A: Mathematical, Physical and Engineering Sciences*, 239 (1216):113–133, 1957. ISSN 0080-4630. doi: 10.1098/rspa.1957.0026. URL http://rspa.royalsocietypublishing.org/content/239/1216/113.

C. Palerme, J. E. Kay, C. Genthon, T. L'Ecuyer, N. B. Wood, and C. Claud. How much snow falls on the antarctic ice sheet? *The Cryosphere*, 8(4):1577–1587, 2014. doi: 10.5194/tc-8-1577-2014. URL https://tc.copernicus.org/articles/8/1577/2014/.

F. S. Paolo, H. A. Fricker, and L. Padman. Volume loss from antarctic ice shelves is accelerating. *Science*, 348(6232):327–331, 2015. ISSN 0036-8075. doi: 10.1126/science.aaa0940. URL https://science.sciencemag.org/content/348/6232/327.

B. R. Parizek, K. Christianson, R. B. Alley, D. Voytenko, I. Vaňková, T. H. Dixon, R. T. Walker, and D. M. Holland. Ice-cliff failure via retrogressive slumping. *Geology*, 47(5): 449–452, 03 2019. ISSN 0091-7613. doi: 10.1130/G45880.1. URL https://doi.org/10.1130/G45880.1.

F. Pattyn and M. Morlighem. The uncertain future of the antarctic ice sheet. *Science*, 367(6484):1331–1335, 2020. ISSN 0036-8075. doi: 10.1126/science.aaz5487. URL https://science.sciencemag.org/content/367/6484/1331.

F. Pattyn, L. Perichon, G. Durand, L. Favier, O. Gagliardini, R. C. A. Hindmarsh, T. Zwinger, T. Albrecht, S. Cornford, D. Docquier, J. J. Fürst, D. Goldberg, G. H. Gudmundsson, A. Humbert, M. Hütten, P. Huybrechts, G. Jouvet, T. Kleiner, E. Larour, D. Martin, M. Morlighem, A. J. Payne, D. Pollard, M. Rückamp, O. Rybak, H. Seroussi, M. Thoma, and N. Wilkens. Grounding-line migration in plan-view marine ice-sheet models: results of the ice2sea mismip3d intercomparison. *Journal of Glaciology*, 59(215): 410–422, 2013. doi: 10.3189/2013JoG12J129.

D. Pollard, R. M. DeConto, and R. B. Alley. Potential antarctic ice sheet retreat driven by hydrofracturing and ice cliff failure. *Earth and Planetary Science Letters*, 412:112–121, 2015. ISSN 0012-821X. doi: http://dx.doi.org/10.1016/j.epsl.2014.12.035. URL http://www.sciencedirect.com/science/article/pii/S0012821X14007961.

A. Pralong and M. Funk. Dynamic damage model of crevasse opening and application to glacier calving. *Journal of Geophysical Research (Solid Earth)*, 110:B01309, 2005. doi: 10.1029/2004JB003104.

A. Pralong, M. Funk, and M. P. Lüthi. A description of crevasse formation using continuum damage mechanics. *Annals of Glaciology*, 37(1):77–82, 2003.

W. Rack and H. Rott. Pattern of retreat and disintegration of the larsen b ice shelf, antarctic peninsula. *Annals of Glaciology*, 39:505–510, 2004. doi: 10.3189/172756404781814005.

R. Reese, G. H. Gudmundsson, A. Levermann, and R. Winkelmann. The far reach of ice-shelf thinning in antarctica. *Nature Climate Change*, 8(1):53–57, Jan. 2018. ISSN 1758-6798. URL https://doi.org/10.1038/s41558-017-0020-x.

E. Rignot, G. Casassa, P. Gogineni, W. Krabill, A. Rivera, and R. Thomas. Accelerated ice discharge from the antarctic peninsula following the collapse of larsen b ice shelf. *Geophysical Research Letters*, 31(18), 2004. ISSN 1944-8007. doi: 10.1029/2004GL020697. URL http://dx.doi.org/10.1029/2004GL020697. L18401.

E. Rignot, J. Mouginot, M. Morlighem, H. Seroussi, and B. Scheuchl. Widespread, rapid grounding line retreat of pine island, thwaites, smith, and kohler glaciers, west antarctica, from 1992 to 2011. *Geophysical Research Letters*, 41(10):3502–3509, 2014. ISSN 1944-8007. doi: 10.1002/2014GL060140. URL http://dx.doi.org/10.1002/2014GL060140.

E. Rignot, J. Mouginot, B. Scheuchl, M. van den Broeke, M. J. van Wessem, and M. Morlighem. Four decades of antarctic ice sheet mass balance from 1979–2017. *Proceedings of the National Academy of Sciences*, (116), 2019. doi: 10.1073/pnas.1812883116.

C. Ritz, Edwards, Tamsin L., Durand, Gaël, Payne, Antony J., Peyaud, Vincent, and Hindmarsh, Richard C. A. Potential sea-level rise from Antarctic ice-sheet instability constrained by observations. *Nature*, 528(7580):115–118, 2015. ISSN 0028-0836. doi: http://dx.doi.org/10.1038/nature1614710.1038/nature16147. URL http://www.nature.com/nature/journal/v528/n7580/abs/nature16147.html#supplementary-information.

A. A. Robel. Thinning sea ice weakens buttressing force of iceberg mélange and promotes calving. *Nature Communications*, 8:14596, Mar. 2017. URL https://doi.org/10.1038/ncomms14596.

A. A. Robel and A. F. Banwell. A speed limit on ice shelf collapse through hydrofracture. *Geophysical Research Letters*, 46(21):12092–12100, 2019. doi: 10.1029/2019GL084397. URL https://agupubs.onlinelibrary.wiley.com/doi/abs/10.1029/2019GL084397.

J. C. Ryan, L. C. Smith, D. van As, S. W. Cooley, M. G. Cooper, L. H. Pitcher, and A. Hubbard. Greenland ice sheet surface melt amplified by snowline migration and bare ice exposure. *Science Advances*, 5(3), 2019. doi: 10.1126/sciadv.aav3738. URL https://advances.sciencemag.org/content/5/3/eaav3738.

T. A. Scambos, C. Hulbe, M. Fahnestock, and J. Bohlander. The link between climate warming and break-up of ice shelves in the antarctic peninsula. *Journal of Glaciology*, 46(154):516–530, 2000. ISSN 0022-1430. doi: doi:10.3189/172756500781833043. URL http://www.ingentaconnect.com/content/igsoc/jog/2000/00000046/00000154/art00018.

T. A. Scambos, J. A. Bohlander, C. A. Shuman, and P. Skvarca. Glacier acceleration and thinning after ice shelf collapse in the larsen b embayment, antarctica. *Geophysical Research Letters*, 31(18), 2004. ISSN 1944-8007. doi: 10.1029/2004GL020670. URL http://dx.doi.org/10.1029/2004GL020670. L18402.

T. A. Scambos, R. E. Bell, R. B. Alley, S. Anandakrishnan, D. H. Bromwich, K. Brunt, K. Christianson, T. Creyts, S. B. Das, R. DeConto, P. Dutrieux, H. A. Fricker, D. Holland, J. MacGregor, B. Medley, J. P. Nicolas, D. Pollard, M. R. Siegfried, A. M. Smith, E. J. Steig, L. D. Trusel, D. G. Vaughan, and P. L. Yager. How much, how fast?: A science review and outlook for research on the instability of antarctica's thwaites glacier in the 21st century. *Global and Planetary Change*, 153:16–34, 2017. ISSN 0921-8181. doi: https://doi.org/10.1016/j.gloplacha.2017.04.008. URL https://www.sciencedirect.com/science/article/pii/S092181811630491X.

T. Schlemm and A. Levermann. A simple stress-based cliff-calving law. *The Cryosphere*, 13 (9):2475–2488, 2019. doi: 10.5194/tc-13-2475-2019. URL https://www.the-cryosphere.net/13/2475/2019/.

T. Schlemm and A. Levermann. A simple parametrization of mélange buttressing for calving glaciers. *The Cryosphere*, 15(2):531–545, 2021. doi: 10.5194/tc-15-531-2021. URL https://tc.copernicus.org/articles/15/531/2021/.

T. Schlemm, J. Feldmann, R. Winkelmann, and A. Levermann. Stabilizing effect of mélange buttressing on the marine ice-cliff instability of the west antarctic ice sheet. *The Cryosphere*, 16(5):1979–1996, 2022. doi: 10.5194/tc-16-1979-2022. URL https://tc.copernicus.org/articles/16/1979/2022/.

S. Schmidtko, K. J. Heywood, A. F. Thompson, and S. Aoki. Multidecadal warming of antarctic waters. *Science*, 346(6214):1227–1231, 2014. ISSN 0036-8075. doi: 10.1126/science.1256117. URL https://science.sciencemag.org/content/346/6214/1227.

M. P. Schodlok, H. H. Hellmer, G. Rohardt, and E. Fahrbach. Weddell sea iceberg drift: Five years of observations. *Journal of Geophysical Research: Oceans*, 111(C6), 2006. doi: https://doi.org/10.1029/2004JC002661. URL https://agupubs.onlinelibrary.wiley.com/doi/abs/10.1029/2004JC002661.

C. Schoof. A variational approach to ice stream flow. *Journal of Fluid Mechanics*, 556: 227–251, 2006. doi: 10.1017/S0022112006009591.

C. Schoof. Ice sheet grounding line dynamics: Steady states, stability, and hysteresis. *Journal of Geophysical Research: Earth Surface*, 112(F3), 2007. ISSN 2156-2202. doi: 10.1029/2006JF000664. URL http://dx.doi.org/10.1029/2006JF000664. F03S28.

E. M. Schulson. Brittle failure of ice. *Engineering Fracture Mechanics*, 68(17 – 18): 1839–1887, 2001. ISSN 0013-7944. doi: http://dx.doi.org/10.1016/S0013-7944(01)00037-6. URL http://www.sciencedirect.com/science/article/pii/S0013794401000376.

E. M. Schulson, D. Iliescu, and C. E. Renshaw. On the initiation of shear faults during brittle compressive failure: A new mechanism. *Journal of Geophysical Research: Solid Earth*, 104(B1):695–705, 1999. ISSN 2156-2202. doi: 10.1029/1998JB900017. URL http://dx.doi.org/10.1029/1998JB900017.

H. Seroussi, S. Nowicki, E. Simon, A. Abe-Ouchi, T. Albrecht, J. Brondex, S. Cornford, C. Dumas, F. Gillet-Chaulet, H. Goelzer, N. R. Golledge, J. M. Gregory, R. Greve, M. J. Hoffman, A. Humbert, P. Huybrechts, T. Kleiner, E. Larour, G. Leguy, W. H. Lipscomb, D. Lowry, M. Mengel, M. Morlighem, F. Pattyn, A. J. Payne, D. Pollard, S. F. Price, A. Quiquet, T. J. Reerink, R. Reese, C. B. Rodehacke, N.-J. Schlegel, A. Shepherd, S. Sun, J. Sutter, J. Van Breedam, R. S. W. van de Wal, R. Winkelmann, and T. Zhang. initmip-antarctica: an ice sheet model initialization experiment of ismip6. *The Cryosphere*, 13(5):1441–1471, 2019. doi: 10.5194/tc-13-1441-2019. URL https://www.the-cryosphere.net/13/1441/2019/.

H. Seroussi, S. Nowicki, A. J. Payne, H. Goelzer, W. H. Lipscomb, A. Abe-Ouchi, C. Agosta, T. Albrecht, X. Asay-Davis, A. Barthel, R. Calov, R. Cullather, C. Dumas, B. K. Galton-Fenzi, R. Gladstone, N. R. Golledge, J. M. Gregory, R. Greve, T. Hattermann, M. J. Hoffman, A. Humbert, P. Huybrechts, N. C. Jourdain, T. Kleiner, E. Larour, G. R. Leguy, D. P. Lowry, C. M. Little, M. Morlighem, F. Pattyn, T. Pelle, S. F. Price, A. Quiquet, R. Reese, N.-J. Schlegel, A. Shepherd, E. Simon, R. S. Smith, F. Straneo, S. Sun, L. D. Trusel, J. Van Breedam, R. S. W. van de Wal, R. Winkelmann, C. Zhao, T. Zhang, and T. Zwinger. Ismip6 antarctica: a multi-model ensemble of the antarctic ice sheet evolution over the 21st century. *The Cryosphere*, 14(9):3033–3070, 2020. doi: 10.5194/tc-14-3033-2020. URL https://tc.copernicus.org/articles/14/3033/2020/.

A. Shepherd, D. Wingham, and E. Rignot. Warm ocean is eroding west antarctic ice sheet. *Geophysical Research Letters*, 31(23), 2004. ISSN 1944-8007. doi: 10.1029/2004GL021106. URL http://dx.doi.org/10.1029/2004GL021106. L23402.

A. Shepherd, H. A. Fricker, and S. L. Farrell. Trends and connections across the antarctic cryosphere. *Nature*, 558(7709):223–232, June 2018. ISSN 1476-4687. URL https://doi.org/10.1038/s41586-018-0171-6.

A. B. A. Slangen, F. Adloff, S. Jevrejeva, P. W. Leclercq, B. Marzeion, Y. Wada, and R. Winkelmann. *A Review of Recent Updates of Sea-Level Projections at Global and Regional Scales*, pages 395–416. Springer International Publishing, Cham, 2017. ISBN 978-3-319-56490-6. doi: 10.1007/978-3-319-56490-6_17. URL https://doi.org/10.1007/978-3-319-56490-6_17.

B. Smith, H. A. Fricker, A. S. Gardner, B. Medley, J. Nilsson, F. S. Paolo, N. Holschuh, S. Adusumilli, K. Brunt, B. Csatho, K. Harbeck, T. Markus, T. Neumann, M. R. Siegfried, and H. J. Zwally. Pervasive ice sheet mass loss reflects competing ocean and atmosphere processes. *Science*, 368(6496):1239–1242, 2020. ISSN 0036-8075. doi: 10.1126/science.aaz5845. URL https://science.sciencemag.org/content/368/6496/1239.

S. Sun, F. Pattyn, E. G. Simon, T. Albrecht, S. Cornford, R. Calov, C. Dumas, F. Gillet-Chaulet, H. Goelzer, N. R. Golledge, R. Greve, M. J. Hoffman, A. Humbert, E. Kazmierczak, T. Kleiner, G. R. Leguy, W. H. Lipscomb, D. Martin, M. Morlighem, S. Nowicki, D. Pollard, S. Price, A. Quiquet, H. Seroussi, T. Schlemm, J. Sutter, R. S. W. van de Wal, R. Winkelmann, and T. Zhang. Antarctic ice sheet response to sudden and sustained ice-shelf collapse (abumip). *Journal of Glaciology*, 66(260):891–904, 2020. doi: 10.1017/jog.2020.67.

J. Todd, P. Christoffersen, T. Zwinger, P. Råback, N. Chauché, D. Benn, A. Luckman, J. Ryan, N. Toberg, D. Slater, and A. Hubbard. A full-stokes 3-d calving model applied to a large greenlandic glacier. *Journal of Geophysical Research: Earth Surface*, 123(3):410–432, 2018. doi: 10.1002/2017JF004349. URL https://agupubs.onlinelibrary.wiley.com/doi/abs/10.1002/2017JF004349.

J. Todd, P. Christoffersen, T. Zwinger, P. Råback, and D. I. Benn. Sensitivity of a calving glacier to ice–ocean interactions under climate change: new insights from a 3-d full-stokes model. *The Cryosphere*, 13(6):1681–1694, 2019. doi: 10.5194/tc-13-1681-2019. URL https://www.the-cryosphere.net/13/1681/2019/.

L. D. Trusel, K. E. Frey, S. B. Das, K. B. Karnauskas, P. Kuipers Munneke, E. van Meijgaard, and M. R. van den Broeke. Divergent trajectories of antarctic surface melt under two twenty-first-century climate scenarios. *Nature Geoscience*, 8(12):927–932, Dec. 2015. ISSN 1752-0908. URL https://doi.org/10.1038/ngeo2563.

L. Ultee and J. N. Bassis. Sermeq model produces a realistic upper bound on calving retreat for 155 greenland outlet glaciers. *Geophysical Research Letters*, 47(21):e2020GL090213, 2020. doi: https://doi.org/10.1029/2020GL090213. URL https://agupubs.onlinelibrary.wiley.com/doi/abs/10.1029/2020GL090213. e2020GL090213 10.1029/2020GL090213.

J. van Der Veen. Tidewater calving. *Journal of Glaciology*, 42(141):375–385, 1996. ISSN 0022-1430. doi: doi:10.3198/1996JoG42-141-375-385. URL http://www.ingentaconnect.com/content/igsoc/jog/1996/00000042/00000141/art00018.

D. G. Vaughan, J. Comiso, I. Allison, J. Carrasco, G. Kaser, R. Kwok, P. Mote, T. Murray, F. Paul, J. Ren, et al. *Observations: cryosphere*. Cambridge University Press, 2014.

A. Vieli, J. Jania, and L. Kolondra. The retreat of a tidewater glacier: observations and model calculations on hansbreen, spitsbergen. *Journal of Glaciology*, 48(163):592–600, 2002. ISSN 0022-1430. doi: doi:10.3189/172756502781831089. URL http://www.ingentaconnect.com/content/igsoc/jog/2002/00000048/00000163/art00013.

J. I. Walter, J. E. Box, S. Tulaczyk, E. E. Brodsky, I. M. Howat, Y. Ahn, and A. Brown. Oceanic mechanical forcing of a marine-terminating greenland glacier. *Annals of Glaciology*, 53(60):181–192, 2012. doi: 10.3189/2012AoG60A083.

J. Weertman. Stability of the junction of an ice sheet and an ice shelf. *Journal of Glaciology*, 13(67):3–11, 1974. doi: 10.3189/S0022143000023327.

R. Winkelmann, M. A. Martin, M. Haseloff, T. Albrecht, E. Bueler, C. Khroulev, and A. Levermann. The Potsdam Parallel Ice Sheet Model (PISM-PIK) – Part 1: Model description. *The Cryosphere*, 5(3):715–726, 2011. doi: 10.5194/tc-5-715-2011. URL http://www.the-cryosphere.net/5/715/2011/.

R. Winkelmann, A. Levermann, A. Ridgwell, and K. Caldeira. Combustion of available fossil fuel resources sufficient to eliminate the antarctic ice sheet. *Science Advances*, 1(8), 2015. doi: 10.1126/sciadv.1500589. URL http://advances.sciencemag.org/content/1/8/e1500589.

M. G. Wise, J. A. Dowdeswell, M. Jakobsson, and R. D. Larter. Evidence of marine ice-cliff instability in pine island bay from iceberg-keel plough marks. *Nature*, 550(7677): 506–510, Oct. 2017. ISSN 1476-4687. URL https://doi.org/10.1038/nature24458.

S. Xie, T. H. Dixon, D. M. Holland, D. Voytenko, and I. Vaňková. Rapid iceberg calving following removal of tightly packed pro-glacial mélange. *Nature Communications*, 10(1): 3250, July 2019. ISSN 2041-1723. URL https://doi.org/10.1038/s41467-019-10908-4.

H. Zhang, L. Ju, M. Gunzburger, T. Ringler, and S. Price. Coupled models and parallel simulations for three-dimensional full-stokes ice sheet modeling. *Numerical Mathematics: Theory, Methods and Applications*, 4(3):396–418, 2011. doi: 10.1017/S1004897900000416.